Heavy Ion Collisions at the LHC - Last Call for Predictions

N Armesto[1], N Borghini[2], S Jeon[3] and U A Wiedemann[4] (editors)

S Abreu[5], S V Akkelin[6], J Alam[7], J L Albacete[8], A Andronic[9], D Antonov[10], F Arleo[4]‡, N Armesto[1], I C Arsene[11], G G Barnaföldi[12], J Barrette[3], B Bäuchle[13,14], F Becattini[15], B Betz[13,16], M Bleicher[13], M Bluhm[17], D Boer[18], F W Bopp[19], P Braun-Munzinger[9,20], L Bravina[11,21], W Busza[22], M Cacciari[23], A Capella[24], J Casalderrey-Solana[25], R Chatterjee[8,7], L-W Chen[26,27], J Cleymans[28], B A Cole[29], Z Conesa Del Valle[30], L P Csernai[14,12], L Cunqueiro[1], A Dainese[31], J Dias de Deus[5], H-T Ding[32], M Djordjevic[8], H Drescher[33], I M Dremin[34] A Dumitru[13], A El[13], R Engel[35], D d'Enterria[36], K J Eskola[37,38], G Fai[39], E G Ferreiro[1], R J Fries[40,41], E Frodermann[8], H Fujii[42], C Gale[3], F Gelis[4], V P Gonçalves[43], V Greco[44], C Greiner[13], M Gyulassy[45,33], H van Hees[40], U Heinz[4]§, H Honkanen[37,38,46], W A Horowitz[45,33], E Iancu[47], G Ingelman[48], J Jalilian-Marian[49], S Jeon[3], A B Kaidalov[50], B Kämpfer[17,51], Z-B Kang[52], Iu A Karpenko[6], G Kestin[8], D Kharzeev[53], C M Ko[40], B Koch[33,13], B Kopeliovich[54,55,10], M Kozlov[2], I Kraus[20,56], I Kuznetsova[57], S H Lee[58], R Lednicky[55,59], J Letessier[23], E Levin[60], B-A Li[61], Z-W Lin[62], H Liu[63], W Liu[40], C Loizides[22], I P Lokhtin[21], M V T Machado[43], L V Malinina[21,55], A M Managadze[21], M L Mangano[4], M Mannarelli[64], C Manuel[64], G Martínez[30], J G Milhano[5], Á Mócsy[41], D Molnár[65,41], M Nardi[66], J K Nayak[7], H Niemi[37,38], H Oeschler[20], J-Y Ollitrault[47], G Paić[67], C Pajares[1], V S Pantuev[68], G Papp[69], D Peressounko[70], P Petreczky[53], S V Petrushanko[21], F Piccinini[71], T Pierog[35], H J Pirner[10], S Porteboeuf[30], I Potashnikova[54], G Y Qin[3], J-W Qiu[52,53], J Rafelski[57,4], K Rajagopal[63], J Ranft[19], R Rapp[40], S S Räsänen[37], J Rathsman[48], P Rau[13], K Redlich[72], T Renk[37,38], A H Rezaeian[54], D Rischke[13,33], S Roesler[73], J Ruppert[3], P V Ruuskanen[37,38], C A Salgado[1,74], S Sapeta[4,75], I Sarcevic[57], S Sarkar[7], L I Sarycheva[21], I Schmidt[54], A I Shoshi[2], B Sinha[7], Yu M Sinyukov[6], A M Snigirev[21], D K Srivastava[7], J Stachel[76], A Stasto[77], H Stöcker[13,33,9], C Yu Teplov[21], R L Thews[57], G Torrieri[13,33], V Topor Pop[3], D N Triantafyllopoulos[78], K L Tuchin[52,41], S Turbide[3], K

‡ On leave from Laboratoire d'Annecy-le-Vieux de Physique Théorique (LAPTH), UMR 5108 du CNRS associée à l'Université de Savoie, B.P. 110, 74941 Annecy-le-Vieux Cedex, France.
§ On leave from [8].

Tywoniuk[11], A Utermann[18], R Venugopalan[53], I Vitev[79], R Vogt[80,81], E Wang[32,25], X N Wang[25], K Werner[30], E Wessels[18], S Wheaton[20,28], S Wicks[45,33], U A Wiedemann[4], G Wolschin[10], B-W Xiao[45], Z Xu[13], S Yasui[57], E Zabrodin[11,21], K Zapp[77], B Zhang[82], B-W Zhang[40]||, H Zhang[32] and D Zhou[32] (authors)¶

[1] Departamento de Física de Partículas and IGFAE, Universidade de Santiago de Compostela, 15782 Santiago de Compostela, Spain
[2] Fakultät für Physik, Universität Bielefeld, D-33501 Bielefeld, Germany
[3] Department of Physics, McGill University, Montréal, Canada H3A 2T8
[4] CERN, PH Department, TH Division, 1211 Geneva 23, Switzerland
[5] Instituto Superior Técnico/CENTRA, Av. Rovisco Pais, P-1049-001 Lisboa, Portugal
[6] Bogolyubov Institute for Theoretical Physics, Metrolohichna str. 14-b, 03680 Kiev-143, Ukraine
[7] Variable Energy Cyclotron Centre, 1/AF Bidhan Nagar, Kolkata 700 064, India
[8] Department of Physics, The Ohio State University, 191 W. Woodruff Avenue, OH-43210, Columbus, USA
[9] Gesellschaft für Schwerionenforschung, GSI, D-64291 Darmstadt, Germany
[10] Institut für Theoretische Physik, Universität Heidelberg, Philosophenweg 19, D-69120 Heidelberg, Germany
[11] Department of Physics, University of Oslo, N-0316 Oslo, Norway
[12] MTA KFKI RMKI, P.O. Box 49, Budapest 1525, Hungary
[13] Institut für Theoretische Physik, Universität Frankfurt, Max-von-Laue-Straße 1, D-60438 Frankfurt am Main, Germany
[14] Section for Theoretical Physics, Departement of Physics, University of Bergen, Allégaten 55, 5007 Bergen, Norway
[15] Università di Firenze and INFN Sezione di Firenze, Via G. Sansone 1, I-50019, Sesto F.no, Firenze, Italy
[16] Helmholtz Research School, GSI, FIAS and Universität Frankfurt, Germany
[17] Forschungszentrum Dresden-Rossendorf, PF 510119, 01314 Dresden, Germany
[18] Department of Physics and Astronomy, VU University Amsterdam, De Boelelaan 1081, 1081 HV Amsterdam, The Netherlands
[19] Siegen University, Siegen, Germany
[20] Institut für Kernphysik, Technical University Darmstadt, D-64283 Darmstadt, Germany
[21] Skobeltsyn Institute of Nuclear Physics, Moscow State University, RU-119899 Moscow, Russia
[22] Massachusetts Institute of Technology, Cambridge MA, USA
[23] LPTHE, Université Pierre et Marie Curie (Paris VI), France
[24] Laboratoire de Physique Théorique, Université de Paris XI, Bâtiment 210, 91405 Orsay Cedex, France
[25] Lawrence Berkeley National Laboratory, 1 Cyclotron Road, MS 70R0319, Berkeley, CA 94720, USA
[26] Institute of Theoretical Physics, Shanghai Jiao Tong University, Shanghai 200240, China
[27] Center of Theoretical Nuclear Physics, National Laboratory of Heavy Ion Accelerator, Lanzhou 730000, China
[28] UCT-CERN Research Centre and Department of Physics, University of Cape Town, Rondebosch 7701, South Africa

|| On leave from [32].
¶ The contributors on this author list have contributed only to those subsections of the report, which they cosign with their name. Only those have collaborated together, whose names appear together in the header of a given subsection.

[29] Nevis Laboratory, Columbia University, New York, USA
[30] Subatech (CNRS/IN2P3 - Ecole des Mines - Université de Nantes) Nantes, France
[31] INFN, Laboratori Nazionali di Legnaro, Legnaro (Padova), Italy
[32] Institute of Particle Physics, Central China Normal University, Wuhan, China
[33] Frankfurt Institute for Advanced Studies (FIAS), Johann Wolfgang Goethe-Universität, Max-von-Laue-Str. 1, 60438 Frankfurt am Main, Germany
[34] Lebedev Physical Institute, Leninsky pr. 53, 119991 Moscow, Russia
[35] Forschungszentrum Karlsruhe, Karlsruhe, Germany
[36] CERN/PH, CH-1211 Geneva 23, Switzerland
[37] Department of Physics, P.O. Box 35, FI-40014, University of Jyväskylä, Finland
[38] Helsinki Institute of Physics, P.O. Box 64, FI-00014, University of Helsinki, Finland
[39] Department of Physics, Kent State University, Kent, OH, USA
[40] Cyclotron Institute and Department of Physics, Texas A&M University, College Station TX 77843, USA
[41] RIKEN/BNL Research Center, Brookhaven National Laboratory, Upton NY 11973, USA
[42] Institute of Physics, University of Tokyo, Komaba, Tokyo 153-8 902, Japan
[43] Universidade Federal de Pelotas, Caixa Postal 354, CEP 96010-090, Pelotas, RS, Brazil
[44] Dipartimento di Fisica e Astronomia, Via S. Sofia 64, I-95125 Catania, Italy
[45] Physics Department, Columbia University, New York, New York 10027, USA
[46] Department of Physics, University of Virginia, Charlottesville, VA, USA
[47] Service de Physique Théorique, CEA/DSM/SPhT, CNRS/MPPU/URA2306, CEA Saclay, F-91191 Gif-sur-Yvette Cedex
[48] High Energy Physics, Uppsala University, Box 535, S-75121 Uppsala, Sweden
[49] Department of Natural Sciences, Baruch College, New York, NY 10010, USA
[50] Institute of Theoretical and Experimental Physics, RU-117259 Moscow, Russia
[51] Institut für Theoretische Physik, TU Dresden, 01062 Dresden, Germany
[52] Department of Physics and Astronomy, Iowa State University, Ames IA 50011, USA
[53] Physics Department, Brookhaven National Laboratory, Upton, NY 11793-5000, USA
[54] Departamento de Física y Centro de Estudios Subatómicos, Universidad Técnica Federico Santa María, Casilla 110-V, Valparaíso, Chile
[55]Joint Institute for Nuclear Research, Dubna, Moscow Region, 141980, Russia
[56] Nikhef, Kruislaan 409, 1098 SJ Amsterdam, The Netherlands
[57] Department of Physics, University of Arizona, Tucson, Arizona 85721, USA
[58] Institute of Physics and Applied Physics, Yonsei University, Seoul 120-749, Korea
[59] Institute of Physics ASCR, Prague, 18221, Czech Republic
[60] HEP Department, School of Physics, Raymond and Beverly Sackler Faculty of Exact Science, Tel Aviv University, Tel Aviv 69978, Israel
[61] Department of Physics, Texas A&M University-Commerce, Commerce, Texas 75429-3011, USA
[62] Mail Stop VP62, NSSTC, 320 Sparkman Dr., Huntsville, AL 35805 and Department of Physics, East Carolina University, Greenville, North Carolina 27858-4353, USA
[63] Center for Theoretical Physics, MIT, Cambridge, MA 02139, USA
[64] Instituto de Ciencias del Espacio (IEEC/CSIC), Campus U.A.B., Fac. de Ciències, Torre C5, E-08193 Bellaterra (Barcelona), Spain
[65] Physics Department, Purdue University, West Lafayette, IN 47907, USA
[66] INFN, Sezione di Torino, via Giuria N.1, 10125 Torino, Italy
[67] Instituto de Ciencias Nucleares, UNAM, Mexico City, Mexico
[68] University at Stony Brook, Stony Brook, New York 11794, USA
[69] Department of Theoretical Physics, ELTE, Pázmány P. 1/A, Budapest 1117, Hungary
[70] RRC "Kurchatov Institute", Kurchatov Sq. 1, Moscow 123182, Russia
[71] INFN Sezione di Pavia, Pavia, Italy

[72] Institute of Theoretical Physics, University of Wrocław, PL-50204 Wrocław, Poland
[73] CERN/SC, CH-1211 Geneva 23, Switzerland
[74] Dipartimento di Fisica, Università di Roma "La Sapienza" and INFN, Roma, Italy
[75] M. Smoluchowski Institute of Physics, Jagellonian University, Reymonta 4, 30-059 Cracow, Poland
[76] Physikalisches Institut der Universität Heidelberg, D-69120 Heidelberg, Germany
[77] Physics Department, Penn State University, PA 16802-6300, USA
[78] ECT*, Villa Tambosi, Strada delle Tabarelle 286, I-38050 Villazzano (TN), Italy
[79] Los Alamos National Laboratory, Theoretical Division, Mail Stop B283, Los Alamos, NM 87545, USA
[80] Lawrence Livermore National Laboratory, Livermore, CA, USA
[81] Physics Department, University of California at Davis, Davis, CA, USA
[82] Department of Chemistry and Physics, Arkansas State University, State University, Arkansas 72467-0419, USA

Abstract. This writeup is a compilation of the predictions for the forthcoming Heavy Ion Program at the Large Hadron Collider, as presented at the CERN Theory Institute 'Heavy Ion Collisions at the LHC - Last Call for Predictions', held from May 14th to June 10th 2007.

Contents

Preface

In August 2006, the CERN Theory Unit announced to restructure its visitor program and to create a "CERN Theory Institute", where 1-3 month long specific programs can take place. The first such Institute was held from 14 May to 10 June 2007, focussing on "Heavy Ion

Collisions at the LHC - Last Call for Predictions". It brought together close to 100 scientists working on the theory of ultra-relativistic heavy ion collisions. The aim of this workshop was to review and document the status of expectations and predictions for the heavy ion program at the Large Hadron Collider LHC before its start. LHC will explore heavy ion collisions at ~ 30 times higher center of mass energy than explored previously at the Relativistic Heavy Ion Collider RHIC. So, on the one hand, the charge of this workshop provided a natural forum for the exchange of the most recent ideas, and allowed to monitor how the understanding of heavy ion collisions has evolved in recent years with the data from RHIC, and with the preparation of the LHC experimental program. On the other hand, the workshop aimed at a documentation which helps to distinguish pre- from post-dictions. An analogous documentation of the "Last Call for Predictions" [1] was prepared prior to the start of the heavy-ion program at the Relativistic Heavy Ion Collider RHIC, and it proved useful in the subsequent discussion and interpretation of RHIC data. The present write-up is the documentation of predictions for the LHC heavy ion program, received or presented during the CERN TH Institute.

The set-up of the CERN TH Institute allowed us to aim for the wide-most coverage of predictions. There were more than 100 presentations and discussions during the workshop. Moreover, those unable to attend could still participate by submitting predictions in written form during the workshop. This followed the spirit that everybody interested in making a prediction had the right to be heard. The subsequent editorial process aimed at maintaining the breadth of alternative approaches raised, but it was based on the standard criteria of scientific interest and novelty. To arrive at a concise document, we required that each prediction should be summarized on at most two pages, and that predictions should be presented, whenever possible, in figures which display measurable quantities. Full model descriptions were not accepted - the authors were encouraged to indicate the relevant references for the interested reader. Participants had the possibility to submit multiple contributions on different topics, but it was part of the subsequent editing process to ensure that predictions on neighboring topics were merged wherever possible.

The contributions summarized here are organized in several sections, - though some of them contain material related with more than one section -, roughly by going from low transverse momentum to high transverse momentum and from abundant to rare measurements. In the low transverse momentum regime, we start with predictions on multiplicity distributions, azimuthal asymmetries in particle production and hadronic flavor observables, followed by correlation and fluctuation measurements. The contributions on hard probes at the LHC start with predictions for single inclusive high transverse momentum spectra, and jets, followed by heavy quark and quarkonium measurements, leptonic probes and photons. A final section "Others" encompasses those predictions which do not fall naturally within one of the above-mentioned categories, or discuss the more speculative phenomena that may be explored at the LHC. On purpose, we refrain in this preface from a significantly expanded introduction to these different sections, since we do not want to single out a particular point of view from which the various contributions should be viewed or even ranked. We limit ourselves to remarking that soft low-momentum measurements can be typically thought of as characterizing the final remnants of the medium formed in a heavy ion

collision, while measurements of leptonic spectra or of hadronic quantities at sufficiently large transverse momentum may be better thought of as having been in contact with that medium but not a part of it. So, the medium dependence of hard processes probes the properties of the produced medium. The LHC heavy ion program is expected to significantly advance our understanding of hot and dense QCD matter, and this article summarizes the majority of recent ideas on how such advances can be achieved in an interplay between theory and experiment in the LHC era.

We would like to end this Preface by thanking the TH Unit at CERN for its generous support of this workshop. Special thanks go to Elena Gianolio, Michelle Mazerand, Nanie Perrin and Jeanne Rostant, whose help and patience was invaluable.

Néstor Armesto
Nicolas Borghini
Sangyong Jeon
Urs Achim Wiedemann

1. Multiplicities and multiplicity distributions

1.1. Multiplicity distributions in rapidity for Pb-Pb and p-Pb central collisions from a simple model

S. Abreu, J. Dias de Deus and J. G. Milhano

The simple model [2] for the distribution of rapidity extended objects (longitudinal glasma colour fields or coloured strings) created in a heavy ion collision combines the generation of lower centre-of-mass rapidity objects from higher rapidity ones with asymptotic saturation in the form of the well known logistic equation for population dynamics

$$\frac{\partial\rho}{\partial(-\Delta)} = \frac{1}{\delta}(\rho - A\rho^2), \tag{1}$$

where $\rho \equiv \rho(\Delta, Y)$ is the particle density, Y is the beam rapidity, and $\Delta \equiv |y| - Y$. The Y-dependent limiting value of ρ is determined by the saturation condition $\partial_{(-\Delta)}\rho = 0 \longrightarrow \rho_Y = 1/A$, while the separation between the low density (positive curvature) and high density (negative curvature) regions is given by $\partial^2{}_{(-\Delta)}\rho|_{\Delta_0} = 0 \longrightarrow \rho_0 \equiv \rho(\Delta_0, Y) = \rho_Y/2$. Integrating (1) we get

$$\rho(\Delta, Y) = \frac{\rho_Y}{\mathrm{e}^{\frac{\Delta-\Delta_0}{\delta}} + 1}. \tag{2}$$

In the String Percolation Model [2] the particle density is proportional, once the colour reduction factor is taken into account, to the average number of participants $\rho \propto N_A$; the normalized particle density at mid-rapidity is related to the gluon distribution at small Bjorken-x, $\rho \propto \mathrm{e}^{\lambda Y}$; and the dense-dilute separation scale decreases, from energy conservation, linearly with Y, $\Delta_0 = -\alpha Y$ with $0 < \alpha < 1$. Rewriting (2) in rapidity

$$\rho \equiv \frac{\mathrm{d}N}{\mathrm{d}y} = \frac{N_A \cdot \mathrm{e}^{\lambda Y}}{\mathrm{e}^{\frac{|y|-(1-\alpha)Y}{\delta}} + 1}. \tag{3}$$

The values $\lambda = 0.247$, $\alpha = 0.269$ and $\delta = 0.67$ for the parameters in the solution (3) are fixed by an overall fit [3] of Au-Au RHIC data [4].

In Fig. 1 we show the predicted multiplicity distribution for the 10% most central Pb-Pb collisions at $\sqrt{s_{\rm NN}} = 5.5$ TeV with $N_A = 173.3$ taken from the Glauber calculation in [5].

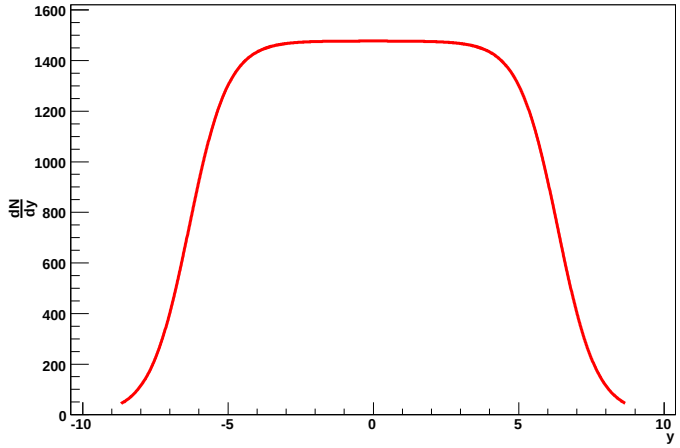

Figure 1: $\frac{{\rm d}N}{{\rm d}y}$ from (3) for Pb-Pb (0-10% central) collisions at $\sqrt{s_{\rm NN}} = 5.5$ TeV with $N_A = 173.3$

In Fig. 2 we show the predicted multiplicity distribution for the 20% most central p-Pb collisions at $\sqrt{s_{\rm NN}} = 8.8$ TeV with $N_{part} = 13.07$ also from [5]. In this case the solution (3) have been modified to account for the asymmetric geometry and the shift of the centre of mass of the system relatively to the laboratory centre of mass [2]. The resulting rapidity shift $y_c = -2.08$ is marked in Fig. 2.

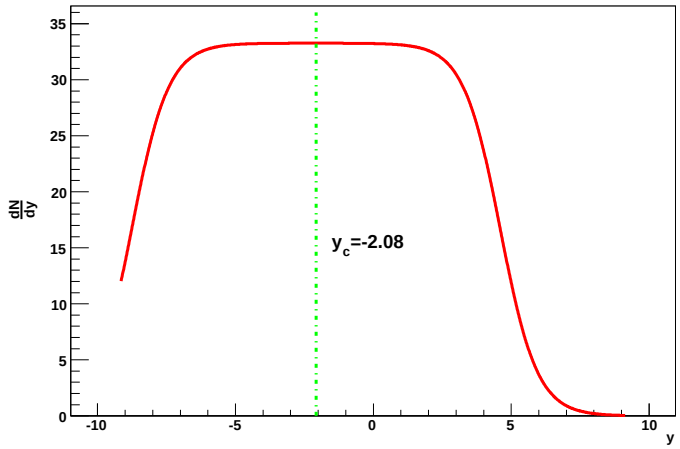

Figure 2: $\frac{{\rm d}N}{{\rm d}y}$ from asymmetric version of (3) [2] for p-Pb (0-20% central) collisions at $\sqrt{s_{\rm NN}} = 8.8$ TeV with $N_{\rm part} = 13.07$.

1.2. Multiplicities in Pb-Pb central collisions at the LHC from running coupling evolution and RHIC data

J. L. Albacete

Predictions for the pseudorapidity density of charged particles produced in Pb-Pb central collisions at $\sqrt{s_{NN}} = 5.5$ TeV are presented. Particle production in such collisions is computed in the framework of k_t-factorization, using running coupling non-linear evolution to determine the transverse momentum and rapidity dependence of the nuclear unintegrated gluon distributions.

Predictions for the pseudorapidity density of charged particles produced in Pb-Pb central collisions at $\sqrt{s_{NN}} = 5.5$ TeV presented in [6] are summarized. Primary gluon production in such collisions can be computed perturbatively in the framework of k_t-factorization. Under the additional assumption of local parton-hadron duality, the rapidity density of produced charged particles in nucleus-nucleus collisions at energy $\sqrt{s}$ and impact parameter b is given by, [7]:

$$\frac{dN}{dy\,d^2b} = C\frac{4\pi N_c}{N_c^2-1}\int^{p_{kin}}\frac{d^2p_t}{p_t^2}\int^{p_t} d^2k_t\,\alpha_s(Q)\,\varphi\left(x_1,\frac{|\underline{k_t}+\underline{p_t}|}{2}\right)\varphi\left(x_2,\frac{|\underline{k_t}-\underline{p_t}|}{2}\right), \tag{4}$$

where p_t and y are the transverse momentum and rapidity of the produced particle, $x_{1,2} = (p_t/\sqrt{s})\,e^{\pm y}$ and $Q = 0.5\max\{|p_t \pm k_t|\}$. The lack of impact parameter integration in this calculation and the gluon to charged hadron ratio are accounted for by the constant C, which sets the normalization. The nuclear unintegrated gluon distributions (u.g.d.), $\varphi(x,k)$, entering Eq. (4) are taken from numerical solutions of the Balitsky-Kovchegov evolution equation including running coupling corrections, [8]:

$$\frac{\partial N(Y,r)}{\partial Y} = \mathcal{R}[N(Y,r)] - \mathcal{S}[N(Y,r)] \tag{5}$$

Explicit expressions for the *running*, $\mathcal{R}[N]$, and *subtraction*, $\mathcal{S}[N]$, functionals in the r.h.s. of Eq. (5) can be found in [8]. The nuclear u.g.d. are given by the Fourier transform of the dipole scattering amplitude evolved according to Eq. (5), $\varphi(Y,k) = \int \frac{d^2r}{2\pi r^2}\,e^{i\underline{k}\cdot\underline{r}}\mathcal{N}(Y,r)$, with $Y = \ln(0.05/x) + \Delta Y_{ev}$, where ΔY_{ev} is a free parameter. Large-x effects have been included by replacing $\varphi(x,k) \to \varphi(x,k)(1-x)^4$. The initial condition for the evolution is taken from the McLerran-Venugopalan model [9], which is believed to provide a good description of nuclear distribution functions at moderate energies:

$$N^{MV}(Y=0,r) = 1 - \exp\left\{-\frac{r^2Q_0^2}{4}\ln\left(\frac{1}{r\Lambda}+e\right)\right\}, \tag{6}$$

where Q_0 is the initial saturation scale and $\Lambda = 0.2$ GeV. In order to compare Eq. (4) with experimental data it is necessary to correct the difference between rapidity, y, and the experimentally measured pseudorapidity, η. This is managed by introducing an effective hadron mass, m_{eff}. The variable transformation, $y(\eta, p_t, m_{eff})$, and its corresponding jacobian are given by Eqs.(25-26) in [7]. Corrections to the kinematics due to the hadron mass are also considered by replacing $p_t \to m_t = \left(p_t^2 + m_{eff}^2\right)^{1/2}$ in the evaluation of $x_{1,2}$. This replacement affects the predictions for the LHC by less than a 5%, [6].

The results for the pseudorapidity density of charged particles in central Au-Au collisions at $\sqrt{s_{NN}} = 130$, 200 and 5500 GeV are shown in Fig. 3. A remarkably good description of RHIC data is obtained with $Q_0 = 0.75 \div 1.25$ GeV, $\Delta Y_{ev} \lesssim 3$ and $m_{eff} = 0.2 \div 0.3$ GeV. Assuming no difference between Au and Pb nuclei, the extrapolation of the fits to RHIC data yields the following band: $\frac{dN_{ch}^{Pb-Pb}}{d\eta}(\sqrt{s_{NN}} = 5.5\,\text{TeV})|_{\eta=0} \approx 1290 \div 1480$ for central Pb-Pb collisions at the LHC. The central value of our predictions $\frac{dN_{ch}^{Pb-Pb}}{d\eta}(\sqrt{s_{NN}} = 5.5\,\text{TeV})|_{\eta=0} \approx 1390$ corresponds to the best fits to RHIC data.

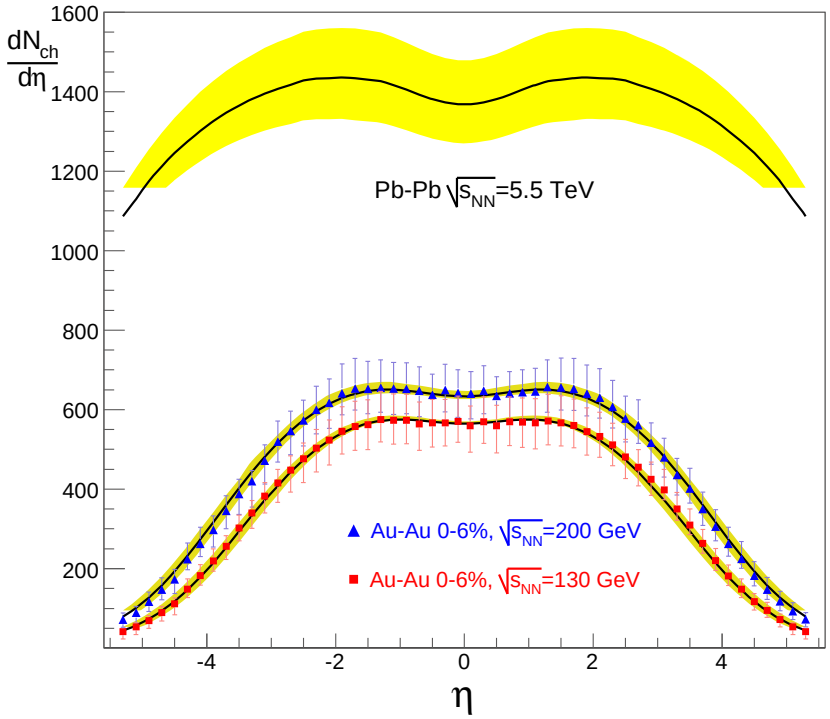

Figure 3: Multiplicity densities for Au-Au central collisions at RHIC (experimental data taken from [4]), and prediction for Pb-Pb central collisions at $\sqrt{s_{NN}} = 5.5$ TeV. The best fits to data (solid lines) are obtained with $Q_0 = 1$ GeV, $\Delta Y_{ev} = 1$ and $m_{eff} = 0.25$ GeV. The upper limit of the error bands correspond to $\Delta Y_{ev} = 3$ and $Q_0 = 0.75$ GeV, and the lower limit to $\Delta Y_{ev} = 0.5$ and $Q_0 = 1.25$ GeV, with $m_{eff} = 0.25$ GeV in both cases.

1.3. Identified hadron spectra in Pb-Pb at $\sqrt{s_{NN}}$ = 5.5 TeV: hydrodynamics+pQCD predictions

F. Arleo, D. d'Enterria and D. Peressounko

The single inclusive charged hadron p_T spectra in Pb-Pb collisions at the LHC, predicted by a combined hydrodynamics+perturbative QCD (pQCD) approach are presented.

We present predictions for the inclusive transverse momentum distributions of pions, kaons and (anti)protons produced at mid-rapidity in Pb-Pb collisions at $\sqrt{s_{NN}}$ = 5.5 TeV

based on hydrodynamics+pQCD calculations. The bulk of the spectra ($p_T \lesssim 5$ GeV/c) in central Pb-Pb at the LHC is computed with a hydrodynamical model – successfully tested at RHIC [10] – using an initial entropy density extrapolated empirically from the hadron multiplicities measured at RHIC: $dN_{\rm ch}/d\eta|_{\eta=0}/(0.5\,N_{\rm part}) \approx 0.75\ln(\sqrt{s_{\rm NN}}/1.5)$ [11]. Above $p_T \approx 3$ GeV/c, additional hadron production from (mini)jet fragmentation is computed from collinearly factorized pQCD cross sections at next-to-leading-order (NLO) accuracy [12]. We use recent parton distribution functions (PDF) [13] and fragmentation functions (FF) [14], modified respectively to account for initial-state shadowing [15] and final-state parton energy loss [16].

We use cylindrically symmetric boost-invariant 2+1-D relativistic hydrodynamics, fixing the initial conditions for Pb-Pb at $b = 0$ fm and employing a simple Glauber prescription to obtain the corresponding source profiles at all other centralities [10]. The initial source is assumed to be formed at a time $\tau_0 = 1/Q_s \approx 0.1$ fm/c, with an initial entropy density of $s_0 = 1120$ fm^{-3} (i.e. $\varepsilon_o \propto s_0^{4/3} \approx 650$ GeV/fm^3) so as to reproduce the expected final hadron multiplicity $dN_{\rm ch}/d\eta|_{\eta=0} \approx 1300$ at the LHC [11]. We follow the evolution of the system by solving the equations of ideal hydrodynamics including the current conservation for net-baryon number (the system is almost baryon-free, $\mu_B \approx 5$ MeV). For temperatures above (below) $T_{\rm crit} \approx 170$ MeV the system is described with a QGP (hadron gas) equation of state (EoS). The QGP EoS – obtained from a parametrization to recent lattice QCD results – is Maxwell connected to the hadron resonance gas phase assuming a first-order phase transition. As done for RHIC energies, we chemically freeze-out the system (i.e. fix the hadron ratios) at $T_{\rm crit}$. Final state hadron spectra are obtained with the Cooper-Frye prescription at $T_{\rm fo} \approx 120$ MeV followed by decays of unstable resonances using the known branching ratios. Details can be found at [10].

Our NLO pQCD predictions are obtained with the code of ref. [12] with all scales set to $\mu = p_T$. Pb-Pb yields are obtained scaling the NLO cross-sections by the number of incoherent nucleon-nucleon collisions for each centrality class given by a Glauber model ($N_{\rm coll} = 1670$, 12.9 for 0-10%-central and 60-90%-peripheral). Nuclear (isospin and shadowing) corrections of the CTEQ6.5M PDFs [13] are introduced using the NLO nDSg parametrization [15]. Final-state energy loss in the hot and dense medium is accounted for by modifying the AKK FFs [14] with BDMPS quenching weights as described in [16]. The BDMPS medium-induced gluon spectrum depends on a single scale $\omega_c = \langle\hat{q}\rangle\, L^2$, related to the transport coefficient and length of the medium. We use $\omega_c \approx 50$ GeV, from the expected energy dependence of the quenching parameter and the measured $\omega_c \approx 20$ GeV at RHIC [16]. The inclusive hadron spectra in central Pb-Pb are suppressed by up to a factor ~10 (2), $R_{PbPb} \approx 0.1$ (0.5), at $p_T =$ 10 (100) GeV/c.

Our predictions for the identified hadron spectra in Pb-Pb collisions at 5.5 TeV are shown in Figure 4. The hydrodynamical contribution dominates over the (quenched) pQCD one up to $p_T \approx 4$ (1.5) GeV/c in central (peripheral) Pb-Pb. As expected, the hydro-pQCD p_T crossing

point increases with the hadron mass. In the absence of recombination effects (not included here), bulk protons may be boosted up to $p_T \approx 5$ GeV/c in central Pb-Pb at the LHC.

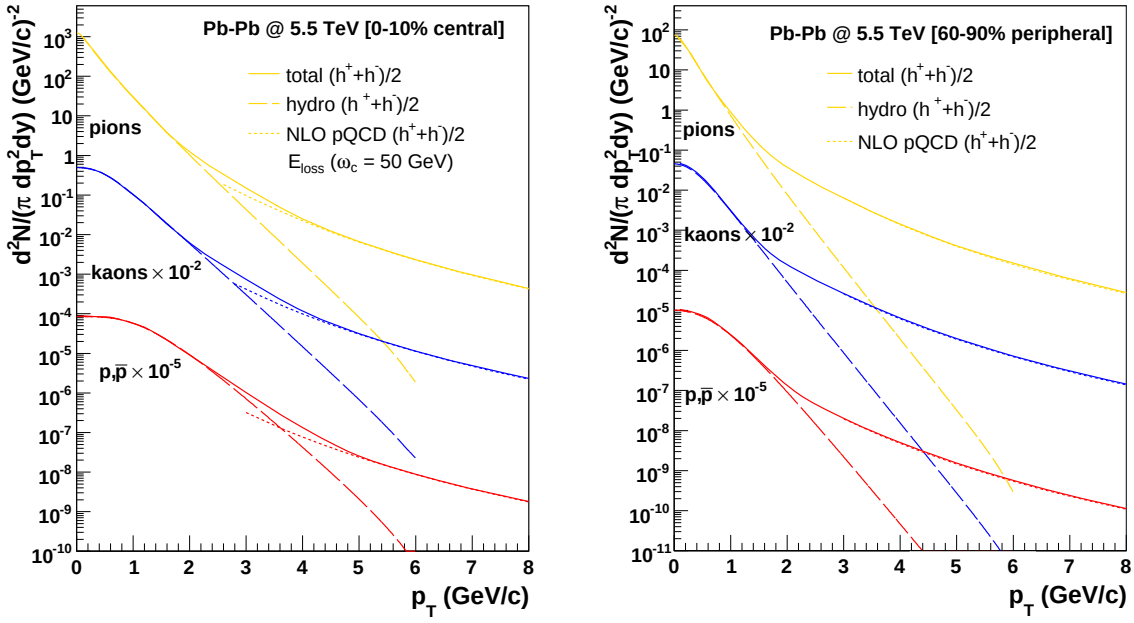

Figure 4: Spectra at y=0 for $\pi^{\pm}$,$K^{\pm}$, $p, \bar{p}$ in 0-10% central (left) and 60-70% peripheral (right) Pb-Pb at $\sqrt{s_{\rm NN}}$ = 5.5 TeV, obtained with hydrodynamics + (quenched) pQCD calculations.

1.4. Multiplicities at the LHC in a geometric scaling model

N. Armesto, C. A. Salgado and U. A. Wiedemann

We present predictions for charged multiplicities at mid-rapidity in PbPb collisions, as well as transverse momentum distributions at different pseudorapidities in pPb collisions, at LHC energies. We use geometric scaling as found in lepton-proton and lepton-nucleus scattering, to determine the evolution of multiplicities with energy, pseudorapidity and centrality. The only additional free parameter required to obtain the multiplicities is fixed from RHIC data.

Geometric scaling - the phenomenological finding that virtual photon-hadron cross sections in lepton-proton [17] and lepton-nucleus [18, 19] collisions, are functions of a single variable which encodes all dependences on Bjorken-x, virtuality Q^2 and nuclear size A - is usually considered as one of most important evidences in favor of saturation physics at work [19] . In the scaling variable $\tau_A = Q^2/Q^2_{s,A}(x)$ the quantity $Q_{s,A}$, the saturation momentum, shows a behavior with energy or Bjorken-x determined by lepton-proton data, while the dependence on A is fixed by lepton-nucleus data [18]:

$$Q^2_{s,A}(x) \propto x^{-\lambda} A^{1/(3\delta)}, \quad \lambda = 0.288, \quad \delta = 0.79 \pm 0.02. \tag{7}$$

To compute particle production, we assume that geometric scaling holds for the distributions assigned to the projectile and target. Without invoking factorization, dimensional

analysis allows us to factor out the geometrical information. Then, the multiplicity at central pseudorapidity can be written in the form [18] (with $N_{\rm part} \propto A$)

$$\left.\frac{2}{N_{\rm part}}\frac{dN^{AA}}{d\eta}\right|_{\eta\sim 0} = N_0 \left(s/{\rm GeV}^2\right)^{\lambda/2} N_{\rm part}^{\frac{1-\delta}{3\delta}} . \tag{8}$$

The only new parameter is N_0, a normalization constant which takes into account the parton-hadron conversion and the change from mid-rapidity to mid-pseudorapidity. Once fixed for a set of data ($N_0 = 0.47$), this formula has predictive power and establishes a factorization of the energy and centrality dependences in agreement with data. In Fig. 5 we show the results of Eq. (8) compared to RHIC data (including those of intermediate energies [20]) and our prediction for the LHC, where our numbers for $dN^{AA}/d\eta|_{\eta\sim 0}$ are $1550 \div 1760$ for $N_{\rm part} = 350$ and $1670 \div 1900$ for $N_{\rm part} = 375$, with the range in the predictions reflecting the uncertainty coming from δ, see Eq. (7). We note that these values are based on a $\sqrt{s}$-powerlaw dependence in Eq. (2) and can be discriminated clearly from a log-extrapolation of RHIC data.

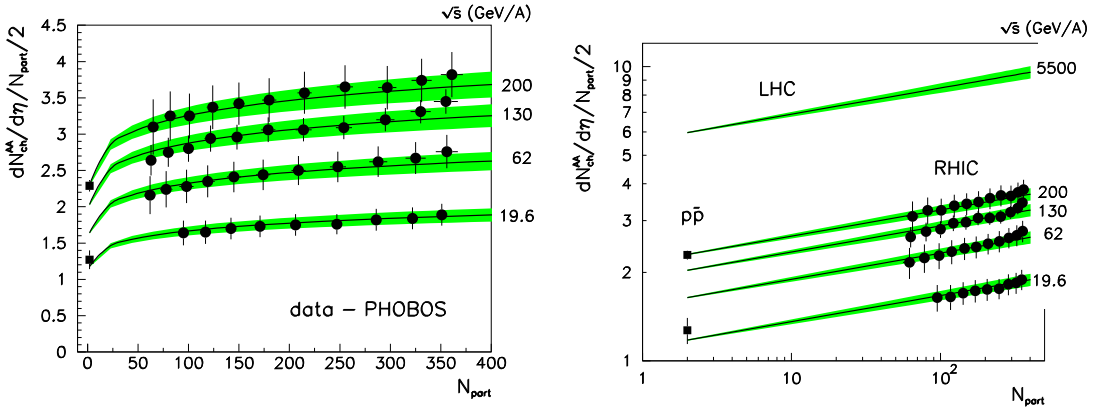

Figure 5: Charged multiplicity at mid-pseudorapidity per participant pair, for four RHIC energies and for LHC energies, from Eq. (8). The band shows the uncertainty coming from δ, see Eq. (7).

A more model-dependent application of this formalism [18] concerns particle production in hadron-nucleus collisions at forward rapidities or large energies. Assuming factorization, geometric scaling and a steeply falling parton distribution in the proton or deuteron, one gets for one-particle distributions in two centrality classes c_1 and c_2

$$\frac{dN^{\rm dAu}_{c_1}}{N_{{\rm coll}_1} d\eta d^2p_t} \Bigg/ \frac{dN^{\rm dAu}_{c_2}}{N_{{\rm coll}_2} d\eta d^2p_t} \approx \frac{N_{{\rm coll}_2}\phi_A(p_t/Q_{{\rm sat}_1})}{N_{{\rm coll}_1}\phi_A(p_t/Q_{{\rm sat}_2})} \approx \frac{N_{{\rm coll}_2}\Phi(\tau_1)}{N_{{\rm coll}_1}\Phi(\tau_2)} , \tag{9}$$

where Φ is the geometric scaling function in lepton-hadron collisions. In this way, particle ratios in hadron-nucleus collisions provide a check of parton densities in the nucleus through geometric scaling. In Fig. 6 we show the results compared to RHIC data and our predictions for the LHC. The definition of the centrality classes is $N_{{\rm coll}_1} = 13.6 \pm 0.3$ (central), 7.9 ± 0.4 (semicentral) and $N_{{\rm coll}_2} = 3.3 \pm 0.4$ (peripheral). The suppression for mid-pseudorapidities at the LHC turns out to be as large as that for forward pseudorapidities at RHIC.

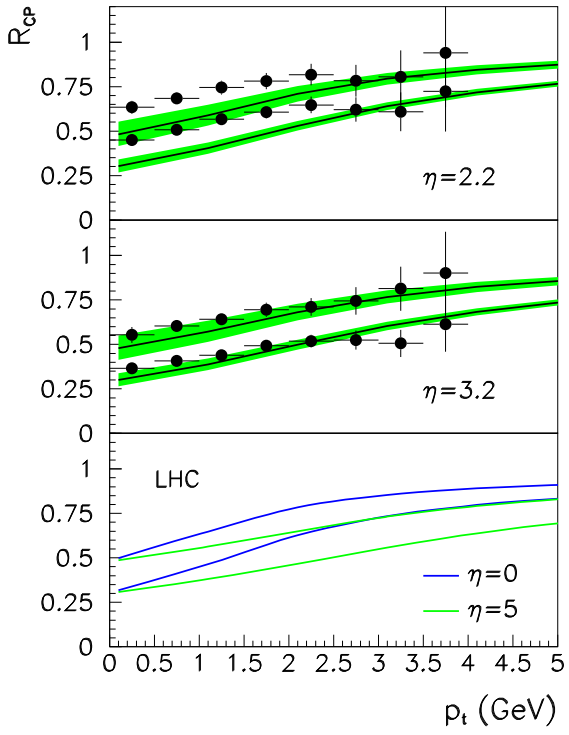

Figure 6: R_{CP} versus p_t, Eq. (9), in dAu collisions at RHIC compared to experimental data (upper and middle plots), and in pPb collisions at the LHC (lower plot), for different pseudorapidities and centrality classes: central to peripheral (lower curves) and semicentral to peripheral (upper curves). The bands reflect the uncertainty in the definition of the centrality class.

1.5. Multiplicity and cold-nuclear matter effects from Glauber-Gribov theory

I. C. Arsene, L. Bravina, A. B. Kaidalov, K. Tywoniuk and E. Zabrodin

We present predictions for nuclear modification factor in proton-lead collisions at LHC energy 5.5 TeV from Glauber-Gribov theory of nuclear shadowing. We have also made predictions for baseline cold-matter nuclear effects in lead-lead collisions at the same energy.

1.5.1. Introduction The system formed in nucleus-nucles (AA) collisions at LHC will provide further insight into the dynamics of the deconfined state of nuclear matter. There are also interesting effects anticipated for the initial state of the incoming nuclei related to shadowing of nuclear parton distributions and the space-time picture of the interaction. These should be studied in the more "clean" environment of a proton-nucleus collision. The initial-state effects constitute a baseline for calculation of the density of particles at all rapidities and affect therefore also high-$p_\perp$ particle suppression and jet quenching, as well as the total multiplicity.

Both soft and relatively high-$p_\perp$, $p_\perp < 10$ GeV/c, particle production in pA at LHC energies probe the low-x gluon distribution of the target nucleus at moderate scales, $Q^2 \sim p_\perp^2$, and is therefore mainly influenced by nuclear shadowing. In the Glauber-Gribov theory [21],

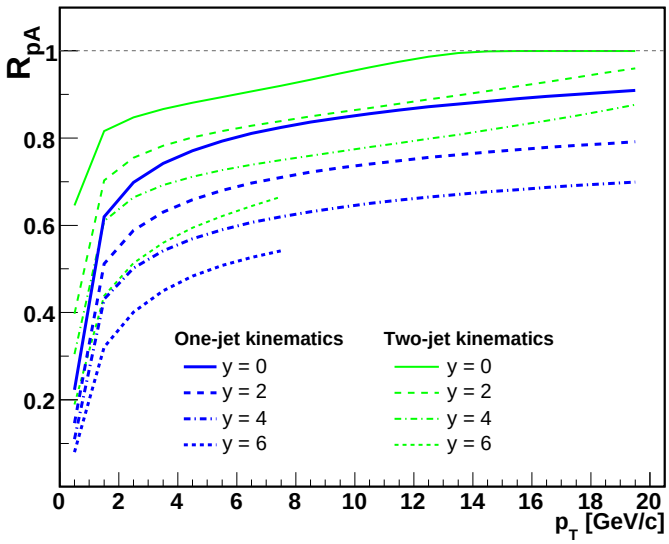

Figure 7: Shadowing as a function of transverse for p+Pb collisions at $\sqrt{s} = 5.5$ TeV.

shadowing at low-x is related to diffractive structure functions of the nucleon, which are studied at HERA. The space-time picture of the interaction is altered from a longitudinally ordered rescattering at low energies, to a coherent interaction of the constituents of the incoming wave-functions at high energy. Shadowing affects both soft and hard processes. Calculation of gluon shadowing was performed in our recent paper [22], where Gribov approach for the calculation of nuclear structure functions was used. The Schwimmer model was used to account for higher-order rescatterings. The gluon diffractive distributions are taken from the most recent experimental parameterizations [23].

1.5.2. Particle production at LHC Shadowing will lead to a suppression both at mid- and forward rapidities in p+Pb collisions at $\sqrt{s} = 5.5$ TeV as seen in Fig. 7. We have plotted the curves for two distinct kinematical scenarios of particle production; one-jet kinematics which may be well motivated for particle production at $p_\perp < 2$ GeV/c and two-jet kinematics that apply for high-$p_\perp$ particle producion. The uncertainty in the curves is due to uncertainty in the parameterization of gluon diffractive distribution functions. Cronin effect is not included in the curves of Fig. 7. We estimate it to be a 10% effect at these energies.

In Fig. 8 we present the suppresion due to cold-nuclear effects in Pb+Pb collisions at $\sqrt{s} = 5.5$ TeV as a function of centrality (top) and rapidity (bottom). Also here we present the results for two kinematics.

1.6. Stopping Power from SPS to LHC energies.

V. Topor Pop, J. Barrette, C. Gale, S. Jeon and M. Gyulassy

We investigate the energy dependence of hadron production and of stopping power based on

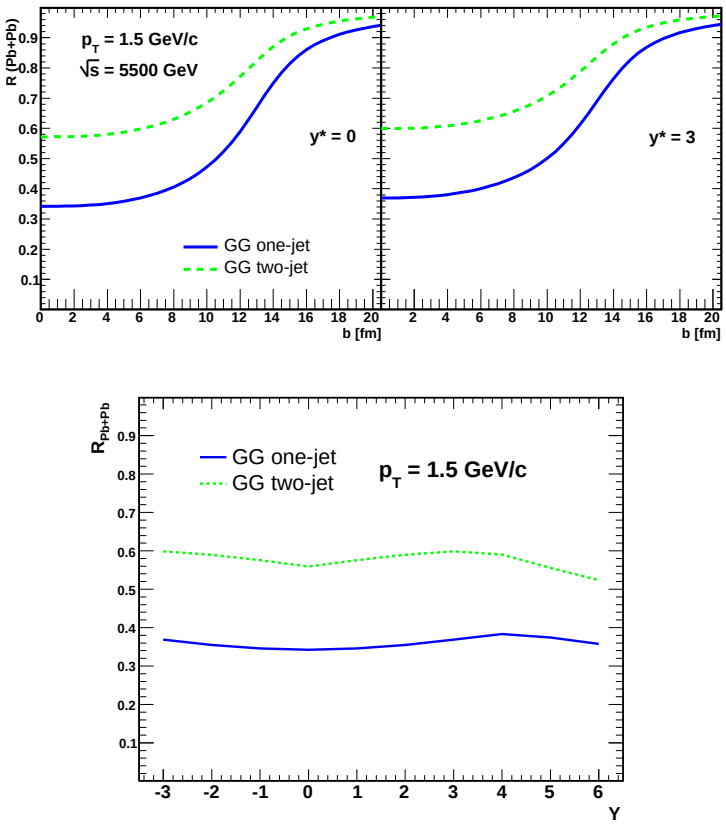

Figure 8: Shadowing as a function of centrality (top) and rapidity (bottom) for Pb+Pb collisions at $\sqrt{s} = 5.5$ TeV.

HIJING/B$\bar{\text{B}}$ v2.0 model calculations. Pseudorapidity spectra and p_T distributions for produced charged particles as well as net baryons (per pair of partcipants) and their rapidity loss are compared to data at RHIC and predictions for LHC energies are discussed.

In previous papers [24] we studied the possible role of topological baryon junctions [25] [26], and the effects of strong color field (SCF) in nucleus-nucleus collisions at RHIC energies. In the framework of HIJING/B$\bar{\text{B}}$ v2.0 model, the new algorithm for junction anti-junction J$\bar{\text{J}}$ loops provide a possible explanation for baryon/meson anomaly. The SCF effects as implemented within our model gives a better description of this anomaly. At LHC energies, due to higher initial energy density (or temperature) we expect an increase of the mean value of the string tension (κ) [27].

The day 1 measurements at the LHC will include results on multiplicity distributions with important consequences for our understanding of matter produced in the collisions [28], [29]. From our model calculations one expects $\mathrm{dN^{ch}_{PbPb}}/\mathrm{d}\eta \approx 3500$ at $\eta = 0$ in central (0-5 %) Pb +Pb collision. This correspond to ≈ 17.5 produced charged hadrons per participant pair. These values are higher than those obtained by requiring that both limiting fragmentation and the trapezoidal shape of the pseudo-rapidity distribution persist at the LHC [29]. Our model predicts a characteristic violations of the apparently universal trend, seen up to maximum

RHIC energy. In contrast saturation models [5] offer a justification for the predicted very weak $\sqrt{s_{\rm NN}}$ dependence of event multiplicity.

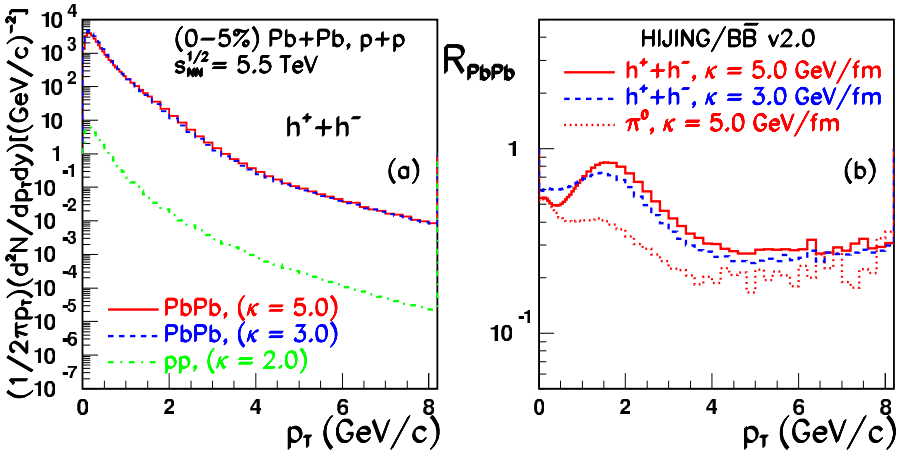

Figure 9: Left: HIJING/B$\bar{\rm B}$ v2.0 predictions for p_T spectra at mid-rapidity of total inclusive charged hadrons for central (0-5%) Pb+Pb and $p+p$ collisions. Right: Predicted nuclear modification factors for charged hadrons and for neutral pions.

Figure 9 presents predictions for p_T spectra at midrapidity and NMF $R^{\rm ch}_{\rm PbPb}$ of total inclusive charged hadrons for central (0-5%) Pb+Pb and $p+p$ collisions at $\sqrt{s_{\rm NN}} = 5.5$ TeV. The predicted NMF $R^{\pi^0}_{\rm PbPb}$ of neutral pions is also presented. From our model calculations we conclude that baryon/meson anomaly, will persist at the LHC with a slight increase for increasing strength of the chromoelectric field ($\kappa = e_{eff}E$). A somewhat higher sensitivity to κ is obtained for NMF of identified particles [27].

The net-baryon rapidity distribution measured at RHIC is both qualitatively and quantitatively very different from those at lower energies indicating that a significantly different system is formed near mid rapidity [30]. Fig. 10 (left panel) presents the energy dependence of net-baryon at mid-rapidity per participant pair. Shown are the results for central (0-5%) Au+Au collisions, which indicate a net decrease with increasing energy. This picture, corroborated with an increase of the ratio $\bar{p}/p$ to ≈ 1 suggests that the reaction at the LHC is more transparent in contrast to the situation at lower energy. For central (0-5%) Pb+Pb collisions at $\sqrt{s_{\rm NN}} = 5.5$ TeV, our prediction for net-baryon per participant pair is ≈ 0.065 with $N_{\rm part} = 398$, assuming $\kappa = 5$ GeV/fm. Similar values (open squares) are obtained within pQCD+hydro model [31]. However, this model predicts (Fig. 15 from ref. [31]) much steeper slopes of charged hadron p_T spectra.

In our model the main mechanisms for baryon production are quark di-quark ($q-{\rm qq}$) strings fragmentation and J$\bar{\rm J}$ loops in which baryons are produced approximatively in pairs. The energy dependence is $\propto (s/s_0)^{-1/4+\Delta/2}$ similar with those predicted in ref. [25] (eq. 11) with the assumption that J$\bar{\rm J}$ is a dominant mechanisms. This dependence is obtained if we choose for the parameters: $s_0 = 1$ GeV^2 the usual parameter of Regge theory, $\alpha(0) = 1/2$ the reggeon (M_0^J) intercept and $\alpha_P(0) = 1+\Delta$ (where $\Delta \approx 0.01$) for the pomeron intercept. If confirmed, the measurements at LHC energies will help us to determine better these values.

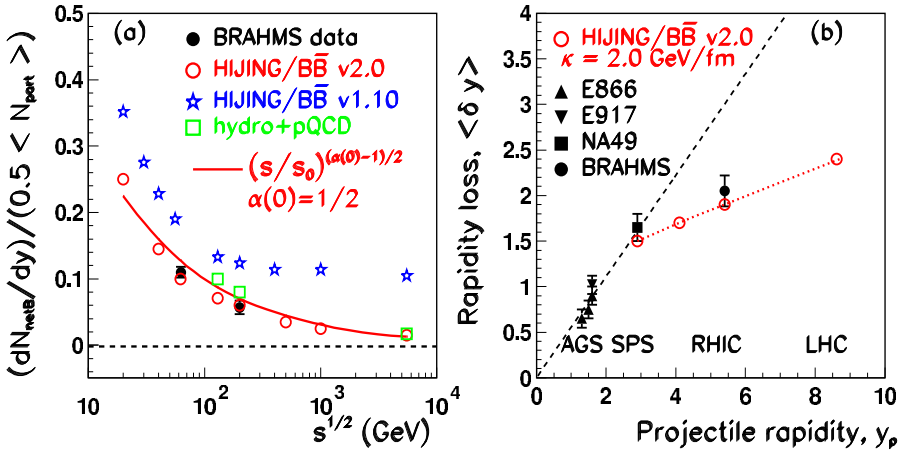

Figure 10: Left: HIJING/B$\bar{\text{B}}$ v2.0 predictions for net-baryon (per participant pair) at mid-rapidity as function of $\sqrt{s_{\rm NN}}$. Right: Average rapidity loss versus beam rapidity. The data and dashed line extrapolation are from ref. [30] and from BRAHMS [32].

In contrast, results from HIJING/B$\bar{\text{B}}$ v1.10 model [26] (star symbol) give a slow energy dependence with a higher pomeron intercept $\alpha_P(0) = 1 + 0.08$ and over-estimate the stopping in the entire energy region.

Baryon conservation in the reactions can be used to predict rapidity loss and the energy loss per baryon. The results are illustrated in Fig. 10 (right panel) for average rapidity loss $< \delta y >$ defined as in ref. [24]. The predicted values for RHIC and LHC energies, clearly depart from the linear extrapolation for constant relative rapidity loss [30], which seems to be valid only at lower energies ($\sqrt{s_{\rm NN}} \leq 20$ GeV).

1.7. Investigating the extended geometric scaling region at LHC with polarized and unpolarized final states

D. Boer, A. Utermann and E. Wessels

We present predictions for charged hadron production and Λ polarization in p-p and p-Pb collisions at the LHC using the saturation inspired DHJ model for the dipole cross section in the extended geometric scaling region.

At high energy, scattering of a particle off a nucleus can be described in terms of a colour dipole scattering off small-x partons, predominantly gluons, in the nucleus. At very high energy (small x), the dipole amplitude starts to evolve nonlinearly with x, leading to saturation of the density of these small-x gluons. The scale associated with this nonlinearity, the saturation scale $Q_s(x)$, grows exponentially with $\log(1/x)$.

The nonlinear evolution of the dipole amplitude is expected to be characterized by geometric scaling, which means that the dipole amplitude depends only on the combination $r_t^2 Q_s^2(x)$, instead of on r_t^2 and x independently. Moreover, the scaling behaviour is expected to hold approximately in the so-called extended geometric scaling (EGS) region between $Q_s^2(x)$ and $Q_{gs}^2(x) \sim Q_s^4(x)/\Lambda^2$.

The small-x DIS data from HERA, which show geometric scaling, were successfully described by the GBW model [33]. To describe the RHIC data on hadron production in d-Au in the EGS region a modification of the GBW model was proposed by Dumitru, Hayashigaki and Jalilian-Marian (DHJ), incorporating scaling violations in terms of a function γ^+ [34]. This DHJ model also describes p-p data at forward rapidities [35].

1.7.1. DHJ model prediction for charged hadron production Using the DHJ model we can make a prediction for the p_t-spectrum of charged hadron production in both p-Pb and p-p collisions at the LHC, at respectively $\sqrt{s} = 8.8$ TeV and $\sqrt{s} = 14$ TeV. Figure 11a shows the minimum bias invariant yield for an observed hadron rapidity of $y_h = 2$ in the centre of mass frame, which for 1 GeV $\lesssim p_t \lesssim$ 10 GeV predominantly probes the EGS region. We note that at this rapidity the result is not sensitive to details of the DHJ model in the saturation region $r_t^2 > 1/Q_s^2$. Further, from [34] we expect that p_t-independent K-factors are needed to fix the normalization. We conclude that the LHC data on hadron production in both p-Pb and p-p collisions will provide valuable data to further study the dipole scattering amplitude near the onset of saturation, particularly the behaviour of the function γ, which is discussed in e.g. [36].

1.7.2. DHJ model prediction for Λ *polarization* Another interesting small-x observable is the polarization of Λ hyperons produced in p-A collisions, P_Λ. This polarization, oriented transversely to the production plane, was shown to essentially probe the derivative of the dipole scattering amplitude, hence displaying a peak around Q_s when described in the McLerran-Venugopalan model [37]. If this feature persists when x-evolution of the dipole scattering amplitude is taken into account, P_Λ would be a valuable probe of saturation effects. Using the DHJ model for the x-evolution of the scattering amplitude, we find that P_Λ displays similar behaviour as in the MV model. This is depicted for fixed Λ rapidities of 2 and 4 in figure 11b. The position of the peak scales with the average value of the saturation scale $\langle Q_s(x)\rangle$. In the plotted region, the peak is located roughly at $\langle Q_s(x)\rangle/2$.

The figure also shows that, like in the MV model, in the DHJ model $|P_\Lambda|$ scales approximately linearly with x_F, which means that at the LHC it is very small due to $\sqrt{s}$ being very large: rapidities around 6 are required for P_Λ to be on the 1% level, although there is a considerable model uncertainty in the normalization.

We conclude that the polarization of Λ particles in p-Pb collisions is an interesting probe of $\langle Q_s(x)\rangle$, but is probably of measurable size only at very forward rapidities.

1.8. Inclusive distributions at the LHC as predicted from the DPMJET-III model with chain fusion

F. Bopp, R. Engel, J. Ranft and S. Roesler

DPMJET-III with chain fusion is used to calculate inclusive distributions of Pb-Pb collisions at LHC energies. We present rapidity distributions as well as scaled multiplicities at mid-rapidity as

[+] We note that at central rapidities we cannot reproduce exactly the results of [34] for large p_t. Therefore, a modification of the model may be needed to describe all RHIC data.

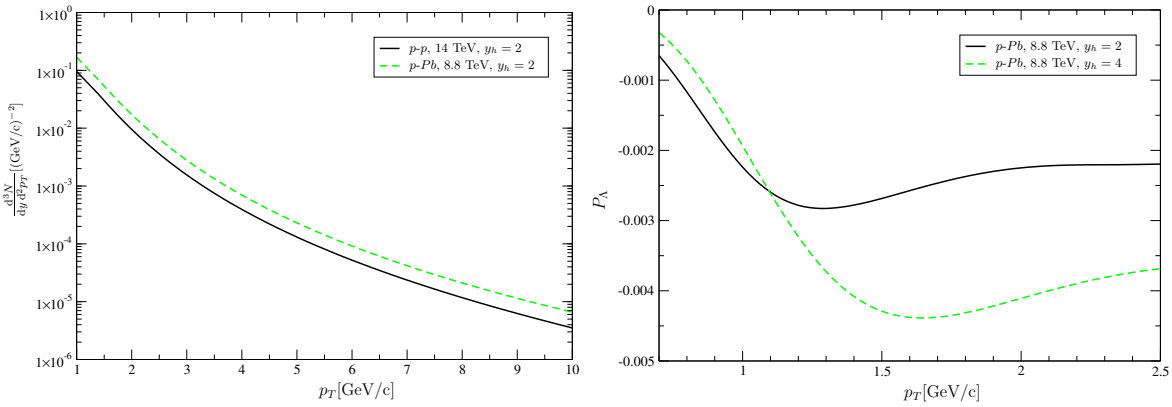

Figure 11: a. Charged hadron production. b. Λ polarization. In both plots, $A_{\rm eff} = 20$, and parton distributions and fragmentation functions of [34] and [37] were used.

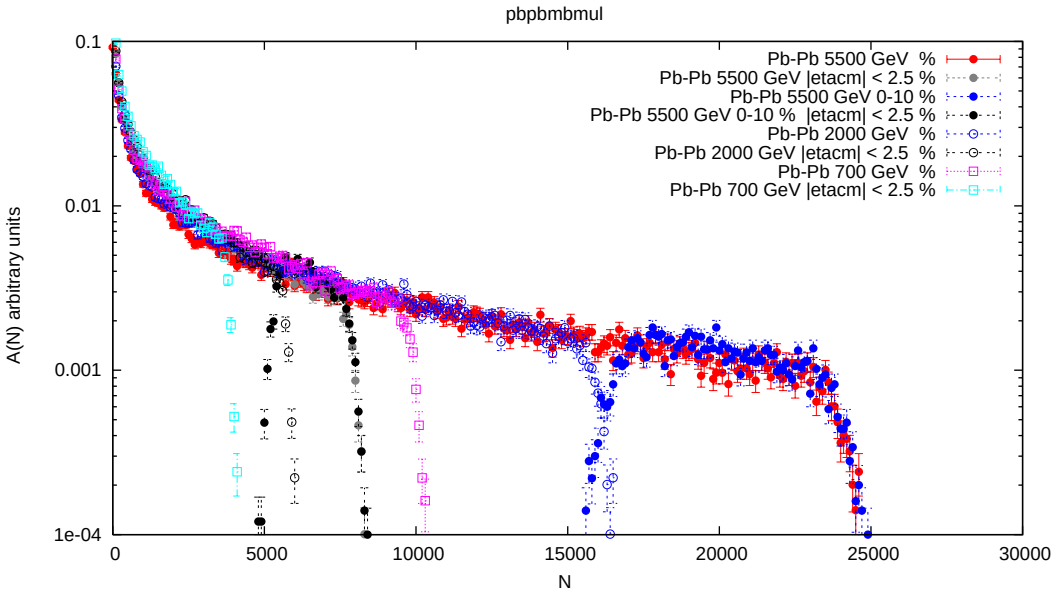

Figure 12: Multiplicity distributions in minimum bias and 0-10% central collisions in Pb-Pb collisions in the full $\eta_{\rm cm}$ range and for $|\eta_{\rm cm}| \leq 2.5$ (from DPMJET-III).

function of the collision energy and the number of participants.

Monte Carlo codes based on the two–component Dual Parton Model (soft hadronic chains and hard hadronic collisions) are available since 10–20 years: The present codes are PHOJET for *hh* and γh collisions [38, 39] and DPMJET-III based on PHOJET for *h*A and AA collisions [40]. To apply DPMJET–III to central collisions of heavy nuclei, the percolation and fusion of the hadronic chains had to be implemented [41].

In figures 12 and 13 we apply this model to minimum bias and central collisions of heavy nuclei at the LHC and at RHIC. We find an excellent agreement to RHIC data on inclusive distributions.

The behaviour of the inclusive hadron production becomes particular simple if we plot

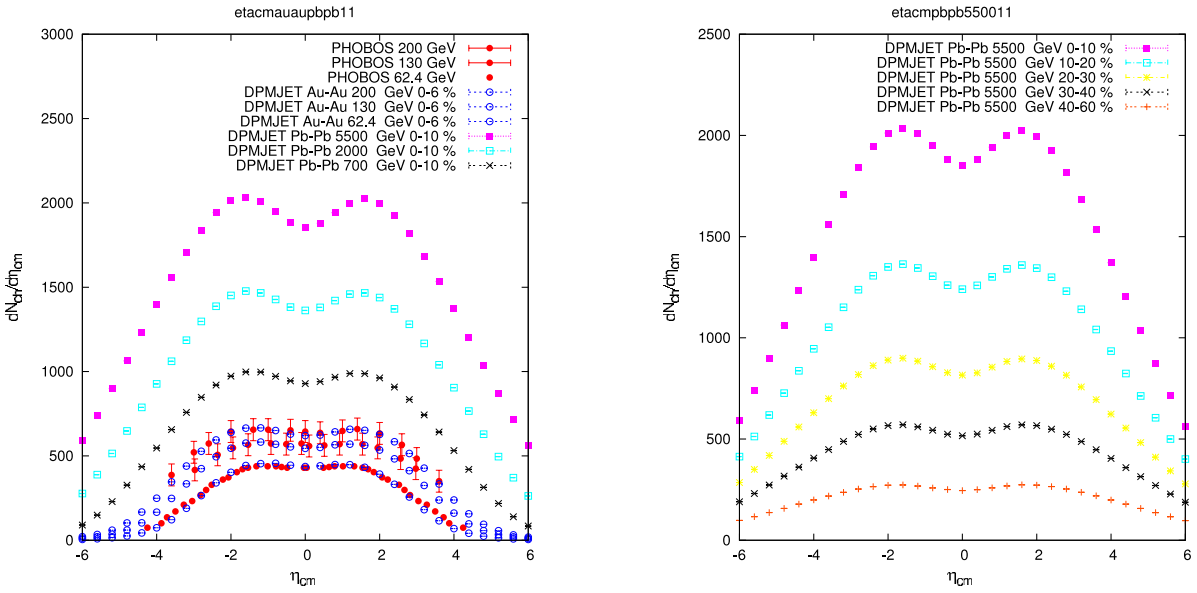

Figure 13: (left) Central RHIC and LHC collisions. (right) LHC Pb-Pb collisions from DPMJET-III.

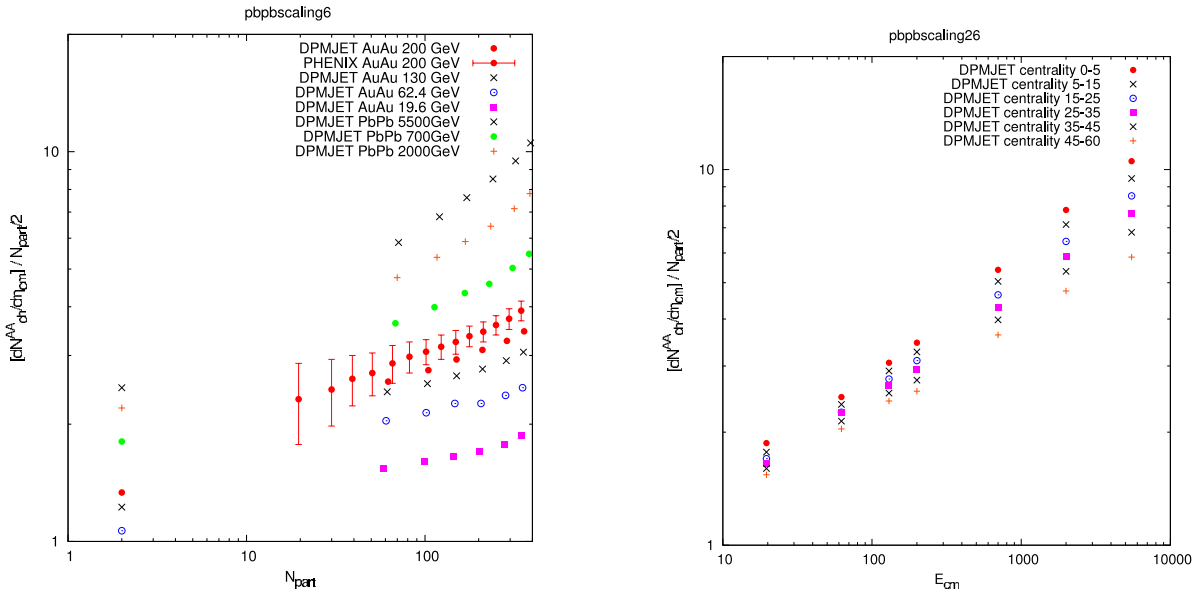

Figure 14: $\frac{\mathrm{d}N}{\mathrm{d}\eta_{\mathrm{cm}}} / \frac{N_{\mathrm{part}}}{2}$ (left) over N_{part} (right) over E_{cm}, Pb-Pb and Au-Au collisions.

it in the form $\frac{\mathrm{d}N}{\mathrm{d}\eta_{\mathrm{cm}}} / \frac{N_{\mathrm{part}}}{2}$. N_{part} is the number of participants in the AA collisions. In figure 14 we plot this quantity as function of N_{part} and as function of E_{cm}, in both plots we find a rather simple behaviour.

The limiting fragmentation hypothesis was proposed in 1969 by Benecke *et al* [42]. If we apply it to nuclear collisions we have to plot $\frac{\mathrm{d}N}{\mathrm{d}\eta_{\mathrm{cm}}} / \frac{N_{\mathrm{part}}}{2}$ as function of $\eta_{\mathrm{cm}} - y_{\mathrm{beam}}$. In figure 15 we plot central and less central Au-Au collisions at RHIC and LHC energies in this

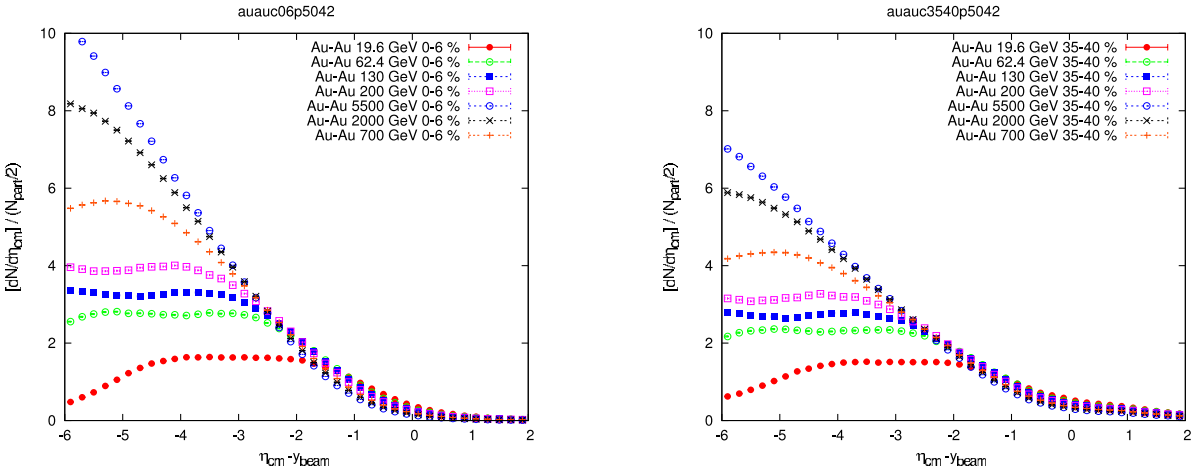

Figure 15: $\frac{\mathrm{d}N}{\mathrm{d}\eta_{\mathrm{cm}}}/\frac{N_{\mathrm{part}}}{2}$ in Au-Au collisions over $\eta_{cm} - y_{beam}$ (left) central, (right) less central.

form. We find that DPMJET-III shows in the fragmentation region only small deviations from limiting fragmentation.

1.9. Some "predictions" for PbPb and pp at LHC, based on the extrapolation of data at lower energies

W. Busza

The global characteristics of multiparticle production in pp, pA, AA and even e^+e^- collisions, over the entire energy range studied to date, show remarkably similar trends. Furthermore it is a fair characterization of the data to say that the data appears simpler than current explanations of it. These trends allow us to "predict", with high precision, several important results which will be seen in pp and PbPb collisions at LHC.

Such predictions are valuable from a practical point of view. More important, if they turn out to be correct, and the trends seen to date are not some accidental consequence of averaging over many species and momenta, the observed trends must be telling us something profound about how QCD (most likely how the vacuum) determines particle production. At a minimum, if the current belief is correct that the intermediate state between the instant of collision and final free-streaming of the produced particles is very different in e^+e^- and AA colisions, or for that matter, in pp collisions, AA collisions below SPS energies and AA collisions at the top RHIC energy, the global characteristics of multiparticle productions must be insensitive to the intermediate state. One consequence is that no successful prediction of any selected set of global properties can be used as evidence that a particular model correctly describes the intermediate state.

On the other hand, if these "predictions" turn out to be false, it will be a strong indicator of the onset of some new physics at LHC.

So what are these universal simple trends?

We find [43, 44], as a first approximation, that

(i) The global distributions of charged particles factorize into an energy dependent part and a geometry, or incident system, dependent part.

(ii) At a given energy, in pA and AA the distributions do depend in detail on the colliding systems or geometry (eg. impact parameter). However the total number of produced particles is simply proportional to the total number of participants N_{part} (or wounded nucleons, in the language of Bialas and Czyz). [Note: there is a systematic difference in the constant of proportionality in pA and AA, that can be attributed to the leading particle effect in pp collisions]

(iii) The total charged particle density $dN/d\eta$ (where η is the pseudorapidity), and the directed and elliptic flow parameters v_1 and v_2 satisfy extended longitudinal scaling. Furthermore, over most of its range the “limiting curve" is linear.

(iv) The mid-rapidity (in the cm system) particle density $\frac{dN}{d\eta}|_{y=0}$ and the elliptic flow parameter v_2 both increase linearly with $ln\sqrt{s}$. It is not clear if this is the origin or consequence of item (iii) above. [Note: for elliptic flow, (iii) and (iv) are directly related only if we postulate that at all energies there is a “pedestal" in the value of v_2, i.e. there is a part of the source of flow that is independent of energy]

In the figures 16, 17 and 18 we use the above observed trends at lower energies to “predict" LHC results. A more detailed version of this work will be submitted to Acta Physica Polonica.

1.10. Multiplicities and J/ψ suppression at LHC energies

A. Capella and E. G. Ferreiro

We present our predictions on multiplicities and J/ψ suppression at LHC energies. Our results take into account shadowing effects in the initial state and final state interactions with the hot medium. We obtain 1800 charged particles at LHC and the J/ψ suppression increases by a factor 5 to 6 compared to RHIC.

1.10.1. Multiplicities with shadowing corrections At high energy, different mechanisms in the initial state -*shadowing*-, that lower the total multiplicity, have to be taken into account. The shadowing makes the nuclear structure functions in nuclei different from the superposition of those of their constituents nucleons. Its effect increases with decreasing x and decreases with increasing Q^2. We have included a dynamical, non linear of shadowing [49], controlled by triple pomeron diagrams. It is determined in terms of the diffractive cross sections. Our results for charged particles multiplicities at RHIC and LHC energies are presented in Fig. 19. In absence of shadowing we obtain a maximal multiplicity, $dN_{AA}/dy = A^{4/3}$. With shadowing corrections the multiplicity behaves as $dN_{AA}/dy = A^{\alpha}$, with $\alpha = 1.13$ at RHIC and $\alpha = 1.1$ at LHC.

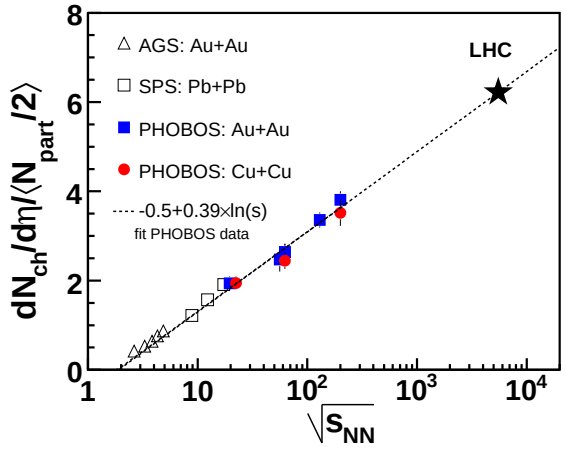

Figure 1 Extrapolation of midrapidity particle density per participant pair, for central PbPb collisions at $\sqrt{s_{NN}}$ = 5.5TeV. The data are from a PHOBOS compilation [4, 45]. The predicted value for $\frac{dN_ch}{d\eta}/(N_{part}/2) = 6.2 \pm 0.4$, which for N_{part} = 386 (top 3 %) corresponds to $dN_{ch}/d\eta = 1200 \pm 100$.

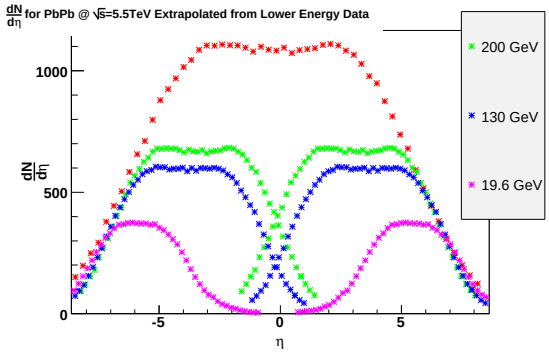

Figure 2 Extrapolated central (N_{part} = 360, 0-10% centrality) PbPb pseudorapidity distribution at $\sqrt{s_{NN}}$ = 5.5TeV. PHOBOS AuAu data [4, 45], longitudinal scaling with a linear "limiting curve", and the observed $ln\sqrt{s_{NN}}$ energy dependence of the mid rapidity density were used in the extrapolation.

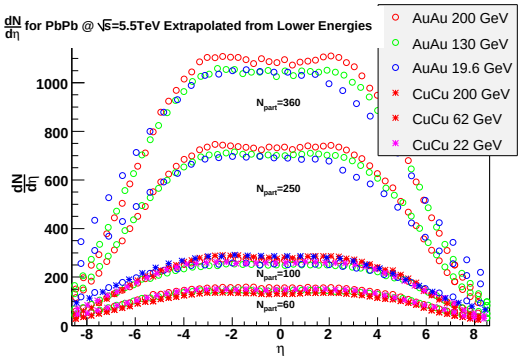

Figure 3 Predictions of PbPb LHC pseudorapidity distributions for different centrality collisions. For each extrapolated curve, PHOBOS AuAu or CuCu data [4, 45], with N_{part} closest to the required value, were taken and normalized to the quoted N_{part} value. The vertical and horizontal scales were then re-scaled by $ln\sqrt{s_{NN}}$. This is equivalent to trends (iii) and (iv), provided that $dn/d\eta \to 0$ as $\eta \to beamrapidity$. It must be emphasized that each curve is an independent extrapolation, however each extrapolation relies on the same method.

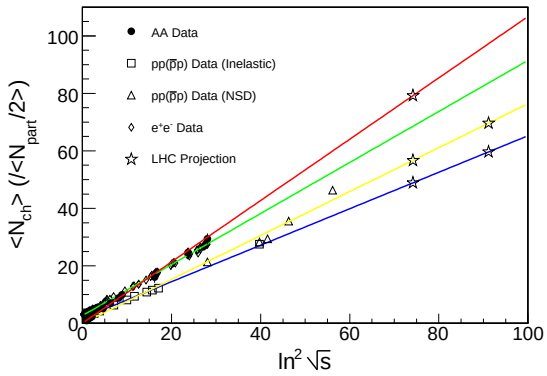

Figure 4 Total charged particle multiplicity per participant pair plotted as a function of $ln^2\sqrt{s}$ (with $\sqrt{s}$ in GeV) for various colliding systems. The data are taken from the compilation in Busza [43]. The extrapolation of the AA data to $\sqrt{s_{NN}}$=5.5 TeV predicts 15000 ± 1000 charges particles at LHC for N_{part} = 386 (top 3%). Extrapolation of the non-single diffractive (NSD) pp data to $\sqrt{s_{NN}}$ = 14 TeV predicts 70 ± 8 charged particles at LHC. The $ln^2\sqrt{s}$ extrapolation for the total multiplicity is a consequence of the extrapolation procedure described in the caption of fig 3.

Figure 16:

1.10.2. J/ψ suppression An anomalous J/ψ suppression -that clearly exceeds the one expected from nuclear absorption- has been found in *PbPb* collisions at SPS. Such a phenomenon was predicted by Matsui and Satz as a consequence of deconfinement in a dense medium. It can also be described as a result of final state interaction of the $c\bar{c}$ pair with

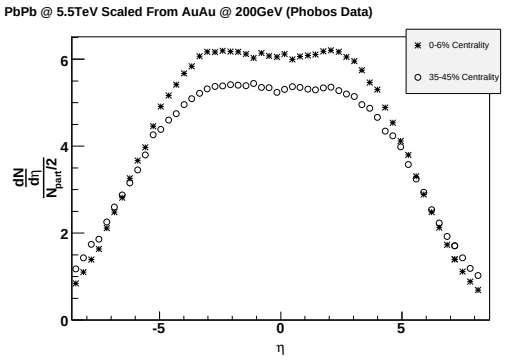

Figure 1 Predicted PbPb pseudorapidity distributions of charged particles at $\sqrt{s_{NN}}$=5.5 TeV for two centralities, 0-6% and 35-45%. These predicted curves are obtained by extrapolating the corresponding centrality 200GeV PHOBOS AuAu data [4, 45] using the same procedure as in fig. 16.3.

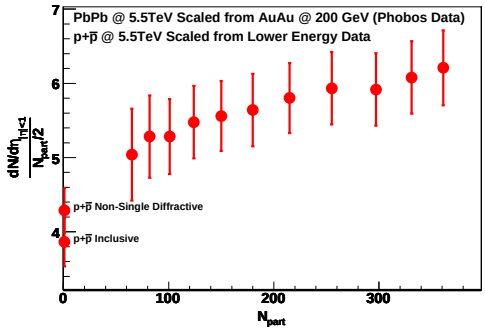

Figure 2 Predicted N_{part} dependence of the mid rapidity charged particle density per participant pair for PbPb at $\sqrt{s_{NN}}$ = 5.5 TeV. These results are obtained from the PHOBOS 200 GeV AuAu data [4, 45] scaled by $ln\sqrt{s_{NN}}$ (see trends (i) and (iv) in the text).

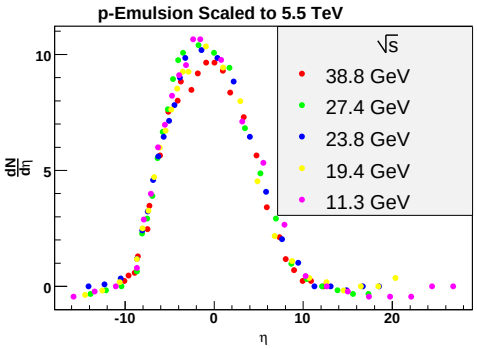

Figure 3 Predicted pA pseudorapidity distribution for $\sqrt{s_{NN}}$ = 5.5 TeV for N_{part} = 3.4. Each curve is an independent extrapolation of lower energy p-emulsion data using the same procedure as in Fig. 16.3. The p-emulsion data are from ref [46], and covers the energy range $\sqrt{s_{NN}}$ = 11.3 GeV to 38.8 GeV (ie. proton beams with momentum 67 GeV/c to 800 GeV/c)

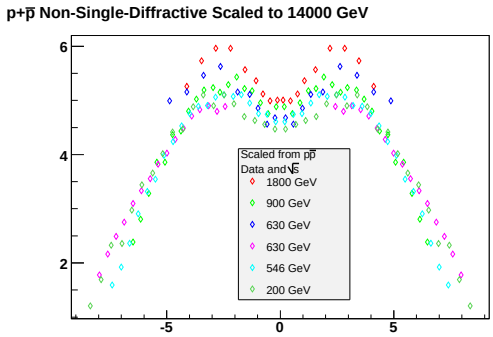

Figure 4 Predicted pp Non-Single-Diffractive (NSD) pseudorapidity distributions at $\sqrt{s_{NN}}$ = 14 TeV. Each curve is an independent extrapolation of lower energy $p\bar{p}$ data [47], using the same procedure as in Fig. 16.3. The scatter of points at central rapidities most likely reflects systematic errors in these difficult measurements.

Figure 17:

the dense medium produced in the collision: *comovers interaction* [50]. Here we present our results for the ratio of the J/ψ yield over the average number of binary nucleon-nucleon collisions at RHIC and LHC energies:

$$R_{AB}^{J/\psi}(b) = \frac{dN_{AB}^{J/\psi}(b)/dy}{n(b)} = \frac{dN_{pp}^{J/\psi}}{dy} \frac{\int d^2s\, \sigma_{AB}(b)\, n(b,s)\, S^{abs}(b,s)\, S^{co}(b,s)}{\int d^2s\, \sigma_{AB}(b)\, n(b,s)} \,. \quad (10)$$

S^{abs} refers to the survival probability due to nuclear absorption and S^{co} is the survival probability due to the medium interactions. The data on dAu collisions at RHIC favorize a small σ_{abs} = 0 mb, so S^{abs} = 1 [51]. The interaction of a particle or a parton with the

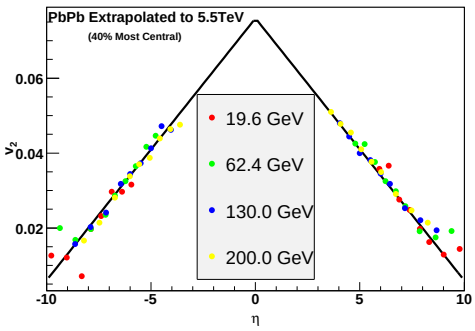

Figure 1 Predicted pseudorapidity dependance of the elliptic flow parameter v_2 for the 40% most central collisions of PbPb at $\sqrt{s_{NN}}$ = 5.5 TeV. An extrapolation procedure similar to that in fig. 16.2 was used, with input data from PHOBOS [47].

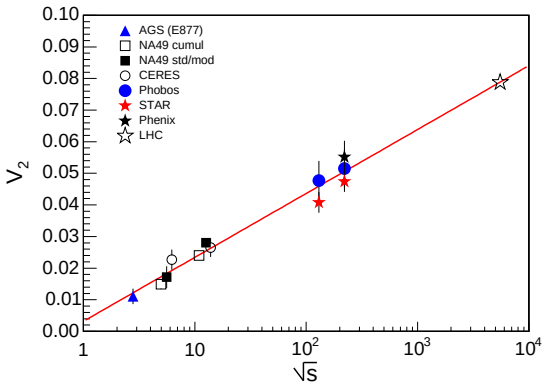

Figure 2 Extrapolation of the elliptic flow parameter v_2 for the 40% most central collisions in PbPb at $\sqrt{s_{NN}}$ = 5.5 TeV. The data is a compilation in [48].

Figure 18:

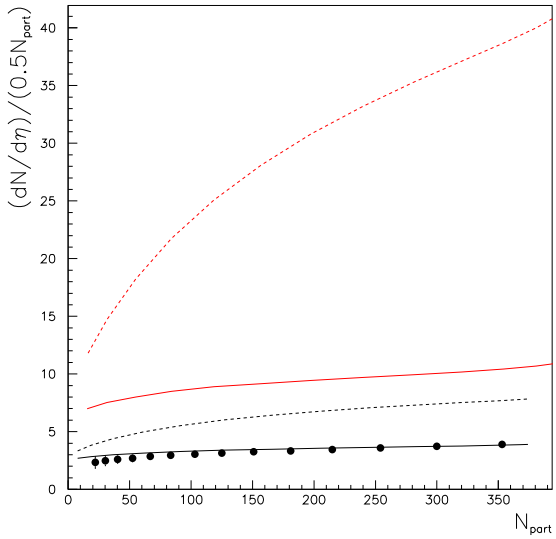

Figure 19: Multiplicities of charged particles with (solid lines) and without (dashed lines) shadowing corrections at RHIC and LHC.

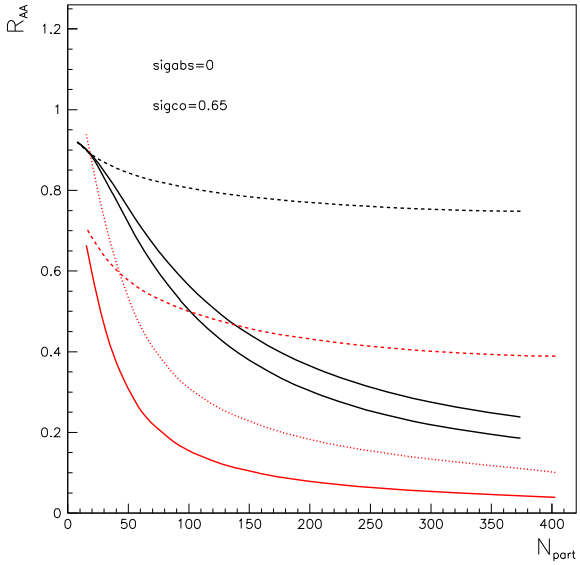

Figure 20: J/ψ production at RHIC and LHC. Dashed: J/ψ shadowing, pointed: comovers suppression, continuous: total suppression.

medium is described by the gain and loss differential equations which govern the final state interactions:

$$\tau \frac{d\rho^{J/\psi}(b,s,y)}{d\tau} = -\sigma_{co}\, \rho^{J/\psi}(b,s,y)\, \rho^{medium}(b,s,y)\,, \tag{11}$$

where $\rho^{J/\psi}$ and $\rho^{co} = \rho^{medium}$ are the densities of J/ψ and comovers. We neglect a gain term resulting from the recombination of c-$\overline{c}$ into J/ψ. Our equations have to be integrated between initial time τ_0 and freeze-out time τ_f. We use the inverse proportionality between proper time and densities, $\tau_f/\tau_0 = \rho(b,s,y)/\rho_{pp}(y)$. Our densities can be either hadrons or partons, so σ_{co} represents an effective cross-section averaged over the interaction time. We obtain the survival

probability $S_{co}(b,s)$ of the J/ψ due to the medium interaction:

$$S^{co}(b,s) \equiv \frac{N^{J/\psi(final)}(b,s,y)}{N^{J/\psi(initial)}(b,s,y)} = \exp\left[-\sigma_{co}\,\rho^{co}(b,s,y)\ell n\left(\frac{\rho^{co}(b,s,y)}{\rho_{pp}(0)}\right)\right]. \quad (12)$$

The shadowing produces a decrease of the medium density. Because of this, the shadowing corrections on comovers increase the J/ψ survival probability S^{co}. On the other side, the shadowing corrections on J/ψ decrease the J/ψ yield. Our results for RHIC and LHC are presented in Fig. 20. We use the same value of the comovers cross-section, $\sigma_{co} = 0.65$ mb that we have used at SPS energies. We neglect the nuclear absorption. The shadowing is introduced in both the comovers and the J/ψ yields.

1.11. Heavy ion collisions at LHC in a Multiphase Transport Model

L.-W. Chen, C. M. Ko, B.-A. Li, Z.-W. Lin and B.-W. Zhang

The AMPT model [52] is a hybrid model that uses the HIJING model [53] to generate the initial conditions, the ZPC [54] for modeling the partonic scatterings, and the ART model [55] for treating hadronic scatterings. In the default version [56], the initial conditions are strings and minijets from the HIJING model and particle production is based on the Lund string fragmentation, while in the string melting version [57], the initial conditions are valence quarks and antiquarks from hadrons produced in the HIJING model and hadronization is described by a coordinate-space coalescence model. Using the AMPT model, we predict in the following the hadron rapidity and transverse momentum distributions, the elliptic flows of both light and heavy hadrons, the two-pion and two-kaon correlation functions in Pb+Pb collisions at center-of-mass energy of $\sqrt{s_{NN}} = 5.5$ TeV at LHC [58].

Shown in the left window of Fig. 21 are the charged hadron pseudorapidity distribution and the rapidity distributions of identified hadrons obtained with (lines with circles) and without (solid lines) nuclear shadowing of nucleon parton distribution functions. Compared to results from the AMPT model for RHIC [59], the distributions at LHC are significantly wider and higher. For mid-pseudorapidity charged hadrons, the distribution shows a clear plateau structure with a value of about 4500 and 2500, respectively, without and with nuclear shadowing. The latter is more than a factor of three higher than that at RHIC. The transverse momentum spectra of identified midrapidity hadrons are shown in the right window of Fig. 21 by lines with circles. The inverse slope parameters, particularly for kaons and protons with transverse momenta below 0.5 GeV/c and 1 GeV/c, respectively, are larger than those at RHIC (solid lines) as a result of stronger final-state rescatterings at LHC than at RHIC. Similar to that observed at RHIC, the proton spectrum is below that of pions at low transverse momenta, but they become comparable at about 2 GeV/c.

Hadron elliptic flows based on a parton scattering cross section of 10 mb, which is needed to describe observed hadron elliptic flows at RHIC [57], are shown in Fig. 22. The left window gives the elliptic flows of light and heavy quarks as functions of their transverse momenta, and they display the expected mass ordering at low transverse momenta, i.e., the elliptic flow is smaller for quarks with larger masses. At larger transverse momenta, the elliptic flows of

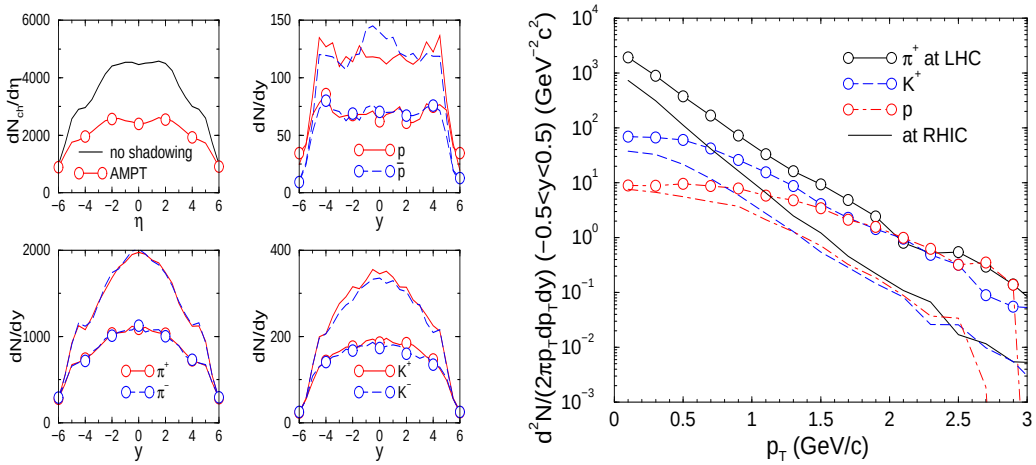

Figure 21: Left window: Pseudorapidity distributions of charged hadrons and rapidity distributions of identified hadrons in central ($b \leq 3$ fm) Pb+Pb collisions at $\sqrt{s_{NN}} = 5.5$ TeV from the default AMPT model with (lines with circles) and without (solid lines) nuclear shadowing. Right window: Transverse momentum spectra of identified midrapidity hadrons from same collisions as well as central Au+Au collisions at $\sqrt{s_{NN}} = 200$ GeV.

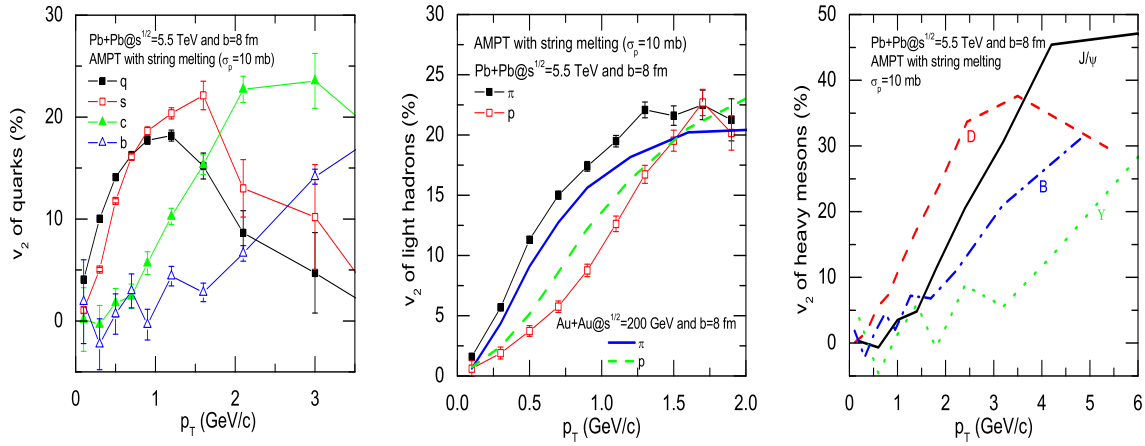

Figure 22: Elliptic flows of quarks (left window), light hadrons (middle window), and heavy mesons (right window) in Pb+Pb collisions at $\sqrt{s_{NN}} = 5.5$ TeV and $b = 8$ fm from the AMPT model with string melting and a parton scattering cross section of 10 mb.

heavy quarks become, however, larger than those of light and strange quarks, which peak at around 1-1.5 GeV/c. The elliptic flows of pions and protons at LHC are shown in the middle window of Fig. 22. Compared to corresponding ones at RHIC for Au+Au collisions at $\sqrt{s_{NN}} = 200$ GeV and same impact parameter shown in the figure, the elliptic flow of pions at LHC is larger while that of protons is smaller. As at RHIC [60], elliptic flows of heavy mesons are estimated from those of quarks using the quark coalescence or recombination model [61, 62] and are shown in the right window of Fig. 22. While elliptic flows of heavy

mesons are dominated by those of heavy quarks, particularly for bottomed mesons, those of heavy mesons with hidden charm or bottom, i.e., quarkonia J/ψ and Υ consisting of a heavy quark and its antiquark, at transverse momentum p_T are simply twice those of their constituent heavy quarks at $p_T/2$.

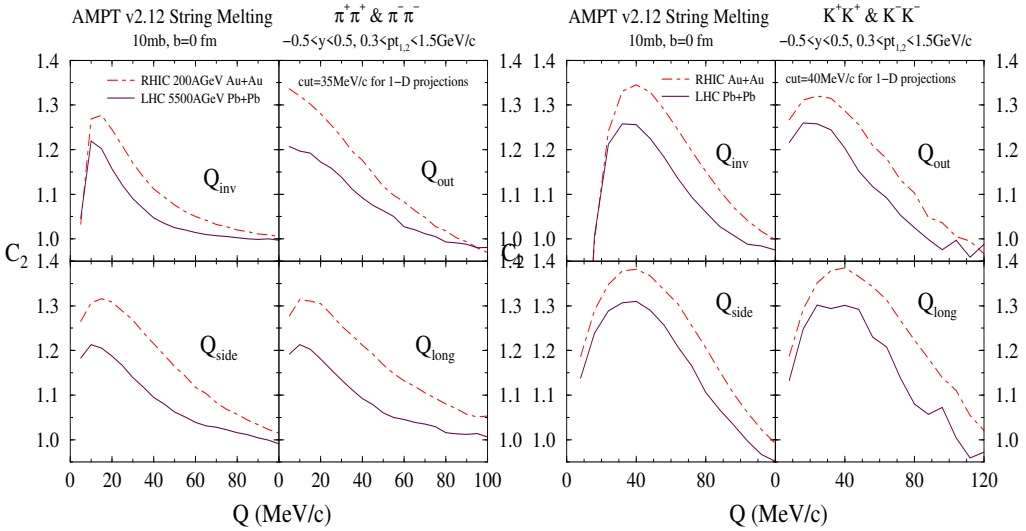

Figure 23: Correlation functions for midrapidity charged pions (left windows) and kaons (right window) with $300 < p_{\rm T} < 1500$ MeV/c from the AMPT model with string melting and a parton cross section of 10 mb for central ($b = 0$ fm) Pb+Pb collisions at $\sqrt{s_{NN}} = 5.5$ TeV (solid lines) and Au+Au collisions at $\sqrt{s_{NN}} = 200$ GeV (dashed lines).

From the positions and momenta of pions or kaons at freeze out, their correlation functions in the longitudinally comoving frame can be calculated using the program Correlation After Burner [63] to take into account their final-state strong and Coulomb interactions. Shown in the left and right windows of Fig. 23 are, respectively, one-dimensional projections of the correlation functions of midrapidity ($-0.5 < y < 0.5$) charged pions and kaons with transverse momentum $300 < p_{\rm T} < 1500$ MeV/c and their comparison with corresponding ones for central Au+Au collisions at $\sqrt{s_{NN}} = 200$ GeV at RHIC, which have been shown to reproduce reasonably measured ones for pions [64]. The correlation functions at LHC are seen to be narrower than at RHIC.

Table 1: Radii from Gaussian fit to correlation functions.

	$R_{\rm out}$(fm)	$R_{\rm side}$(fm)	$R_{\rm long}$(fm)	λ	$R_{\rm out}/R_{\rm side}$
RHIC (π)	3.60	3.52	3.23	0.50	1.02
LHC (π)	4.23	4.70	4.86	0.43	0.90
RHIC (K)	2.95	2.79	2.62	0.94	1.06
LHC (K)	3.56	3.20	3.16	0.89	1.11

Fitting the correlation functions by the Gaussian function $C_2(\mathbf{Q},\mathbf{K}) = 1 + \lambda \exp(-\sum_i R_{ii}^2(K) Q_i^2)$, where $\mathbf{K}$ is the average momentum of two mesons. Extracted radii of

the emission source are shown in Table I. Predicted source radii at LHC are larger than those at RHIC, consistent with the narrower correlation functions at LHC than at RHIC. In both collisions, radii of the emission source for pions are larger than those for kaons. The smaller lambda parameter for pions than for kaons is due to the large halo in the pion emission source from decays of omega mesons. Also, the emission source is non-Gaussian and shifted in the direction of pion or kaon transverse momentum.

1.12. Multiplicity distributions and percolation of strings

J. Dias de Deus and C. Pajares

In the framework of percolations of strings the rapidity distributions for central AA collisions are shown for SPS, RHIC and LHC energies. The obtained value for LHC is lower than the one predicted for the rest of models but larger than the linear energy extrapolation from SPS and RHIC.

Multiparticle production is currently described in terms of color strings stretched between the partons of the projectile and the target these color strings may be viewed as small areas in the transverse space πr_0^2, $r_0 \simeq 0.2 - 0.3$ fm, filled with color field created by the colliding partons. Particles are produced via emision of $q\bar{q}$ pairs in this field. With growing energy and/or atomic number of colliding nuclei, the number of strings grows, and they start to overlap, forming clusters, very much similar to disks in the two dimensional percolation theory. At a certain critical density a macroscopical cluster appears that marks the percolation phase transition [65]. A cluster behaves as a single string with a higher color field $\vec{Q}_n$ corresponding to the vectorial sum of the color changes of each individual $\vec{Q}_1$ string. The resulting color field covers the area S_n of the cluster. As $\vec{Q}_n = \sum \vec{Q}_1$, and the individual string colors may be oriented in an arbitrary manner respective to one another, the average $\vec{Q}_{1i} \cdot \vec{Q}_{1j}$ is zero and $\vec{Q}_n^2 = n\vec{Q}_1^2$.

In this way, the multiplicity μ_n and the average p_T^2 of particles $< p_T^2 >_n$ produced by a cluster of n strings, are given by

$$\mu_n = \sqrt{\frac{nS_n}{S_1}}\mu_1 \; ; \; \langle p_T^2 \rangle_n = \sqrt{\frac{nS_1}{S_n}}\langle p_T^2 \rangle_1 \tag{13}$$

where μ_1 and $\langle p_T^2 \rangle_1$ are the mean multiplicity and the mean transverse momentum of particles produced by a simple string with a transverse area $S_1 = \pi r_0^2$.

Equation (13) is the main tool of our calculations. In order to compute the multiplicities we generate strings according to the quark gluon string model and using a Monte Carlo code. Each string is produced at an identified impact parameter. From this, knowing the transverse area of each string, we identify all the clusters formed is each collision and subsequently compute for each of them the rapidity multiplicity spectrum.

In figure 24 is shown the results, (see reference [3] for details) for central Au-Au collisions at different energies, including the curve for $\sqrt{s_{\rm NN}} = 5.5$ TeV. The value at midrapidity 8.5 is similar to other computations in the same framework (7.3 [66], 8.6 [67]). This strong reduction of the multiplicities relative to simple multicollision models, due to the interaction of strings, was anticipated 12 years ago [68]. Nowdays models have incorporated

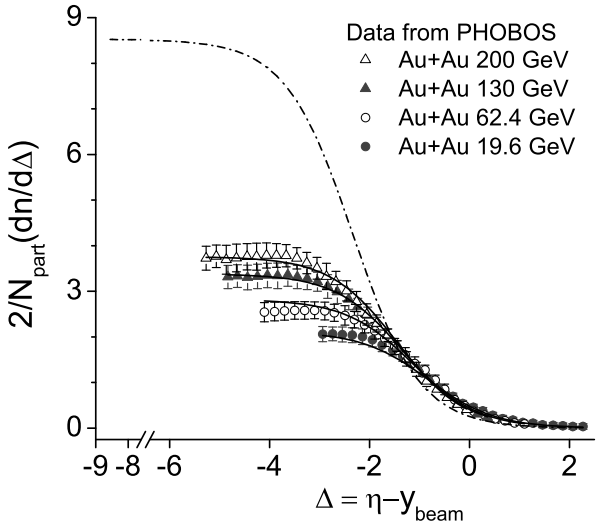

Figure 24: LHC prediction, together with RHIC data and results.

effects, like strong shadowing or triple pomeron couplings to suppress their original values. However, our value is smaller than the one obtained by most of the other existing models. Only, the extrapolation of the observed geometrical scaling in lN to AA given a close value: 9.5. The linear log of energy extrapolation of the SPS and RHIC values gives a lower value of around 6.5.

At SPS and RHIC has been observed an aproximated limiting fragmentation scaling, which is well reproduced in our approach. A clear breaking of this scaling is predicted at LHC.

1.13. Shear Viscosity to Entropy within a Parton Cascade

A. El, C. Greiner and Z. Xu

The shear viscosity is calculated by means of the perturbative kinetic partonic cascade BAMPS with CGC initial conditons for various saturation momentum scale Q_s. $\eta/s \approx 0.15$ stays approximately constant when going from RHIC to LHC.

The measured momentum anisotropy parameter v_2 at RHIC energy can be well understood if the expanding quark-gluon matter is assumed to be described by ideal hydrodynamics. This suggests that a strongly interacting and locally thermalized state of matter has been created which behaves almost like a perfect fluid. Since the initial situation of the quark-gluon system is far from thermal equilibrium, it is important to understand how and which microscopic partonic interactions can thermalize the system within a short timescale and can be responsible as well for its (nearly) ideal hydrodynamical behaviour. Furthermore one would like to know the transport properties of the QGP, most prominently the shear viscosity.

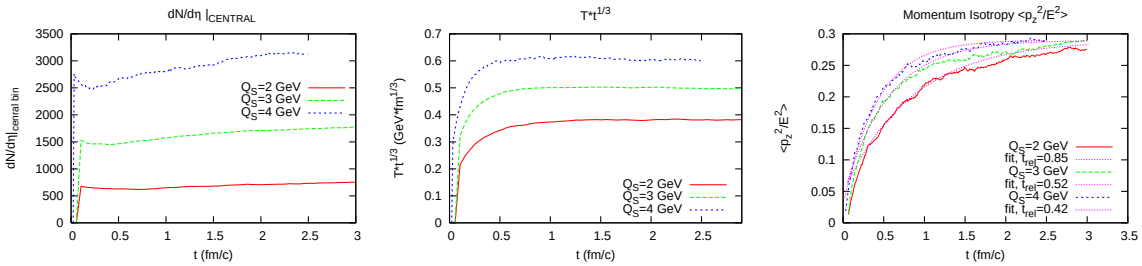

Figure 25: Time evolution of $\frac{dN}{d\eta}$ (left), of the effective temperature (middle) and of the momentum anisotropy (right).

A kinetic parton cascade (BAMPS) [69,70] has been developed with strictly perturbative QCD inspired processes including for the first time inelastic ("Bremsstrahlung") collisions $gg \leftrightarrow ggg$. The multiparticle back reation channel is treated fully consistently by respecting detailed balance within the same algorithm. In [70] it is demonstrated that the inelastic processes dominate the total transport collision rate and thus contribute much stronger to momentum isotropization then elastic ones. Within a default setting of minijet initial conditions, the overall build up of elliptic flow v_2 can be reasonably described [71] (a more dedicated study is presently undertaken [72]).

One can thus expect to see thermalization of a QGP on a short time scale less than 1 fm/c for LHC relevant initial conditions as can be seen in the evolution in time of the temperature and the momentum isotropy depicted in Fig. 25. We apply Bjorken expanding geometry in one dimension. For the initial condition a simple Color Glass Condensate (CGC) gluon distribution is assumed: The initial partons are described by the boost-invariant form of the distribution function $f(x,p)|_{z=0} = \frac{c}{\alpha_s N_c}\frac{1}{\tau_f}\delta(p_z)\Theta(Q_s^2 - p_T^2)$ at a characteristic time $\tau_0 = c/(\alpha_s N_c Q_s)$.

Due to $3 \rightarrow 2$ collisions the particle number first decreases (see Fig. 25) [73]. This is in contrast to the idealistic "Bottom-Up" scenario of thermalization, where an ongoing particle production in the soft sector ($p_T < \alpha_s Q_S$) is predicted with a strong increase in the total particle number. The present calculation show that the particle number roughly stays constant. For the above simple CGC parametrization $Q_s = 2$ GeV corresponds to RHIC energy whereas $Q_s \approx 3-4$ GeV is expected for LHC.

For all energies a nearly ideal hydrodynamical behavior is observed after 0.5 fm/c (middle Fig. 25). The thermalization time lies in the same range when looking at the momentum isotropy. It is of crucial importance to extract out of these simulations the transport properties of QCD matter to quantify the dissipative properties of the fluid. Using standard dissipative hydrodynamics in expanding geometry shear viscosity and ratio $\frac{\eta}{s}$ can be calculated [73]: $\eta = \frac{\tau}{4}\left(T_{xx} + T_{yy} - 2\cdot T_{zz}\right)$ and $s = 4n - n\cdot ln(\lambda)$, where λ denotes the gluon fugacity. As depicted in Fig. 26, the value $\frac{\eta}{s} \approx 0.15$ proves to be a universal number within the BAMPS simulations, being nearly independent of Q_S. This is in line also with full 3-

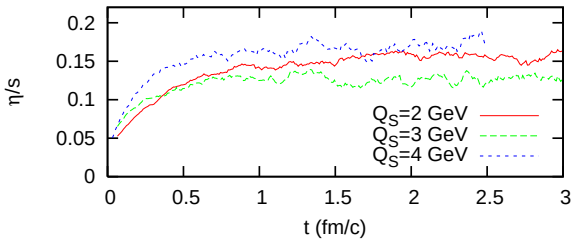

Figure 26: Ratio of the shear viscosity to entropy density ($\alpha_s = 0.3$).

dim calculations employing minijets and Glauber geometry for the initial condition [72]. $\frac{\eta}{s}$ basically only depends on the employed coupling strength α_s (taken to be 0.3 as default setting). Hence, within BAMPS, we do not expect any change in the shear viscosity ratio η/s when going from RHIC to LHC.

1.14. Hadron multiplicities, p_T spectra and net-baryon number in central Pb+Pb collisions at the LHC

K. J. Eskola, H. Honkanen, H. Niemi, P. V. Ruuskanen and S. S. Räsänen

We summarize here our recent LHC predictions [31], obtained in the framework of perturbative QCD (pQCD)+saturation+hydrodynamics (EKRT model for brief) [74]. This model has successfully predicted [74,75] the charged particle multiplicities in central Au+Au collisions at different $\sqrt{s_{\rm NN}}$, and it also describes the low-p_T spectra of pions and kaons at RHIC quite well [31,76].

Primary parton production in the EKRT model is computed from collinearly factorized pQCD cross sections [77] by extending the calculation towards smaller p_T until the abundant gluon production vertices overlap and gluon fusions [78] saturate the number of produced partons (gluons). The saturation scale is determined as $p_0 = p_{\rm sat}$ from a saturation condition [74] $N_{\rm AA}(p_0, \sqrt{s}) \cdot \pi/p_0^2 = c \cdot \pi R_{\rm A}^2$, where $N_{\rm AA}(p_0, \sqrt{s})$ is the average number of partons produced at $|y| \leq 0.5$ and $p_T \geq p_0$. With a constant $c = 1$ the framework is closed. For central Pb+Pb collisions at the LHC $p_{\rm sat} \approx 2$ GeV. We obtain the initial conditions for the cylindrically symmetric boost invariant (2+1)-dimensional hydrodynamical description by converting the computed transverse energy $E_T(p_{\rm sat})$ and net-baryon number $N_B(p_{\rm sat})$ into densities $\epsilon(r, \tau_0)$ and $n_B(r, \tau_0)$ using binary collision profiles and formation time $\tau_0 = 1/p_{\rm sat}$.

Assuming a fast thermalization at τ_0, and zero initial transverse fluid velocity, we proceed by solving the standard equations of ideal hydrodynamics including the current conservation equation for net-baryon number. In the Equation of State we assume an ideal gas of gluons and massless quarks ($N_f = 3$), the QGP, with a bag constant B at $T > T_c$, and a hadron resonance gas of all states with $m < 2$ GeV at $T < T_c$. Taking $B^{1/4} = 239$ MeV leads to first-order transition with $T_c = 165$ MeV. Final state hadron spectra are obtained with Cooper-Frye procedure on a decoupling surface at $T_{\rm dec}$ followed by strong and electromagnetic

2- and 3-body decays of unstable states using the known branching ratios. Extensive comparison [31,76] with RHIC data suggests a single decoupling temperature $T_{\rm dec} = 150$ MeV which is also used to calculate the predictions for the LHC. For details, see [31].

Our predictions [31] for the LHC multiplicities, transverse energies and net-baryon number at $y = \eta = 0$ for 5% most central Pb+Pb collisions at $\sqrt{s_{\rm NN}} = 5.5$ TeV are summarized in table 2. Note that the predicted charged particle multiplicity $\mathrm{d}N_{\rm ch}/\mathrm{d}\eta$ is 2570, i.e. only a third of the initial ALICE design value (see also [75]). Whereas the multiplicity of initially produced partons and observable hadrons are close to each other, the transverse energy is reduced by a factor as large as 3.4 in the evolution from initial state to final hadrons. Due to this reduction the very high initial temperature, $T_0 \gtrsim 1$ GeV, possibly observable through the emission of photons, need not lead to contradiction between predicted and observed E_T.

Table 2:

$\frac{\mathrm{d}N^{\rm tot}}{\mathrm{d}y}$	$\frac{\mathrm{d}N^{\rm tot}}{\mathrm{d}\eta}$	$\frac{\mathrm{d}N^{\rm ch}}{\mathrm{d}y}$	$\frac{\mathrm{d}N^{\rm ch}}{\mathrm{d}\eta}$	$\frac{\mathrm{d}N^{B}}{\mathrm{d}y}$	$\frac{\mathrm{d}E^{T}}{\mathrm{d}y}$	$\frac{\mathrm{d}E^{T}}{\mathrm{d}\eta}$	$\frac{\mathrm{d}N^{\pi\pm}}{\mathrm{d}y}$	$\frac{\mathrm{d}N^{\pi 0}}{\mathrm{d}y}$	$\frac{\mathrm{d}N^{K\pm}}{\mathrm{d}y}$	$\frac{\mathrm{d}N^{p}}{\mathrm{d}y}$	$\frac{\mathrm{d}N^{\bar{p}}}{\mathrm{d}y}$	$p/\bar{p}$
4730	4240	2850	**2570**	3.11	4070	3710	1120	1240	214	70.8	69.6	0.98

Our prediction for the charged hadron p_T spectrum is the lower limit of the red band (HYDRO, the width corresponding to $T_{\rm dec} = 120 \ldots 150$ MeV) in the l.h.s. of figure 27 [31]. The corresponding p_T distributions of π^+ and K^+ are shown in the r.h.s. of the figure (solid lines). The pQCD reference spectra, obtained by folding the LO pQCD cross sections with the nuclear PDFs and fragmentation functions (KKP) and accounting for the NLO contributions with a $\sqrt{s_{\rm NN}}$-dependent K-factor from [79], are also shown (pQCD) on the r.h.s. The yellow bands (pQCD+E-loss) show the results with parton energy losses included as in [80]. We thus predict the applicability region of hydrodynamics at the LHC to be $p_T \lesssim 4 \ldots 5$ GeV, i.e. a wider region than at RHIC.

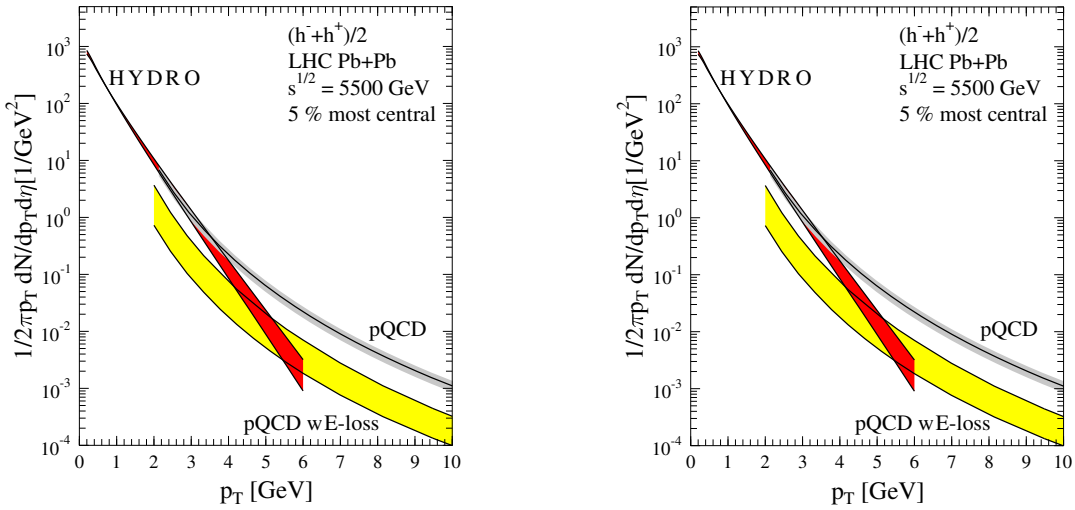

Figure 27:

1.15. Melting the Color Glass Condensate at the LHC

H. Fujii, F. Gelis, A. Stasto and R. Venugopalan

The charged particle multiplicity in central AA collisions and the production of heavy flavors in pA collisions at the LHC is predicted in the CGC framework.

1.15.1. Introduction In the Color Glass Condensate (CGC) framework, fast (large x) partons are described as frozen light cone color sources while the soft (small x) partons are described as gauge fields. The distribution of the fast color sources and their evolution with rapidity is described by the JIMWLK evolution equation; it is well approximated for large nuclei by the Balitsky-Kovchegov (BK) equation. When two hadrons collide, a time dependent color field is produced that eventually decays into gluons [81]. When the projectile is dilute (e.g.,AA collisions at forward rapidity or pA collisions), $k_\perp$ factorization holds for gluon production, thereby simplifying computations. For quark production, $k_\perp$ factorization breaks down and is recovered only for large invariant masses and momenta.

1.15.2. Particle multiplicity in central AA collisions The $k_\perp$ factorized cross-sections are convolutions over "dipole" scattering amplitudes in the projectile and target. Initial conditions for the BK evolution of these are specified at an initial $x = x_0$ (chosen here to be $x_0 \approx 10^{-2}$). In this work [82], we consider two initial conditions, based respectively on the McLerran-Venugopalan (MV) model or on the Golec-Biernat–Wusthoff (GBW) model.We adjust the free parameters to reproduce the limiting fragmentation curves measured at RHIC from $\sqrt{s} =$ 20 GeV to $\sqrt{s} = 200$ GeV. The value of α_s in the *fixed coupling* BK equation is tuned to obtain the observed rate of growth of the saturation scale.The rapidity distribution dN/dy is converted into the pseudo-rapidity distribution $dN/d\eta$ by asuming the produced particles have $m \sim 200$ MeV. A prediction for AA collisions at the LHC is obtained by changing $\sqrt{s}$ to

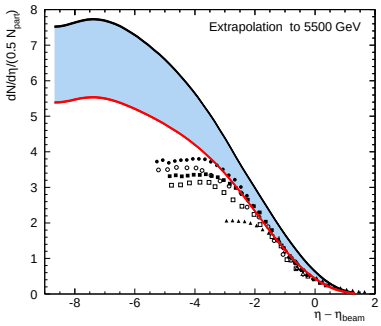

Figure 28: Number of charged particles per unit of pseudo-rapidity at the LHC energy.

5.5 GeV. From Fig. 28, we can infer $dN_{\rm ch}/d\eta|_{\eta=0} = 1000 - 1400$; the two endpoints correspond to GBW and MV initial conditions respectively.

1.15.3. Heavy quark production in pA collisions The cross-section for the production of a pair of heavy quarks [83] is the simplest process for which $k_\perp$-factorization breaks down [84]

in pA collisions. This is due to the sensitivity of the cross-section to 3- and 4-point correlations in the nucleus. Integrating out the antiquark and convoluting with a fragmentation function, one obtains the cross-section for open heavy flavor production, e.g., D mesons. Alternatively, one can use the Color Evaporation Model to obtain the cross-section for quarkonia bound states. The nuclear modification ratio is displayed in figure 29. The main difference at the LHC compared to RHIC energy is that this ratio is smaller than unity already at mid rapidity, and decreases further towards the proton fragmentation region.

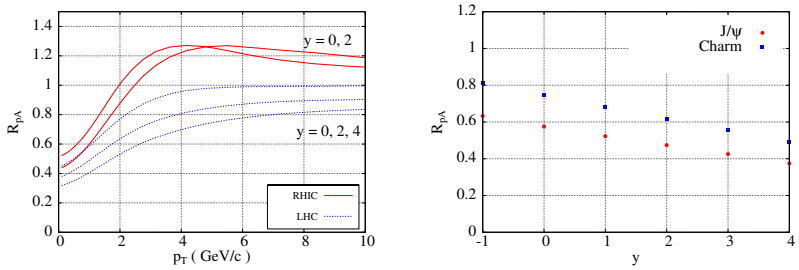

Figure 29: Left: nuclear modification factor for D mesons as a function of $p_\perp$. Right: the same ratio as a function of rapidity, for D mesons and for J/ψ.

1.16. $R_{\rm pA}$ ratio: total shadowing due to running coupling

E. Iancu and D. N. Triantafyllopoulos

We predict that the R_{pA} ratio at the most forward rapidities to be measured at LHC should be strongly suppressed, close to "total shadowing" ($R_{pA} \simeq A^{-1/3}$), as a consequence of running coupling effects in the nonlinear QCD evolution.

We present predictions for the nuclear modification factor, or "R_{pA} ratio", at forward pseudorapidities ($\eta > 0$) and relatively large transverse momenta ($p_\perp$) for the produced particles, in the kinematical range to be accessible at LHC. These predictions are based on a previous, systematic, study of the R_{pA} ratio within the Color Glass Condensate formalism with running coupling [85]. The ratio can be approximated by

$$R_{pA} \simeq \frac{1}{A^{1/3}} \frac{\Phi_A(Y, p_\perp)}{\Phi_p(Y, p_\perp)}, \tag{14}$$

where $Y = \eta + \ln \sqrt{s}/p_\perp$ and $\Phi(Y, p_\perp)$ is the unintegrated gluon distribution of the corresponding target hadron at fixed impact parameter. When the energy increases one expects more and more momentum modes of this distribution to saturate to a value of order $1/\alpha_s$, and the corresponding saturation momentum reads

$$Q_s^2(Y) = \Lambda^2 \exp \sqrt{B(Y - Y_0) + \ln^2 \frac{Q_s^2(Y_0)}{\Lambda^2}}, \tag{15}$$

with $\Lambda = 0.2$ GeV, $B = 2.25$ and $Y_0 = 4$. The initial condition for the nucleus and the proton are taken as $Q_s^2(A, Y_0) = 1.5$ GeV^2 and $Q_s^2(p, Y_0) = 0.25$ GeV^2 respectively, so that

$Q_s^2(\mathrm{A}, Y_0) = \mathrm{A}^{1/3} Q_s^2(p, Y_0)$ for A = 208. The functional form of this expression is motivated by the solution to the nonlinear QCD evolution equations with running coupling [86, 87], while the actual values of the numbers B and Y_0 have been chosen in such a way to agree with the HERA/RHIC phenomenology. As shown in Fig. 30, with increasing Y the two saturation momenta approach to each other and clearly for sufficiently large Y, a nucleus will not be more dense than a proton [87].

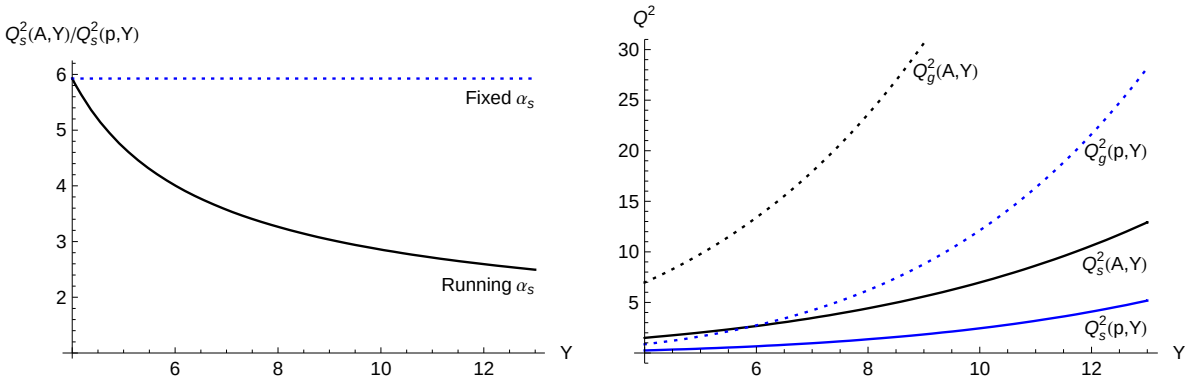

Figure 30: Left: The ratio of the saturation momenta. ($Y = 12$ corresponds to a pseudorapidity $\eta = 6$ for the produced particles). Right: Geometric scaling windows.

For momenta $p_\perp$ larger than Q_s, the gluon distribution satisfies geometrical scaling [86, 88], i.e. it is a function of only the combined variable $p_\perp / Q_s(Y)$:

$$\Phi(p_\perp, Y) \propto \left[\frac{Q_s^2(Y)}{p_\perp^2}\right]^\gamma \left(\ln \frac{p_\perp^2}{Q_s^2(Y)} + c\right), \tag{16}$$

with $\gamma = 0.63$ and $c = O(1)$. This holds within the scaling window $Q_s \lesssim p_\perp \lesssim Q_g$, where $\ln Q_g^2(Y)/Q_s^2(Y) \sim [\ln Q_s^2(Y)/\Lambda^2]^{1/3}$ and for large Y this is proportional to $Y^{1/6}$. The geometrical scaling lines for a proton and a nucleus are shown in Fig. 30. Note that, since Q_g is increasing much faster than Q_s, a *common scaling window* exists, at $Q_s(\mathrm{A}, Y) \lesssim p_\perp \lesssim Q_g(p, Y)$ (and for sufficiently large Y), where the gluon distributions for both the nucleus and the proton are described by Eq. (16).

Within this window, it is straightforward to calculate the $R_{p\mathrm{A}}$ ratio. This is shown in Fig. 31 for two values of pseudorapidity. The upper, dotted, line is the asymptotic prediction of a fixed-coupling scenario, in which the ratio $Q_s^2(\mathrm{A}, Y)/Q_s^2(p, Y) = \text{const.} = \mathrm{A}^{1/3}$, while the lowest, straight, curve is the line of total shadowing $R_{p\mathrm{A}} = 1/\mathrm{A}^{1/3}$. Our prediction with running coupling is the line in between and it is very close to total shadowing. This is clearly a consequence of the fact that the proton and the nuclear saturation momenta approach each other with increasing energy.

Note finally that in the present analysis we have neglected the effects of particle number fluctuations (or "Pomeron loops"). This is appropriate since Pomeron loops effects are suppressed by the running of the coupling [89], and thus can be indeed ignored at all energies of phenomenological interest (in particular, at LHC).

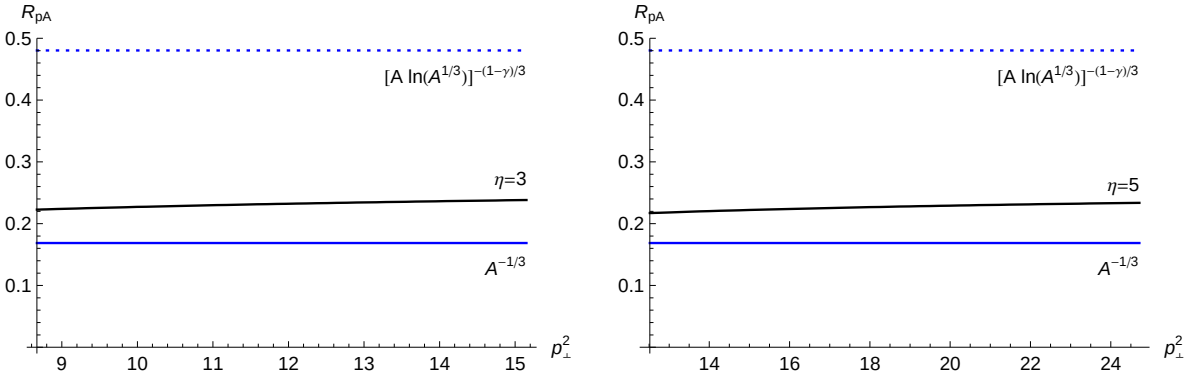

Figure 31: The ratio R_{pA} as a function of $p_\perp^2$ at $\sqrt{s} = 8.8\,\text{TeV}$.

1.17. LHC $\mathrm{d}N_{\mathrm{ch}}/\mathrm{d}\eta$ *and* N_{ch} *from Universal Behaviors*

S. Jeon, V. Topor Pop and M. Bleicher

RHIC $\mathrm{d}N_{\mathrm{ch}}/\mathrm{d}\eta$ contains *two* universal curves, one for limiting fragmentation and one for the transition region. By extrapolating, we predict $\mathrm{d}N_{\mathrm{ch}}/\mathrm{d}\eta$ and $N_{\mathrm{ch}}/N_{\mathrm{part}}$ at the LHC energy.

Data from RHIC at all energies clearly show limiting fragmentation phenomena [90] for very forward and very backward rapidities. In reference [91], we have shown that in the RHIC $\mathrm{d}N/\mathrm{d}\eta$ (normalized to the number of colliding nucleon pairs) spectra at various energies, there are in fact *two* universal curves. This fact is not readily visible if one compares the $\mathrm{d}N/\mathrm{d}\eta$ from different energies directly. It is, however, clearly visible in the slope $\mathrm{d}^2N/\mathrm{d}\eta^2$ as shown in the left panel in figure 32 In this panel, we have plotted $\mathrm{d}N/\mathrm{d}\eta$ per participant pair from the

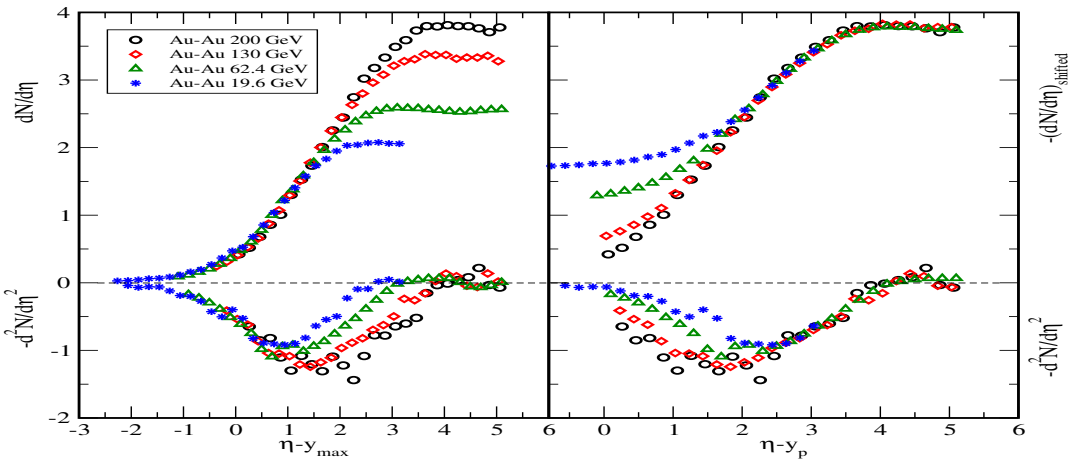

Figure 32: Evidence of two universal curves in RHIC $\mathrm{d}N/\mathrm{d}\eta$ data. The slope $\mathrm{d}^2N/\mathrm{d}\eta^2$ is inverted for visibility. In the left panel, $y_{\mathrm{max}} \approx \ln(\sqrt{s}/m_N)$ are matched whereas in the right panel, the shoulders of $\mathrm{d}N/\mathrm{d}\eta$ are matched.

PHOBOS collaboration for $\sqrt{s_{\mathrm{NN}}} = 19.6, 62.4, 130, 200$ GeV as a function of $\eta - y_{\mathrm{max}}$ with the

corresponding $d^2N/d\eta^2$.

Even though the curves all look similar in $dN/d\eta$, it is rather obvious in $d^2N/d\eta^2$ that the true universal behavior is maintained only up to about 50% of the maximum height. More interestingly, there emerges another universal behavior beyond that point as shown in the right panel in Fig.1. In this panel, we have shifted $dN/d\eta$ vertically and horizontally to match the shoulder. The *common* straight line in $d^2N/d\eta^2$ in this region clearly show that the shoulder region in $dN/d\eta$ is a quadratic function of η. Moreover the *curvature* of the quadratic function is independent of the colliding energy. The universality of these two curves also implies that $(dN/d\eta)_{\eta=0}$ will at most grow like $\ln^2(\sqrt{s_{\rm NN}}/m_N)$ and the total number of produced particle $N_{\rm ch}$ can at most grow like $\ln^3(\sqrt{s_{\rm NN}}/m_N)$.

Parameterizing the $d^2N/d\eta^2$ with simple functions in two slightly different ways (for details see reference [91], we can easily extrapolate to the LHC energy as shown in figure 33. Our prediction is slightly higher than purely linear extrapolation carried out by W. Busza in reference [44].

	$(dN/d\eta)_0$	$N_{\rm total}$
Param I	6.9	87
Param II	6.5	83
K & L	10.7	110
HIJING w/ $p_0 = 3.5\,$GeV	21.4	160
HIJING w/ $p_0 = 5.0\,$GeV	13.6	110

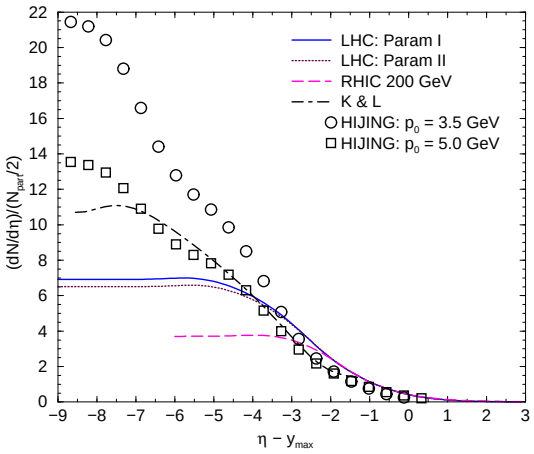

Figure 33: Predictions for 6% central Au-Au collisions at LHC. Curves and rows labeled Param I & II are our predictions. For comparison, HIJING predictions with two different minijet parameters and Kharzeev and Levin formula [7] extrapolated to LHC are also shown.

1.18. Hadron multiplicities at the LHC

D. Kharzeev, E. M. Levin and M. Nardi

We present the predictions for hadron multiplicities in pp, pA and AA collisions at the LHC based on our approach to the Color Glass Condensate.

We expect that at LHC energies, the dynamics of soft and semi-hard interactions will be dominated by parton saturation. In this short note we summarize our results for hadron multiplicities basing on the approach that we have developed and tested at RHIC energies in recent years [7, 92–94]; a detailed description of our predictions for the LHC energies can be found in reference [5]. In addition, we will briefly discuss the properties

of non-linear evolution at high energies, and their implications; details will be presented elsewhere [95]. Our approach is based on the description of initial wave functions of colliding hadrons and nuclei as sheets of Color Glass Condensate. We use a corresponding ansatz for the unintegrated parton distributions, and compute the inclusive cross sections of parton production using $k_\perp$-factorization. The hadronization is implemented through the local parton-hadron duality – namely, we assume that the transformation of partons to hadrons is a soft process which does not change significantly the angular (and thus pseudo-rapidity) distribution of the produced particles. Because of these assumptions, we do not expect our results be accurate for the transverse momentum distributions in AA collisions, but hope that our calculations (see figure 34a) will apply to the total multiplicities.

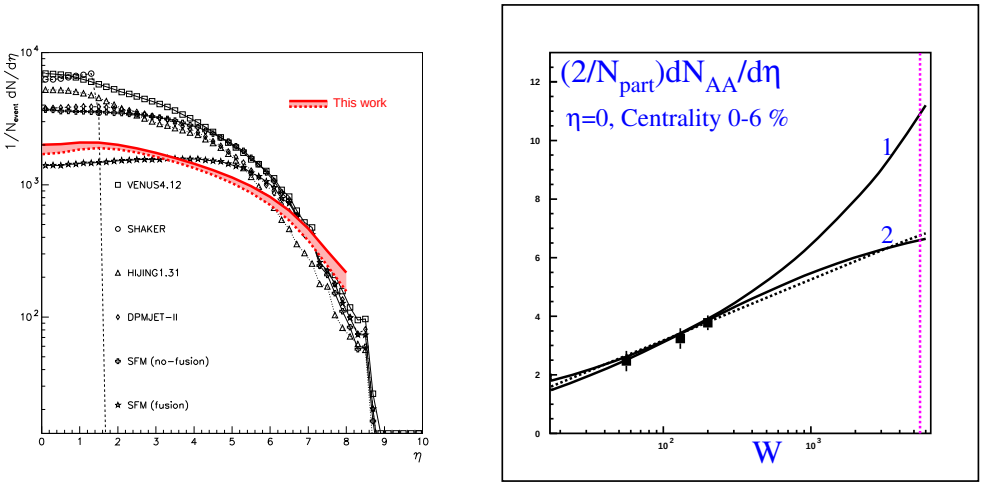

(a) (b)

Figure 34: (a) Charged hadron multiplicity in Pb-Pb collisions as a function of pseudo-rapidity at $\sqrt{s_{\rm NN}} = 5.5$ TeV; also shown are predictions from other approaches (from [5]); (b) Energy dependence of charged hadron multiplicity per participant pair in central AA collisions for different approaches to parton evolution (curves 1 and 2); also shown is the logarithmic fit, dashed curve (from [95]).

While our approach has been extensively tested at RHIC, an extrapolation of our calculations to the LHC energies requires a good theoretical control over the rapidity dependence of the saturation momentum $Q_s(y)$. The non-linear parton evolution in QCD is a topic of vigorous theoretical investigations at present. Recently, we have investigated the role of longitudinal color fields in parton evolution at small x, and found that they lead to the following dependence of the saturation momentum on rapidity [95]:

$$Q_s^2(Y) = \frac{Q_s^2(Y=Y_0)\exp\left(\frac{2\alpha_S}{\pi}(Y-Y_0)\right)}{1+B\,Q_s^2(Y=Y_0)\left(\exp\left(\frac{2\alpha_S}{\pi}(Y-Y_0)\right)-1\right)}, \tag{17}$$

where $B = 1/(32\pi^2)\,(\pi R_A^2/\alpha_S)$; R_A is the area of the nucleus, and α_S is the strong coupling constant. At moderate energies, equation (17) describes an exponential growth of the saturation momentum with rapidity; when extrapolated to the LHC energy this results in the

corresponding growth of hadron multiplicity, see curve "1" in figure 34b. At high energies, equation (17) predicts substantial slowing down of the evolution, which results in the decrease of hadron multiplicity as shown in figure 34b by the curve "2". In both cases, the growth of multiplicity is much slower than predicted in the conventional "soft plus hard" models, see figure 34. We thus expect that the LHC data on hadron multiplicities will greatly advance the understanding of QCD in the strong color field regime.

1.19. CGC at LHC

B. Kopeliovich and I. Schmidt

Data strongly indicate the localization of glue in hadrons within small spots. This leads to a small transverse overlap of gluons in nuclei, i.e. to weak CGC effects. We predict a weak Cronin effect for LHC, not considerably altered by gluon shadowing.

There are many experimental evidences for the localization of the glue in hadrons within spots of small size, $r_0 \approx 0.3$ fm [96, 97]. Correspondingly, the mean transverse momentum of gluons in the proton should be rather large, about 700 MeV/c. One of the manifestation of this phenomenon is a weak Cronin enhancement for gluons. Indeed, the Cronin effect is a result of the interplay between the primordial transverse momentum, $\langle k_T^2 \rangle$, of the incoming parton and the additional momentum, $\Delta\langle k_T^2 \rangle$, gained in the nucleus (broadening). The relative significance of the latter controls the magnitude of the Cronin enhancement. Apparently, the larger the original $\langle k_T^2 \rangle$ is, the weaker is the Cronin effect. The p_T-slope of the cross section also matters: the steeper it is, the stronger is the nuclear enhancement.

Although a rather strong Cronin effect was observed in fixed target experiments, the production of high-p_T hadrons is dominated by scattering of valence quarks [98]. One can access the gluons only at sufficiently high energies. Relying on the above consideration, a very weak Cronin enhancement was predicted in [98] at $\sqrt{s_{\rm NN}} = 200$ GeV, as is depicted in figure 35. A several times stronger effect was predicted in [99]*, and a suppression, rather than enhancement, was the expectation of the color glass condensate (CGC) model [100]. The latest data from the PHENIX experiment at RHIC support the prediction of [98].

At LHC energies one can access quite small values of Bjorken x, such that the lifetime of gluonic fluctuations, $t_c \approx 0.05/(xm_N)$ [101], becomes longer than the nuclear size. Then one might expect coherence effects, in particular pronounced signatures of CGC. However, the longitudinal overlap of gluons is not sufficient, since they also have to overlap in impact parameter, which is something problematic for small gluonic spots. The mean number of gluons overlapping with a given one in a heavy nucleus is, $\langle n \rangle = \frac{3\pi}{4} r_0^2 \langle T_A \rangle = \pi r_0^2 \rho_A R_A = 0.3$, and such a small overlap results in a quite weak CGC and gluon shadowing. The latter is confirmed by the NLO analysis of nuclear structure functions performed in [15]. Missing this important observation, one could easily overestimate both the CGC and gluon shadowing.

Thus, we expect that the effects of CGC, both the Cronin enhancement and shadowing

* The extremely strong gluon shadowing implemented into the HIJING model is ruled out by the recent NLO analysis [15] of DIS data.

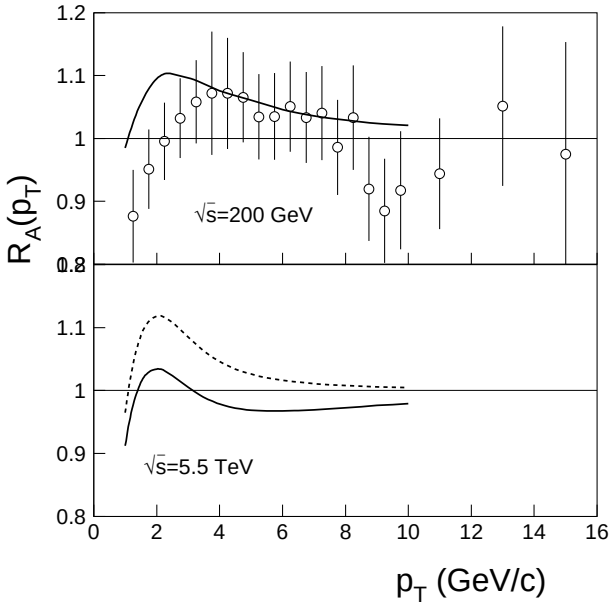

Figure 35: Nucleus-to-proton ratio for pion production versus p_T. Dashed and solid curves correspond to calculations without or with gluon shadowing [98].

suppression, to be rather weak at the LHC, and nearly compensating each other. Therefore in this case the nucleus-to proton ratio is expected to approach unity from below at high p_T.

1.20. Fluctuation Effects on R_{pA} at High Energy

M. Kozlov, A. I. Shoshi and B.-W. Xiao

We discuss a new physical phenomenon for R_{pA} in the fixed coupling case, the total gluon shadowing, which arises due to the effect of gluon number fluctuations.

We study the ratio of the unintegrated gluon distribution of a nucleus $h_A(k_\perp, Y)$ over the unintegrated gluon distribution of a proton $h_p(k_\perp, Y)$ scaled up by $A^{1/3}$

$$R_{pA} = \frac{h_A(k_\perp, Y)}{A^{\frac{1}{3}}\, h_p(k_\perp, Y)} \,. \tag{18}$$

This ratio is a measure of the number of particles produced in a proton-nucleus collision versus the number of particles in proton-proton collisions times the number of collisions. The transverse momentum of gluons is denoted by $k_\perp$ and the rapidity variable by Y.

In the geometric scaling region shown in Fig. 36a the small-x physics is reasonably described by the BK-equation which emerges in the mean field approximation. Using the BK-equation one finds in the geometric scaling regime in the fixed coupling case that the shape of the unintegrated gluon distribution of the nucleus and proton as a function of $k_\perp$ is preserved with increasing Y, because of the geometric scaling behaviour $h_{p,A}(k_\perp, Y) = h_{p,A}(k_\perp^2/Q_s^2(Y))$, and therefore the leading contribution to the ratio R_{pA} is $k_\perp$ and Y independent, scaling with the atomic number A as $R_{pA} = 1/A^{1/3(1-\gamma_0)}$, where $\gamma_0 = 0.6275$ [87]. This means that gluons inside the nucleus and proton are somewhat shadowed since $h_A/h_p = A^{\gamma_0/3}$ lies between total

($h_A/h_p = 1$) and zero ($h_A/h_p = A^{1/3}$) gluon shadowing. The *partial gluon shadowing* comes from the anomalous behaviour of the unintegrated gluon distributions which stems from the BFKL evolution.

We have recently shown [102] that the behaviour of R_{pA} as a function of $k_\perp$ and Y in the fixed coupling case is completely changed because of the effects of gluon number fluctuations or Pomeron loops at high rapidity. According to [103] the influence of fluctuations on the unintegrated gluon distribution is as follows: Starting with an intial gluon distribution of the nucleus/proton at zero rapidity, the stochastic evolution generates an ensamble of distributions at rapidity Y, where the individual distributions seen by a probe typically have different saturation momenta and correspond to different events in an experiment. To include gluon number fluctuations one has to average over all individual events, $h^{fluc.}_{p,A}(k_\perp, Y) = \langle h_{p,A}(k_\perp, Y)\rangle$, with $h_{p,A}(k_\perp, Y)$ the distribution for a single event. The main consequence of fluctuations is the replacement of the geometric scaling by a new scaling, the diffusive scaling [103, 104], $\langle h_{p,A}(k_\perp, Y)\rangle = h_{p,A}\Big(\ln(k_\perp^2/\langle Q_s(Y)\rangle^2))/[DY]\Big)$. The diffusive scaling, see Fig. 36a, sets in when the dispersion of the different events is large, $\sigma^2 = \langle \rho_s(Y)^2\rangle - \langle \rho_s(Y)\rangle^2 = DY \gg 1$, i.e., $Y \gg Y_{DS} = 1/D$, where $\rho_s(Y) = \ln(Q_s^2(Y)/k_0^2)$ and D is the diffusion coefficient, and is valid in the region $\sigma \ll \ln(k_\perp^2/\langle Q_s(Y)\rangle^2) \ll \gamma_0\,\sigma^2$. The new scaling means that the shape of the unintegrated gluon distribution of the nucleus/proton becomes flatter and flatter with increasing rapidity Y, in contrast to the preserved shape in the geometric scaling regime. This is the reason why the ratio in the diffusive scaling regime [102]

$$R_{pA}(k_\perp, Y) \simeq \frac{1}{A^{\frac{1}{3}\left(1-\frac{\ln A^{1/3}}{2\sigma^2}\right)}} \left[\frac{k_\perp^2}{\langle Q_s(A,Y)\rangle^2}\right]^{\frac{\ln A^{1/3}}{\sigma^2}} \tag{19}$$

yields *total gluon shadowing*, $R_{pA} = 1/A^{1/3}$, at asymptotic rapidity Y (at fixed A). This result is universal since it does not depend on the initial conditions. Moreover the slope of R_{pA} as a function of $k_\perp$ descreases with increasing Y. The qualitative behaviour of R_{pA} at fixed α_s due to fluctuation effects is shown in Fig. 36b.

The above effects of fluctuations on R_{pA} are valid in the fixed coupling case and at very large energy. It isn't clear yet whether the energy at LHC is high enough for them to become important. Moreover, in the case where fluctuation effects are neglected but the coupling is allowed to run, a similar behaviour for R_{pA} is obtained [85], including the total gluon shadowing. It remains for the future to be clarified how important fluctuation or running coupling effects are at given energy windows, e.g., at LHC energy.

1.21. Particle Production at the LHC: Predictions from EPOS

S. Porteboeuf, T. Pierog and K. Werner

We present EPOS predictions for proton-proton scattering and for lead-lead collisions at different centralities at LHC energies. We focus on soft physics and show particle spectra of identified particles and some results on elliptical flow. We claim that collective affects are already quite important in proton-proton scattering.

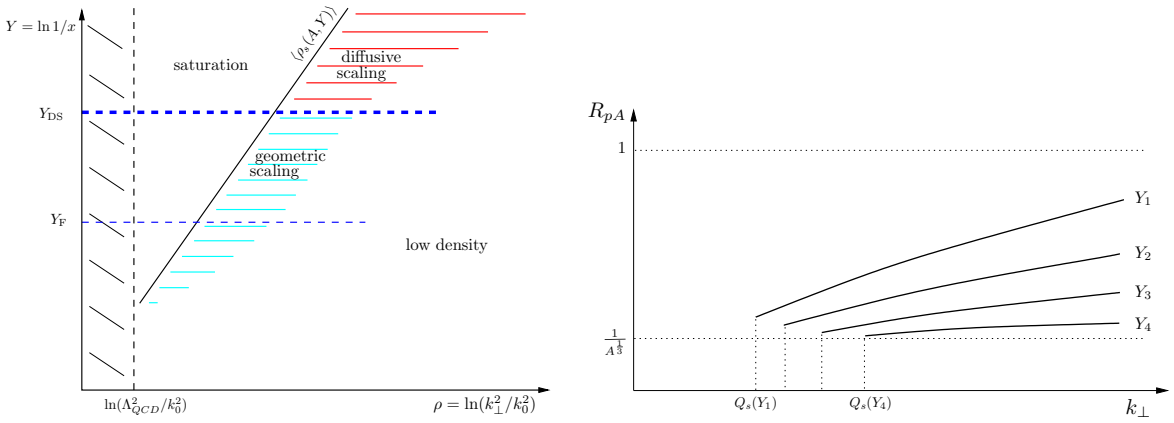

Figure 36: (a) Phase diagram of a highly evolved nucleus/proton. (b) $R_{p,A}$ versus $k_\perp$ at different rapidities $Y_4 \gg Y_3 \gg Y_2 \gg Y_1$.

EPOS is a consistent quantum mechanical multiple scattering approach based on partons and strings, where cross sections and the particle production are calculated consistently, taking into account energy conservation in both cases [105]. A special feature is a careful treatment of projectile and target remnants.

Nuclear effects related to Cronin transverse momentum broadening, parton saturation, and screening have been introduced into EPOS [106].

Furthermore, high density effects leading to collective behavior in heavy ion collisions are also taken into account ("plasma core") [107].

We first show in fig. 37 pseudorapidity and transverse momentum spectra of charged particles and of different identified hadrons, as well as some particle ratios, in proton-proton scattering at 14 TeV. As for heavy ions, the default version of EPOS considers also in proton-proton scattering the formation of a core (dense area), with a hydrodynamical collective expansion. Whereas such "mini-plasma cores" are negligible in proton-proton scattering at RHIC, they play an important role at the LHC, which can be seen from the difference between the full curves (full EPOS, including "mini-plasma") and the dotted curves ("mini-plasma option turned off"). The effect is even more drastic when we investigate the multiplicity dependence of particle production, see fig. 37.

In the following, we investigate lead-lead collisions at 5.5 TeV. In fig. 38, we plot the centrality dependence of particle yields for charged particles and different identified hadrons. We observe an increase by roughly 2.5 for pions, and a bigger factor for the heavier particles.

In fig. 39, we show pseudorapidity spectra, for different particles, at different centralities. The pseudorapidity density of charged particles at $\eta = 0$ is around 2500, for central collisions.

In fig. 40, we show nuclear modification factors $R_{\rm AA}$ (ratios with respect to proton-proton, divided by $N_{\rm coll}$), considering charged particles and different identified hadrons. The peak structure of the baryon results is related to the concave form of the baryon spectra from the radially flowing core in PbPb collisions. All curves are well below one, indicating strong screening effects.

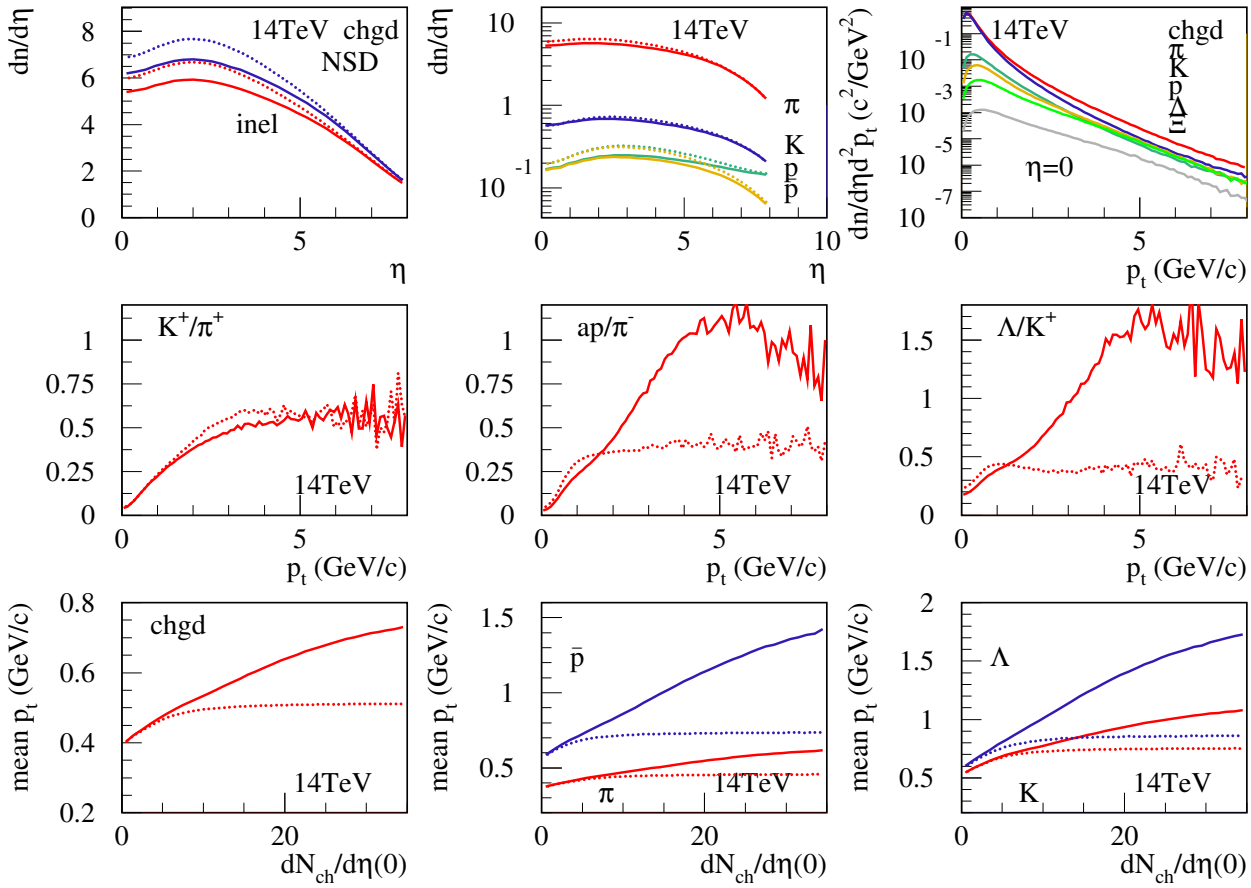

Figure 37: Proton-proton scattering at 14 TeV: pseudorapidity distributions of charged particles (upper row left), and of different identified hadrons (upper row middle), as well as tranverse momentum spectra of different identified hadrons at $\eta = 0$ (upper row right),transverse momentum dependence of particle ratios at $\eta = 0$ (middle row),the average transverse momentum of charged particles and of different identified hadrons at $\eta = 0$ (lower row). The full lines refer to the "mini-plasma option", the dotted ones refer to the "conventional option (mini-plasma turned off)".

In fig. 41, we finally show the transverse momentum dependence of the elliptical flow. The full line is the full calculation, the dashed one only the core contribution. The big difference between the two is due to the fact that high p_t jets are allowed to freely leave the core (no jet quenching).

1.22. Forward hadron production in high energy pA collisions

K. L. Tuchin

We present a calculation of π, D and B production at RHIC and LHC energies based upon the KKT model of gluon saturation.

In this proceedings we present a calculation of forward hadron production in pA

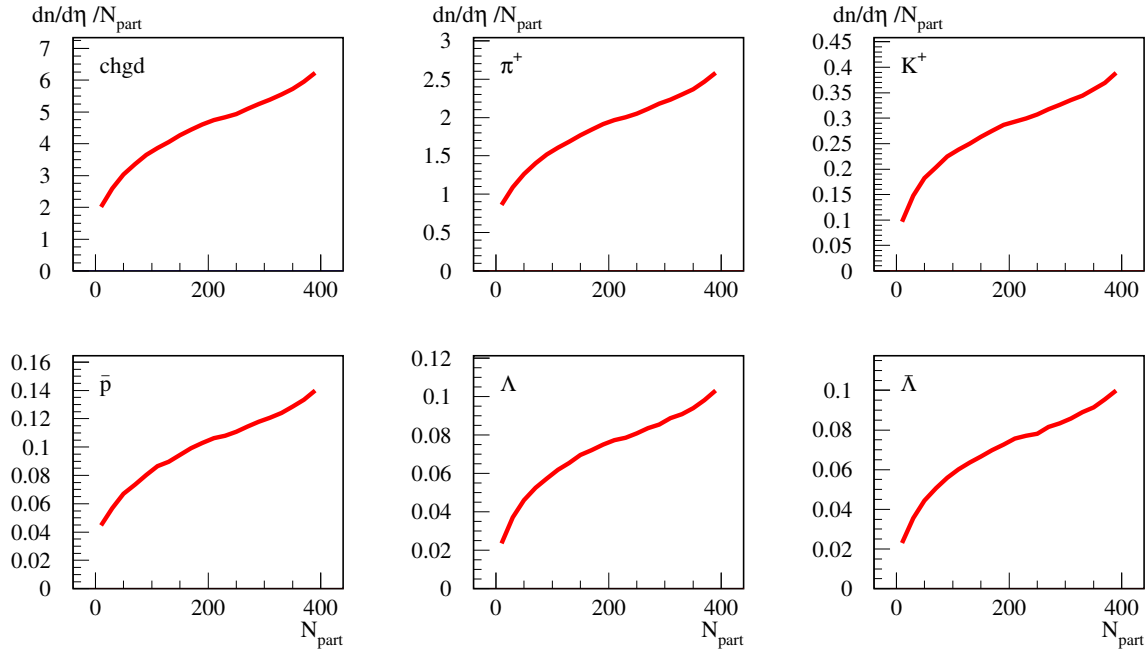

Figure 38: Lead-lead collisions at 5.5 TeV: centrality dependence of particle yields (central pseudorapidity density per participant), for charged particles and different identified hadrons.

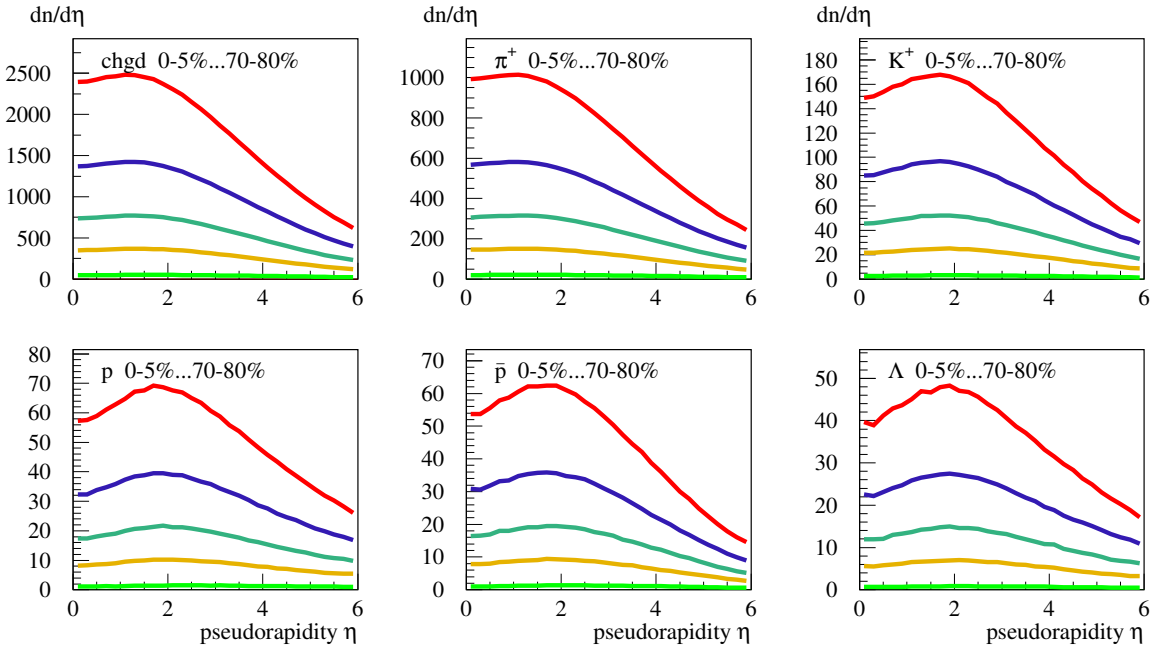

Figure 39: Lead-lead collisions at 5.5 TeV: pseudorapidity distributions of charged particles and of different identified hadrons, at different centralities. For each plot, from top to bottom: 0-5%, 10-20%, 25-35%, 40-50% 70-80%.

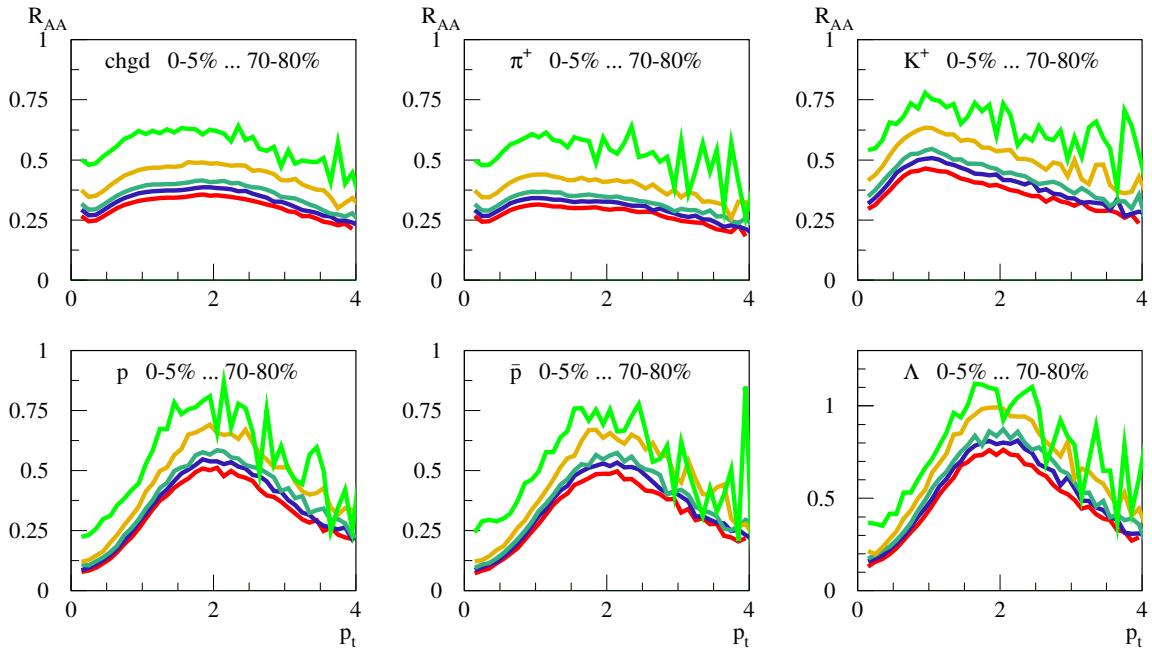

Figure 40: Lead-lead collisions at 5.5 TeV: the nuclear modification factor $R_{\rm AA}$ at $\eta = 0$ of charged particles and of different identified hadrons, at different centralities. For each plot, from top to bottom: 70-80%, 40-50%, 25-35%, 10-20%, 0-5%.

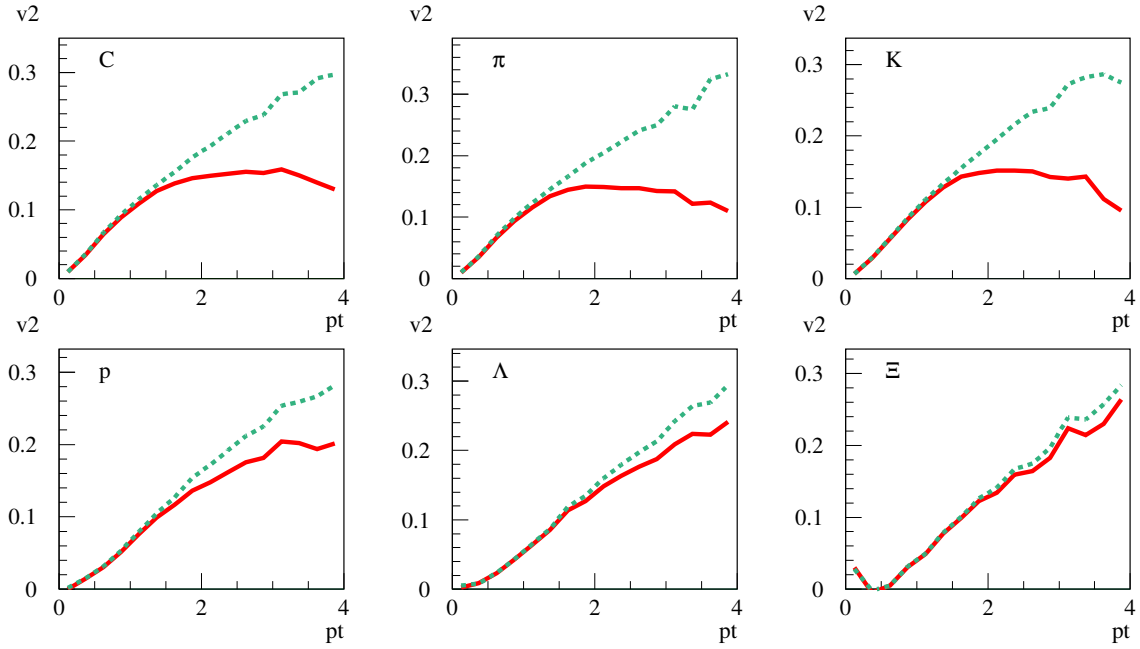

Figure 41: Lead-lead collisions at 5.5 TeV: the transverse momentum dependence of the elliptical flow at $\eta = 0$ of charged particles and of different identified hadrons, for minimum bias collisions. The full line is the full calculation, the dashed one only the core contribution.

collisions at RHIC and LHC. The theoretical framework for inclusive gluon production including the effect of gluon saturation was set up in Ref. [108]. It has been successfully applied to study the inclusive light hadron production at RHIC [109]. Since the KKT model of Ref. [109] works so well at RHIC we decided to extend it to the LHC kinematical region. Doing so we explicitly neglect a possible effect of gluon saturation in a proton which is perhaps a good approximation for the nuclear modification factor. The results of calculation of inclusive pion production are shown in Fig. 42.

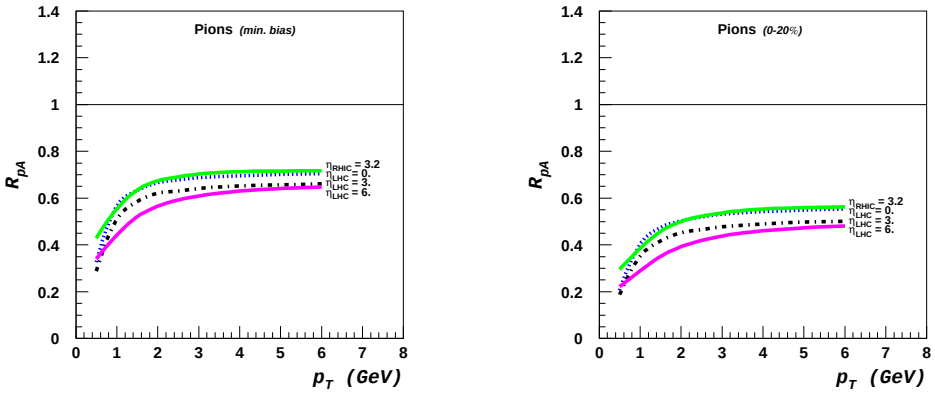

Figure 42: Nuclear modification factor for pion production at RHIC and LHC.

Production of heavy quarks at small x is also affected by gluon saturation in a way similar to that of gluons [110]. The main difference, however, is that the effect of gluon saturation is postponed to higher energies/rapidities for heavier quarks as compared to lighter quarks and gluons. This is because the relevant x is proportional to $m_\perp = (m^2 + k_\perp^2)^{1/2}$ and hence is higher for heavier quarks at the same values of $\sqrt{s}, y, k_\perp$. In Fig. 43 and Fig. 44 the nuclear modification factors for open charm and beauty are shown. The calculations are based upon the theoretical result of Ref. [111] and the KKT model [108].

If the nuclear modification factor is measured to as high transverse mass as possible, we can observe transition from the geometric scaling (described by the KKT model) to the collinear factorization regime. This is shown in Fig. 45. Had the geometric scaling held for all $m_\perp$ and $x < 0.01$, the nuclear modification factor would have been described by the solid line. However, one expect the breakdown of the geometric scaling as illustrated by the dotted lines.

A more detailed description of the theoretical approach to the heavy quark production as well as discussion of the obtained results will be provided in a forthcoming publication.

1.23. Rapidity distributions at LHC in the Relativistic Diffusion Model

G. Wolschin

Stopping and particle production in heavy-ion collisions at LHC energies are investigated in a

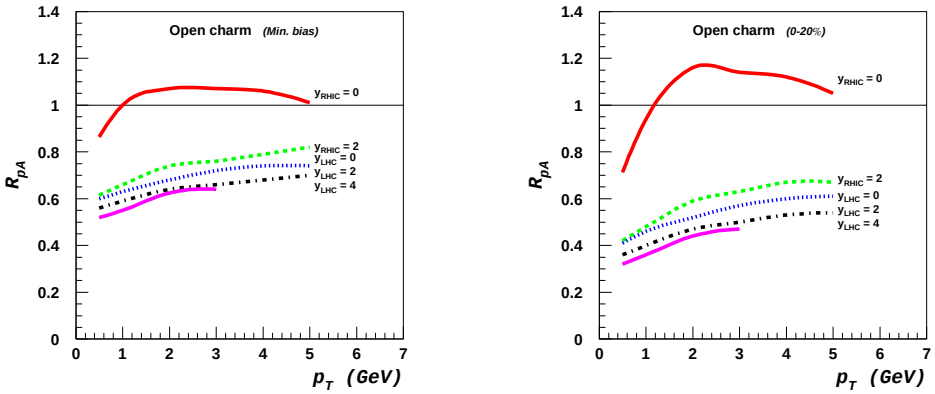

Figure 43: Nuclear modification factor for open charm production at RHIC and LHC.

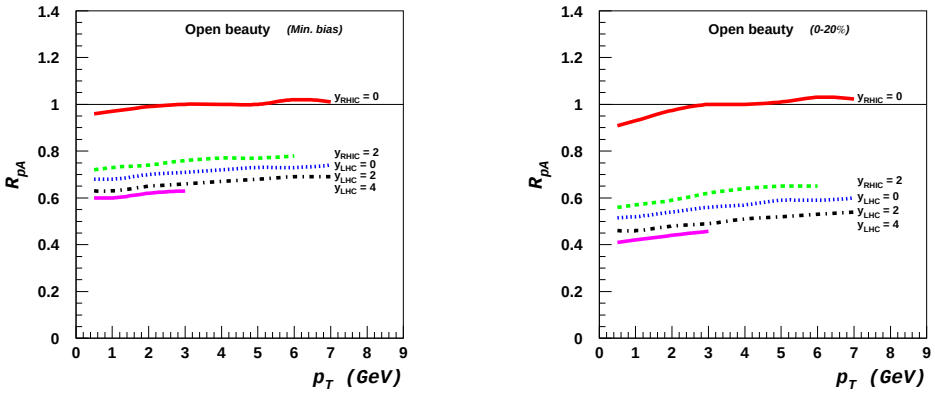

Figure 44: Nuclear modification factor for open beauty production at RHIC and LHC. Note, that the calculations of [111] break down at $y = 0$ at RHIC (x is not small enough); the corresponding result (solid line) is shown for completeness.

Relativistic Diffusion Model (RDM). Using three sources for particle production, the energy- and centrality dependence of rapidity distributions of net protons, and pseudorapidity spectra of charged hadrons in heavy systems are studied from SPS to LHC energies. The transport coefficients are extrapolated from Au + Au at RHIC energies ($\sqrt{s_{NN}}$=19.6 - 200 GeV) to Pb + Pb at LHC energies of $\sqrt{s_{NN}}$= 5.52 TeV. Rapidity distributions for net protons, and pseudorapidity spectra for produced charged particles are calculated at LHC energies.

Net-proton and charged-hadron distributions in collisions of heavy systems have been calculated in a three-sources Relativistic Diffusion Model (RDM) for multiparticle interactions from SPS to LHC energies. Analytical results for the rapidity distribution of net protons in central collisions, and produced charged hadrons are found to be in good agreement

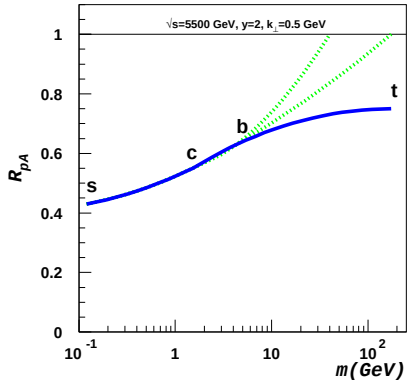

Figure 45: Dependence of the nuclear modification factor on quark mass. Solid line is R_{pA} for quarks. Geometric scaling is expected to break down at $m_\perp \sim Q_{\rm geom} \simeq Q_s^2/\Lambda$, and therefore R_{pA} is anticipated to deviate from the solid line towards unity. Dotted lines illustrate a possible behavior of R_{pA}.

with the available data (Figs. 46, 47) at RHIC.

An extrapolation of the transport coefficients for net protons, and produced hadrons to Pb + Pb at LHC energies of $\sqrt{s_{NN}}$= 5.52 TeV has been performed in [112, 113], and the corresponding rapidity distributions have been calculated as shown in Figs. 46, 47.

The net-proton result for LHC is shown for particle contents of 7 % and 14 % in the central source, respectively [112]. Kinematical constraints will modify the result at large values of the rapidity y. For produced particles, the curves (A) - (D) in Fig. 47 are discussed in [113]. The essential parameters relaxation time, diffusion coefficients or widths of the distribution functions of the three sources, and number of particles in the local equilibrium source will have to be adjusted to the ALICE data.

2. Azimuthal asymmetries

2.1. Transverse momentum spectra and elliptic flow: Hydrodynamics with QCD-based equations of state

M. Bluhm, B. Kämpfer and U. Heinz

We present a family of equations of state within a quasiparticle model adjusted to lattice QCD and study the impact on azimuthal flow anisotropies and transverse momentum spectra within hydrodynamic simulations for heavy-ion collisions at energies relevant for LHC.

2.1.1. Introduction The equation of state (EoS) represents the heart of hydrodynamic simulations for ultra-relativistic heavy-ion collisions. Here, we present a realistic EoS for QCD matter delivered by our quasiparticle model (QPM) faithfully reproducing lattice QCD results. The approach is based on [114–118] adjusted to the pressure p and energy density

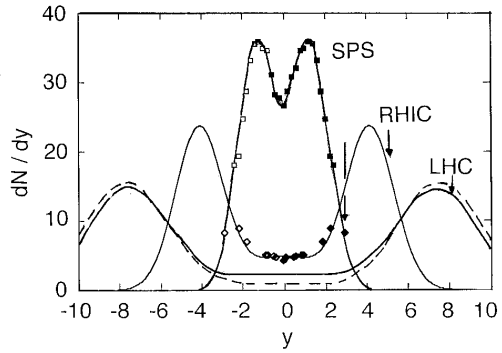

Figure 46: Net-proton rapidity spectra [112] in the Relativistic Diffusion Model (RDM), solid curves: Transition from the double-humped shape at SPS energies of $\sqrt{s_{NN}} = 17.3$ GeV to a broad midrapidity valley at RHIC (200 GeV) and LHC (5.52 TeV).

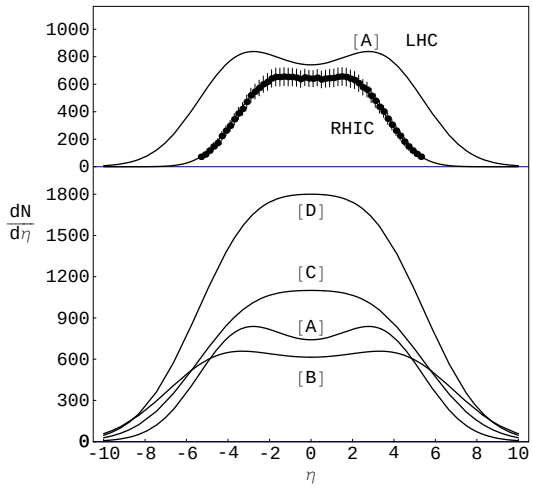

Figure 47: Produced charged hadrons for central Au + Au collisions at RHIC compared with 200 A GeV PHOBOS data, and diffusion-model extrapolation to Pb + Pb at LHC energies of 5520 GeV. See [113] for curves [A] to [D] at LHC energies.

e of $N_f = 2 + 1$ quark flavors [119, 120]. As the QPM EoS does not automatically fit to the hadron resonance gas EoS in the confinement region, we construct a family of EoS's by an interpolation between the hadron resonance gas at $e_1 = 0.45$ GeV/fm^3 and the QPM at flexible e_m (cf. [121] for details). In this way, the influence of details in the transition region on hydrodynamic flow can be studied, since for $e < e_1$ and $e > e_m$ the EoS is uniquely given by the resonance gas and the QCD-based QPM, respectively. In Figure 48, we exhibit the EoS family in the form $p = p(e)$ and the corresponding speed of sound $v_s^2 = \partial p/\partial e$. For LHC, baryon density effects are negligible.

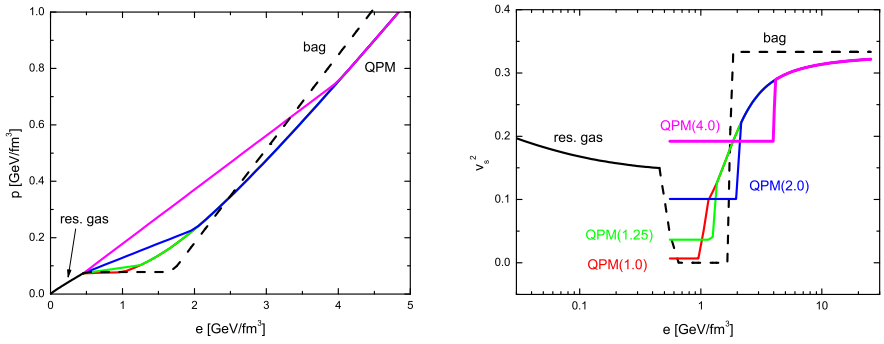

Figure 48: Left panel: Family of EoS's $p(e)$ labelled in the following as QPM(e_m) with e_m = 4.0, 2.0, 1.25, 1.0 GeV/fm^3 (solid curves) combining QPM adjusted to lattice data [119, 120] and hadron resonance gas at matching point e_m. For comparison the bag model EoS (dashed line) is shown. Right panel: corresponding v_s^2.

2.1.2. Predictions for heavy-ion collisions at LHC We concentrate on two extreme EoS's, QPM(4.0) and the bag model EoS being similar to QPM(1.0). We calculate transverse momentum spectra and elliptic flow $v_2(p_T)$ using the relativistic hydrodynamic program package [122, 123] with initial conditions for Pb+Pb collisions at impact parameter $b = 5.2$ fm. For the further initial parameters required by the program we conservatively guess $s_0 = 330$ fm^{-3}, $n_0 = 0.4$ fm^{-3} and $\tau_0 = 0.6$ fm/c for initial entropy density, baryon density and time. Within the QPM these translate into $e_0 = 127$ GeV/fm^3, $p_0 = 42$ GeV/fm^3 and $T_0 = 515$ MeV. The freeze-out temperature is set $T_{f.o.} = 100$ MeV. In Figure 49, we exhibit our results at midrapidity for various primordial hadron species. Striking is the strong radial flow as evident from the flat p_T-spectra and a noticeably smaller $v_2(p_T)$ than at RHIC in particular at low p_T [121]. Details of the Eos in the transition region as mapped out by our family are still visible.

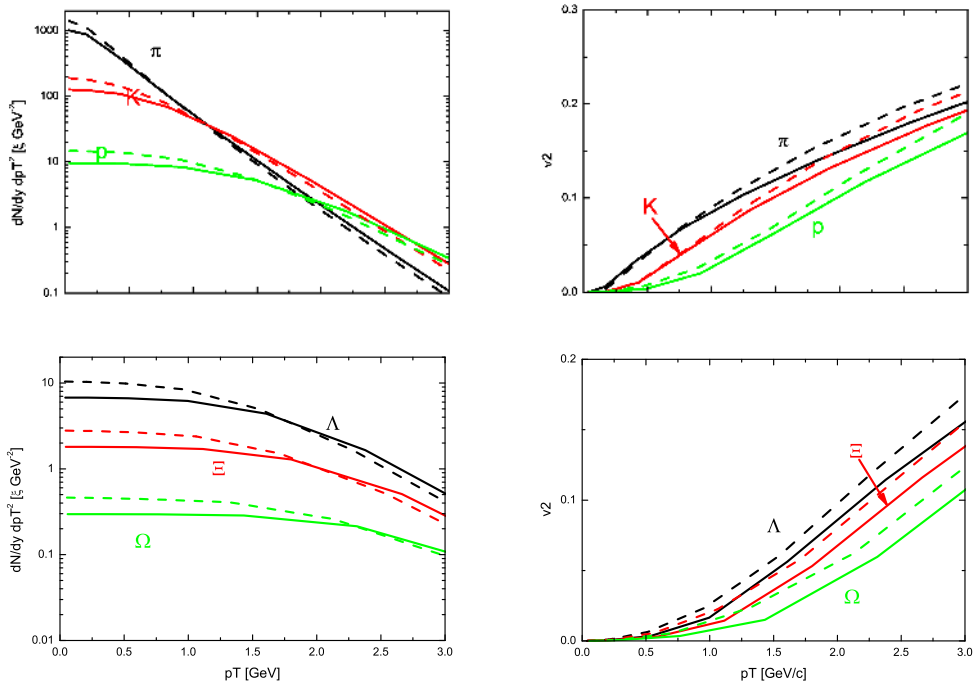

Figure 49: Transverse momentum spectra (left panels) and azimuthal anisotropy (right panels) for directly emitted pions, kaons and protons (upper row) and strange baryons (lower row). Solid and dashed curves are for EoS QPM(4.0) and the bag model EoS, respectively.

2.2. The centrality dependence of elliptic flow at LHC

H.-J. Drescher, A. Dumitru and J.-Y. Ollitrault

We present predictions for the centrality dependence of elliptic flow at mid-rapidity in Pb-Pb collisions at the LHC.

The centrality and system-size dependence of elliptic flow (v_2) provides direct information on the thermalization of the matter created in the collision. Ideal (non-viscous)

hydrodynamics predicts that v_2 scales like the eccentricity, ε, of the initial distribution of matter in the transverse plane. Our predictions are based on this eccentricity scaling, together with a simple parameterization of deviations from hydrodynamics [124]:

$$v_2 = \frac{h\varepsilon}{1 + K/0.7}, \tag{20}$$

where the scale factor h is independent of system size and centrality, but may depend on the collision energy. The Knudsen number K can be expressed as

$$\frac{1}{K} = \frac{\sigma}{S}\frac{\mathrm{d}N}{\mathrm{d}y}\frac{1}{\sqrt{3}}.$$

It vanishes in the hydrodynamic limit. $\mathrm{d}N/\mathrm{d}y$ is the total (charged + neutral) multiplicity per unit rapidity, S is the transverse overlap area between the two nuclei, and σ is an effective (transport) partonic cross section.

The model has two free parameters, the "hydrodynamic limit" h, and the partonic cross section σ. The other quantities, ε, S, $\mathrm{d}N/\mathrm{d}y$, must be obtained from a model for the initial condition. Here, we choose the Color Glass Condensate (CGC) approach, including the effect of fluctuations in the positions of participant nucleons, which increase ε [125]. The model provides a perfect fit to RHIC data for Au-Au and Cu-Cu collisions with $h = 0.22$ and $\sigma = 5.5$ mb [124].

We now briefly discuss the extrapolation to LHC. The hydrodynamic limit h is likely to increase from RHIC to LHC, as the QGP phase will last longer; however, we do not have a quantitative prediction for h. We predict only the centrality dependence of v_2, not its absolute value. Figure 50 is drawn with $h = 0.22$.

The second parameter is σ, which parameterizes deviations from ideal hydrodynamics, i.e., viscous effects. We consider two possibilities: 1) $\sigma = 5.5$ mb at LHC, as at RHIC. 2) $\sigma \sim 1/T^2$ (on dimensional grounds, assuming that no non-perturbative scales arise), where the temperature $T \sim (\mathrm{d}N/\mathrm{d}y)^{1/3}$. This gives the value 3.3 mb in figure 50.

The remaining quantities (S, $\mathrm{d}N/\mathrm{d}y$ and ε) are obtained by extrapolating the CGC from RHIC to LHC, either with fixed-coupling (fc) or running-coupling (rc) evolution of the saturation scale Q_s. The multiplicity per participant increases by a factor of 3 (resp. 2.4) with fc (resp. rc). The eccentricity ε is 10% larger with fc (solid curve in figure 50) than with rc (dash-dotted curve) evolution. Deviations from hydrodynamics (the K-dependent factor in equation (20)) are somewhat smaller than at RHIC: v_2 is 90% (resp. 80%) of the hydrodynamic limit for central collisions if $\sigma = 5.5$ mb (resp. 3.3 mb). Our predictions lie between the dashed and dotted curves, up to an overall normalization factor. The maximum value of v_2 occurs for N_{part} between 60 ($\sigma \approx$ const.) and 80 ($\sigma \sim 1/T^2$).

Elliptic flow will be a first-day observable at LHC. Both its absolute magnitude and its centrality dependence are sensitive probes of initial conditions, and will help to improve our understanding of high-density QCD.

2.3. Elliptic flow from pQCD+saturation+hydro model

K. J. Eskola, H. Niemi and P. V. Ruuskanen

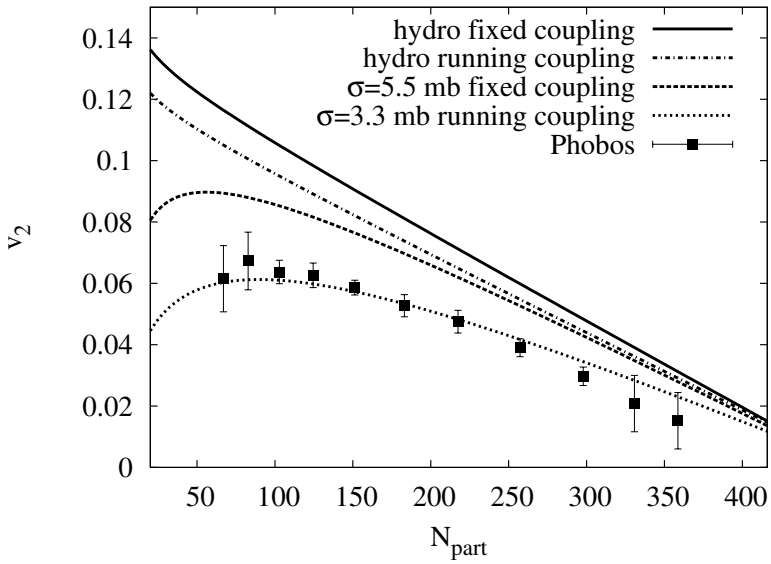

Figure 50: v_2 as a function of $N_{\rm part}$ at mid-rapidity for Pb-Pb collisions at LHC ($\sqrt{s_{\rm NN}}$ = 5.5 TeV). solid- and dash-dotted lines: ε scaling ($K = 0$ in (20)); dashed- and dotted lines: incl. incomplete thermalization, with two values of the partonic cross section. Squares: PHOBOS data for Au-Au collisions at RHIC [126]. The vertical scale is arbitrary (see text).

We have previously predicted multiplicities and transverse momentum spectra for the most central LHC Pb+Pb collisions at $\sqrt{s_{\rm NN}}$ = 5.5 TeV using pQCD + saturation + hydro (EKRT model) [31, 74]. We now extend these calculations for non-central collisions and predict low-p_T elliptic flow. Our model is in good agreement with RHIC data for central collisions, and we show that our extension of the model is also in good agreement with minimum bias v_2 data from RHIC Au+Au collisions at $\sqrt{s_{\rm NN}}$ = 200 GeV.

We obtain the primary partonic transverse energy production and the formation time in central AAcollisions from the EKRT model [74]. With the assumption of immediate thermalization we can use these to estimate the initial state for hydrodynamic evolution. For centrality dependence we consider here two limits which correspond to models eWN and eBC in [127], where the profile and normalization are obtained from optical Glauber model, once the parameters in central collisions are fixed. In the eWN (eBC) model the energy density profile and normalization are proportional to the density and the number of wounded nucleons (binary collisions), respectively. These energy density profiles are used to initialize boost invariant hydro code with transverse expansion. We use the bag model equation of state with massless gluons and quarks ($N_f = 3$), and hadronic phase with all hadronic states up to a mass 2 GeV included. Phase transition temperature is fixed to 165 MeV. Decoupling is calculated using standard Cooper-Frye formula, and all decays of unstable hadronic states are included. Freeze-out temperature is fixed from RHIC p_T spectra for the most central collisions and is 150 MeV for binary collision profile [31] and 140 MeV for wounded nucleon profile. The same freeze-out temperatures are used at the LHC. Both initializations give a good description of the low-p_T spectra for different centralities at RHIC.

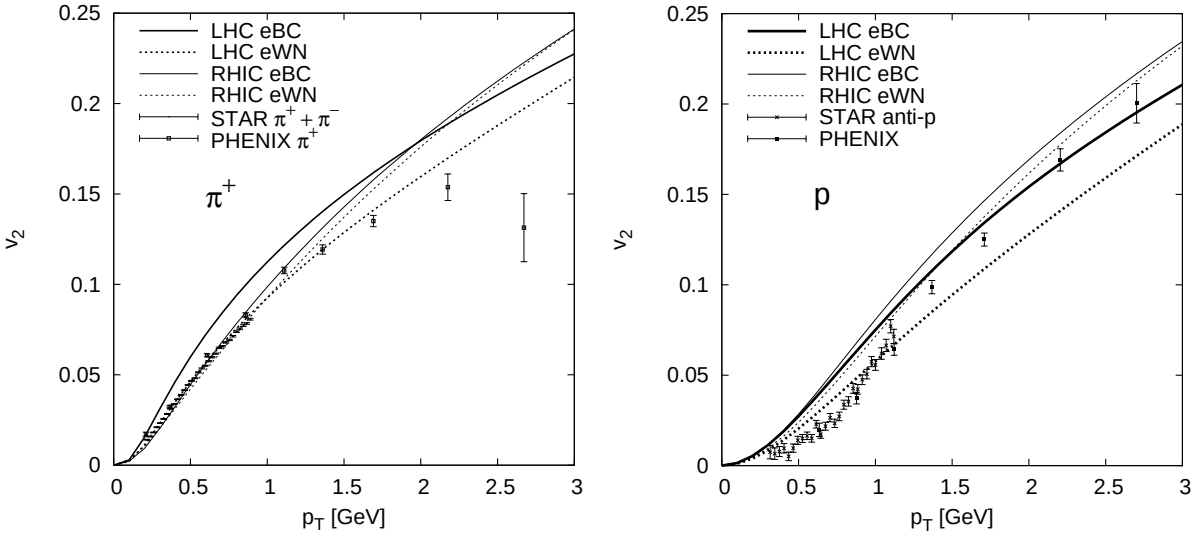

Figure 51:

The left panel of figure 51 shows our calculations for p_T dependence of minimum bias v_2 for positive pions. RHIC results are compared with STAR [128] and PHENIX [129] data. Our minimum bias centrality selection $(0-80\%)$ corresponds to the one used by STAR collaboration. Solid lines are calculations with the eBC model and dashed lines are from the eWN model. Thin lines are our results for RHIC Au+Au collisions at $\sqrt{s_{\rm NN}} = 200$ GeV and thick lines show our predictions for the LHC Pb+Pb collisions at $\sqrt{s_{\rm NN}} = 5.5$ TeV. Largest uncertainty in v_2 calculations for pions comes here from the initial transverse profile of the energy density. Sensitivity to initial time and freeze-out temperature is much weaker. In general the eWN profile leads to weaker elliptic flow than the eBC profile. At the LHC the lifetime of the QGP phase is longer, which results in stronger flow asymmetry than at RHIC. On the other hand the magnitude of transverse flow is also larger, which decreases the v_2 value at fixed p_T. The net effect is that, for a given profile, v_2 of low-p_T pions is larger at the LHC than at RHIC. Since jet production at the LHC starts to dominate over the hydrodynamic spectra at larger p_T than at RHIC [31], we expect that the hydrodynamic calculations should cover a larger p_T range at the LHC. Thus we predict that the minimum bias v_2 of pions at fixed p_T is larger at the LHC than at RHIC, and can reach values as high as 0.2.

Our model clearly overshoots the proton v_2 data from STAR [128] and PHENIX [129]. A more detailed treatment of the hadron gas dynamics and freeze-out is needed to describe both the proton spectra and elliptic flow simultaneously. However, we can still predict the *change* in the behaviour of v_2 of protons when going from RHIC to the LHC. This is shown in the r.h.s. of figure 51. Although the flow asymmetry increases at the LHC, for more massive particles like protons the overall increase in the magnitude of radial flow is more important than for light pions. This results in smaller v_2 at the LHC than at RHIC in the whole p_T range for protons. Even if v_2 at fixed p_T is smaller at the LHC, p_T-integrated v_2 is always larger at the LHC for all particles, due to the increase in the relative weight at larger p_T's.

2.4. From RHIC to LHC: Elliptic and radial flow effects on hadron spectra

G. Kestin and U. Heinz

Using (2+1)-d ideal hydrodynamics [130], we computed the evolution from AGS to LHC energies of the p_T-spectra and elliptic flow at midrapidity for several hadrons [131]. While ideal fluid dynamics begins to break down below RHIC energies, due to viscous effects in the late hadronic stage which persist even at RHIC [132], its validity is expected to improve at the LHC where the elliptic flow saturates in the quark-gluon plasma (QGP) stage, and effects from late hadronic viscosity become negligible [133]. Early QGP viscous effects seem small at RHIC [132, 134], and recent results from Lattice QCD indicate little change of its specific shear viscosity η/s from RHIC to LHC [135]. The following *ideal fluid* dynamical predictions for soft ($p_T \lesssim 2{-}3\,\mathrm{GeV}/c$) hadron production in ($A{\approx}200$)+($A{\approx}200$) collisions at the LHC should thus be robust.

For Au+Au at RHIC we use standard initial ($s_0 = 117/\mathrm{fm}^3$, $n_{B0} = 0.44/\mathrm{fm}^3$ at $\tau_0 = 0.6\,\mathrm{fm}/c$, corresponding to $dN_{\mathrm{ch}}/dy(y{=}b{=}0) = 680$) and final conditions ($e_{\mathrm{f}} = 75\,\mathrm{MeV}/\mathrm{fm}^3$, $T_{\mathrm{f}} = 100\,\mathrm{MeV}$) [130, 134]. For the LHC we assume $dN_{\mathrm{ch}}/dy(y{=}b{=}0) = 1200$ (the lower end of the predicted range), using $s_0 = 271/\mathrm{fm}^3$ and $n_{B0} = 0$ at $\tau_0 = 0.45\,\mathrm{fm}/c$, keeping the product $T_0\tau_0$ and T_{f} unchanged. Predictions for other multiplicities, for interpolation to the actually measured LHC value, can be found in [131].

1. Elliptic flow of pions and protons: Figure 52 shows the pion and proton elliptic flow at RHIC and LHC. While the total (p_T-integrated) pion elliptic flow increases from RHIC to

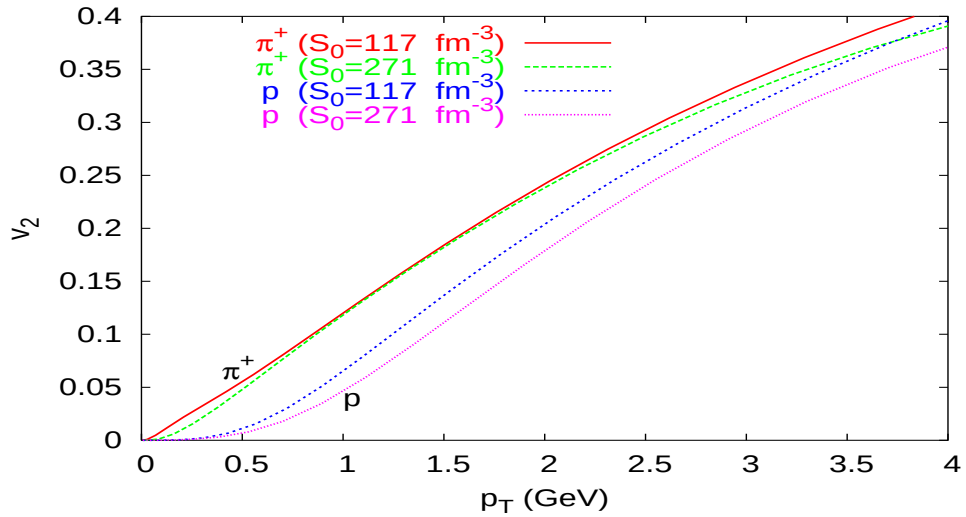

Figure 52: (Color online) Pion and proton elliptic flow as function of p_T for $b = 7$ fm Au+Au collisions at RHIC (s_0=117 fm^{-3}) and LHC (s_0=271 fm^{-3}).

LHC by about 25% [133], very little of this increase ($\sim 5\%$) is of ideal fluid dynamical origin, most of it stemming from the *disappearance* of late hadronic viscous effects between RHIC and LHC. At fixed p_T, Figure 52 shows a *decrease* of v_2, reflecting a shift of the momentum anisotropy to larger p_T by increased radial flow, which flattens the LHC p_T-spectra, affecting

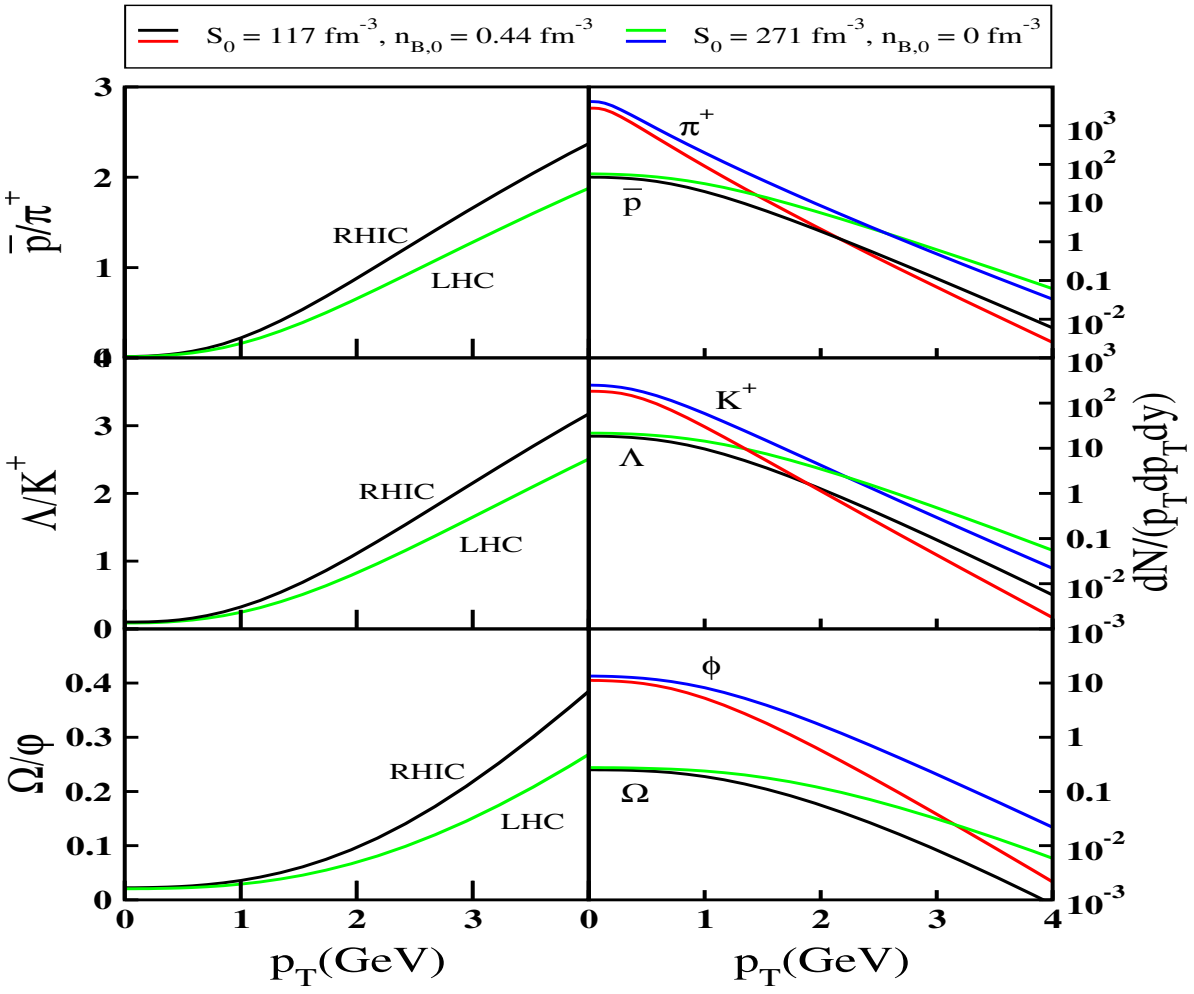

Figure 53: (Color online) Normalized p_T-spectra (right) and p_T-dependent particle ratios (left) for $(\bar{p},\pi^+)$, (Λ,K^+), and (Ω,ϕ) in central Au+Au collisions at RHIC and LHC. Hadron yields are assumed to freeze out at $T_c = 164$ MeV.

the heavier protons more than the lighter pions (Figure 53, right column). These radial flow effects on $v_2(p_T)$ are very small for pions but clearly visible for protons.

2. p_T-dependence of hadron ratios: Hydrodynamic flow, which leads to flatter p_T-spectra for heavy than light particles, is a key contributor to the observed strong rise of the $\bar{p}/\pi$ and Λ/K ratios at low p_T at RHIC [134]. Figure 53 shows that this rise is slower at LHC than at RHIC (left column) since *all* spectra are flatter at LHC due to increased radial flow (right column) while their asymptotic ratios at $p_T \to \infty$ (given by their fugacity and spin degeneracy ratios [134]) remain similar.

2.5. Differential elliptic flow prediction at the LHC from parton transport

D. Molnár

Introduction. General physics arguments and calculations for a class of conformal

field theories suggest [136, 137] that quantum effects impose a lower bound on transport coefficients. For example, the shear viscosity to entropy density ratio is above a small value $\eta/s \gtrsim 0.1$ ("most perfect fluid" limit). Dissipative effects can therefore never vanish in a finite, expanding system. On the other hand, ideal (nondissipative) hydrodynamic modelling of Au+Au collisions at RHIC ($\sqrt{s_{\rm NN}} \sim 100$ GeV) is rather successful, leading many to *postulate* that the hot and dense QCD matter created is in fact such a "most perfect fluid" (at least during the early stages of the RHIC evolution). We predict here how differential elliptic flow $v_2(p_T)$ changes from RHIC to LHC collision energies (Pb+Pb at $\sqrt{s_{\rm NN}} = 5.5$ TeV), *if the quark-gluon system created at both RHIC and the LHC has a "minimal" shear viscosity* $\eta/s = 1/(4\pi)$.

Covariant transport theory is a nonequilibrium framework with two main advantages: i) it has a hydrodynamic limit (i.e., capable of thermalization); and ii) it is *always* causal and stable. In contrast, hydrodynamics (whether ideal, Navier-Stokes, or second-order Israel-Stewart theory [138]) shows instabilities and acausal behavior in certain, potentially large, regions of the hydrodynamic "phase space".

We consider here Lorentz-covariant, on-shell Boltzmann transport theory, with a $2 \to 2$ rate [54, 139]

$$p_1^\mu \partial_\mu f_1 = S(x,\vec{p}_1) + \frac{1}{\pi}\int_2\int_3\int_4 (f_3 f_4 - f_1 f_2) W_{12\to 34}\, \delta^4(p_1+p_2-p_3-p_4)$$

The integrals are shorthands for $\int_i \equiv \int {\rm d}^3 p_i/(2E_i)$. For dilute systems, f is the phase space distribution of quasi-particles, while the transition probability $W = s(s-4m^2){\rm d}\sigma/{\rm d}t$ is given by the scattering matrix element. Our interest here, on the other hand, is to study the theory *near its hydrodynamic (local equilibrium) limit*.

Near local equilibrium, the transport evolution can be characterized via transport coefficients of shear and bulk viscosities (η, ζ) and heat conductivity (λ) that are determined by the differential cross section. For the massless dynamics ($\epsilon = 3p$ equation of state) considered here $\eta \approx 0.8T/\sigma_{\rm tr}$, $\zeta = 0$, and $\lambda \approx 1.3/\sigma_{\rm tr}$, $\tau_\pi \approx 1.2\lambda_{\rm tr}$ [138, 140] ($\sigma_{\rm tr}$ and $\lambda_{\rm tr}$ are the *transport* cross section and mean free path, respectively).

Minimal viscosity and elliptic flow. Finite cross sections lead to dissipative effects that reduce elliptic flow [141, 142]. For a system near thermal and chemical equilibrium undergoing longitudinal Bjorken expansion, $T \sim \tau^{-1/3}$, $s \approx 4n \sim T^3$, and thus $\eta/s = {\rm const}$ requires a growing $\sigma_{\rm tr} \sim \tau^{2/3}$. With $2 \to 2$ processes chemical equilibrium is broken, therefore $\sigma_{\rm tr}$ also depends on the density through $\mu/T \sim \ln n$ (because $s = 4(n - \mu/T)$). We ignore this weak logarithm and take $\sigma_{\rm tr}(\tau) = \sigma_{0,{\rm tr}}(\tau/0.1\ {\rm fm})^{2/3}$ with $\sigma_{0,{\rm tr}}$ large enough to ensure that most of the system is at, or below, the viscosity bound (thus we somewhat *underestimate* viscous effects, i.e., overestimate $v_2(p_T)$).

For AA at $b = 8$ fm impact parameter we use the class of initial conditions in [139] that has three parameters: parton density ${\rm d}N/{\rm d}\eta$, formation time τ_0, and effective temperature T_0 that sets the momentum scale. Because of scalings of the transport solutions [139], $v_2(p_T/T_0)$ only depends on two combinations $\sigma_{\rm tr}{\rm d}N/{\rm d}\eta \sim A_\perp \tau_0/\lambda_{\rm tr}$ and τ_0. This may look worrisome because ${\rm d}N/{\rm d}\eta$ at the LHC is uncertain by at least a factor of two. However, the "minimal viscosity" requirement $T\,\lambda_{\rm tr} \approx 0.5$ *fixes* $\sigma_{\rm tr}{\rm d}N/{\rm d}\eta$ (e.g., with ${\rm d}N/{\rm d}\eta(b{=}0) = 1000$ at RHIC, $\sigma_{0,{\rm tr}} \approx 2.7$ mb), while on dimensional grounds $\tau_0 \sim 1/T_0$.

This means that the *main difference between LHC and RHIC is in the typical momentum scale* T_0 (gold and lead nuclei are basically identical), and therefore to good approximation *one expects the simple scaling* $v_2^{\rm LHC}(p_T) \approx v_2^{\rm RHIC}(p_T T_0^{\rm LHC}/T_0^{\rm RHIC})$. From gluon saturation physics we estimate $r \equiv T_0^{\rm LHC}/T_0^{\rm RHIC} \approx 1.3-1.5$ at $b = 8$ fm via Gribov-Levin-Ryshkin formula as applied in [143] (we take $T_{\rm eff} \sim Q_s \sim \sqrt{\langle p_T^2 \rangle}$).

As depicted in figure 54, at a given p_T the scaling predicts a striking *reduction* of $v_2(p_T)$ at the LHC relative to RHIC. This is the opposite of both ideal hydrodynamic expectations and what was seen going from SPS to RHIC (where $v_2(p_T)$ increased slightly with energy). Experimental determination of the scaling factor $r \equiv Q_s^{\rm LHC}/Q_s^{\rm RHIC}$ would provide a further test of gluon saturation models.

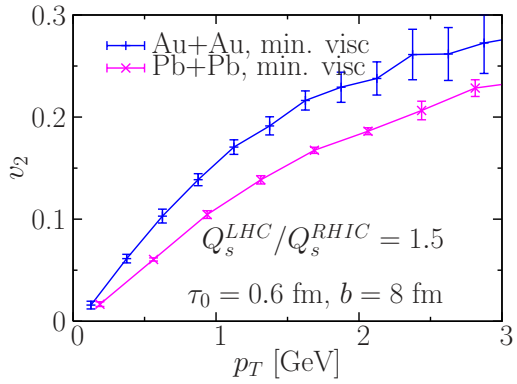

Figure 54: Differential elliptic flow at RHIC and the LHC, assuming a "minimally viscous" quark-gluon system $\eta/s = 1/(4\pi)$ at both energies.

We note that higher momenta at the LHC would also imply somewhat earlier thermalization $\tau_0 \sim 1/T_0$. This is expected to prolong longitudinal Bjorken cooling at the LHC, changing the scale factor in $v_2(p_T)$ from r towards $r^{1-1/3} = r^{2/3} \approx 1.2-1.3$.

3. Hadronic flavor observables

3.1. Thermal model predictions of hadron ratios

A. Andronic, P. Braun-Munzinger and J. Stachel

We present predictions of the thermal model for hadron ratios in central Pb+Pb collisions at LHC.

Based on the latest analysis within the thermal model of the hadron yields in central nucleus-nucleus collisions [144], the expected values at LHC for the chemical freeze-out temperature and baryochemical potential are T=161±4 MeV and μ_b=$0.8^{+1.2}_{-0.6}$ MeV, respectively. For these values, the thermal model predictions for hadron yield ratios in central Pb+Pb collisions at LHC are shown in Table 3. We have assumed no contribution of weak decays to the yield of pions, kaons and protons.

The antiparticle/particle ratios are all very close to unity, with the exception of the ratio $\bar{p}/p$, reflecting the expected small, but nonzero, μ_b value. The errors are determined by the

Table 3: Predictions of the thermal model for hadron ratios in central Pb+Pb collisions at LHC. The numbers in parantheses represent the error in the last digit(s) of the calculated ratios.

π^-/π^+	K^-/K^+	$\bar{p}/p$	$\bar{\Lambda}/\Lambda$	$\bar{\Xi}/\Xi$	$\bar{\Omega}/\Omega$
1.001(0)	0.993(4)	$0.948^{-0.013}_{+0.008}$	$0.997^{-0.011}_{+0.004}$	$1.005^{-0.007}_{+0.001}$	1.013(4)

p/π^+	K^+/π^+	K^-/π^-	Λ/π^-	Ξ^-/π^-	Ω^-/π^-
0.074(6)	0.180(0)	0.179(1)	0.040(4)	0.0058(6)	0.00101(15)

errors of μ_b in case of antiparticle/particle ratios and by the errors of T for all other ratios.

Table 4: Predictions for the relative abundance of resonances at chemical freeze-out.

ϕ/K^-	K^{*0}/K^0_S	Δ^{++}/p	$\Sigma(1385)^+/\Lambda$	Λ^*/Λ	$\Xi(1530)^0/\Xi^-$
0.137(5)	0.318(9)	0.216(2)	0.140(2)	0.075(3)	0.396(7)

Assuming that the yield of resonances is fixed at chemical freeze-out, we show in Table 4 predictions for the relative yield of various resonance species. We emphasize that the above hypothesis needs to be checked at LHC, in view of the data at RHIC [145], which may indicate rescattering and regeneration of resonances after chemical freeze-out.

3.2. (Multi)Strangeness Production in Pb+Pb collisions at LHC. HIJING/B$\bar{\text{B}}$ v2.0 predictions.

V. Topor Pop, J. Barrette, C. Gale, S. Jeon and M. Gyulassy

Strangeness and multi-strangeness particles production can be used to explore the initial transient field fluctuations in heavy ion collisions. We emphasize the role played by Junction anti-Junction (J$\bar{\text{J}}$) loops and strong color electric fields (SCF) in these collisions. Transient field fluctuations of SCF on the baryon production in central (0-5 %) Pb+Pb collisions at $\sqrt{s_{\rm NN}}$ = 5.5 TeV will be discussed in the framework of HIJING/B$\bar{\text{B}}$ v2.0 model, looking in particular to the predicted evolution of nuclear modification factors ($R_{\rm AA}$) from RHIC to LHC energies. Our results indicate the importance of a good description of the baseline elementary $p+p$ collisions at this energy.

In previous publications [146] we studied the possible role of topological baryon junctions [25], and the effects of strong color field (SCF) in nucleus-nucleus collisions at RHIC energies. We have shown that the dynamics of the production process can deviate considerably from that based on Schwinger-like estimates for homogeneous and constant color fields. An increase of the string tension from κ_0= 1 GeV/fm, to *in medium mean*

values of 1.5-2.0 GeV/fm and 2.0-3.0 GeV/fm, for d+Au and Au+Au respectively, results in a consistent description of the observed nuclear modification factors (NMF) $R_{\rm AA}$ in both reactions and point to the relevance of fluctuations on transient color fields. The model provides also an explanation of the baryon/meson anomaly, and is an alternative dynamical description of the data to recombination models [147].

Strangeness enhancement [148], strong baryon transport, and increase of intrinsic transverse momenta k_T [149] are all expected consequences of SCF. These are modeled in our microscopic models as an increase of the effective string tension that controls the quark-anti-quark ($q\bar{q}$) and diquark - anti-diquark ($qq\overline{qq}$) pair creation rates and the strangeness suppression factors. A reduction of the strange (s) quark mass from M_s=350 MeV to the current quark mass of approximately m_s=150 MeV, gives a strangeness suppression factor $\gamma_s^1 \approx 0.70$. A similar value of γ_s^1 (0.69) is obtained by increasing the string tension from κ_0=1.0 GeV/fm to κ=3.0 GeV/fm [146]. Howeover, if we consider that Schwinger tunneling could explain the thermal character of hadron spectra we can define an apparent temperature as function of the average value of string tension ($<\kappa>$), $T = \sqrt{3<\kappa>/4\pi}$ [150]. The predictions at LHC for initial energy density and temperature are $\epsilon_{\rm LHC} \approx 200$ GeV/fm^3 and $T_{\rm LHC} \approx 500$ MeV, respectively [151]. Both values would lead in the framework of our model to an estimated increase of the average value of string tension to $\kappa \approx 5.0$ GeV/fm at LHC energy.

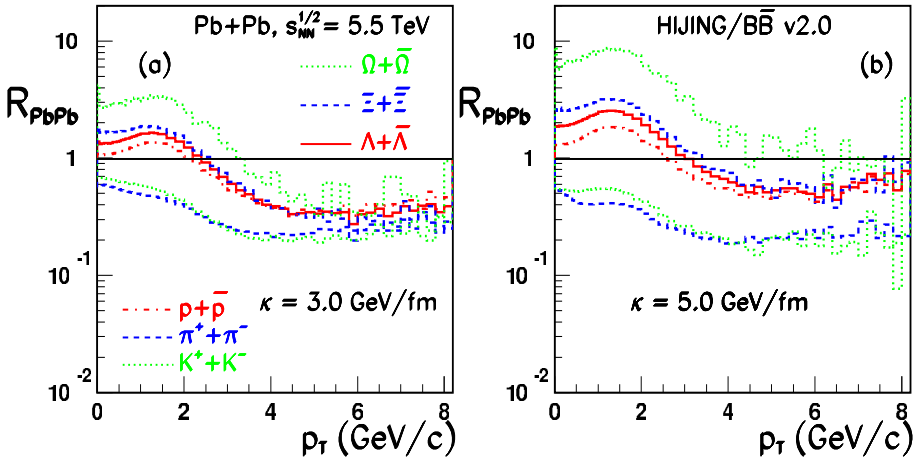

Figure 55: HIJING/B$\bar{\rm B}$ v2.0 predictions including SCF effects for NMF of identified particles. The results for proton and lambda particles are for inclusive measurements.

The p+p cross sections serve as a baseline reference to calculate NMF for $A+A$ collisions ($R_{\rm AA}$). In $p+p$ collisions high baryon/mesons ratio (i.e. close to unity) at intermediate p_T were reported at $\sqrt{s_{\rm NN}}$= 1.8 TeV [152]. These data could be fitted assuming a string tension κ=2.0 GeV/fm. This value is used in our calculations at $\sqrt{s_{\rm NN}}$= 5.5 TeV. This stresses the need for a reference $p+p$ measurements at LHC energies.

The predictions for NMF $R_{\rm PbPb}$ of identified particles at the LHC energy are presented in Fig. 55 for two values of the string tension. From our model we conclude that baryon/meson anomaly, will persist at the LHC with a slight increase for increasing strength of the

chromoelectric field. The NMF $R_{\rm PbPb}$ also exhibit an ordering with strangeness content at low and intermediate p_T. The increase of the yield being higher for multi-strange hyperons than for (non)strange hyperons ($R_{\rm PbPb}(\Omega) > R_{\rm PbPb}(\Xi) > R_{\rm PbPb}(\Lambda) > R_{\rm PbPb}(p)$). At high $p_T > 4GeV/c$ for κ=3.0 GeV/fm, a suppression independent of flavours is predicted due to quench effects. In contrast, this independence seems to happen at $p_T > 8$ GeV/c for κ=5.0 GeV/fm.

As expected, a higher sensitivity to SCF effects on the p_T dependence of multi-strange particle yield ratio is predicted. As an example, Fig. 56 presents our results for the ratio $(\Omega^- + \Omega^+)/\Phi$ in central (0-5%) Pb+Pb collisions and $p+p$ collisions. The results and data at RHIC top energy are also included (left panel).

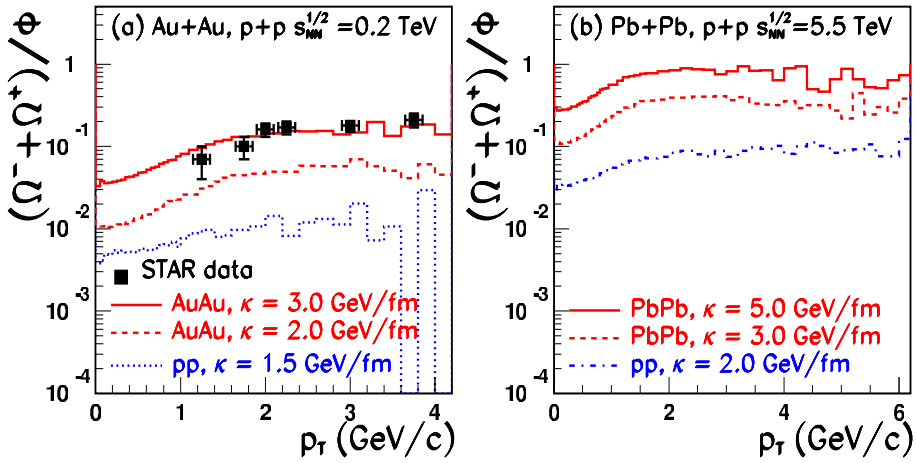

Figure 56: Predictions of HIJING/B$\bar{\rm B}$ v2.0 for the $(\Omega^+ + \Omega^-)/\Phi$ ratio as function of p_T for RHIC (left panel) and LHC (right panel) energies. The experimental data are from STAR [153].

The mechanisms of (multi)strange particles production is very sensitive to the early phase of nuclear collisions, when fluctuation in the color field strength are highest. Their mid-rapidity yield favors a large value of the average string tension as shown at RHIC and we expect similar dynamical effects at LHC energy. The precision of these predictions depens on our knowledge of initial conditions, parton distribution functions at low Bjorken-x, the values of the scale parameter p_0, constituent and current (di)quark masses, energy loss for gluon and quark jets.

3.3. Antibaryon to Baryon Production Ratios in Pb-Pb and p-p collision at LHC energies of the DPMJET-III Monte Carlo

F. Bopp, R. Engel, J. Ranft and S. Roesler

A sizable component of stopped baryons is predicted for *pp* and *PbPb* collisions at LHC. Based on an analysis of RHIC data within framework of our multichain Monte Carlo DPMJET-III the LHC predictions are presented.

This addendum to Ranft's talk about the main DPMJET III prediction addresses

baryon stopping. The interest is a component without leading quarks. Where the flavor decomposition is not determined by final state interactions the valence-quarkless component can be enhanced by considering net strange baryons.

In models, in which soft gluons can arbitrarily arrange colors, a configuration can appear in which the baryonic charge ends up moved to the center. The actual transport is just an effect of the orientation of the color-compensation during the soft hadronisation. Various other ideas about fast baryon stopping exist but to have it caused by such an "initial" process is an attractive option.

The "Dual-Topological" phenomenology of such baryon transport processes was developed 30 years ago [154]. Critical are various baryonium-exchange intercepts which were estimated at that time. Some ambiguity remains until today for the quarkless component (also called "string junction" exchange denoted as $\{SJ\}$) and a confirmation of the flat net-baryon distribution indicated by RHIC data at LHC would be helpful.

Nowadays it is postulated that at very high energy hadronic scattering can be understood as extrapolation of BFKL Pomeron exchanges [155] and their condensates in the minimum bias region. BFKL Pomerons are described by ladders of dispersion graphs, in which soft effects are included using effective gluons. In principle these soft effects include the color compensating mechanism usually modelled as two strings neutralizing triplet colors. A necessary ingredient in this approach are *Odderons* exchanges with Pomeron-like intercepts and with presumably much smaller couplings. As these Odderons can produce a baryon exchange of the type discussed above, a small rather flat net baryon component is expected.

Experimentally, the first indication for a flat component came from never finalized preliminary ZEUS data at HERA. As RHIC runs pp or *heavy ions* instead of $p\bar{p}$ this question could be addressed much better than before and the data seem to require a flat contribution. In a factorizing Quark-Gluon-String model calculation [156] the best fit to RHIC BRAHMS pp data at $\sqrt{s} = 200$ GeV required diquarks with a probability of $\epsilon = 0.024$ to involve a quarkless baryonium-exchange with an intercept $\alpha_{\{SJ\}} = 0.9$.

To obtain such a quarkless baryonium-exchange in the microscopic generator DPMJET III [157] a new string interaction reshuffling the initial strings was introduced. It introduces an exchange with a conservative intercept of $\alpha_{\{SJ\}} = 0.5$. With this baryonium addition good fits were obtained for various baryon ratios in $p-p$ and $d-Au$ RHIC and $\pi-p$ FERMILAB processes [158]. There are of course a number of more conventional baryon transport mechanisms implemented in the model. As the string interaction requires multiple Pomeron exchanges the new mechanism is actually only a 10% effect at pp RHIC. It is, however, important for heavy ion scattering or at LHC energies.

For pp LHC the DPMJET III prediction for the pseudo rapidity of p, $\bar{p}$, and $p-\bar{p}$ is shown in the Figure on the right. The new baryon stopping is now a 40% effect. Of course, with the effective intercept of 0.5 the present implementation of the baryon stopping is a rather conservative estimate. For an intercept of 1.0 the value at $\eta = 0$ would roughly correspond to the present value of $\eta = 4$

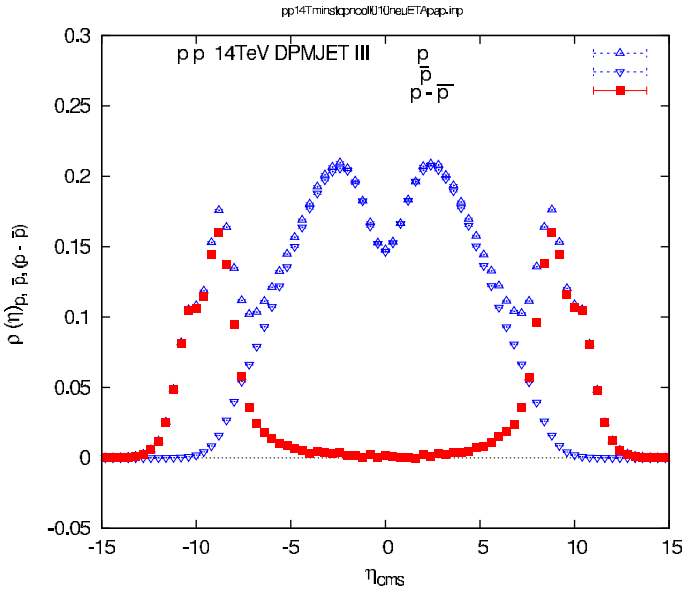

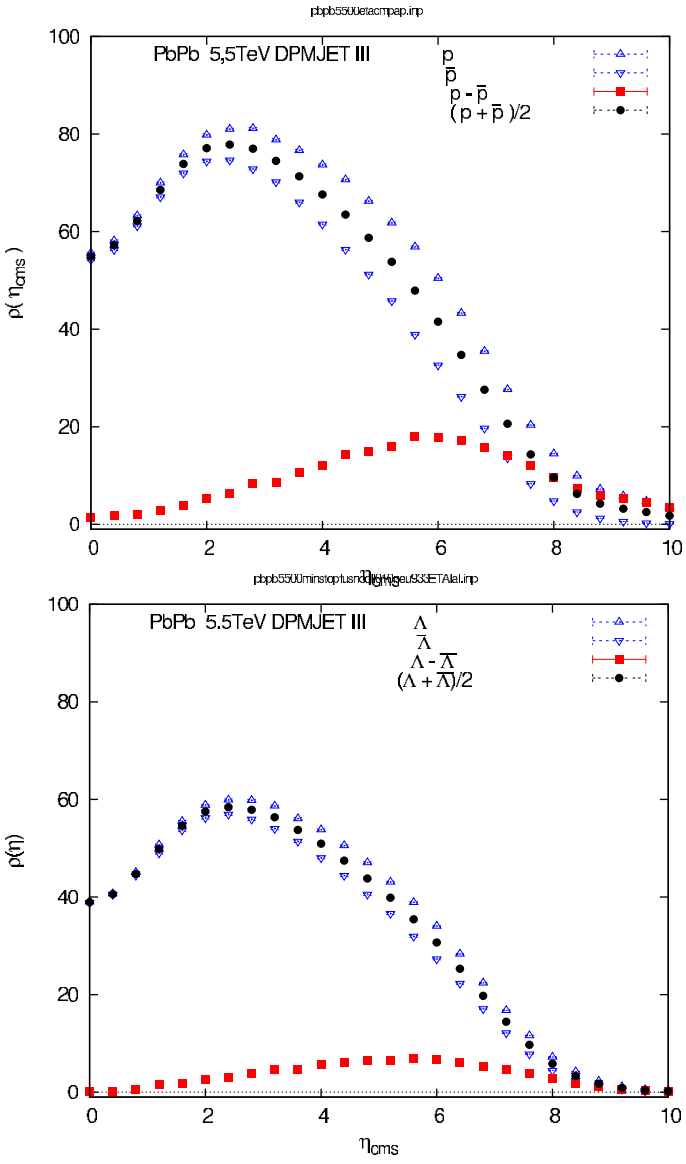

We now turn to DPMJET III prediction for central *PbPb* LHC. For the most central 10% of the heavy ion events the pseudorapidity proton and Λ distributions are given in figures below. The *PbPb* results are preliminary, as the model is not well tested in this region.

3.4. Statistical model predictions for pp and Pb-Pb collisions at LHC

I. Kraus, J. Cleymans, H. Oeschler, K. Redlich and S. Wheaton

Predictions for particle production at LHC are discussed in the context of the statistical model. Moreover, the capability of particle ratios to determine the freeze-out point experimentally is studied, and the best suited ratios are specified. Finally, canonical suppression in pp collisions at LHC energies is discussed in a cluster framework. Measurements with pp collisions will allow us to estimate the strangeness correlation volume and to study its evolution over a large range of incident energies.

Particle production in heavy-ion collisions is, over a wide energy range, consistent with the assumption that hadrons originate from a thermal source with a given temperature T and a given baryon chemical potential μ_B. In the framework of the statistical model, we exploit the feature that the freeze-out points appear on a common curve in the $T - \mu_B$ plane. The parameterization of this curve, taken from reference [159], is used to extrapolate to the LHC energy of $\sqrt{s_{\rm NN}} = 5.5$ TeV: $T \approx 170$ MeV, $\mu_B \approx 1$ MeV.

For the given thermal conditions, particle ratios in central Pb-Pb collisions were calculated; numerical values are given in reference [160]. As soon as experimental results become available, the extrapolation can be cross-checked with particle ratios that exhibit a large sensitivity to the thermal parameters. The ratios shown in figure 57 (left) hardly vary over a broad range of T and μ_B. This feature can be used to investigate the validity of the statistical model at LHC: Especially the prediction for the K/π ratio is limited to a narrow range. It would be hard to reconcile experimental results outside of this band with the statistical model.

Antiparticle over particle ratios, on the other hand, strongly depend on μ_B (figure 57, middle panel). Most of all, the $\bar{p}/p$ ratio almost directly translates to the baryon chemical potential, since the T dependence is very weak. Better suited for the temperature determination are ratios with large mass differences, i.e. Ω/π and Ω/K, which increase in the studied range by 25% per 10 MeV change in T. The astonishing similarity between K and π in this respect is caused by the huge contribution of 75% from resonance decays to pions for the given thermal conditions [161].

In collisions of smaller systems, the strange-particle phase-space exhibits a suppression beyond the expected canonical suppression. A modification of the statistical model is proposed in references [162, 163], which is based on the assumption that strangeness conservation is maintained in correlated sub-volumes of the fireball. The size of these clusters, which could be smaller than the volume defined by all hadrons, was estimated from relative strangeness production in collisions of small systems at top SPS and RHIC energy. The radius R_C of a spherical cluster is of the order of 1 - 2 fm and shows only a weak energy dependence. Additionally it is not clear at which stage of the interaction the strangeness abundance is formed. Possibly the early, dense phase is crucial, so the cluster size should be the same at RHIC and LHC, or, on the contrary, the total number of particles at the late stage of hadronisation is relevant; thus R_C should increase as the multiplicity will increase with colliding energy.

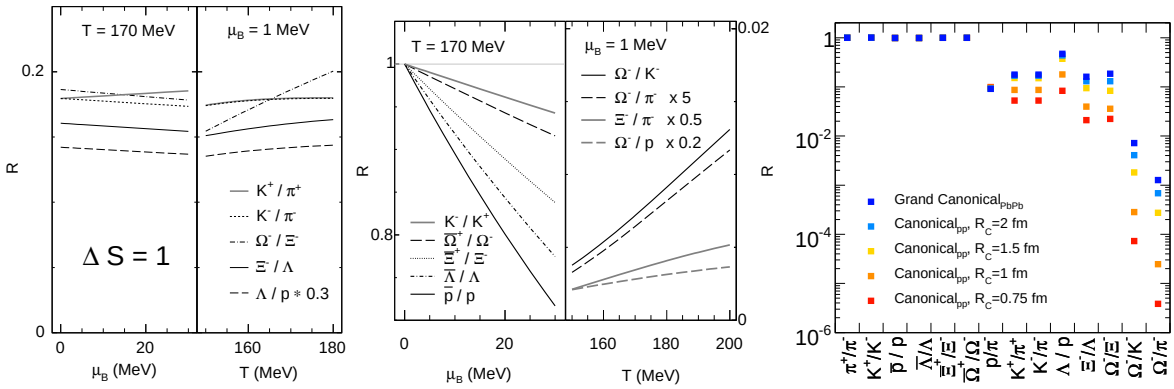

Figure 57: Left: Ratios R of particles with unequal strangeness content as a function of μ_B for $T = 170$ MeV (left) and as a function of T for $\mu_B = 1$ MeV (right).
Middle: Antiparticle/particle ratios R as a function of μ_B for $T = 170$ MeV (left) (the horizontal line at 1 is meant to guide the eye). Particle ratios R involving hyperons as a function of T for $\mu_B = 1$ MeV (right).
Right: Ratios R of particles in the grand-canonical ensemble and with suppressed strange-particle phase-space in different canonical volumes indicated by the spherical radius R_C, calculated at $\mu_B = 1$ MeV and $T = 170$ MeV.

Instead of precise predictions as shown for Pb-Pb collisions, the correlation volume will be extracted from measurement. As displayed in figure 57 (right), especially the Ω/π ratio varies over orders of magnitude in a reasonable range of the correlation length. This allows for a good estimate of the cluster size which will give us more insight into the mechanism of strangeness production.

3.5. Universal behavior of baryons and mesons transverse momentum distributions in the framework of percolation of strings

L. Cunqueiro, J. Dias de Deus, E. G. Ferreiro and C. Pajares

The clustering of color sources [65] reduces the average multiplicity and enhances the average $\langle p_T \rangle$ of an event in a factor $F(\eta)$ with respect to those resulting from pure superposition of strings:

$$\langle \mu \rangle = N_s F(\eta) \langle \mu \rangle_1, \; \langle p_T^2 \rangle = \langle p_T^2 \rangle_1 / F(\eta) \tag{21}$$

where N_s is the number of strings and $F(\eta) = \sqrt{(1 - e^{-\eta})/\eta}$ is a function of the density of strings η [164]. The invariant cross section can be written as a superposition of the transverse momentum distributions of each cluster, $f(x, p_T)$ (Schwinger formula for the decay of a cluster), weighted with the distribution of the different tension of the clusters, $W(x)$ ($W(x)$ is the gamma function whose width is proportional to $1/k$ where k is a determined function of η related to the measured dynamical transverse momentum and multiplicity

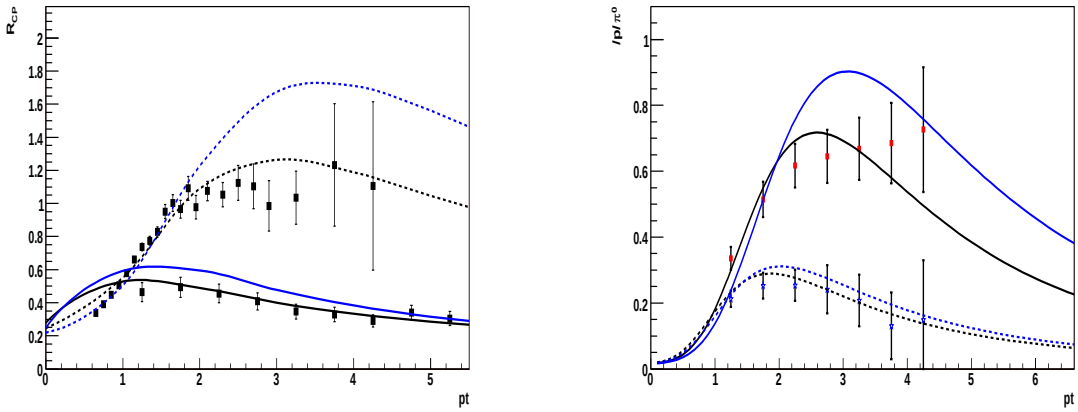

Figure 58: Left: R_{CP} for neutral pions (solid) and antiprotons (dashed). Right: $\bar{p}$ to π^0 ratio for the centrality bins 0-10% (solid) and 60-92% (dashed). RHIC results in black and LHC predictions in blue.

fluctuations) [67, 165–167]:

$$\frac{\mathrm{d}N}{\mathrm{d}p_T^2\mathrm{d}y} = \int_0^\infty \mathrm{d}x\, W(x) f(p_T, x) = \frac{\mathrm{d}N}{\mathrm{d}y}\frac{k-1}{k}\frac{1}{\langle p_T^2\rangle_{1i}} F(\eta) \frac{1}{(1+\frac{F(\eta)p_T^2}{k\langle p_T^2\rangle_{1i}})^k}. \tag{22}$$

For (anti)baryons, equation (21) must be changed to $\langle\mu_{\bar{B}}\rangle = N_s^{1+\alpha} F(\eta_{\bar{B}})\langle\mu_{1\bar{B}}\rangle$ to take into account that baryons are enhanced over mesons in the fragmentation of a high density cluster. The parameter $\alpha = 0.09$ is fixed from the experimental dependence of $\bar{p}/\pi$ on N_{part}. The (anti)baryons probe higher densities than mesons, $\eta_B = N_s^\alpha \eta$. On the other hand, from the constituent counting rules applied to the high p_T behavior we deduce that for baryons $k_B = k(\eta_B) + 1$. In figure 58, we show the ratios R_{CP} and $\bar{p}/\pi^0$ defined as usual, compared to RHIC experimental data for pions and antiprotons together with the LHC predictions. In figure 59 left we show the nuclear modification factor R_{AA} for pions and protons for central collisions at RHIC. LHC predictions are also shown. We note that pp collisions at LHC energies will reach enough string density for nuclear-like effects to occur. In this respect, in figure 59 right, we show the ratio R_{CP} for $pp \to \pi X$ as a function of p_T, where the denominator is given by the minimum bias inclusive cross section and the numerator is the inclusive cross section corresponding to events with twice multiplicity than minimum bias. According to our formula (22) a suppression at large p_T occurs.

3.6. Bulk hadron(ratio)s at the LHC-ions

J. Rafelski and J. Letessier

The expected LHC-heavy ion yields of strange and non-strange hadrons, mesons and baryons, are evaluated within the statistical hadronization model.

This summary of our recent work on bulk hadronization in LHC-ion interactions is based on methods and ideas presented in [168], with the present update using the results obtained

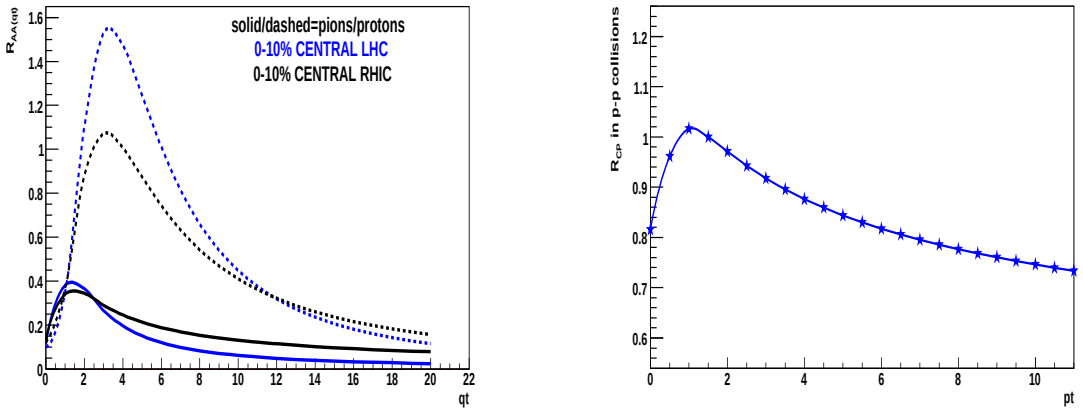

Figure 59: Left: Nuclear modification factor for π^0 (solid) and $\bar{p}$ (dashed) for 0-10% central events, RHIC results in black and LHC predictions in blue. Right: R_{CP} for pions in pp collisions at LHC.

for strangeness production in [169]. This presentation is more specific regarding the yields in order to allow "first-day" understanding of the mechanisms of hadronization dynamics of the deconfined quark–gluon plasma phase formed in most central $\sqrt{s_{\rm NN}} = 5520$ GeV Pb–Pb reactions at the LHC.

Our detailed results rely on SHARE-2.2 suite of programs [170], which have been extensively tested, with several typos, and errors corrected compared to earlier releases SHARE-1.x [171], and SHARE-2.1 . An important feature of the SHARE suite of programs is that one can obtain the particle multiplicities for any consistent *mixed* set of extensive/intensive bulk matter parameters and/or particle yields. What 'consistency' means can be understood considering the variables in the Gibbs-Duham relation:

$$PV + E = TS + \sum_a \mu_a N_a, \quad \mu_a = \sum_{i\in a} T \ln\gamma_i + b_i\mu_B + s_i\mu_S \,, \tag{23}$$

where the extensive V (volume), $E \equiv V\epsilon$ (energy), $S \equiv V\sigma$ (entropy), $N_i \equiv V\rho_i$ (particle number) appears along with intensive P (pressure), T (temperature), and μ_i (particle chemical potential). Aside of the above strict constraint, other qualitative constraints arise and thus, in our approach, we allow for a deviation from prescribed parameter values within a margin of a few percent, to be chosen in a quasi-fit procedure in order to alleviate inconsistencies in the choices made.

Considering the limited central rapidity experimental coverage, we refer instead of the total volume V to the range associated with the central rapidity dV/dy, thus $dS/dy = (dS/dV)(dV/dy)$ is the entropy (multiplicity) yield per unit of rapidity. One can show that dS/dy is conserved in the hydrodynamic expansion of the bulk matter, thus the final observed entropy (multiplicity) content per unit of rapidity is the outcome of the initial state entropy production.

The soft hadron production at LHC-Ion relies on the following input:

I The entropy content: $dS/dy \equiv$ hadron multiplicity — this is normalizer of all particle

yields for which the predictions most widely vary. The straight line extrapolation as function of ln $\sqrt{s_{\rm NN}}$ implies an increase of dS/dy by only a factor 1.65 from RHIC top energy reach $\sqrt{s_{\rm NN}}$ = 200 GeV to the LHC-ion top energy of $\sqrt{s_{\rm NN}}$ = 5520 GeV. The charged particle yield per unit rapidity is expected, in this case, at about $h_{\rm ch}$ = 1150. Since this extrapolation is done based on PHOBOS multiplicity, only partial K_s weak interaction decay is allowed for. We will also state the corresponding $h^{\rm vis}_{\rm ch}$ which is computed assuming acceptance of weak decays akin to the STAR detector. The entropy content determines up to about 15% the energy content $dE/dy \simeq T_h dS/dy$ which thus increases, in essence, by the same factor. We note that model differences in hadronization temperature T_h which are in the range of up to 20% impact accordingly the thermal energy content.

However, one can wonder if the factor 1.65 correctly accounts for the 28-fold reaction energy increase between RHIC and LHC-ion. The widening of the particle production rapidity window accounts for much of the collision energy increase. How this widening occurs i.e the strength of stopping, determines the central rapidity energy deposition. We thus consider in the second example the case with 3.4-fold increase in entropy/multiplicity content per unit of rapidity. This value is fine-tuned such that the visible charged hadron yield is identical to the TPC-visible charged hadron multiplicity yield in the chemical equilibrium model, where the hadronization volume was set to be $V = 6200\,{\rm fm}^3$ (our 3rd table entry). This allows to compare the yields of both models normalized to same hadron yield.

II The strangeness content $ds/dy = d\bar{s}/dy$ and/or $(ds/dy)/(dS/dy) = s/S$. The production of strangeness has been evaluated within pQCD, for a given entropy content. The final strangeness yield does not depend in a significant way on how the parton entropy content is implemented in the early reaction times where thermal distributions are reached (e.g., high T, low chemical abundances, low T, high chemical abundances). This is so, since strangeness, being a relatively strongly interacting probe, does not convey a detailed information about the early $\tau < 2$ fm/c times of the heavy ion collision. For the case of a greater (3.4-times increased) entropy/multiplicity content, the pQCD computation suggests $s/S \simeq 0.037$ yield, which is 10–15% above QGP chemical equilibrium, the lower entropy variant (extrapolated factor 1.65 increase in multiplicity) implies for QGP-strangeness a small excess above chemical equilibrium, we will use $s/S \simeq 0.034$. For the third case, the hadron chemical equilibrium, the ratio $s/S = 0.025$ results. Thus, strangeness enhancement, where it is not washed out by a lower hadronization temperature, is the salient feature of the non-equilibrium hadronization picture we have developed and present here.

III The net baryon stopping $d(b-\bar{b})/dy$ is unknown, and will be difficult to measure. An extrapolation of the energy per baryon retained per unit of rapidity yields $E/b \simeq 412 \pm 20$ GeV at LHC. This value is consistent with the here considered two cases, when, as an example, we fix $\lambda_q = 1.0056$ which determines the baryon and hyperon chemical potentials $\mu_{\rm B}$ and $\mu_{\rm S}$. We note, in passing, that in all the cases considered here, we find for the baryon asymmetry at LHC $(b-\bar{b})/(b+\bar{b}) \simeq 0.015$, which is 6–7 orders of magnitude larger compared to the conditions prevailing in the early universe.

There are constrains which we use to fully determine the system properties:
1) For the chemical non-equilibrium hadronization we will use $T_h = 140\,{\rm MeV}$ while for

chemical equilibrium we adopt $T_h = 162\,\mathrm{MeV}$. Both values are taken from the study of highest RHIC energies. The lower T arises due to supercooling expansion, leading to sudden hadronization [172], and thus, we also impose a bias for $E/TS > 1$.
2) Strangeness balance $\langle s \rangle = \langle \bar{s} \rangle$ in the central unit of rapidity.
3) Net charge per net baryon ratio $Q/b = 0.4$ (value in colliding nuclei) is implemented. Since the net baryon number is rather small, the charge asymmetry is for all purposes invisible, the purpose of this exercise is to assure physical consistency and to fix the isospin asymmetry statistical parameter λ_3.

Our results are presented in detail in the table. We note that the total charged hadron multiplicity will be a first-day observable at LHC and hence much of the uncertainty we have in discussing the absolute hadron yields will disappear. When comparing hadronization models at fixed total hadron yield one sees clear differences in yield pattern:
a) Multi-strange hadron yields are, in general, greatly enhanced in our non-equilibrium approach as compared to yields assuming chemical equilibrium hadronization, yet single strange yields are often similar, since the differences in hadronization (temperature) conditions compensate for the strangeness yield enhancement;
b) The yields of non-strange resonances are, in general, significantly greater in the chemical equilibrium model, due to the higher hadronization temperature.
c) This suppression is compensated in resonances with single and partial multi-strange content (η, η').
The above differences, already seen at RHIC, are much more striking at LHC, since the specific strangeness per entropy yield enhancement is by factor 1.5. Even the visible $\mathrm{K}^+/\pi^+_{\mathrm{vis}}$ ratio is increased from the RHIC level, to $\mathrm{K}^+/\pi^+_{\mathrm{vis}} \simeq 0.17$ –0.18, however this enhancement effect is much better visible once weak decays have been vetoed in the pion yield, in which case, we predict $\mathrm{K}^+/\pi^+ \simeq 0.21$. While the yield of nucleons may be difficult to determine, the measurement of baryon resonances such as $\Delta(1230)$ could help considerably in the characterization of the baryon yield.

T[MeV]	140*	140*	162*
dV/dy[fm^3]	2036	4187	6200*
dS/dy	7517	15262	18021
$dh_{\rm ch}/dy$	1150*	2351	2430
$dh_{\rm ch}^{\rm vis}/dy$	1351	2797*	2797
$1000\cdot(\lambda_{\rm q,s}-1)$	5.6*, 2.1	5.6*, 2.1	5.6*, 2.0
$\mu_{\rm B,S}$[MeV]	2.4, 0.5	2.3, 0.5	2.7, 0.6
$\gamma_{q,s}$	1.62, 2.42	1.6*, 2.6	1*, 1*
s/S	0.034*	0.037*	0.025
E/b	420*	428	408
E/TS	1.02	1.05	0.86
P/E	0.165	0.164	0.162
E/V[MeV/fm^3]	530	538	400
P[MeV]	87	88	65
p	25/45	49/95	66/104
$b-\bar{b}$	2.6	5.3	6.1
$(b+\bar{b})/h^-$	0.335	0.345	0.363
$0.1\cdot\pi^{\pm}$	49/67	99/126	103/126
K$^{\pm}$	94	207	175
ϕ	14	33	23
Λ	19/28	41/62	37/50
Ξ^-	4	9.5	5.8
Ω^-	0.82	2.08	0.98
Δ^0,Δ^{++}	4.7	9.3	13.7
$K_0^*(892)$	22	48	52
η	62	136	127
η'	5.2	11.8	11.5
ρ	36	73	113
ω	32	64	104
f_0	2.7	5.5	9.7
K$^+/\pi^+_{\rm vis}$	0.165	0.176	0.148
$\Xi^-/\Lambda_{\rm vis}$	0.145	0.153	0.116
$\Lambda(1520)/\Lambda_{\rm vis}$	0.043	0.042	0.060
$\Xi(1530)^0/\Xi^-$	0.33	0.33	0.36
ϕ/K$^+$	0.15	0.16	0.13
$K_0^*(892)/K^-$	0.236	0.234	0.301

Table: LHC predictions, two variants of our non-equilibrium hadronization model are shown on left, the chemical equilibrium model results are stated for comparison in the right column. To obtain results n the first column, we considered an overall hadron yield chosen to increase at central rapidity by factor 1.65 compared to PHOBOS results (star '*' indicates a fixed input value). The chemical equilibrium model shown on right is matched in the middle column by assuming a TPC-visible charged hadron yield to be the same, 2797. These characteristic properties along with the entropy content, and chemical conditions at hadronization, are stated in the two top sections of the table. In the third section, we show bulk properties at hadronization, with specific strangeness content prescribed as arising in pQCD computation [169], except for the equilibrium model in which case the specific yield s/S is a consequence of the equilibrium assumption. One notes for the equilibrium model that the energy density and pressure at hadronization is smaller, which agrees with the greater volume of hadronization required to obtain the same hadron yield. This is due to particle density scaling roughly with $\gamma_q^2 T^3$, the change in γ_q outweighs that in T. When we present the hadron yields, we give (separated by slash) the ranges with/without weak decays for protons p, π and Λ. Clearly the properties of the detector will impact the uncorrected yields. We also note that, while baryon density in rapidity can vary depending on dynamics of the reaction, the specific total baryon yield, compared to that of mesons, remains nearly constant and model independent. The difference to the equilibrium model is most pronounced in the multi-strange hadron Ξ, ω and ϕ yields. The ratios or resonances with the stable decay product are shown in the bottom section of the table.

4. Correlations at low transverse momentum

4.1. Pion spectra and HBT radii at RHIC and LHC

Yu. M. Sinyukov, S. V. Akkelin and Iu. A. Karpenko

We describe RHIC pion data in central A+A collisions and make predictions for LHC based on hydro-kinetic model, describing continuous 4D particle emission, and initial conditions taken from Color Glass Condensate (CGC) model.

Hydro-kinetic approach to heavy ion collisions proposed in Ref. [173] accounts for continuous particle emission from 4D volume of hydrodynamically expanding fireball as well as back reaction of the emission on the fluid dynamics. The approach is based on the generalized relaxation time approximation for relativistic finite expanding systems,

$$\frac{p^\mu}{p_0}\frac{\partial f(x,p)}{\partial x^\mu} = -\frac{f(x,p) - f^{l.eq.}(x,p)}{\tau_{rel}(x,p)}, \tag{24}$$

where $f(x,p)$ is phase-space distribution function (DF), $f^{(l.eq.)}(x,p)$ is local equilibrium distribution and $\tau_{rel}(x,p)$ is relaxation time, $\tau_{rel}(x,p)$ as well as $f^{l.eq}$ are functional of hydrodynamic variables. Complete algorithm described in detail in Ref. [174] includes: solution of equations of ideal hydro; calculation of a non local equilibrium DF and emission function in the first approximation; solution of equations for ideal hydro with non-zero right-hand-side that accounts for conservation laws at the particle emission during expansion; calculation of "improved" DF and emission function; evaluation of spectra and Bose-Einstein correlations. Here we present our results for the pion momentum spectra and interferometry radii calculated for RHIC and LHC energies in the first approximation of the hydro-kinetic approach.

For simulations we utilize ideal fluid model [175–177] and realistic equation of state (EoS) that combines high temperature EoS with crossover transition [178] adjusted to the QCD lattice data and EoS of hadron resonance gas with partial chemical equilibrium [175–177]. The gradual disappearance of pions during the crossover transition to deconfinement and different intensity of interactions of pions in pure hadronic and "mixed" phases are taken into account in the hydro-kinetic model (HKM), but resonance contribution to pion spectra and interferometry radii is not taken into account in the present version of the HKM. We assume the following initial conditions at proper time $\tau_0 = 1$ fm/c for HKM calculations: boost-invariance of a system in longitudinal direction and cylindrical symmetry with Gaussian energy density profile in transverse plane. The maximal energy densities at RHIC, $\epsilon_0 = 30$ GeV/fm^3 and at LHC, $\epsilon_0 = 70$ GeV/fm^3, were calculated from Ref. [179] in approximation of Bjorken expansion of free ultrarelativistic partons till τ_0 and adjusted for transverse Gaussian density profile. The (pre-equilibrium) initial transverse flows at τ_0 were estimated assuming again a free-streaming of partons, with transverse modes distributed according to CGC picture, from proper time ≈ 0.1 fm/c till $\tau_0 = 1$ fm/c. Finally, we approximate the transverse velocity profile by $v_T = \tanh(\alpha \cdot \frac{r_T}{R_T})$ where $\alpha = 0.2$ both for RHIC and LHC energies and we suppose the fitting Gaussian radius for RHIC top energy, $R_T = 4.3$, to be the same for LHC

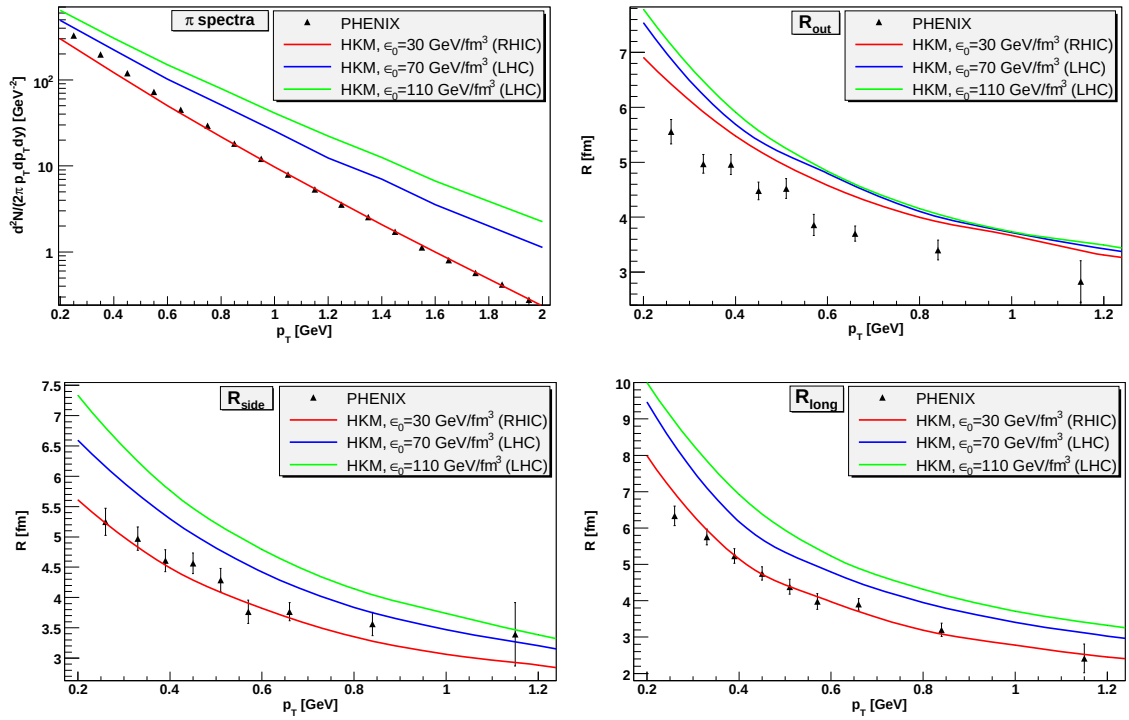

Figure 60: Comparison of the single-particle momentum spectra of pions and pion R_{out}, R_{side}, R_{long} radii measured by the PHENIX Collaboration for Au+Au central collisions (HBT radii data were recalculated for $0-5\%$ centrality) at RHIC with the HKM calculations, and HKM predictions for Pb+Pb central collisions at LHC. For the sake of convenience the calculated one-particle spectra are enhanced in 1.4 times.

energy. Our results for RHIC and predictions for LHC are presented in Fig. 60. The relatively small increase of the interferometry radii with energy in HKM calculations is determined by early (as compare to sharp freeze-out prescription) emission of hadrons, and also by increase of transverse flow at LHC caused by longer time of expansion. It is noteworthy that in the case of EoS related to first order phase transition, the satisfactory fitting of the RHIC HBT data requires non-realistic high initial transverse flows at $\tau_0 = 1$ fm/c: $\alpha = 0.3$.

4.2. Mach Cones at central LHC Collisions via MACE

B. Bäuchle, H. Stöcker and L. P. Csernai

The shape of Mach Cones in central lead on lead collisions at $\sqrt{s_{NN}} = 5.5$ TeV are calculated and discussed using MACE.

4.2.1. Introduction After the discovery of "non-trivial parts" in three-particle correlations at RHIC [180], which are compatible with the existence of Mach cones [181], it is interesting to see how the signal for Mach cones will look like under the influence of a medium created at the LHC in PbPb-Collisions.

Mach cones caused by ultrarelativistic jets going in midrapidity will create a double-peaked two-particle correlation function $\mathrm{d}N/\mathrm{d}(\Delta\varphi)$. Those peaks are located at $\Delta\varphi = \pi \pm \cos^{-1} c_S$, where c_S is the speed of sound as obtained by the equation of state. The model MACE ("Mach Cones Evolution") has been introduced to simulate the propagation of sound

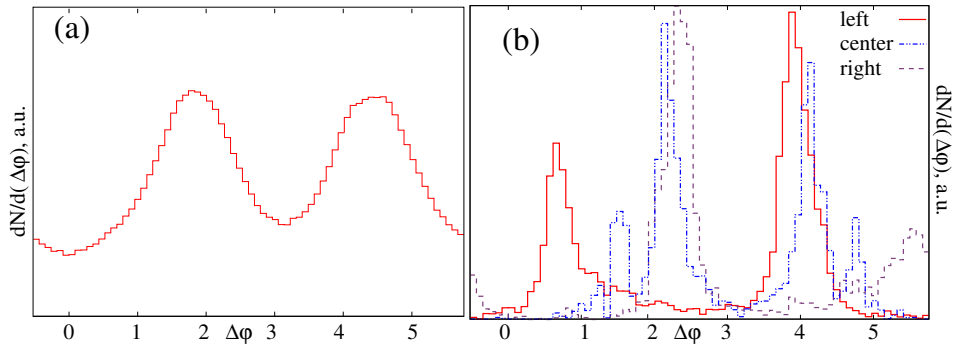

Figure 61: Two-particle-correlation function (away-side-part) for central PbPb-Collisions at $\sqrt{s_{\mathrm{NN}}} = 5.5$ TeV. The peak created by the forward jet is not calculated. (a): minimum jet bias (see text) with peaks at $\Delta\varphi \approx \pi \pm 1.2$. (b): Midrapidity jets starting from a position 70 % on the way outside left and right of as well as in the middle.

waves through a medium and recognize and evaluate mach cones [182].

The medium is calculated without influence of a jet using the hydrodynamical Particle-in-Cell-method (PIC) [183]. For the equation of state, a massless ideal gas is assumed, so that $c_{\mathrm{S}} = 1/\sqrt{3}$ and $\cos^{-1} c_{\mathrm{S}} = 0.96$. The sound waves are propagated independently of the propagation of the medium and without solving hydrodynamical equations. Only the velocity field created by PIC is used. To recognize collective phenomena, the shape of the region affected by sound waves is evaluated.

4.2.2. Correlation functions The correlation functions from the backward peak show a clear double-peaked structure. The data for arbitrary jet origin and jet direction (minimum jet bias) is shown in figure 61 (a). Here, the peaks are visible at $\Delta\varphi \approx \pi \pm 1.2$. This corresponds to a speed of sound of $c_{\mathrm{S}} \approx 0.36$. Note that the contributions from the forward jet are not shown. Deeper insight into different jet directions do not show a qualitatively different picture.

Triggers on the origin of the jet, though, show the dependence of the correlation function

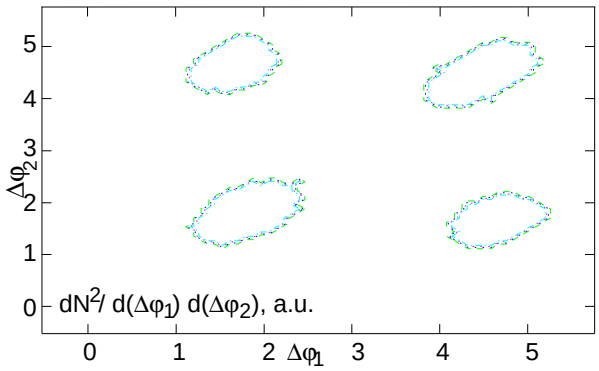

Figure 62: Three-particle-correlation function for the same data as in figure 61.

on the position where the jet was created (see figure 61 (b)). It shows that only the jet coming from the middle of the reaction results in a symmetric correlation function with peaks at the mach angle $\Delta\varphi = \pi \pm 0.96$. All other jets result in correlations that have peaks at different angles, with the deviation getting bigger when going away from the middle. Therefore, the speed of sound will always appear to be smaller than it actually is.

4.2.3. Conclusions If sound waves are produced from jet quenching in LHC-Collisions, the two-particle correlation function will show the expected double-humped structure in the backward region. The peaks will, though, be further apart than $\delta(\Delta\varphi) = 2\cos^{-1} c_S$, thus alluding to a speed of sound smaller than is actually present in the medium.

The only case in which the true speed of sound can be measured is a midrapidity jet that creates a symmetric correlation function.

4.3. Study of Mach Cones in (3+1)d Ideal Hydrodynamics at LHC Energies

B. Betz, P. Rau, G. Torrieri, D. Rischke and H. Stöcker

The energy loss of jets created in heavy–ion collisions shows an anomalous behaviour of the angular distribution of particles created by the away-side jet due to the interaction of the jet with the medium [184, 185]. Recent three–particle correlations [180, 186, 187] confirm that a Mach cone is created. Ideal (3+1)d hydrodynamics [188] is used to study the creation and propagation of such Mach cones under LHC conditions.

Jets are one possible probe to study the medium created in a heavy–ion collision. They are assumed to be formed in an early stage of the collision and to interact with the hot and dense nuclear matter.

Experimental results from the Relativistic Heavy Ion Collider (RHIC) show a suppression of the away–side jet in Au+Au collisions for high-$p_\perp$ particles as compared to the away–side jet in p+p collisions. This effect is commonly interpreted as jet energy loss or jet quenching [184, 185]. However, studies including low-$p_\perp$ particles [180, 186, 187] exhibit a double peaked away–side jet. Recent three–particle correlations confirm that this pattern is due to a creation of a Mach cone [180, 186, 187].

The interaction of a jet with the medium is theoretically not well enough understood. Therefore, we compare two models of energy loss under LHC conditions. We consider a medium with an initial radius of 3.5 fm and an initial energy density of $e_0 = 1.7$ GeV/fm^3 that undergoes a Bjorken–like expansion according to a bag–model equation of state (EoS) with a first–order phase transition from a hadron gas to the quark–gluon plasma (QGP) with a mixed phase between $e_H = 0.1$ GeV/fm^3 and $e_Q = 1.69$ GeV/fm^3.

In the first scenario, we implement a jet that completely deposits its energy and momentum during a very short time in a 0.25 fm^3 spatial volume. Initially, the jet is located between $-3.5\,\text{fm} < x < -2.5\,\text{fm}$, $|y| < 0.25\,\text{fm}$, $|z| < 0.25\,\text{fm}$, has a velocity of $v_x = 0.99$ c and traverses the medium along the x-axis. Totally, it deposits an energy of 15 GeV, no rapidity cut is applied.

In a second step, we study a 15 GeV jet that gradually deposits its energy and momentum in equal time steps of Δt = 0.8 fm/c. As in the first scenario, the jet traverses the medium with a velocity of v_x = 0.99 c along the x–axis.

The hydrodynamic evolution is stopped after a time of 7.2 fm/c. Using a Monte Carlo simulation based on the SHARE program [171], an isochronous freezeout according to the Cooper–Frye formula is performed, considering a gas of rhos, pions and etas in the pseudorapidity interval of [-2.3,2.3].

Figure 63 shows the angular distribution of particles for the first (left panel) and second (right panel) scenario, without any background subtraction. The omitted near–side jet would appear at $\phi = 0$.

In case of a short–time energy and momentum deposition, a broad away–side distribution (left panel) occurs, due to the deposition and dissipation of kinetic energy caused by the jet. However, if the jet gradually dispenses its energy and momentum (right panel), two maxima appear. This Mach cone–like structure agrees with the recent STAR and PHENIX data [180, 186, 187].

4.4. Forward-Backward (F-B) rapidity correlations in a two step scenario

J. Dias de Deus and J. G. Milhano

We argue that in models where particles are produced in two steps, formation first of longitudinal sources (glasma and string models), followed by local emission, the Forward-Backward correlation parameter b must have the structure $b = (\langle n_B\rangle/\langle n_F\rangle)/(1 + K/\langle n_F\rangle)$ where $\langle n_B\rangle(\langle n_F\rangle)$ is the multiplicity in the backward (forward) rapidity window and $1/K$ is the (centrality and energy dependent) normalized variance of the number of sources.

Two-step scenario models for particle production are based on:

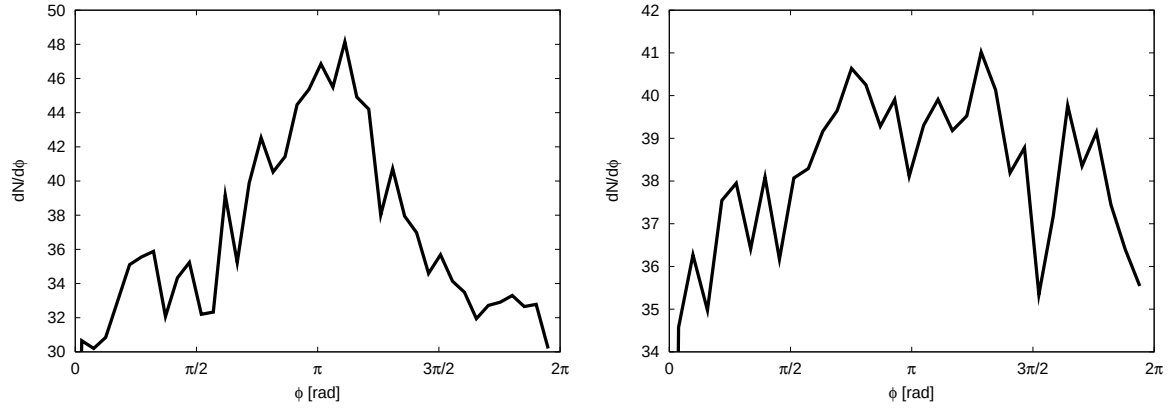

Figure 63: Angular distribution of particles after isochronous freeze–out of a (3+1)d ideal hydrodynamical evolution for a jet that deposits its energy and momentum a) completely within a very short time (left panel) b) in equal timesteps (right panel) in a medium that undergoes a Bjorken–like expansion according to a bag–model eos.

(i) creation of extended objects in rapidity (glasma longitudinal colour fields or coloured strings); followed by

(ii) local emission of particles.

The first step guarantees the presence of F-B correlations due to fluctuations in the colour/number of sources, while the second step accounts for local effects such as resonances.

The F-B correlation parameter b is defined via

$$\langle n_B\rangle_F = a + bn_F\,, \quad b \equiv D^2_{FB}/D^2_{FF}\,, \tag{25}$$

where D^2 is the variance. In general, correlations are measured in two rapidity windows separated by a rapidity gap so that F-B short range correlations are eliminated. In the two-step scenario models we write [189–192],

$$D^2_{FB} \equiv \langle n_F n_B\rangle - \langle n_F\rangle\langle n_B\rangle = \frac{\langle n_F\rangle\langle n_B\rangle}{K}\,, \tag{26}$$

$$D^2_{FF} \equiv \langle n_F^2\rangle - \langle n_F\rangle^2 = \frac{\langle n_F\rangle^2}{K} + \langle n_F\rangle\,, \tag{27}$$

where $1/K$ is the normalized — e.g., in the number of elementary collisions — long range fluctuation and depends on centrality, energy and rapidity length of the windows. We have assumed, for simplicity, that local emission is of Poisson type.

From equations (25, 26, 27) we obtain

$$b = \frac{\langle n_B\rangle/\langle n_F\rangle}{1 + K/\langle n_F\rangle}\,. \tag{28}$$

It should be noticed that b may be larger than 1, and that a Colour Glass Condensate (CGC) model calculation [193] shows a structure similar to (28): $b = A[1+B]^{-1}$ (for a discussion on general properties of (28) and on the CGC model, see [192]).

A simple way of testing (28) is by fixing the backward rapidity window, or $\langle n_B\rangle$, in the region of high particle density and move the forward window along the rapidity axis. We can rewrite equation (28) in the form

$$b = \frac{x}{1 + K'x}\,, \tag{29}$$

where $K' \equiv K/\langle n_B\rangle$ is a constant and $x \equiv \langle n_B\rangle/\langle n_F\rangle$. In (29), one has $1 < x < \infty$ with the limiting behaviour:

$$x \to 1\,, \quad b \to \frac{1}{1+K'}\,; \qquad x \to \infty\,,\, b \to \frac{1}{K'}\,. \tag{30}$$

The behaviour of (29) is shown in figure 64 (drawn for $K' = 1$).

A similar curve is obtained for B-F correlations in the backward region of rapidity. Note that in aA collisions, $a \le A$, the centrality and energy dependence of K' is given by [2, 191],

$$K' \sim a^{1/2}A^{-1/6}\mathrm{e}^{\lambda Y}\,,$$

where Y is the beam rapidity and λ a positive parameter. In the symmetric situation, $a = A$ and K' **increases** with centrality (and the curve of the figure moves down) while in the asymmetric situation, $a = 1,2 \ll A$ and K' **decreases** with centrality (and the curve in the figure moves up). As the energy increases K' increases (and the curve moves down).

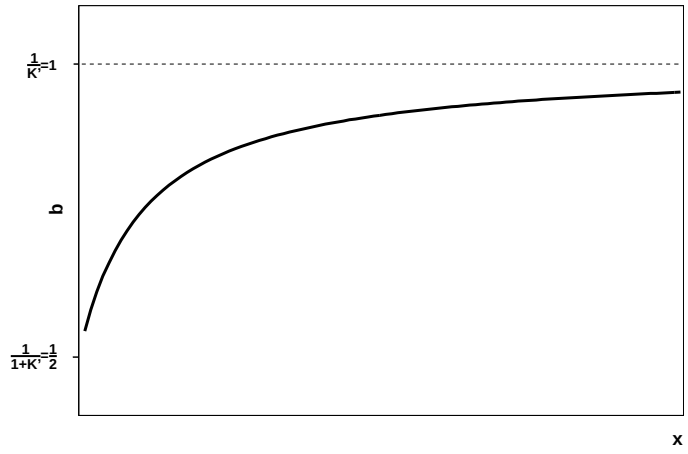

Figure 64: F-B correlation parameter b (29) with $K' = 1$.

4.5. Cherenkov rings of hadrons

I. M. Dremin

The ring-like structure of inelastic events in heavy ion collisions becomes pronounced when the condition for the emission of Cherenkov gluons is fulfilled.

In heavy ion collisions any parton can emit a gluon. On its way through the nuclear medium the gluon collides with some internal modes. Therefore it affects the medium as an "effective" wave which accounts also for the waves emitted by other scattering centers. Beside incoherent scattering, there are processes which can be described as the refraction of the initial wave along the path of the coherent wave. The Cherenkov effect is the induced coherent radiation by a set of scattering centers placed on the way of propagation of the gluon. Considered first for events at very high energies [194, 195], the idea about Cherenkov gluons was extended to resonance production [196, 197]. The refractive index and the forward scattering amplitude $F(E, 0^o)$ at energy $E = \sqrt{s}$ are related as

$$\Delta n = \mathrm{Re}n - 1 = \frac{8\pi N_s \mathrm{Re}F(E, 0^o)}{E^2}. \tag{31}$$

N_s is the density of the scattering centers in the medium.

The necessary condition for Cherenkov radiation is

$$\Delta n > 0 \quad \text{or} \quad \mathrm{Re}F(E, 0^o) > 0. \tag{32}$$

If these inequalities are satisfied, Cherenkov gluons are emitted along the cone with half-angle θ_c in the rest system of the medium determined by n:

$$\cos\theta_c = \frac{1}{n} \tag{33}$$

Prediction The rings of hadrons similar to usual Cherenkov rings of photons can be observed in the plane perpendicular to the cone (jet) axis if $n > 1$.

Proposal Plot the one-dimensional pseudorapidity ($\eta = -\ln\tan\theta/2$) hadron distribution with trigger jet momentum as z-axis. It should have maximum at (33).

This is the best possible one-dimensional projection of the ring. To define the refractive index in the absence of the theory of nuclear media (for a simplified approach see [198]) I prefer to rely on our knowledge of hadronic reactions. From experiments at comparatively low energies we learn that the resonances are abundantly produced. They are described by the Breit-Wigner amplitudes which have a common feature of the positive real part in the low-mass wing (e.g., see Feynman lectures). Therefore the hadronic refractive index exceeds 1 in these energy regions.

At high energies the experiment and dispersion relations indicate on positive real parts of amplitudes for all hadronic reactions above a very high threshold. Considering gluons as carriers of strong forces one can assume that the similar features are typical for their amplitude as well. Then one should await for two energy regions in which Cherenkov gluons play a role. Those are either gluons with energies which fit the left wings of resonances produced in their collisions with internal modes of the medium or with very high energies over some threshold.

The indications on "low" energy effects come from RHIC [187] where the two-bump structure of the angular distribution of hadrons belonging to the so-called companion (away-side) jet in central heavy-ion collisions has been observed. It arises as the projection of a ring on its diameter and provides important information on the properties of the nuclear medium [196, 197]. From the distance between peaks the cone half-angle is found to be about $60^o - 70^o$ in the c.m.s. which is equivalent to the target rest system for the trigger at central rapidities. Derived from it and Eq.(33) are the large refractive index ($n \approx 3$) and parton density ($\nu \approx 20$ within a nucleon volume) that favor the state of a liquid. The energy loss ($dE/dx \approx 1\mathrm{GeV/fm}$) is moderate and the free path length is of a nuclear size. The three-particle correlations also favor the ring-like structure.

The indications on high energy effects came from the cosmic ray event [199] at energy about 10^{16}eV (LHC!) with two ring-like regions. They are formed at such angles in the target rest system which are equivalent to $60^o - 70^o$ and $110^o - 120^o$ in c.m.s. It corresponds to the refractive index close to 1 that well fits results of dispersion relations and experiment at these energies. Such dependence on parton energy shows that the same medium could be seen as a liquid by rather slow partons and as a gas by very fast ones.

It is crucial for applicability of Eq.(33) to define properly the target rest system. In RHIC experiments the parton-trigger moves in the transverse direction to the collision axis and, on the average, "sees" the target (the primary fireball) at rest in c.m.s. dealing with rather low x and Q^2. In the cosmic event the narrow forward ring is produced by fast forward moving partons (large x) which "see" the target at rest in the lab. system. At LHC one can await for both types of Cherenkov gluons produced. Thus, the hadronic Cherenkov effect can be used as a tool to scan $(1/x, Q^2)$-plane and plot on it the parton densities (see Eq.(31)) corresponding to its different regions.

To conclude, the ring-like structure of inelastic processes must be observed if the gluonic Cherenkov effects are strong enough. The ring parameters reveal the properties of the nuclear medium and their energy dependence.

4.6. Evolution of pion HBT radii from RHIC to LHC – predictions from ideal hydrodynamics

E. Frodermann, R. Chatterjee and U. Heinz

We use the longitudinally boost-invariant relativistic ideal hydrodynamic code AZHYDRO [130] to predict the expected trends for the evolution from RHIC to LHC of the HBT radii at mid-rapidity in central ($A\approx200$)+($A\approx200$) collisions, as well as that of their normalized oscillation amplitudes in non-central collisions. We believe that these trends may be trustworthy, in spite of the model's failure to correctly predict the HBT radii at RHIC [200]. The results shown here are selected from Ref. [201].

Hydrodynamics can not predict the $\sqrt{s}$-dependence of its own initial conditions, but it relates uniquely the initial entropy density to the final hadron multiplicity. We compute hadron spectra and HBT radii as functions of final multiplicity, parametrized by the initial peak entropy density s_0 at thermalization time τ_0 in $b=0$ collisions. We hold $T_0\tau_0$ constant (where

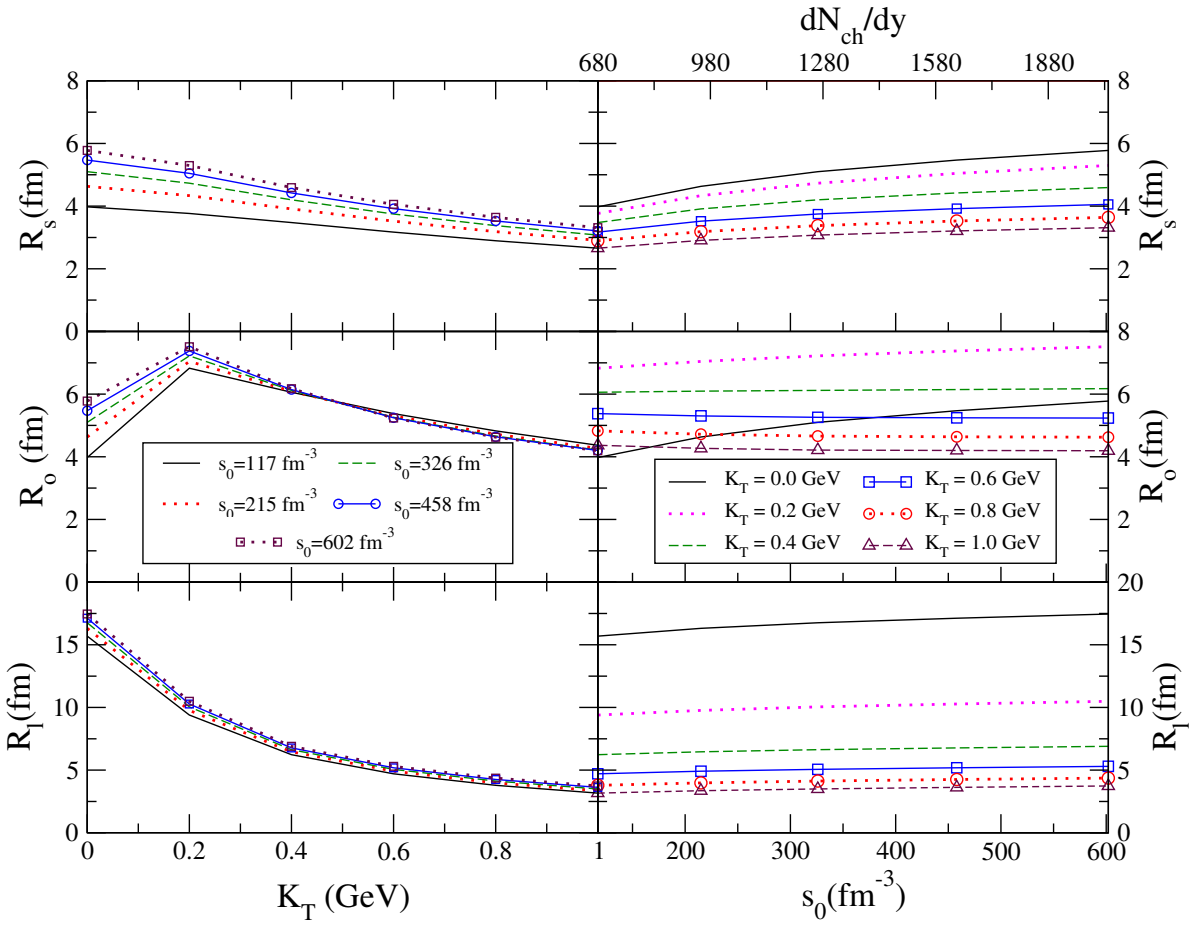

Figure 65: (Color online) Pion HBT radii for central (b=0) Au+Au collisions as a function of transverse pair momentum K_T (left) and of initial entropy density s_0 or final charged multiplicity $\frac{dN_{\rm ch}}{dy}$ (right). For details see [201].

$T_0 \sim s_0^{1/3}$ is the initial peak temperature). Our results cover a range from $\frac{dN_{\rm ch}}{dy}=680$ ("RHIC

initial conditions": $s_0 = 117\,\mathrm{fm}^{-3}$ at $\tau_0 = 0.6\,\mathrm{fm}/c$) to $\frac{dN_{\mathrm{ch}}}{dy} = 2040$ ("LHC initial conditions": $s_0 = 602\,\mathrm{fm}^{-3}$ at $\tau_0 = 0.35\,\mathrm{fm}/c$).

1. Central collisions: Figure 65 shows the pion HBT radii for central Au+Au (Pb+Pb) collisions in the (osl) coordinate system [200]. Since we computed the HBT radii from the space-time variances of the emission function instead of doing a Gaussian fit to the two-pion correlation function, all R_l values should be corrected downward by about 20% [202]. We see no dramatic changes, neither in magnitude nor in K_T-dependence, of the HBT radii as we increase the multiplicity by up to a factor 3. The largest increase (by $\sim 30\%$ at low K_T) is seen for R_s, while R_o even slightly decreases at large K_T. R_l changes hardly at all. The main deficiency of hydrodynamic predictions for the HBT radii at RHIC (too weak K_T-dependence of R_s and R_o and a ratio R_o/R_s much larger than 1) is not likely to be resolved at the LHC unless future LHC data completely break with the systematic tendencies observed so far [200].

2. Non-central collisions: Figure 66 shows the normalized azimuthal oscillation amplitudes [203] of the HBT radii for $b = 7$ fm Au+Au collisions. The dashed line in the lower left panel

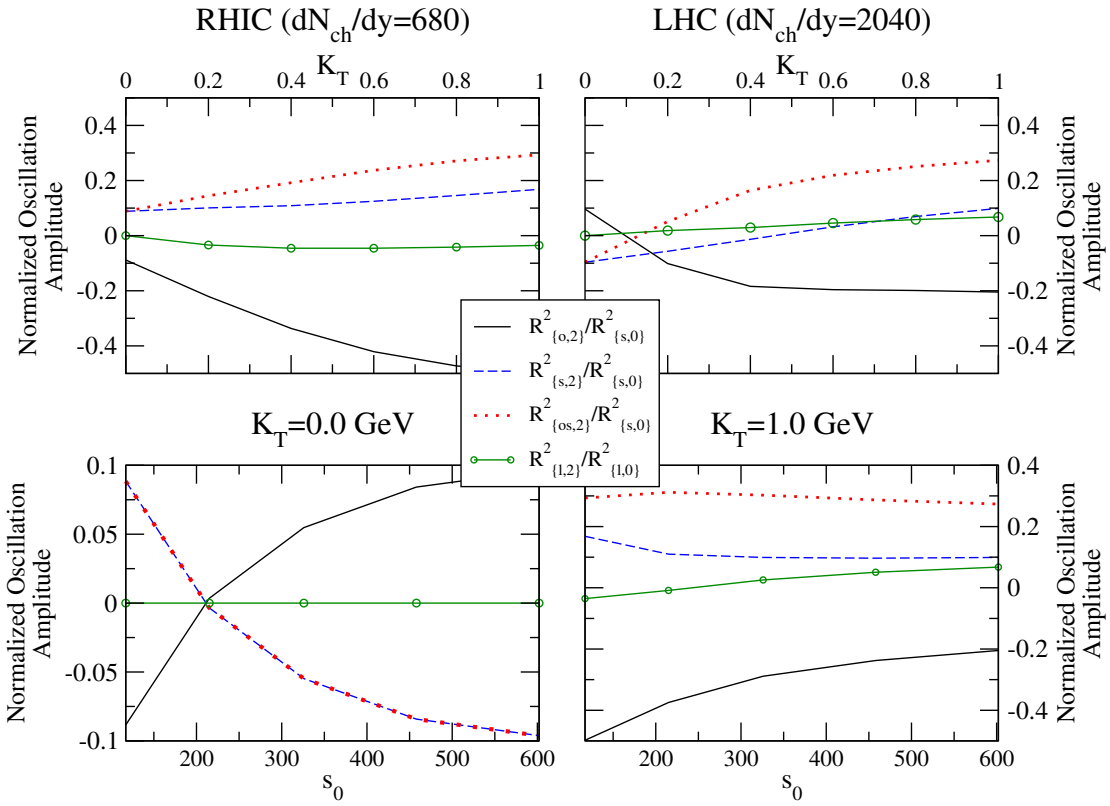

Figure 66: (Color online) Normalized HBT oscillation amplitudes as a function of K_T at RHIC and LHC (top) and as function of s_0 for two values of K_T (bottom).

gives the spatial eccentricity of the source at freeze-out [203]: $\epsilon_x^{\mathrm{f.o.}} \approx 2\lim_{K_T\to 0}\left(R_{s,2}^2/R_{s,0}^2\right)$. The freeze-out eccentricity is seen to flip sign between RHIC and LHC: at the LHC the freeze-out source is elongated *in the reaction plane direction* by almost as much as it was still *out-of-plane elongated* at RHIC.

4.7. Correlation radii by FAST HADRON FREEZE-OUT GENERATOR

Iu. A. Karpenko, R. Lednicky, I. P. Lokhtin, L. V. Malinina, Yu. M. Sinyukov and A. M. Snigirev

The predictions for correlation radii in the central Pb+Pb collisions for LHC $\sqrt{s_{NN}}$ = 5500 GeV are given in the frame of FAST HADRON FREEZE-OUT GENERATOR (FASTMC).

One of the most spectacular features of the RHIC data, refereed as "RHIC puzzle", is the impossibility to describe simultaneously momentum-space measurements and the freeze-out coordinate-space ones (femtoscopy) by the existing hydrodynamic and cascade models or their hybrids. However, a good description of SPS and RHIC data have been obtained in various models based on hydro-inspired parametrizations of freeze-out hypersurface. Thus, we have achieved this goal within our fast hadron freeze-out MC generator (FASTMC) [204]. In FASTMC, particle multiplicities are determined based on the concept of chemical freeze-out. Particles and hadronic resonances are generated on the thermal freeze-out hypersurface, the hadronic composition at this stage is defined by the parameters of the system at chemical freeze-out [204]. The input parameters which control the execution of our MC hadron generator in the case of Bjorken-like parameterization of the thermal freeze-out hypersurface (similar to the well known "Blast-Wave" parametrization with the transverse flow) for central collisions are the following: temperature $T^{\rm ch}$ and chemical potentials per a unit charge $\widetilde{\mu}_B$,$\widetilde{\mu}_S$,$\widetilde{\mu}_Q$ at chemical freeze-out, temperature $T^{\rm th}$ at thermal freeze-out, the fireball transverse radius R, the mean freeze-out proper time τ and its standard deviation $\Delta\tau$ (emission duration), the maximal transverse flow rapidity $\rho_u^{\rm max}$. We considered here the naive "scaling" of the existing physical picture of heavy ion interactions over two order of magnitude in $\sqrt{s}$ to the maximal LHC energy $\sqrt{s_{NN}}$ = 5500 GeV. The model parameters obtained by the fitting within FASTMC generator of the existing experimental data on m_t-spectra, particle ratios, rapidity density dN/dy, k_t-dependence of the correlation radii $R_{\rm out}$,$R_{\rm side}$,$R_{\rm long}$ from SPS ($\sqrt{s_{NN}}$ = 8.7 – 17.3 GeV) to RHIC ($\sqrt{s_{NN}}$ = 200 GeV) are shown in Fig. 67. For LHC energies we have fixed the thermodynamic parameters at chemical freeze-out as the asymptotic ones: $T^{\rm ch}$ = 170 MeV, $\widetilde{\mu}_B = \widetilde{\mu}_S = \widetilde{\mu}_Q$=0 MeV. The linear extrapolation of the model parameters in log($\sqrt{s}$) to LHC ($\sqrt{s_{NN}}$ = 5500 GeV) is shown in Fig. 67 by open symbols. The extrapolated values are the following: $R \sim$ 11 fm, $\tau \sim$ 10 fm/c, $\Delta\tau \sim$ 3.0 fm/c, $\rho_u^{\rm max} \sim$ 1.0, $T^{\rm th} \sim$ 130 MeV. The density of charged particles at mid-rapidity obtained with these parameters is dN/dy = 1400, i.e. twice larger than at RHIC $\sqrt{s_{NN}}$ = 200 GeV in coincidence with the naive extrapolation of dN/dy. These parameters yield only a small increase of the correlation radii $R_{\rm out}$,$R_{\rm side}$,$R_{\rm long}$ (Fig. 68).

4.8. Exciting the quark-gluon plasma with a relativistic jet

M. Mannarelli and C. Manuel

We discuss the properties of a system composed by a static plasma traversed by a jet of particles. Assuming that both the jet and the plasma can be described using a hydrodynamical approach, and in the conformal limit, we find that unstable modes arise when the velocity of the jet is larger than the speed of the sound of the plasma and only modes with momenta smaller than a certain values

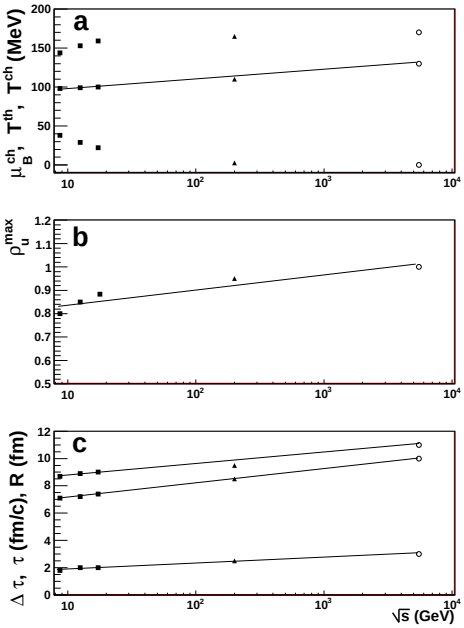

Figure 67: FASTMC parameters versus $\log(\sqrt{s})$ for SPS $\sqrt{s} = 8.7 - 17.3$ GeV (black squares), RHIC $\sqrt{s} = 200$ GeV (black triangles) and LHC $\sqrt{s} = 5500$ GeV(open circles): (**a**) $T^{\rm ch}$, $T^{\rm th}$, μ^B, (**b**) ρ_u^{max}, (**c**) τ, R and $\Delta\tau$.

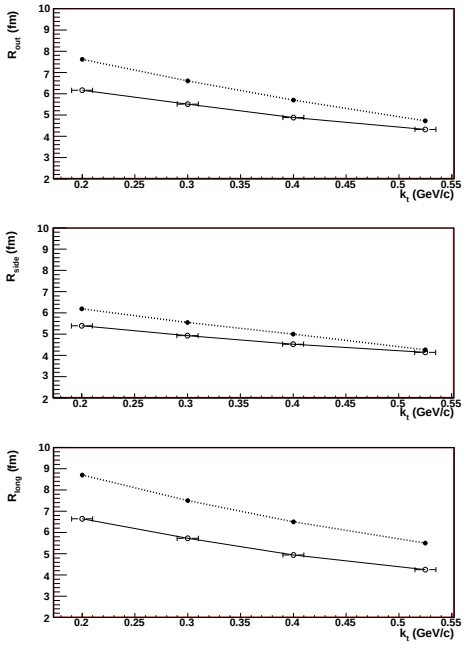

Figure 68: The $\pi^+\pi^+$ correlation radii in longitudinally comoving system at mid-rapidity in central Au+Au collisions at $\sqrt{s_{NN}} = 200$ GeV from the STAR experiment [205] (open circles) and the FASTMC calculations for LHC $\sqrt{s} =$ 5500 GeV (black squares).

are unstable. Moreover, for ultrarelativistic velocities of the jet the most unstable modes correspond to relative angles between the velocity of the jet and momentum of the collective mode $\sim \pi/4$. Our results suggest an alternative mechanism for the description of the jet quenching phenomenon, where the jet crossing the plasma loses energy exciting colored unstable modes. In LHC this effect should be seen with an enhanced production of hadrons for some specific values of their momenta and in certain directions of momenta space.

It has been suggested that a high p_T jet crossing the medium produced after a relativistic heavy ion collision, and travelling at a velocity higher than the speed of sound should form shock waves with a Mach cone structure [206, 207]. Such shock waves should be detectable in the low p_T parton distributions at angles $\pi \pm 1.2$ with respect to the direction of the trigger particle. A preliminary analysis of the azimuthal dihadron correlation performed by the PHENIX Collaboration [208] seems to suggest the formation of such a conical flow.

We propose a novel possible collective process to describe the jet quenching phenomenon. In our approach a neutral beam of colored particles crossing an equilibrated quark-gluon plasma induces plasma instabilities [209]. Such instabilities represent a very efficient mechanism for converting the energy and momenta stored in the total system (composed by the plasma and the jet) into (growing) energy and momenta of gauge fields, which are initially absent. To the best of our knowledge, only reference [210] considers the

possibility of the appearance of filamentation instabilities produced by hard jets in heavy-ion collisions.

We have studied this phenomenon using the chromohydrodynamical approach developed in [211], assuming the conformal limit for the plasma. Since we are describing the system employing ideal fluid-like equations, our results are valid at time scales shorter than the average time for collisions. A similar analysis using kinetic theory, and reaching to similar results, will soon be reported.

We have studied the dispersion laws of the gauge collective modes and their dependence on the velocity of the jet v, the magnitude of the momentum of the collective mode $\mathbf{k}$, the angle θ between these quantities, and of the plasma frequencies of both the plasma ω_p and the jet $\omega_{\rm jet}$. We find that there is always one unstable mode if the velocity of the jet is larger than the speed of sound $c_s = 1/\sqrt{3}$, and if the momentum of the collective mode is in modulus smaller than a threshold value. Quite interestingly we find that the unstable modes with momentum parallel to the velocity of the jet is the dominant one for velocity of the jet $v \lesssim 0.8$. For larger values of the jet velocity only the modes with angles larger than $\sim \pi/8$ are significant and the dominant unstable modes correspond to angles $\sim \pi/4$ (see figure 69).

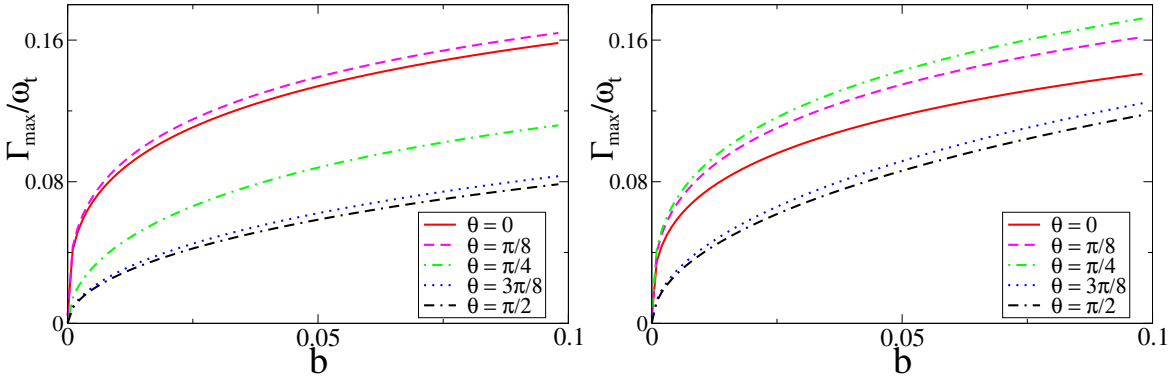

Figure 69: Largest value of the imaginary part of the dispersion law for the unstable mode as a function of $b = \omega^2_{\rm jet}/\omega^2_p$ for two different values of the velocity of the jet v and five different angles between $\mathbf{k}$ and $\mathbf{v}$. The left/right panels correspond to $v = 0.8/0.9$, respectively.

Our numerical results imply that both in RHIC and in the LHC these instabilities develop very fast, faster in the case of the LHC as there one assumes that ω_p will attain larger values. Further, the soft gauge fields will eventually decay into soft hadrons, and may affect the hydrodynamical simulations of shock waves mentioned in reference [206, 207].

5. Fluctuations

5.1. Fluctuations and the clustering of color sources

L. Cunqueiro, E. G. Ferreiro and C. Pajares

We present our results on multiplicity and p_T fluctuations at LHC energies in the framework of the clustering of color sources. In this approach, elementary color sources -strings- overlap forming

clusters, so the number of effective sources is modified. We find that the fluctuations are proportional to the number of those clusters.

Non-statistical event-by-event fluctuations in relativistic heavy ion collisions have been proposed as a probe of phase instabilities near de QCD phase transition. The transverse momentum and the multiplicity fluctuations have been measured at SPS and RHIC energies. These fluctuations show a non-monotonic behavior with the centrality of the collision: they grow as the centrality increases, showing a maximum at mid centralities, followed by a decrease at larger centralities. Different mechanisms have been proposed in order to explain those data. Here, we will apply the clustering of color sources. In this approach, color strings are stretched between the colliding partons. Those strings act as color sources of particles which are successively broken by creation of $q\bar{q}$ pairs from the sea. The color strings correspond to small areas in the transverse space filled with color field created by the colliding partons. If the density of strings increases, they overlap in the transverse space, giving rise to a phenomenon of string fusion and percolation [65]. Percolation indicates that the cluster size diverges, reaching the size of the system. Thus, variations of the initial state can lead to a transition from disconnected to connected color clusters. The percolation point signals the onset of color deconfinement.

These clusters decay into particles with mean transverse momentum and mean multiplicity that depend on the number of elementary sources that conform each cluster, and the area occupied by the cluster. In this approach, the behavior of the p_T [166] and multiplicity [167] fluctuations can be understood as follows: at low density, most of the particles are produced by individual strings with the same transverse momentum $< p_T >_1$ and the same multiplicity $< \mu_1 >$, so fluctuations are small. At large density, above the critical point of percolation, we have only one cluster, so fluctuations are not expected either. Just below the percolation critical density, we have a large number of clusters formed by different number of strings n, with different size and thus different $< p_T >_n$ and different $< \mu >_n$ so the fluctuations are maximal.

The variables to measure event-by-event p_T fluctuations are ϕ and F_{p_T}, that quantify the deviation of the observed fluctuations from statistically independent particle emission:

$$\phi = \sqrt{\frac{< Z^2 >}{< \mu >}} - \sqrt{< z^2 >}\,, \tag{34}$$

where $z_i = p_{T\,i} - < p_T >$ is defined for each particle and $Z_i = \sum_{j=1}^{N_i} z_j$ is defined for each event, and

$$F_{p_T} = \frac{\omega_{data} - \omega_{random}}{\omega_{random}}, \quad \omega = \frac{\sqrt{< p_T^2 > - < p_T >^2}}{< p_T >}\,. \tag{35}$$

Moreover, in order to measure the multiplicity fluctuations, the variance of the multiplicity distribution scaled to the mean value of the multiplicity has been used. Its behavior is similar to the one obtained for $\Phi(p_T)$, used to quantify the p_T-fluctuations, suggesting that they are related to each other. The Φ-measure is independent of the distribution of number of particle

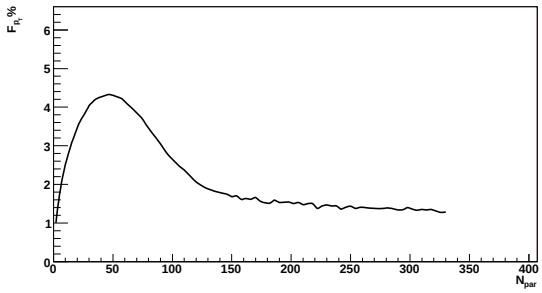

Figure 70: F_{p_T} at LHC.

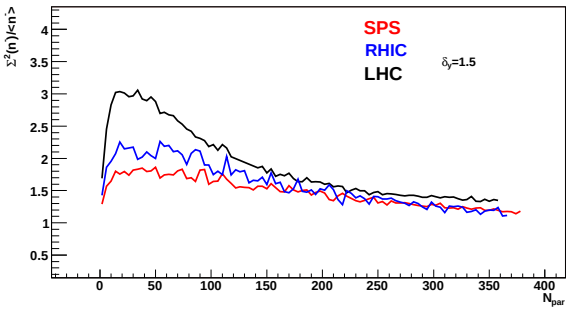

Figure 71: Scaled variance on negatively charged particles at, from up to down, LHC, RHIC and SPS.

sources if the sources are identical and independent from each other. That is, Φ should be independent of the impact parameter if the nucleus-nucleus collision is a simple superposition of nucleon-nucleon interactions.

In Fig. 70 we present our results on p_T fluctuations at LHC. Note that the increase of the energy essentially shifts the maximum position to a lower number of participants [166]. In Fig. 71 we show our values for the scaled variance of negatively charged particles at SPS, RHIC and LHC energies.

Summarizing: the p_T and multiplicity fluctuations are due in our approach to the different mean $< p_T >$ and mean multiplicities of the clusters, and they depend essentially on the number of clusters. In other words, a decrease in the number of effective sources leads to a decrease of the fluctuations.

5.2. Fluctuations of particle multiplicities from RHIC to LHC

G. Torrieri

We define an observable capable of determining which statistical model, if any, governs freeze-out in very high energy heavy ion collisions such as RHIC and LHC. We calculate this observable for K/π fluctuations, and show that it should be the same for RHIC and LHC, as well as independent of centrality, if the Grand-Canonical statistical model is appropriate and chemical equilibrium applies. We describe variations of this scaling for deviations from this scenario, such as light quark chemical non-equilibrium, strange quark over-saturation and local (canonical) equilibrium for strange quarks.

Particle yield fluctuations are a promising observable to falsify the statistical model and to constrain its parameters (choice of ensemble, strangeness/light quark chemical equilibrium) [212]. The uncertainities associated with fluctuations, however, warrant that care be taken to choose a fluctuation observable.

For instance, volume fluctuations could be originating from both initial state effects and dynamical processes, and are not well understood. Their effect has to be factored out from multiplicity fluctuations data. One way to do this is to concentrate on fluctuations of particle ratios, where volume factors out event by event [213]

$$\sigma^2_{N_1/N_2} = \frac{\left\langle (\Delta N_1)^2 \right\rangle}{\langle N_1 \rangle^2} + \frac{\left\langle (\Delta N_2)^2 \right\rangle}{\langle N_2 \rangle^2} - 2\frac{\langle \Delta N_1 \Delta N_2 \rangle}{\langle N_1 \rangle \langle N_2 \rangle}. \tag{36}$$

This, however, introduces an *average* hadronization volume dependence through the $\langle N_{1,2} \rangle$ terms (two in the denominator, one in the numerator of Eq. 36).

This feature allows us to perform an invaluable consistency chech for the statistical model, since the volume going into the ratio fluctuations must, for consistency, be the same as the volume going into the yields. Thus, observables such as $\frac{d\langle N_1 \rangle}{dy}\sigma^2_{N_1/N_2}$ should be strictly independent of multiplicity and centrality, as long as the statistical model holds and the physically appropriate ensemble is Grand Canonical.

We propose doing this test, at both RHIC and LHC, using the corrected variance

$$\Psi^{N_1}_{N_1/N_2} = \frac{dN_1}{dy}\nu^{dyn}_{N_1/N_2} \tag{37}$$

where $\nu^{dyn}_{N_1/N_2}$ is theoretically equal to the corrected mixed variance [214]

$$\begin{aligned} \nu^{dyn}_{N_1/N_2} &= (\sigma^{dyn}_{N_1/N_2})^2 = \sigma^2_{N_1/N_2} - (\sigma^{Poisson}_{N_1/N_2})^2 = \\ &= \frac{\langle N_1(N_1-1) \rangle}{\langle N_1 \rangle^2} + \frac{\langle N_2(N_2-1) \rangle}{\langle N_2 \rangle^2} - 2\frac{\langle N_1 N_2 \rangle}{\langle N_1 \rangle \langle N_2 \rangle} \end{aligned} \tag{38}$$

SHAREv2.X [170] provides the possibility of calculating all ingredients of $\Psi^{N_1}_{N_1/N_2}$ for any hadrons, incorporating the effect of all resonance decays, as well as chemical (non)equilibrium. The calculation for $\Psi^{\pi^-}_{K^-/\pi^-}$, as well as $\Psi^{\pi^-}_{K^-/\pi^-}$ is shown in Fig. 72. These species were chosen because their correlations (from resonance decays, $N^* \to N_1 N_2$), which would need corrections for limited experimental acceptance, are small.

Equilibrium thermal and chemical parameters are very similar at RHIC and the LHC(the baryo-chemical potential will be lower at the LHC, but it is so low at RHIC that the difference is not experimentally detectable). Thus, $\Psi^{N_1}_{N_1/N_2}$ should be identical, to within experimental error, for both the LHC and RHIC, over all multiplicities were the statistical model is thought to apply.

According to [168], chemical conditions at freeze-out deviate from equilibrium, and reflect the higher entropy contect and strangeness per entropy content of the early deconfined phase through an over-saturated phase space occupancy for the light and strange quarks ($\gamma_s > \gamma_q > 1$). If this is true, than $\Psi^{N_1}_{N_1/N_2}$ should still be independent of centrality for a given energy range, but should go markedly up for the LHC from RHIC, because of the increase in γ_q and γ_s. Fig. 72 shows what effect three different sets of $\gamma_{q,s}$ inferred in [168] would have on $\Psi^{\pi^-}_{K^-/\pi^-}$ and $\Psi^{\pi^-}_{K^-/K^+}$

If non-statistical processes (minijets, string breaking etc.) dominate event-by-event physics, the flat $\Psi^{N_1}_{N_1/N_2}$ scaling on centrality/multiplicity should be broken, and $\Psi^{N_1}_{N_1/N_2}$ would exhibit a non-trivial dependence on N_{part} or dN/dy.

This is also true if global correlations persist, such as is the case in Canonical and micro-canonical models [215] If global correlations persist for particle N_2 and/or N_1, than $\Psi^{N_1}_{N_1/N_2}$ becomes reduced, and starts strongly varying with centrality in lower multiplicity events. Thus, if strangeness at RHIC/the LHC is created and maintained locally, $\Psi^{N_1}_{N_1/N_2}$ should develop a "wiggle" at low centrality, and be considerably lower than Grand Canonical expectation. For $\Psi^{\pi^-}_{K^+/K^-}$ it should be lower by a factor of two.

In conclusion, measuring $\Psi^{\pi^-}_{K^-/\pi^-}$ and $\Psi^{\pi^-}_{K^+/K^-}$, at comparing the results between the LHC and RHIC can provide an invaluable falsification of the statistical model, as well as constraints as to *which* statistical model applies in these regimes.

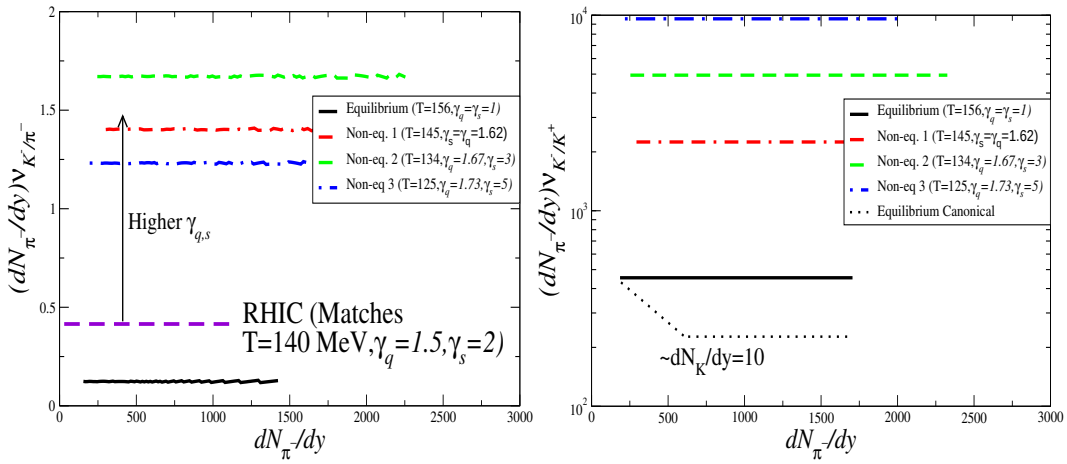

Figure 72:

6. High transverse momentum observables and jets

6.1. Jet quenching parameter $\hat{q}$ from Wilson loops in a thermal environment

D. Antonov and H. J. Pirner

The gluon jet quenching parameter is calculated in SU(3) quenched QCD within the stochastic vacuum model. At the LHC-relevant temperatures, it is defined by the gluon condensate and the vacuum correlation length. Numerically, when the temperature varies from $T_c = 270\,\mathrm{MeV}$ to the inverse vacuum correlation length $\mu = 894\,\mathrm{MeV}$, the jet quenching parameter rises from zero to $1.1\,\mathrm{GeV}^2/\mathrm{fm}$.

At LHC energies, radiative energy loss is the dominant mechanism of jet energy loss in the quark-gluon plasma. The expectation value of a light-like adjoint Wilson loop provides an estimate for the radiative energy loss of a gluon [216]:

$$\left\langle W^{\mathrm{adj.}}_{L_\parallel \times L_\perp} \right\rangle = \exp\left(-\frac{\hat{q}}{4\sqrt{2}} L_\parallel L_\perp^2 \right). \tag{39}$$

The contour of the loop at zero temperature is depicted in Fig. 73. We have calculated the *jet quenching parameter* $\hat{q}$ in the SU(3) quenched theory through the evaluation of the

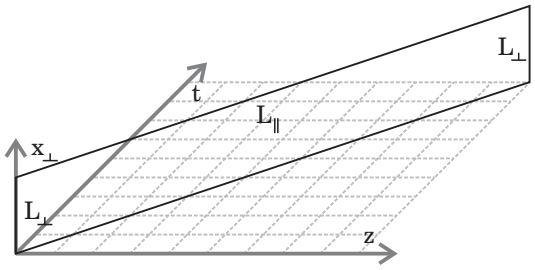

Figure 73: The contour of the Wilson loop of a gluon.

Wilson loop (39). To this end, we have used the stochastic vacuum model [217] at $T > T_c$, where $T_c = 270\,\mathrm{MeV}$ is the deconfinement temperature. This model incorporates the gluon condensate which, together with the vacuum correlation length, defines the jet quenching parameter. This is different from the results obtained within perturbative QCD [218] and conformal field theories [216], where $\hat{q} \propto T^3$.

The hierarchy of scales in our problem is $\mu^{-1} \ll L_\perp \ll \beta \ll L_\parallel$, where β is the inverse temperature, and $\mu = 894\,\mathrm{MeV}$ is the inverse vacuum correlation length. Due to the x_4-periodicity at finite temperature, the contour depicted in Fig. 73 effectively splits into segments whose extensions along the 3rd and the 4th axes are β. Furthermore, due to the short-rangeness of gluonic correlations, which fall off at the vacuum correlation length, the dominant contribution to $\hat{q}$ stems from self-interactions of individual segments. We have also calculated the contribution stemming from the correlations of neighboring segments, which turns out to be parametrically (and numerically) suppressed by the factor $\mathrm{e}^{-\mu/T}$. For this reason, the even smaller contributions from the next-to-nearest neighboring segments on are disregarded. The contributions of individual and neighboring segments read

$$\hat{q} = \frac{g^2 \left\langle (F^a_{\mu\nu})^2 \right\rangle_{T=0}}{16\mu} \left[\sqrt{2} - \frac{T}{\mu}\left(1 - \mathrm{e}^{-\sqrt{2}\mu/T}\right)\right]\left[\coth\left(\frac{\mu}{2T}\right) - \coth\left(\frac{\mu}{2T_c}\right)\right] \text{ and}$$

$$\Delta\hat{q} = \frac{g^2 \left\langle (F^a_{\mu\nu})^2 \right\rangle_{T=0}}{16\mu} \mathrm{e}^{-\mu/T} \left[1 - \frac{T}{\mu}\left(1 - \mathrm{e}^{-\mu/T}\right)\right]\left[\coth\left(\frac{\mu}{2T}\right) - \coth\left(\frac{\mu}{2T_c}\right)\right],$$

respectively. The right most brackets in these equations define the temperature dependence of the gluon condensate, corresponding to the exponential fall-off of its nonlocal counterpart [219]. As for the zero-temperature value of the gluon condensate, it can be expressed through the vacuum correlation length and the string tension in the fundamental representation of SU(3), $\sigma = (440\,\mathrm{MeV})^2$, and reads [220] $g^2 \left\langle (F^a_{\mu\nu})^2 \right\rangle_{T=0} = (72/\pi)\sigma\mu^2 = 3.55\,\mathrm{GeV}^4$. The above contributions together with their sum are plotted in Fig. 74. Note finally that, in the large-N_c limit, our full result for the jet quenching parameter behaves as N_c^0, i.e. it does not scale with N_c. This behavior is similar to those of other models [216, 218].

6.2. Particle Ratios at High p_T at LHC Energies

G. G. Barnaföldi, P. Lévai, B. A. Cole, G. Fai and G. Papp

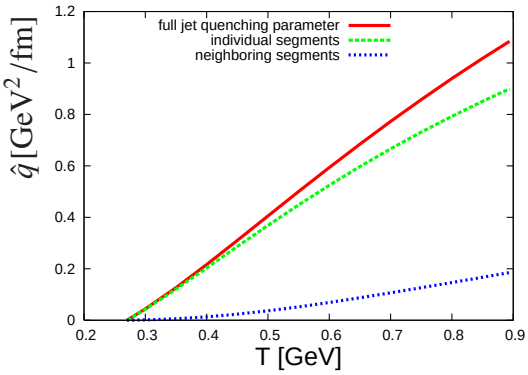

Figure 74: The full jet quenching parameter and relative contributions to it.

Hadron production has been calculated in a pQCD improved parton model for pp, dA and heavy ion collisions. We applied KKP and AKK fragmentation functions. Our jet fragmentation study shows, that hadron ratios at high p_T depend on quark contribution mostly and less on the gluonic one. This finding can be seen in jet-energy loss calculations, also. We display the suppression pattern on different hadron ratios in *PbPb* collisions at LHC energies.

The precision of pQCD based parton model calculations was enhanced during the last decade. The calculated spectra allow to make predictions not only for the hadron yields, but for sensitive particle ratios and nuclear modifications. For the calculation of particle ratios new fragmentation functions are needed not only for the most produced light mesons, but for protons also. From the experimental point of view one requires identified particle spectra by RHIC and LHC. Especially the ALICE detector has a unique capability to measure identified particles at highest transverse momenta via Čherenkov detectors. The $\pi^{\pm}/K^{\pm}$ and $K^{\pm}/p(\bar{p})$ ratios can be measured up to 3 GeV/c and 5 GeV/c respectively.

Here we calculate hadron ratios in our next-to-leading order pQCD improved parton model based on Ref. [221] with intrinsic transverse momenta, determined by the expected c.m. energy evolution along the lines of Ref. [221]. The presented ratios are based on π, K and p spectra which were calculated by AKK fragmentation functions [14]. First we compare calculated particle ratios to the data of the STAR collaboration measured in *AuAu* collisions at $\sqrt{s} = 200$ *A*GeV RHIC energy [222, 223]. Predictions for high-p_T hadron ratios at RHIC and at LHC energies in most central $(0-10\%)$ *PbPb* collisions are also shown in Fig. 75.

On the *left panel* of Fig. 75, particle ratios are compared to *AuAu* collisions at $\sqrt{s} = 200$ *A*GeV STAR K/π (*dots*) and p/π (*triangles*) data. The agreement between the RHIC data and the calculations at RHIC energy can be considered acceptable at $p_T \gtrsim 5$ GeV/c, with an opacity of $L/\lambda = 4$. However, at lower momenta, where pQCD is no longer reliable, the ratios differ from the calculated curves.

The *right panel* shows calculations for *PbPb* collisions for $\sqrt{s} = 5.5$ *A*TeV energy. Using a simple $\mathrm{d}N/\mathrm{d}y \sim 1500-3000$ estimation, we expect a $L/\lambda \approx 8$ opacity in most central *PbPb* collisions. For comparison, we plotted the $L/\lambda = 0$ and 4 values also. The lower- and intermediate-p_T variation of the hadron ratios arise from the different strengths

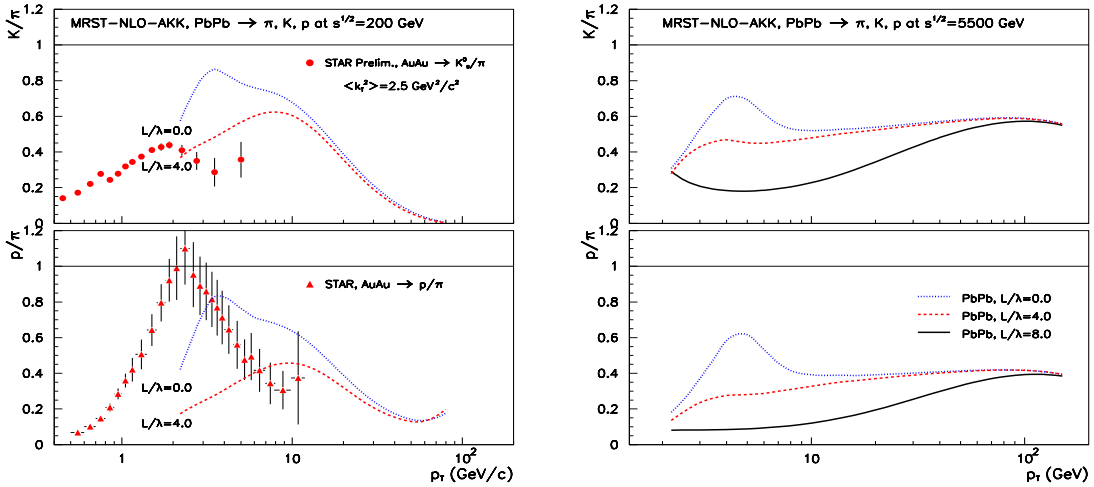

Figure 75: Calculated charge-averaged K/π and p/π ratios in AA collisions at RHIC and LHC energies. RHIC curves are compared to STAR [222, 223] data at $\sqrt{s} = 200$ AGeV.

of the jet quenching for quark and gluon contributions [224]. Due to the quark dominated fragmentation, the difference disappears at high-p_T in the ratios.

6.3. π^0 fixed $p_\perp$ suppression and elliptic flow at LHC

A. Capella, E. G. Ferreiro, A. Kaidalov and K. Tywoniuk

Using a final state interaction model which describes the data on these two observables, at RHIC, we make predictions at the LHC – using the same cross-section and $p_\perp$-shift. The increase in the medium density between these two energies (by a factor close to three) produces an increase of the fixed $p_\perp$ π^0 suppression by a factor 2 at large $p_\perp$ and of v_2 by a factor 1.5.

6.3.1. π^0 fixed $p_\perp$ suppression Final state interaction (FSI) effects have been observed in AA collisions. They are responsible of strangeness enhancement, J/ψ supression, fixed $p_\perp$ supression, azimuthal asymmetry, ... Is it the manifestation of the formation of a new state of matter or can it be described in a FSI model with no reference to an equation of state, thermalization, hydrodynamics, ... ? We take the latter view and try to describe all these obseervables within a unique formalism : the well known gain and loss differential equations. We assume [225] that, at least for particles with $p_\perp$ larger than $< p_\perp >$, the interaction with the hot medium produces a $p_\perp$-shift $\delta p_\perp$ towards lower values and thus the yield at a given $p_\perp$ is reduced. There is also a gain term due to particles produced at $p_\perp + \delta p_\perp$. Due to the strong decrease of the $p_\perp$-distributions with increasing $p_\perp$, the loss is much larger than the gain. Asuming boost invariance and dilution of the densities in $1/\tau$ due to longitudinal expansion, we obtain

$$\frac{\tau dN_{\pi^0}(b,s,p_\perp)}{d\tau} = -\sigma N(b,s)\left[N_{\pi^0}(b,s,p_\perp) - N_{\pi^0}(b,s,p_\perp+\delta p_\perp)\right] \qquad (40)$$

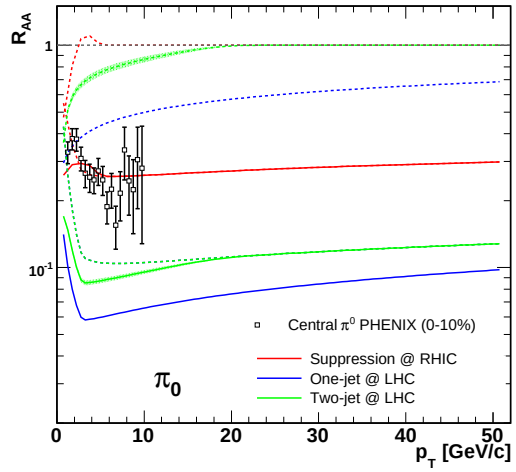

Figure 76: From up to down: RHIC initial, 2 LHC initial, RHIC final, LHC FSI, LHC FSI+shadowing.

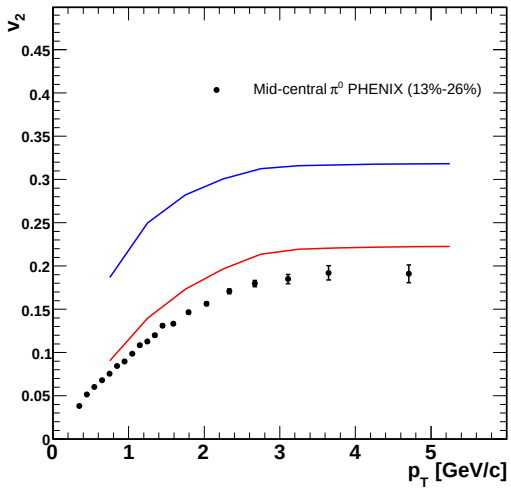

Figure 77: v_2 for π^0 at RHIC (lower curve) and LHC LHC (upper curve).

Here $N \equiv dN/dyd^2s$ is the transverse density of the medium and N_{π^0} the corresponding one of the π^0 [226]. This has to be integrated between initial time τ_0 and freeze-out time τ_f. The solution deepnds only on τ_f/τ_0. We use $\sigma = 1.4$ mb at both energies and $\delta p_\perp = p_\perp^{1.5}/20$ for $p_\perp < 2.9$ GeV and $\delta p_\perp = p_\perp^{0.8}/9.5$ for $p_\perp > 2.9$ GeV [227]. Eq. (40) at small τ describes an interaction at the partonic level. Indeed, here the densities are very large and the hadrons not yet formed. At later times the interaction is hadronic. Most of the effect takes place in the partonic phase. We use a single (effective) value of σ for all values of the proper time τ. The results at RHIC and LHC are given in Fig. 76. At LHC only shadowing [226] has been included in the initial state. The suppression is given by the dashed line. It coincides with R_{AA} for $p_\perp$ large enough – when shadowing and Cronin efffects are no longer present. The LHC suppression is thus a factor of two larger than at RHIC.

6.3.2. Elliptic flow Final state interaction in our approach gives rise to a positive v_2 [227] (no need for an equation of state or hydro). Indeed, when the π^0 is emitted at $\theta_R = 90^\circ$ its path length is maximal (maximal absorption). In order to compute it we assume that the density of the hot medium is proportional to the path length $R_{\theta_R}(b,s)$ of the π^0 inside the interaction region determined by its transverse position s and its azimuthal angle θ_R. Hence, we replace $N(b,s)$ by $N(b,s)R_{\theta_R}(b,s)/ < R_{\theta_R}(b,s) >$ where R_{θ_R} is the π^0 path length and <> denotes its average over θ_R. (In this way the averaged transverse density $N(b,s)$ is unchanged). The suppression $S_{\pi^0}(b,s)$ depends

now on θ_R and v_2 is given by

$$v_2(b, p_\perp) = \frac{\int d\theta_R S_{\pi^0}(b, p_\perp, \theta_R) \cos 2\theta_R}{\int d\theta_R S_{\pi^0}(b, p_\perp, \theta_R)} \tag{41}$$

The results at RHIC and LHC are presented in Fig. 77.

6.4. Energy dependence of jet transport parameter

J. Casalderrey-Solana and X. N. Wang

We study the evolution and saturation of the gluon distribution function in the quark-gluon plasma as probed by a propagating parton and its effect on the computation of the jet quenching or transport parameter $\hat{q}$. For hard probes, this evolution at small $x = Q_s^2/6ET$ leads to a jet energy dependence of $\hat{q}$

Within the picture of multiple parton scattering in QCD, the energy loss for an energetic parton propagating in a dense medium is dominated by induced gluon bremsstrahlung. Taking into account of the non-Abelian Landau-Pomeranchuck-Midgal (LPM) interference, the radiative parton energy loss [228],

$$\Delta E = \frac{\alpha_s N_c}{4} \hat{q}_R L^2, \tag{42}$$

is found to depend on the jet transport or energy loss parameter $\hat{q}$ which describes the averaged transverse momentum transfer squared per unit distance (or mean-free-path). Here R is the color representation of the propagating parton in $SU(3)$.

The transport parameter $\hat{q}_R$ experienced by a propagating parton can be defined in terms of the unintegrated gluon distributions $\phi_k(x, q_T^2)$ of the color sources in the quark-gluon plasma,

$$\hat{q}_R = \frac{4\pi^2 C_R}{N_c^2 - 1} \rho \int_0^{\mu^2} \frac{d^2 q_T}{(2\pi)^2} \int dx \delta(x - \frac{q_T^2}{2p^- \langle k^+ \rangle}) \alpha_s(q_T^2) \phi(x, q_T^2), \tag{43}$$

where $\langle k^+ \rangle$ is the average energy of the color sources and $\phi(x, q_T^2)$ is the corresponding average unintegrated gluon distribution function per color source. The integrated gluon distribution is

$$xG(x, \mu^2) = \int_0^{\mu^2} \frac{d^2 q_T}{(2\pi)^2} \phi(x, q_T). \tag{44}$$

Since we are interested in the determination of $\hat{q}_R$ at large jet energies, we need to know the unintegrated parton distribution $\phi(x, q_T^2)$ in Eq. (43) at small $x \sim \left\langle q_T^2 \right\rangle / 6ET$. For a large path length, the typical total momentum transfer, $\hat{q}L$, which will set the scale of the process, is also large. These scales lead to the evolution of the gluon distribution function. In the medium, this evolution may be modified due to the interaction of the radiated gluons with thermal partons. However, since the medium effects are of the order of $\mu_D << T$, we neglect those at hard scales. Given that both the scale and the rapidity are large, we describe the the (linear) vacuum evolution in the double logarithmic approximation (DLA) [229]. The

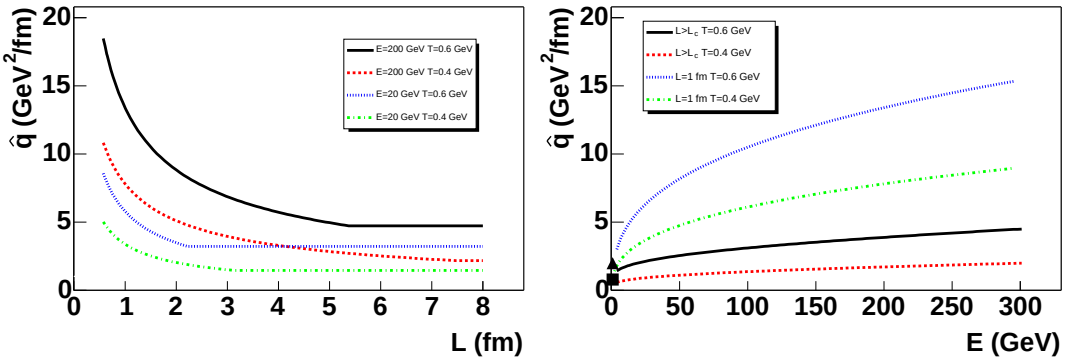

Figure 78: Jet quenching parameter $\hat{q}$ as a function of the path length (left) and jet energy (right). The square (triangle) marks the value of $\hat{q}$ for thermal particle at $T = 0.4$ GeV ($T = 0.6$ GeV). Significant corrections to the energy dependence are expected at low energy which should approach their thermal value at $E = 3\,T$.

thermal gluon distribution function at a scale $\mu^2 = T^2$ is determined via the hard thermal loop approximation and it is used as an initial condition for the evolution. As in vacuum, the growth of the gluon distribution function leads to saturation which tame this growth for scales $\mu^2 < Q_s^2$. The saturation scale is estimated from the linearly evolved distribution. The details of the computation can be found in [230].

The evolution leads to a jet energy dependence of the transport parameter that is stronger than any power of logarithmic dependence. The saturation effect also gives rise to a non-trivial length dependence of the jet transport parameter. These two features are shown in Figure 78, where we compute the transport parameter for $T = 0.4$ GeV (RHIC) and $T = 0.6$ GeV (LHC). In both cases, the energy dependence of $\hat{q}$ is significant, leading to a factor of 2 difference between jets of 20 and 200 GeV. This difference is larger for small jet path lengths. The computation also shows that $\hat{q}$ grows as the path length decreases. Both dependences translate into different amount of radiative energy loss Eq. (42). Let us note, however, that the derivation of Eq. (42) assumes a constant $\hat{q}$; thus, the relation between the radiative energy loss and the transport parameter should be revisited for an energy/length dependent $\hat{q}$.

6.5. PQM prediction of $R_{\rm AA}(p_T)$ and $R_{\rm CP}(p_T)$ at midrapidity in Pb–Pb collisions at the LHC

A. Dainese, C. Loizides and G. Paić

The Parton Quenching Model (PQM) couples the BDMPS-SW quenching weights for radiative energy loss with a realistic description of the nucleus–nucleus collision geometry, based on the Glauber model. We present the predictions for the nuclear modification factors, in Pb–Pb relative to pp collisions ($R_{\rm AA}$) and in central relative to peripheral Pb–Pb collisions ($R_{\rm CP}$), of the transverse momentum distributions of light-flavour hadrons at midrapidity.

The Parton Quenching Model (PQM) [231], which combines the pQCD BDMPS-SW

framework for the probabilistic calculation of parton energy loss in extended partonic matter of given size and density [232] with a realistic description of the collision overlap geometry (Glauber model) in a static medium, was shown to describe the transverse momentum and centrality dependence of the leading particle suppression in Au–Au collisions at top RHIC energy. The model has one single parameter that sets the scale of the BDMPS transport coefficient $\hat{q}$, hence of the medium density. The parameter has been tuned [231] on the basis of the $R_{\rm AA}$ data at $\sqrt{s_{\rm NN}} = 200$ GeV, that indicate a transport coefficient in the range 4–14 GeV^2/fm. We scale the model parameter to LHC energy assuming its proportionality to the expected volume-density of gluons $n^{\rm g}$. Using the value of $n^{\rm g}$ predicted for the LHC by the EKRT saturation model [74] (which gives $\mathrm{d}N_{\rm ch}/\mathrm{d}y \simeq 3000$), we obtain $\hat{q} \simeq 25$–100 GeV^2/fm.

In PQM we obtain the leading-particle suppression in nucleus–nucleus collisions by calculating the hadron-level transverse momentum distributions in a Monte Carlo approach. The 'event loop' that we iterate is the following: 1) Generation of a parton, quark or gluon, with $p_T > 5$ GeV, using the PYTHIA event generator in pp mode with CTEQ 4L parton distribution functions; nuclear shadowing is neglected, since it's effect is expected to be small above 5–10 GeV in p_T ; the p_T -dependence of the quarks-to-gluons ratio is taken from PYTHIA. 2) Sampling of a parton production point and propagation direction in the transverse plane, according to the density of binary collisions, and determination of the in-medium path length and of the path-averaged $\hat{q}$, the inputs for the calculation of the quenching weights, i.e. the energy-loss probability distribution $P(\Delta E)$. 3) Sampling of an energy loss ΔE according to $P(\Delta E)$ (non-reweighted case [231]) and definition of the new parton transverse momentum, $p_T - \Delta E$; 4) Fragmentation of the parton to a hadron using the leading-order Kniehl-Kramer-Pötter (KKP) fragmentation functions. Quenched and unquenched p_T distributions are obtained including or excluding the third step of the chain. The nuclear modification factor $R_{\rm AA}(p_T)$ is given by their ratio.

The left-hand panel of Fig. 79 shows the p_T -dependence of the $R_{\rm AA}$ nuclear modification factor in 0–10% central Pb–Pb at $\sqrt{s_{\rm NN}} = 5.5$ TeV relative to pp. The $R_{\rm AA}$ for central Au–Au collisions at top RHIC energy is also shown and compared to π^0 data from the PHENIX experiment [233]. PQM predicts for central Pb–Pb at the LHC a very slow increase of $R_{\rm AA}$ with p_T , from about 0.1 at 10 GeV to about 0.2 at 100 GeV. The right-hand panel of the figure shows the $R_{\rm CP}$ central-to-peripheral nuclear modification factor for different centrality classes relative to the peripheral class 70–80%.

6.6. Effect of dynamical QCD medium on radiative heavy quark energy loss

M. Djordjevic and U. Heinz

The computation of radiative energy loss in a dynamically screened QCD medium is a key ingredient for obtaining reliable predictions for jet quenching in ultra-relativistic heavy ion collisions. We calculate, to first order in the number of scattering centers, the energy loss of a heavy quark traveling through an infinite and time-independent QCD medium consisting of dynamical constituents. We show that the result for a dynamical medium is almost twice that obtained previously for a medium consisting of randomly distributed static scattering centers. A quantitative description of

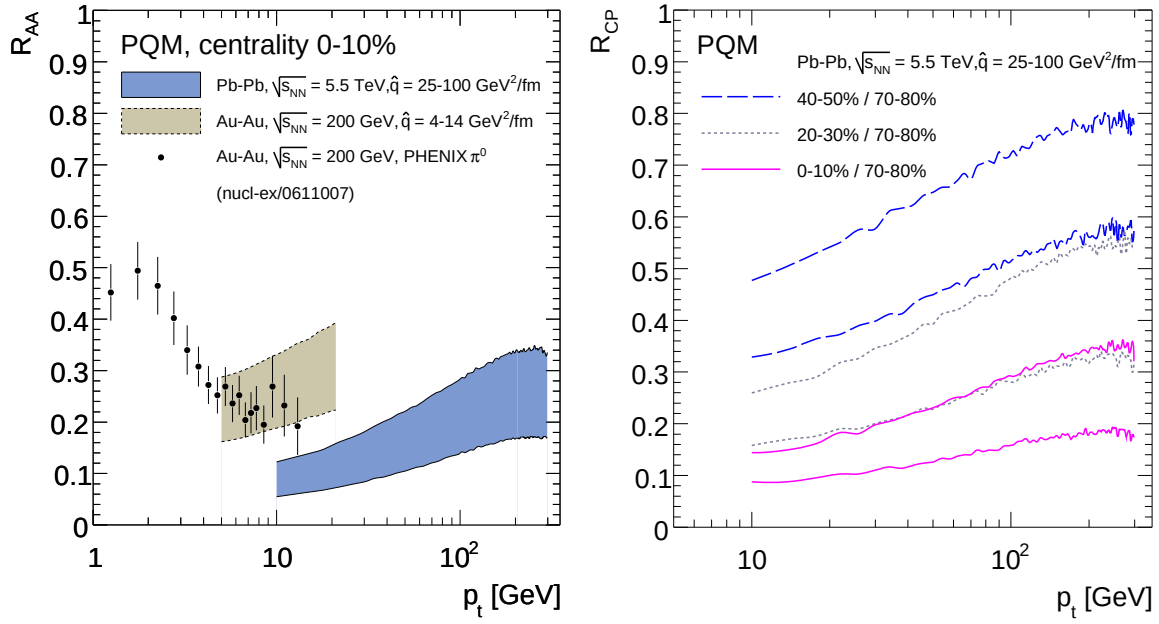

Figure 79: Left: $R_{\mathrm{AA}}(p_T)$ for central Pb–Pb collisions at $\sqrt{s_{\mathrm{NN}}} = 5.5$ TeV and central Au–Au collisions at $\sqrt{s_{\mathrm{NN}}} = 200$ GeV. The PHENIX π^0 data are shown with statistical errors only and they have a 10% normalization systematic error [233]. Right: $R_{\mathrm{CP}}(p_T)$ for Pb–Pb collisions at $\sqrt{s_{\mathrm{NN}}} = 5.5$ TeV.

jet suppression in RHIC and LHC experiments thus must correctly account for the dynamics of the medium's constituents.

Heavy flavor suppression is considered to be a powerful tool to study the properties of a QCD medium created in ultra-relativistic heavy ion collisions [234]. The suppression results from the energy loss of high energy partons moving through the plasma [235]. Therefore, the reliable computations of heavy quark (collisional and radiative) energy loss mechanisms are essential for the reliable predictions of jet suppression.

However, currently available heavy quark radiative energy loss studies suffer from one crucial drawback: The medium induced radiative energy loss is computed in a QCD medium consisting of randomly distributed but static scattering centers ("static QCD medium"). Within such approximation, the collisional energy loss is exactly zero, which is contrary to the recent calculations [236] that showed that the collisional contribution is important and comparable to the radiative energy loss. Due to this, it became necessary to obtain the heavy quark radiative energy loss in a dynamical QCD medium, and to test how good is the static approximation in these calculations.

In this proceeding, we report on a first important step, the calculation of heavy quark radiative energy loss in an infinite and time-independent QCD medium consisting of dynamical constituents. By comparing with the static medium calculation this permits us to qualitatively assess the importance of dynamical effects on radiative energy loss.

We compute the medium induced radiative energy loss for a heavy quark to first (lowest) order in number of scattering centers. To compute this process, we consider the radiation of one gluon induced by one collisional interaction with the medium. In distinction to the static case, we take into account that the collisional interactions are exhibited with dynamical (moving) medium partons. To simplify the calculations, we consider an infinite QCD medium and assume that the on-shell heavy quark is produced at time $x_0 = -\infty$, i.e. we consider the Bethe-Heitler limit. The calculations were performed by using two Hard-Thermal Loop approach, and are presented in [237]. As the end result, we obtained a closed expression for the radiative energy loss in dynamical QCD medium. This result allows us to compare the radiative energy loss in dynamical and static QCD medium, from which we can observe two main differences. First, there is an $O(15\%)$ decrease in the mean free path which increases the energy loss rate in the dynamical medium by $O(20\%)$. Second, there is a change in the shape and normalization of the emitted gluon spectrum. This second difference leads to an additional significant increase of the heavy quark energy loss rate and of the emitted gluon radiation spectrum by about 50% for the dynamical QCD medium. The numerical results are briefly discussed below.

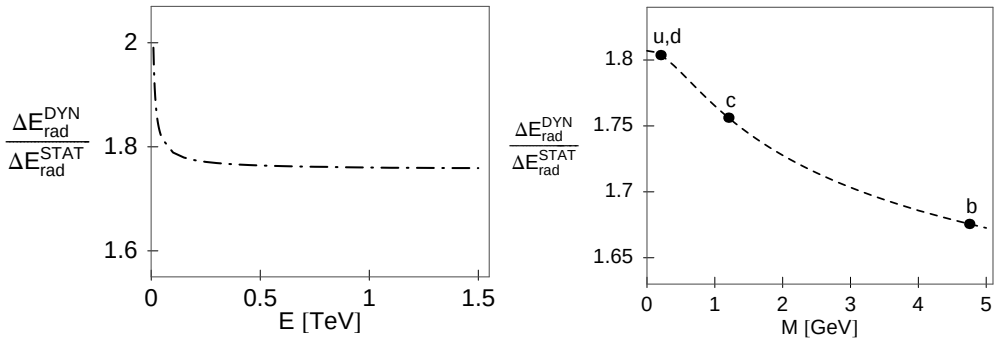

Figure 80: *Left panel:* Ratio of the fractional radiative energy loss in dynamical and static media for charm quarks as a function of initial quark energy E. *Right panel:* Asymptotic value of the radiative energy loss ratio for high energy quarks as a function of their mass, with marks indicating the light, charm and bottom quarks. For the parameter values, see [237].

Left panel of the Fig. 80 shows the energy loss ratio between dynamical and static media for charm quark under the LHC conditions. We see that the ratio is almost independent of the momentum p of the fast charm quark, saturating at $\simeq 1.75$ above $p \gtrsim 100\,\mathrm{GeV}$ and being even somewhat larger at smaller momenta. The dynamical enhancement persists at constant level to the largest possible charm quark energies. Therefore, we can conclude that there is no quark energy domain where the assumption of static scatterers in the medium becomes a valid approximation. Further, the mass of the fast quark plays only a minor role for its energy loss. The right panel in Fig. 80 shows the asymptotic energy loss ratio for very high energy quarks as a function of the quark mass. While the dynamical enhancement is largest for light quarks, the difference between light and bottom quarks is only about 15%, and b quarks still suffer about 70% more energy loss in a dynamical medium than in one with static scattering centers.

In summary, we obtained an important qualitative conclusion that the constituents

of QCD medium can *not* be approximated as static scattering centers in the energy loss computations. Therefore, the dynamical effects have to be included for the reliable prediction of radiative energy loss and heavy flavor suppression in the upcoming high luminosity RHIC and LHC experiments.

6.7. Charged hadron $R_{\rm AA}$ as a function of p_T at LHC

T. Renk and K. J. Eskola

We compute the nuclear suppression factor $R_{\rm AA}$ for charged hadrons within a radiative energy loss picture using a hydrodynamical evolution to describe the soft medium inducing energy loss. A minijet + saturation picture provides initial conditions for LHC energies and leading order perturbative QCD (LO pQCD) is used to compute the parton spectrum before distortion by energy loss.

We calculate the suppression of hard hadrons induced by the presence of a soft medium produced in central Pb-Pb collisions at $\sqrt{s_{\rm NN}} = 5.5$ TeV at the LHC. Note that this prediction depends on knowledge of the medium. In the present calculation, the medium evolution is likewise predicted and has to be confirmed before the suppression can be tested. Note further that the calculation is only valid where hadron production is dominated by fragmentation and that it cannot be generalized to the suppression of jets since the requirement of observing a hard hadron leads to showers in which the momentum flow is predominantly through a single parton. This is not so for jets in which the momentum flow is shared on average among several partons (which requires a different framework).

We describe the soft medium evolution by the boost-invariant hydrodynamical model discussed in [31] where the initial conditions for LHC are computed from perturbative QCD+saturation [74]. Our calculation for the propagation of partons through the medium follows the BDMPS formalism for radiative energy loss using quenching weights [232]. Details of the implementation can be found in [238].

The probability density $P(x_0, y_0)$ for finding a hard vertex at the transverse position $\mathbf{r_0} = (x_0, y_0)$ and impact parameter $\mathbf{b}$ is given by the normalized product of the nuclear profile functions. We compute the energy loss probability $P(\Delta E)_{\rm path}$ for any given path from a vertex through the medium by evaluating the line integrals

$$\omega_c(\mathbf{r_0}, \phi) = \int_0^\infty {\rm d}\xi\, \xi \hat{q}(\xi) \quad \text{and} \quad \langle \hat{q} L \rangle (\mathbf{r_0}, \phi) = \int_0^\infty {\rm d}\xi\, \hat{q}(\xi).$$

Along the path where we assume the relation

$$\hat{q}(\xi) = K \cdot 2 \cdot \epsilon^{3/4}(\xi)(\cosh\rho - \sinh\rho\cos\alpha)$$

between the local transport coefficient $\hat{q}(\xi)$, the energy density ϵ and the local flow rapidity ρ as given in the hydrodynamical model. The angle α is between flow and parton trajectory. We view the constant K as a tool to account for the uncertainty in the selection of α_s and possible non-perturbative effects increasing the quenching power of the medium (see [238]) and adjust it such that pionic $R_{\rm AA}$ for central Au-Au collisions at RHIC is described. The result for LHC is then an extrapolation with K fixed.

Using the numerical results of [232], we obtain $P(\Delta E;\omega_c,R)_{\rm path}$ for ω_c and $R = 2\omega_c^2/\langle\hat{q}L\rangle$. From this distribution given a single path, we can define the averaged energy loss probability distribution $P(\Delta E)\rangle_{T_{\rm AA}}$ by averaging over all possible paths, weighted with the probability density $P(x_0,y_0)$ for finding a hard vertex in the transverse plane.

We consider all partons as absorbed whose energy loss is formally larger than their initial energy. The momentum spectrum of produced partons is calculated in LO pQCD. The medium-modified perturbative production of hadrons is obtained from the convolution

$$\mathrm{d}\sigma^{\mathrm{AA}\to h+X}_{\rm med} = \sum_f \mathrm{d}\sigma^{\mathrm{AA}\to f+X}_{\rm vac} \otimes \langle P(\Delta E)\rangle_{T_{\rm AA}} \otimes D^{\rm vac}_{f\to h}(z,\mu_F^2)$$

with $D^{\rm vac}_{f\to h}(z,\mu_F^2)$ the fragmentation function. From this we compute the nuclear modification factor $R_{\rm AA}$ as

$$R_{\rm AA}(p_T,y) = \frac{\mathrm{d}N^h_{\rm AA}/\mathrm{d}p_T\mathrm{d}y}{T_{\rm AA}(\mathbf{b})\mathrm{d}\sigma^{pp}/\mathrm{d}p_T\mathrm{d}y}.$$

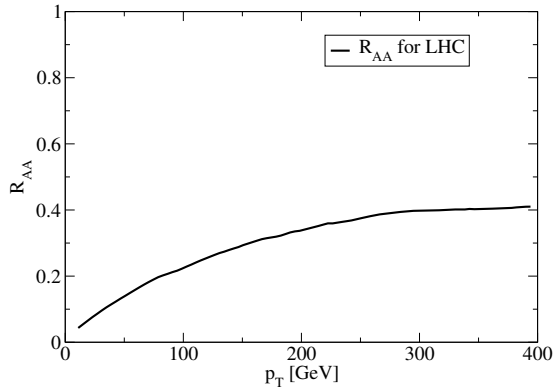

Figure 81: Expectation for the p_T dependence of the nuclear suppression factor $R_{\rm AA}$ for charged hadrons in central Pb-Pb collisions at midrapidity at the LHC.

Figure 81 shows the expected behaviour of $R_{\rm AA}$ with hadronic transverse momentum p_T at midrapidity. On quite general grounds, we expect a rise of $R_{\rm AA}$ with p_T for any energy loss model in which the energy loss probability does not strongly depend on the initial parton energy as more of the shift in energy becomes accessible (see [238]). The detailed form of the rise is then sensitive to the form of $P(\Delta E)\rangle_{T_{\rm AA}}$.

6.8. Nuclear suppression of jets and $R_{\rm AA}$ at the LHC

G. Y. Qin, J. Ruppert, S. Turbide, C. Gale and S. Jeon

The nuclear modification factor $R_{\rm AA}$ for charged hadron production at the LHC is predicted from jet energy loss induced by gluon bremsstrahlung. The Arnold, Moore, and Yaffe [239–241] formalism is used, together with an ideal hydrodynamical model [31].

We present a calculation of the nuclear modification factor $R_{\rm AA}$ for charged hadron production as a function of p_T in Pb+Pb collisions at $\sqrt{s_{\rm NN}}$ = 5.5 TeV in central collisions at

mid-rapidity at the LHC. The net-energy loss of the partonic jets is calculated by applying the Arnold, Moore, and Yaffe (AMY) formalism to calculate gluon bremsstrahlung [239–241]. The details of jet suppression relies on an understanding of the nuclear medium, namely the temperatures and flow profiles that are experienced by partonic jets while they interact with partonic matter at $T \geq T_c$. Our predictions use a boost-invariant ideal hydrodynamic model with initial conditions calculated from perturbative QCD + saturation [31, 74]. It is emphasized that the reliability of this work hinges on the validity of hydrodynamics at the LHC. It has been verified that $R_{\rm AA}$ for π_0 production as a function of p_T as obtained in the same boost-invariant ideal hydrodynamical model adjusted to Au+Au collisions at $\sqrt{s_{\rm NN}} = 0.2$ TeV [31] is in agreement with preliminary data from PHENIX in central collisions at RHIC (and the result is very close to the one obtained in 3D hydrodynamics presented in [242]). In AMY the strong coupling constant α_s is a direct measure of the interaction strength between the jet and the thermalized soft medium and is the only quantity not uniquely determined in the model, once the temperature and flow evolution is fixed by the initial conditions and subsequent hydrodynamical expansion. We found that assuming a constant $\alpha_s = 0.33$ describes the experimental data in most central collisions at RHIC. It is conjectured that α_s should not be changed very much at the LHC since the initial temperature is about twice larger than the one at RHIC whereas α_s is only logarithmically dependent on temperature. We present results for $\alpha_s = 0.33$ and 0.25.

For details of the calculation of nuclear suppression, we refer the reader to [242]. The extension to the LHC once the medium evolution and α_s are fixed is straightforward. The initial jets are produced with an initial momentum distribution of jets computed from pQCD in the factorization formalism including nuclear shadowing effects. The probability density $\mathcal{P}_{\rm AA}(\vec{r}_\perp)$ of finding a hard jet at the transverse position $\vec{r}_\perp$ in central A+A collisions is given by the normalized product of the nuclear thickness functions, $\mathcal{P}_{\rm AA}(\vec{r}_\perp) = T_{\rm A}(\vec{r}_\perp)T_{\rm A}(\vec{r}_\perp)/T_{\rm AA}$ and is calculated for Pb+Pb collisions. The evolution of the jet momentum distribution $P_j(p,t) = {\rm d}N_j(p,t)/{\rm d}p{\rm d}y$ in the medium is calculated by solving a set of coupled rate equations with the following generic form,

$$\frac{{\rm d}P_j(p,t)}{{\rm d}t} = \sum_{ab}\int {\rm d}k\left[P_a(p+k,t)\frac{{\rm d}\Gamma^a_{jb}(p+k,p)}{{\rm d}k{\rm d}t} - P_j(p,t)\frac{{\rm d}\Gamma^j_{ab}(p,k)}{{\rm d}k{\rm d}t}\right],$$

where ${\rm d}\Gamma^j_{ab}(p,k)/{\rm d}{\rm d}t$ is the transition rate for the partonic process $j \to a+b$ which depends on the temperature and flow profiles experienced by the jets traversing the medium. The hadron spectrum ${\rm d}N^h_{\rm AA}/{\rm d}^2p_T{\rm d}y$ is obtained by the fragmentation of jets after their passing through the medium. The nuclear modification factor $R_{\rm AA}$ is computed as

$$R^h_{\rm AA}(\vec{p}_T, y) = \frac{1}{N_{\rm coll}}\frac{{\rm d}N^h_{\rm AA}/{\rm d}^2p_T{\rm d}y}{{\rm d}N^h_{pp}/{\rm d}^2p_T{\rm d}y}.$$

In figure 82 we present a prediction for charged hadron $R_{\rm AA}$ as a function of p_T at mid-rapidity for central collisions at the LHC. We consider that these two values of α_s define a sensible band of physical parameters.

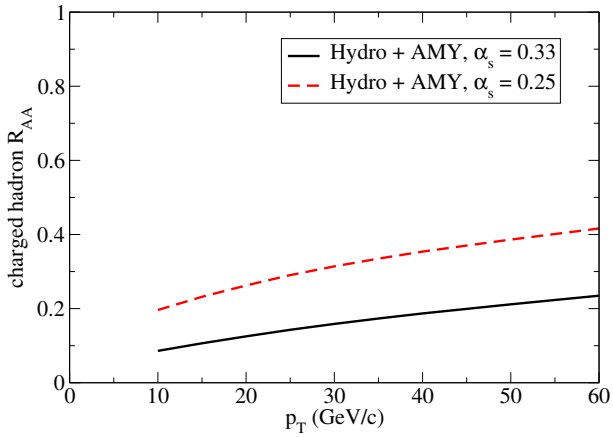

Figure 82: The p_T dependence of the nuclear modification factor $R_{\rm AA}$ for charged hadrons in central Pb+Pb collisions at mid-rapidity at the LHC.

6.9. Perturbative jet energy loss mechanisms: learning from RHIC, extrapolating to LHC

S. Wicks and M. Gyulassy

In many recent papers, collisional energy loss has been found to be of the same order as radiative energy loss for parameters applicable to the QGP at RHIC. As the temperature and jet energy dependence of collisional energy loss differs from that of radiative loss, the interpretation of the results at RHIC affects our extrapolation to predictions for the LHC. We present results from a hybrid collisional plus radiative model, combining DGLV radiative loss with HTL-modified collisional loss, including the fluctuation spectrum for small numbers of collisions and gluons emitted.

Collisional energy loss is an essential component of the physics of high momentum partonic jets traversing the quark-gluon plasma [243, 244]. If we do not properly understand the energy loss mechanisms that are important at RHIC, then we cannot accurately extrapolate in medium density and jet energy to make predictions for the LHC.

WHDG [244] made a first attempt at including both collisional and DGLV radiative energy loss processes. A simple model of the collisional energy loss was used: leading log average loss with a Gaussian distribution around this average, the width given by the fluctuation-dissipation theorem. For the short lengths of interest in the QGP fireball ($\approx 0-6$fm), we expect a jet to undergo only a small number of significant collisions. But the fluctuation spectrum for this will be different than that implemented in the WHDG model: instead, the distinctly non-Gaussian fluctuation in energy loss in 0,1,2,3 collisions is necessary. We present here results and predictions from an improved hybrid radiative plus collisional energy loss model which include a full evaluation of these fluctuations.

A significant uncertainty in the model is the use of a fixed strong coupling constant. In WHDG, a canonical value $\alpha_s = 0.3$ was used, validated by the fitting of the pion $R_{AA}(p_T)$ at RHIC. Here, for a fixed density $dN_g/dy = 1000$, an increased coupling $\alpha_s = 0.4$ is necessary to do the same. In fact, if the collisional component of the energy loss is neglected completely, a further increased coupling of $\alpha_s = 0.5$ would be necessary, as shown in the left-hand side of

Fig. 83. Both values, while large, are still in a possible perturbative kinematical region, and are evaluated with medium densities constrained by the total entropy and multiplicity of the collision.

Is it possible to differentiate between these two scenarios: one including collisional loss, the other neglecting it but increasing the coupling to compensate? Staying with the most simple observables, single particle inclusives in central collisions, we have three dependences to test: the dependence on medium density, jet energy and jet mass. The first is tested by the predicted increased density of the medium to be produced at the LHC (consistency between the left plot and either the central or right plot in Fig. 83). The very high momentum reach available for measurements involving gluon and light quark jets is valuable for the second (radiative versus radiative plus collisional in the central and right hand plots of Fig. 83), and the separate detection of D and B mesons gives us the third (as in Fig. 84). All these together will provide very strong constraints on the energy loss models, even before considering observables beyond the single-particle inclusives.

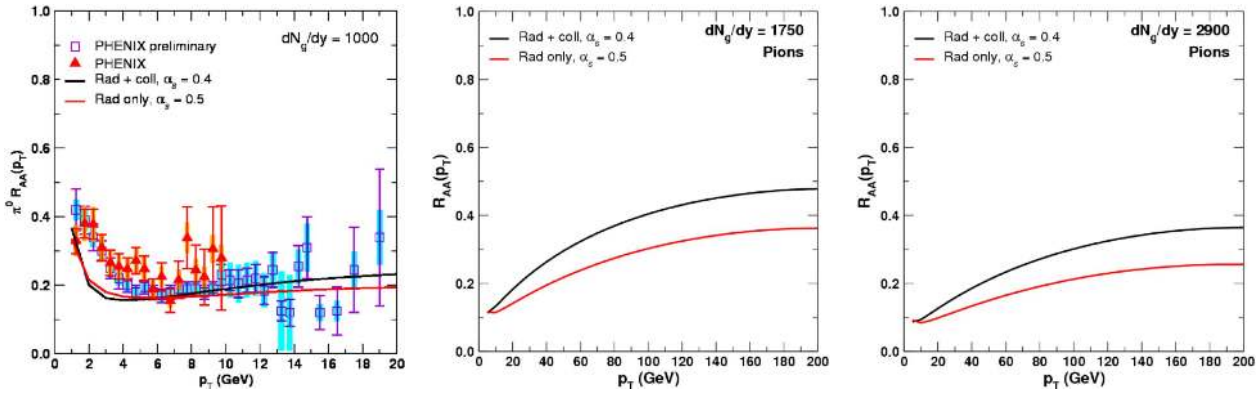

Figure 83: R_{AA} for pions for RHIC (left) and two possible densities at LHC (central and right). The main result, the hybrid radiative plus collisional energy loss model for $\alpha_s = 0.4$, is compared to a radiative energy loss alone model for an increase value of the strong coupling. The increased range in momentum available at the LHC enables the different slopes of the two models to be seen.

There are still significant uncertainties in the energy loss model. The most important kinematic region for evaluation of both the collisional and radiative energy losses are for energy and momentum transfers from the medium greater than μ_D, the Debye mass. This is the region in which we know the least about the physics of the QGP: beyond the HTL region, but before a region of vacuum gluon exchange, especially if processes close to the light-cone of the exchanged gluon are important (as it is for collisional energy loss). This can produce an uncertainty of $\approx 50\%$ for the average collisional loss, which may not be correlated with an uncertainty in the radiative loss. Such large uncertainties affect both the explanation of RHIC data and the extrapolation to the LHC.

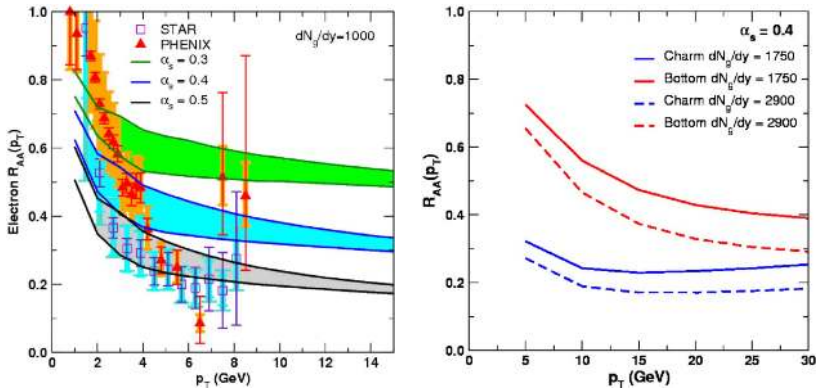

Figure 84: R_{AA} for observable products of heavy quark jets at RHIC (electrons - left) and two possible densities at the LHC (D and B mesons - right). There is considerable uncertainty in the perturbative production of c and b jets. This shows up in the results for electrons at RHIC in the large uncertainty band, ±0.1 or greater - as the ratio of c to b jets is very uncertain. However, the uncertainty in D and B meson R_{AA}s is small (approximately ±0.02) - the different slopes on the individual spectra have very little effect on the meson R_{AA} results.

6.10. Jet evolution in the Quark Gluon Plasma

H. J. Pirner, K. Zapp, J. Stachel, G. Ingelman and J. Rathsman

Jet evolution is calculated in the leading log approximation. We solve the evolution equation for the branching of gluons in vacuum, using a triple differential fragmentation function $D(x, Q^2, p_\perp^2)$. Adding an extra scattering term for evolution in the quark gluon plasma we investigate the influence of the temperature of the plasma on the differential cross section of partons $\mathrm{d}N/\mathrm{d}\ln(1/x)$ in a jet of virtuality $Q^2 = (90\ \mathrm{GeV})^2$. Due to scattering on the gluons in the plasma the multiplicity increases, the centroid of the distribution shifts to smaller x values and the width narrows.

The evolution equation for the transition of a parton i with virtuality Q^2 and momentum $(1, k_\perp)$ into a parton j with momentum $(z, p_\perp)$ can be constructed in leading logarithmic approximation [245]. In a dense medium they are modified due to the possibility that the parton is scattered. The scatterings change the transverse momentum of the leading fast parton by giving it $\vec{q}_\perp$ kicks, but they do not change the mass scale or virtuality of the fast parton. The lifetime of a virtual parton can be estimated as $\mathrm{d}\tau = E/Q_0^2(\mathrm{d}Q^2/Q^2)$ using the uncertainty principle (E is the parton energy and Q_0^2 is the infrared scale). Evolving along a straight line path in a homogeneous plasma with a density of gluons n_g we obtain a modified evolution equation

$$
\begin{aligned}
&Q^2\frac{\partial D_i^j(z,Q^2,\vec{p}_\perp)}{\partial Q^2} = \\
&\frac{\alpha_s(Q^2)}{2\pi}\int_z^1\frac{\mathrm{d}u}{u}P_i^r(u,\alpha_s(Q^2))\frac{\mathrm{d}^2\vec{q}_\perp}{\pi}\delta\left(u(1-u)Q^2-\frac{Q_0^2}{4}-q_\perp^2\right)D_r^j\left(\frac{z}{u},Q^2,\vec{p}_\perp-\frac{z}{u}\vec{q}_\perp\right)\\
&\quad+S(z,Q^2,\vec{p}_\perp)
\end{aligned}
$$

with the scattering term $S(z, Q^2, p_\perp)$

$$S(Q^2, \vec{p}_\perp) = \frac{zEn_g}{Q_0^2} \int_z^1 \mathrm{d}w \int \mathrm{d}^2\vec{q}_\perp \frac{\mathrm{d}\sigma_i^r}{\mathrm{d}^2\vec{q}_\perp} \left[D_r^j(w, Q^2, \vec{p}_\perp - w\vec{q}_\perp) - D_r^j(z, Q^2, \vec{p}_\perp) \right] \delta\left(w - z - \frac{q_\perp^2}{2m_g E} \right).$$

The scattering term includes the probability for scattering into and out of the $p_\perp$ bin as well as the energy loss of the parton. The gluon mass in the plasma m_g is related [246] to the Debye mass $m_g = 1/2m_\mathrm{D}$.

There is an analytic solution for the $p_\perp$ integrated equation restricted to gluons, which give the dominant contribution to the multiplicity. The solution can be found via Mellin transformation in a similar fashion as in vacuum [247], the running of the coupling is taken into account.

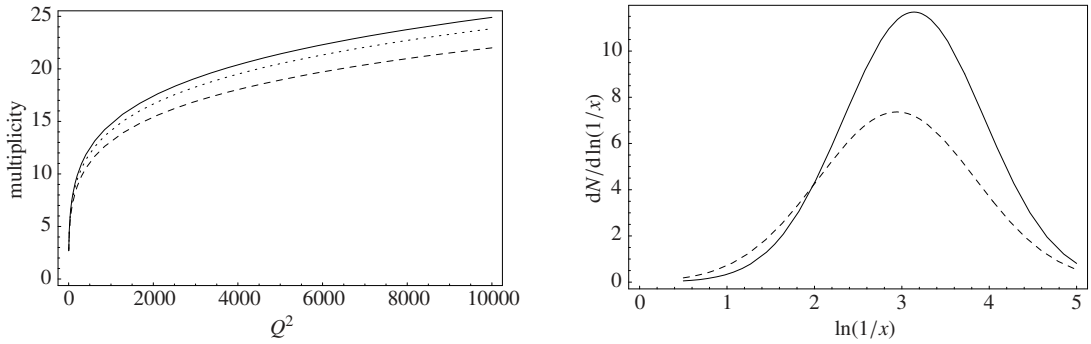

Figure 85: LHS: Multiplicity of two jets with invariant mass Q^2 in vacuum (dashed line), at $T = 0.8$ GeV (dotted line) and at $T = 1.0$ GeV (full line)
RHS: Differential multiplicity $\mathrm{d}N/\mathrm{d}\ln(1/x)$ of jet particles inside a jet with invariant mass $Q^2 = (90\ \mathrm{GeV})^2$ in vacuum (dashed line) and at $T = 1.0$ GeV (full line)

One finds an increase of the multiplicity with temperature and a shift of the centroid of the $\ln(1/x)$ distribution towards smaller x, see figure 85. The width of the distribution, however, becomes smaller. It remains to be studied in vacuum how the choice of the parameters can be optimized to the LEP data, for simplicity the above curves are calculated for $\Lambda_\mathrm{QCD} = 250$ MeV. It is well known that in the evolution equation the QCD scale parameter may well be adjusted. Concerning the effects of the plasma, the form of the cross section and its dependence on $\alpha_s(Q^2)$ has to be further investigated. The results look encouraging and serve as an analytical model with which numerical Monte Carlo calculations can be compared.

There has been a calculation of jet evolution in the modified leading log approximation [248] which has produced similar shapes for the differential multiplicity distribution. The advantage of our calculation is that it takes into account the scattering term explicitly and therefore gives results which depend on the plasma properties. The equation can also be used to investigate the $p_\perp$ broadening of the parton in the medium, since our input function contains the transverse momentum as an extra variable explicitly.

Note added in proof: The calculation described in the text has been undergoing several changes during the last months. Therefore we refer to a forthcoming publication where these

improvements are included.

6.11. Pion and Photon Spectra at LHC

S. Jeon, I. Sarcevic and J. Jalilian-Marian

Using simple modification of jet fragmentation function that is tuned to reproduce the RHIC π^0 data, we had previously predicted photon production at RHIC which is confirmed by recent PHENIX data. Using the same parameter set, we predict hight p_T pion and prompt photon spectra in Pb-Pb collisions at LHC.

In perturbative QCD, the inclusive cross section for pion production in a hadronic collision is given by:

$$E_\pi \frac{\mathrm{d}^3\sigma}{\mathrm{d}^3 p_\pi}(\sqrt{s}, p_\pi) = \int \mathrm{d}x_a \mathrm{d}x_b \mathrm{d}z \sum_{i,j} F_i(x_a, Q^2) F_j(x_b, Q^2) D_{c/\pi}(z, Q_f^2) E_\pi \frac{\mathrm{d}^3\hat{\sigma}_{ij\to cX}}{\mathrm{d}^3 p_\pi}$$

where i and j label hadrons or nuclei and a, b, c label partons.

In heavy-ion collisions, one needs to include nuclear effects. In our model, we take the parton distribution function for a nucleus to be

$$F_{a/A}(x, Q^2, b_t) = T_A(b_t)\, S_{a/A}(x, Q^2)\, F_{a/N}(x, Q^2)$$

where T_A is the nuclear thickness function and $S_{a/A}$ is the shadowing function (we use EKS98 parametrization).

Unfortunately, the interaction of parton-medium cannot be calculated within perturbative QCD, but need to be modeled. The purpose of our model [249–251] is to be as simplistic as possible so that the essential nature of the energy loss process can manifest. To achieve this goal, we modify the fragmentation function in the following way [252]

$$z D_{c/\pi}(z, \Delta L, Q^2) = \sum_{n=0}^{N} P_a(n) z_n^a D^0_{c/\pi}(z_n^a, Q^2) + \langle n_a \rangle z'_a D^0_{g/\pi}(z'_a, Q_0^2),$$

where $z_n^a = z/(1 - n\epsilon_a/E_T)$, $z'_a = zE_T/\epsilon_a$, N is the maximum number of collisions for which $z_n^a \le 1$ and $D^0_{c/\pi}$ is the hadronic fragmentation function. The second term comes from the emitted gluons each having energy ϵ_a on the average. The average number of scatterings within a distance ΔL is $\langle n_a \rangle = \Delta L/\lambda_a$. We take $\lambda_a = 1$ fm and $\Delta L = R_A$. $P_a(n)$ is the Poisson distribution function with $\langle n \rangle = (\Delta L/\lambda_a)$.

The three energy loss models we use are $\Delta E = 1.0$ GeV (Const) $\Delta E = \sqrt{E_{\mathrm{LPM}} E}$ (LPM) and $\Delta E = \kappa E$ (BH) per collision. For RHIC, BH (Bethe-Heitler) gives best description of π^0 data, and predictions for direct photons using the same energy loss is recently found to be in agreement with PHENIX data [253]. Within the same framework we present our predictions for the LHC.

Photons can be either produced during the primary collision or via fragmentation. The reason that the photon R_{AA} behaves qualitatively differently than that of π^0 is because in this energy range, the direct photons that come out of the primary collisions dominate over the fragmentation photons. Therefore the effect of energy loss is substantially reduced compared to the pion case.

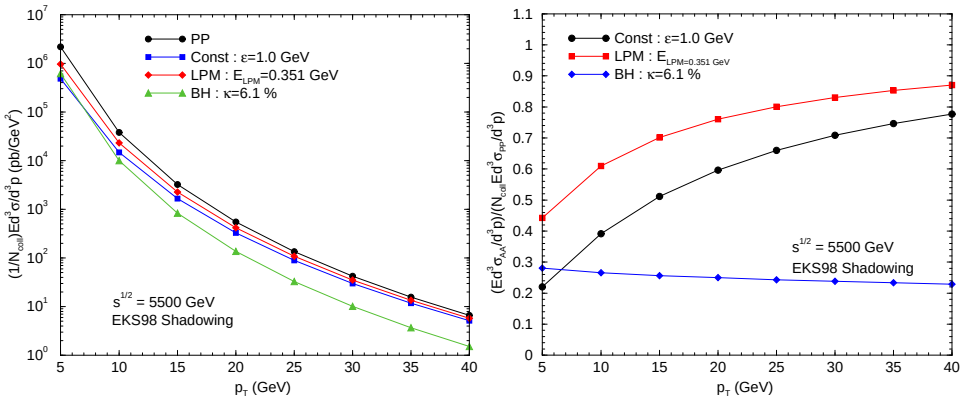

Figure 86: Neutral pion spectrum and $R_{\rm AA}$ at LHC. The energy loss parameter κ is fixed by fitting the RHIC data.

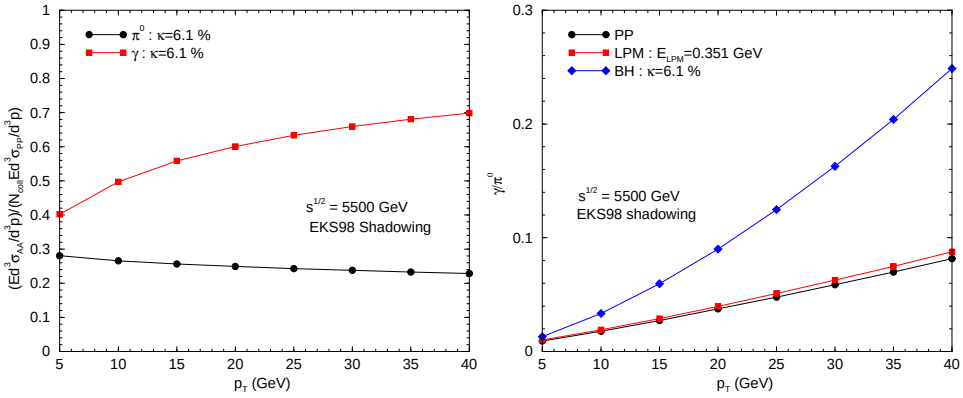

Figure 87: Direct photon $R_{\rm AA}$ and γ/π^0 ratio at LHC.

6.12. Transverse momentum broadening of vector bosons in heavy ion collisions at the LHC

Z.-B. Kang and J.-W. Qiu

We calculate in perturbative QCD the transverse momentum broadening of vector bosons in heavy ion collisions at the Large Hadron Collider (LHC). We predict transverse momentum broadening of W/Z bosons constructed from their leptonic decay channels, which should be a clean probe of initial-state medium effect. We also predict the upper limit of transverse momentum broadening of J/ψ and Υ production as a function of $N_{\rm part}$ at the LHC energy.

Nuclear transverse momentum broadening of heavy vector bosons (γ^*, W/Z, and heavy quarkonia) is defined as a difference between the averaged transverse momentum square measured in nuclear collisions and that measured in collisions of free nucleons,

$$\Delta\langle q_T^2\rangle_{AB} \equiv \langle q_T^2\rangle_{AB} - \langle q_T^2\rangle_{NN} \approx \int dq_T^2\, q_T^2\, \frac{d\sigma_{AB}^{(D)}}{dq_T^2} \Big/ \int dq_T^2\, \frac{d\sigma_{NN}}{dq_T^2}\ . \tag{45}$$

Since single scattering is localized in space, the broadening is a result of multiple parton scattering, and is a good probe for nuclear medium properties. Because the mass scale of the vector bosons is much larger than the characteristic momentum scale of the hot medium, the

broadening is likely dominated by double partonic scattering as indicated in equation (45). The broadening caused by the double scattering can be systematically calculated in terms of high twist formalism in QCD factorization [254, 255].

At the LHC energies, a lot W and Z, and J/ψ and Υ will be produced. Most reconstructed W/Z bosons will come from their leptonic decays. Their transverse momentum broadening is a result of purely initial-state multiple scattering. By calculating the double scattering effect, we obtain [255, 256]

$$\Delta\langle q_T^2\rangle_{pA}^W = \frac{4\pi^2\alpha_s(M_W)}{3}\lambda_W^2 A^{1/3}, \quad \Delta\langle q_T^2\rangle_{pA}^Z = \frac{4\pi^2\alpha_s(M_Z)}{3}\lambda_Z^2 A^{1/3} \tag{46}$$

for hadron-nucleus collisions. The $\lambda^2 A^{1/3}$ in equation (46) was introduced in [254] as a ratio of nuclear four parton correlation function over normal parton distribution. The λ is proportional to the virtuality or transverse momentum of soft gluons participating in the coherent double scattering. For collisions with a large momentum transfer, Q, the λ^2 should be proportional to $\ln(Q^2)$ [256] and the saturation scale Q_s^2 if the active parton x is small. By fitting Fermilab E772 Drell-Yan data, it was found that $\lambda_{\rm DY}^2 \approx 0.01$ GeV^2 at $\sqrt{s} = 38.8$ GeV [255]. From the $\lambda_{\rm DY}^2$, we estimate the value of λ^2 for production of a vector boson of mass M_V at the LHC energy as

$$\lambda_V^2({\rm LHC}) \approx \lambda_{\rm DY}^2 \frac{\ln(M_V^2)}{\ln(Q_{\rm DY}^2)}\left(\frac{M_V/5500}{Q_{\rm DY}/38.8}\right)^{-0.3}, \tag{47}$$

where we used $Q_s^2 \propto 1/x^\delta$ with $\delta \approx 0.3$ [33] and $\sqrt{s_{\rm NN}} = 5500$ GeV for the LHC heavy ion collisions. For an averaged $Q_{\rm DY} \sim 6$ GeV, we obtain $\lambda_{W/Z}^2 \approx 0.05$ at the LHC energy. We can also apply our formula in equation (46) to the broadening in nucleus-nucleus collisions by replacing $A^{1/3}$ by an effective medium length $L_{\rm eff}$. We calculate $L_{\rm eff}$ in Glauber model with inelastic nucleon-nucleon cross section $\sigma_{NN}^{in} = 70$ mb at the LHC energy. We plot our predictions (lower set curves) for the broadening of W/Z bosons in figure 88.

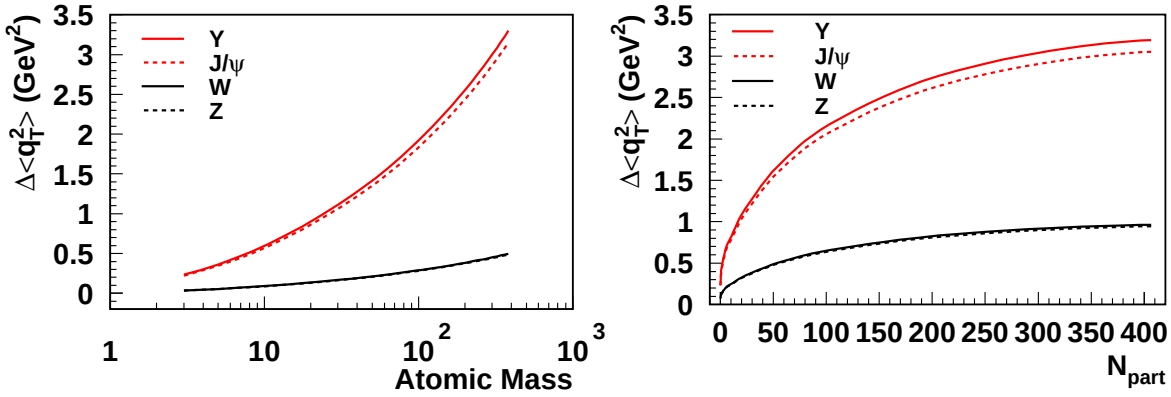

Figure 88: Predicted broadening (maximum broadening) for W and Z (J/ψ and Υ) production in pA (left) and Pb-Pb (right) collisions at $\sqrt{s_{\rm NN}} = 5500$ GeV.

Heavy quark pairs are produced at a distance scale much less than the physical size of heavy quarkonia in high energy collisions. The pairs produced in heavy ion collisions can

have final-state interactions before bound quarkonia could be formed. We found [256] that with both initial- and final-state double scattering, the broadening of heavy quarkonia is close to $2C_A/C_F$ times the Drell-Yan broadening in proton-nucleus collision, which is consistent with existing data [257]. If all soft gluons of heavy ion beams are stopped to form the hot dense medium in nucleus-nucleus collisions, final-state interaction between the almost stationary medium and the fast moving heavy quarks (or quarkonia) of transverse momentum q_T is unlikely to broaden the q_T spectrum, instead, it is likely to slow down the heavy quarks (or quarkonia) [256]. From equation (47). we obtain $\lambda^2_{\mathrm{J}/\psi} \approx 0.035$, and $\lambda^2_{\Upsilon} \approx 0.049$ at the LHC energy; and we predict the maximum broadening for J/ψ and Υ production (upper set curves) in figure 88.

6.13. Nuclear modification factors for high transverse momentum pions and protons at LHC

W. Liu, B.-W. Zhang and C. M. Ko

The inclusion of conversions between quark and gluon jets in a quark-gluon plasma (QGP) via both elastic $qg \leftrightarrow gq$ and inelastic $q\bar{q} \leftrightarrow gg$ reactions [258] has recently been shown to give a plausible explanation for the observed similar p/π^+ and $\bar{p}/\pi^-$ ratios at large transverse momenta in both central Au+Au and pp collisions at $\sqrt{s_{\mathrm{NN}}} = 200$ GeV [223]. Extending this study to LHC, we predict the nuclear modification factor for both protons and pions as well as their ratios at large transverse momenta in central Pb+Pb collisions at $\sqrt{s_{\mathrm{NN}}} = 5.5$ TeV.

For the dynamics of formed QGP at LHC, we assume that it evolves boost invariantly in the longitudinal direction but with an accelerated transverse expansion. Specifically, its volume expands in the proper time τ according to $V(\tau) = \pi R^2(\tau)\tau c$, where $R(\tau) = R_0 + a(\tau - \tau_0)^2/2$ is the transverse radius with an initial value $R_0 = 7$ fm, the QGP formation time $\tau_0 = 0.5$ fm/c, and the transverse acceleration $a = 0.1\ c^2/\mathrm{fm}$. Starting with an initial temperature $T_0 = 700$ MeV, the time dependence of the temperature is obtained from entropy conservation, leading to the critical temperature $T_{\mathrm{C}} = 170$ MeV at proper time $\tau_{\mathrm{C}} = 8.4$ fm/c. For a quark or gluon jet moving through the QGP, the rate for the change in its mean transverse momentum $\langle p_T \rangle$ is given by $\mathrm{d}\langle p_T \rangle/\mathrm{d}\tau \approx \gamma(\langle p_T \rangle, T)\langle p_T \rangle$. The drag coefficient $\gamma(\langle p_T \rangle, T)$ is calculated from two-body scattering with thermal quark and gluon masses and the strong QCD coupling $\alpha_s(T) = g^2(T)/4\pi \approx 2.1\alpha_{\mathrm{pert}}(T)$ from lattice calculations [259]. To take into account the contribution from two-body radiative scattering, we multiply the calculated drag coefficient by a factor $K_E \sim 2$, which is determined from fitting the light meson nuclear modification factor at RHIC. Because of conversion scatterings, the quark or gluon jet can also be converted to a gluon or quark jet with a rate given by corresponding collisional widths, which are also calculated by using the strong QCD coupling constant and multiplying with $K_C = K_E \sim 2$.

Using initial transverse momentum spectra of minijet gluons, quarks, and anti-quarks obtained by multiplying those from the PYTHIA for pp collisions at same energy with the number of binary collisions, we simulate the propagation of jets in the QGP using the Monte

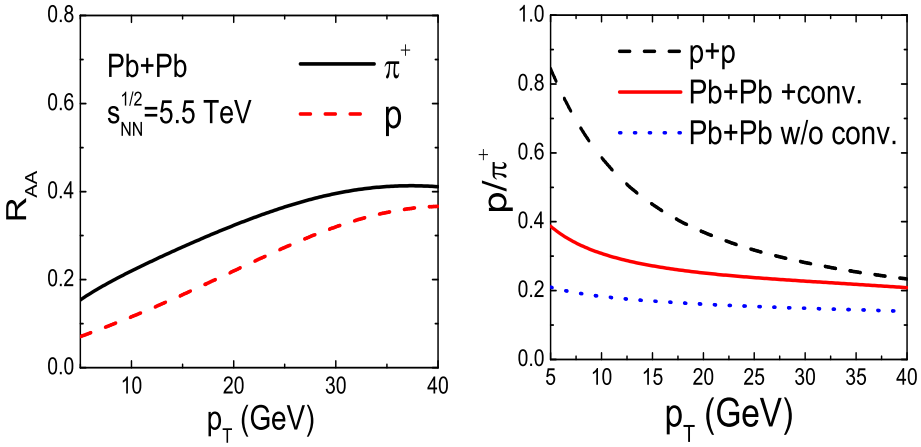

Figure 89: (Color online) Left window: Nuclear modification factor R_{AA} for π^+ (solid line) and proton (dashed line) in central Pb+Pb collisions at $\sqrt{s_{NN}}$ = 5.5 TeV. Right window: p/π^+ ratio without (dotted lines) or with jet conversions (solid lines). Dashed lines correspond to p+p collisions at same energy.

Carlo method with test particles [258]. Resulting charged pion and proton spectra from freeze-out quark and gluon jets are obtained via the AKK fragmentation functions [14]. In the left window of figure 89, we show predicted nuclear modification factor R_{AA} for π^+ and p at large transverse momenta in central Pb+Pb collisions at $\sqrt{s_{NN}}$ = 5.5 TeV at LHC. It is seen that the R_{AA} of pions increases from 0.18 at p_T = 5 GeV/c to 0.4 at p_T = 40 GeV/c due to a smaller drag coefficient at large transverse momenta. The R_{AA} of protons has a similar behavior, but its value is smaller because of stronger suppression of gluon than quark jets. The resulting p/π^+ ratio, shown by the solid line in the right window of figure 89, approaches that in pp collisions at same energy when the transverse momenta become very large. At lower transverse momenta, the p/π^+ ratio in Pb+Pb collisions remains, however, smaller than that in pp collisions, which is different from that in heavy ion collisions at RHIC as a result of the larger ratio of gluon to quark jets at LHC. Without conversions between quark and gluon jets, the p/π^+ ratio decreases by a factor of two as shown by the dotted line.

6.14. Quenching of high-p_T hadrons: Alternative scenario

B .Z. Kopeliovich, I. K. Potashnikova and I. Schmidt

A new scenario, alternative to energy loss, for the observed suppression of high-p_T hadrons observed at RHIC is proposed. In the limit of a very dense medium crated in nuclear collisions the mean free-path of the produced (pre)hadron vanishes, and and the nuclear suppression, R_{AA} is completely controlled by the production length. The RHIC data are well explained in a parameter free way, and predictions for LHC are provided.

The key assumption of the energy loss scenario for the observed suppression of high-p_T hadrons in nuclear collisions is a long length of the quark hadronization which ends up in the

medium. This has got no justification so far and was challenged in [260].

The quark fragmentation function (FF) was calculated in Born approximation in [261]:

$$\frac{\partial D^{Born}_{\pi/q}(z)}{\partial k^2} \propto \frac{1}{k^4}(1-z)^2, \tag{48}$$

where k and z are the transverse and fractional longitudinal momenta of the pion. One can rewrite this in terms of the coherence length $l_c = z(1-z)E/k^2$, where E is the jet energy. Then, $\partial D^{Born}_{\pi/q}(z)/\partial l_c \propto (1-z)$, is l_c independent. Inclusion of gluon radiation leads to the jet lag effect [262] which brings l_c dependence,

$$\frac{\partial D_{\pi/q}(z)}{\partial l_c} \propto (1-\tilde{z})S(l_c, z)\,. \tag{49}$$

Here $\tilde{z} = z[1 + \Delta E(l_c)/E]$ accounts for the higher Fock components of the quark, which are incorporated via the vacuum energy loss $\Delta E(l_c)$ calculated perturbatively with a running coupling. The induced energy loss playing a minor role is added as well. $S(l_c, z)$ is the Sudakov suppression caused by energy conservation. Fig. 90 shows an example for the l_c-distributions calculated for $z = 0.7$ and different jet energies at $\sqrt{s} = 200\,\text{GeV}$.

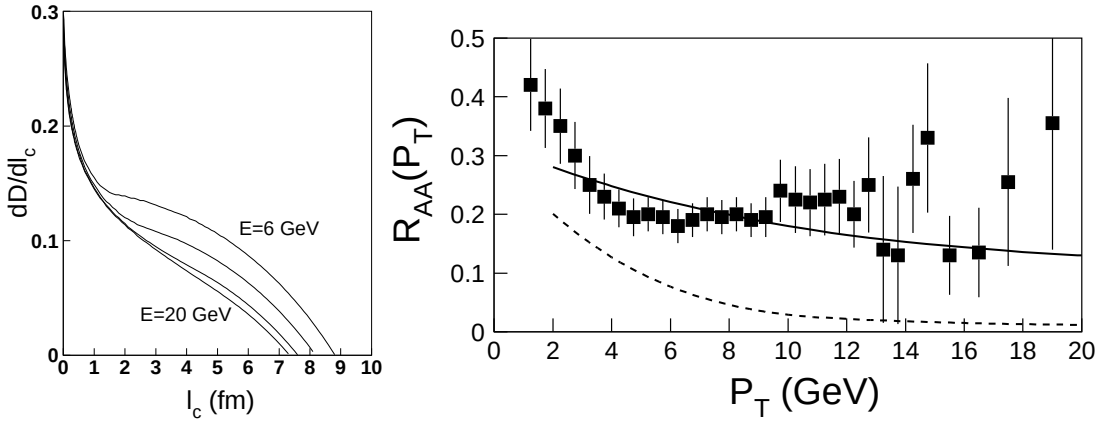

Figure 90: *Left:* $\partial D(z)/\partial l_c$ (in arbitrary units) at jet energies 6, 10, 16, 20 GeV and $z = 0.7$. *Right:* Pion suppression in central AA collisions ($A \sim 200$) at $\sqrt{s} = 200\,\text{GeV}$ (solid) and $\sqrt{s} = 5500\,\text{GeV}$ (dashed). Data are from the PHENIX experiment.

The pre-hadron, a $\bar{q}q$ dipole, may be produced with a rather large initial separation $\langle r_0^2 \rangle \approx 2l_c/E + 1/E^2$ and it keeps expanding.

To keep calculations analytic we consider a central, $b = 0$, collision of identical heavy nuclei with nuclear density $\rho_A(r) = \rho_A \Theta(R_A - r)$. Then we find,

$$R_{AA} = \frac{\langle l_c^2 \rangle}{R_A^2}\left[1 - A\,\frac{L}{\langle l_c \rangle} + B\,\frac{L^2}{\langle l_c^2 \rangle}\right], \tag{50}$$

where the effective absorption length has the form, $L^3 = 3p_T/(8\rho_A^2 R_A X)$, and X includes the unknown density of the medium and is to be fitted to data on R_{AA}. However. if the medium is very dense, i.e. X is large, the last two terms in (50) can be neglected, and we can *predict* R_{AA},

$$R^h_{AA} = \frac{\langle l_c^2 \rangle}{R_A^2}. \tag{51}$$

With this expression we calculated R_{AA} at the energies of RHIC and LHC and in fig. 90 (right). This parameter free result well agrees with the data supporting the assumption that the medium is very dense. Summarizing:

- The A-dependence, eq. (51), predicts $R_{AA} \approx 0.42$ for $Cu-Cu$ confirmed by data.
- Vacuum radiation which depends only on the current trajectory should be flavor independent. This fact and the above consideration explains the strong suppression for heavy flavors observed at RHIC.
- Since the strength of absorption does not affect R_{AA}, eq. (51), a single hadron and a pair of hadrons should be suppressed equally.
- The observed suppression R_{AA} may not contain much information about the medium properties, except it is very dense.

6.15. Expectations from AdS/CFT for Heavy Ion Collisions at the LHC

H. Liu, K. Rajagopal and U. A. Wiedemann

We summarize results obtained by use of the AdS/CFT correspondence for jet quenching and quarkonium dissociation, and we discuss the resulting expectations for heavy ion collisions at the LHC.

The AdS/CFT correspondence maps nonperturbative problems in a large class of strongly coupled non-abelian gauge theories onto calculable problems in dual gravity theories. The gravity dual of Quantum Chromodynamics is not known. However, one finds many commonalities amongst the quark-gluon plasmas in large classes of strongly coupled non-abelian thermal gauge theories, independent of their significantly differing microscopic degrees of freedom and interactions. Since these results are generic and do not seem to depend on microscopic features of the theory such as its particle content at weak coupling, one may expect that they are shared by QCD. Where this can be tested against QCD lattice results, the qualitative agreement is fair (see Ref. [216]). However, many measurements in heavy ion collisions involve strong coupling and real-time dynamics, where lattice QCD results are not available or in their infancy. The practitioner faces the uncomfortable choice of calculating either with inappropriate (e.g. perturbative) techniques in QCD, or using appropriate strong coupling techniques but working in a class of gauge theories that may not include QCD itself and seeking universal commonalities. We report on two results from the latter approach.

6.15.1. Jet quenching In QCD itself, the jet quenching parameter $\hat{q}$ has not been calculated in the strong coupling regime. For the $\mathcal{N} = 4$ SYM theory, it has been calculated for large t'Hooft coupling $\lambda = g^2 N_c$ by use of the AdS/CFT correspondence [263]:

$$\hat{q}_{SYM} = \frac{\pi^{3/2}\Gamma(3/4)}{\Gamma(5/4)} \sqrt{\lambda} T^3 \,. \tag{52}$$

If one relates this to QCD by fixing $N_c = 3$ and $\alpha_{SYM} = .5$, then $\hat{q}_{SYM} = 32.7\, T^3 = 4.5\ \mathrm{GeV}^2/\mathrm{fm}$ at $T = 300$ MeV. This shows that a medium characterized by a momentum scale T can give

rise to an apparently large quenching parameter, significantly larger than T^3. For a certain infinite class of theories with gravity dual, one finds that the quenching parameter scales with the square root of the entropy density [263]. Assuming that QCD follows this systematic, one finds

$$\hat{q}_{QCD} = \sqrt{\frac{s_{QCD}}{s_{N=4}}}\,\hat{q}_{N=4} = \sqrt{\frac{47.5}{120}}\,\hat{q}_{N=4} \simeq 0.63\,\hat{q}_{N=4}\,. \tag{53}$$

In extrapolating from RHIC to LHC, we assume that the change in $\hat{q}$ is dominated by the change in T^3, see eq. (52). In the presence of expansion, the relevant temperature T at RHIC and at the LHC must be compared at the *same* time τ. This can be seen, e.g., in a Bjorken expansion scenario in which $T(\tau) = T_0\,(\tau_0/\tau)^{1/3}$. The time-averaged $\overline{\hat{q}} = (2/L^2)\int_0^L d\tau\,\tau\,\hat{q}(\tau)$, which determines parton energy loss and which is the quantity that has been extracted by comparison with RHIC data, is then $\overline{\hat{q}} \propto (2\tau_0/L)T_0^3 = (2\tau/L)T(\tau)^3$, independent of the reference time τ_0. Since the volume of the collision region at early times depends only on the nuclear overlap and is energy independent, we can assume that at any particular τ, $T^3_{\rm LHC}/T^3_{\rm RHIC} = (dN_{\rm ch}^{\rm LHC}/d\eta)/(dN_{\rm ch}^{\rm RHIC}/d\eta)$ and hence make the prediction $\hat{q}_{\rm LHC} = \hat{q}_{\rm RHIC}(dN_{\rm ch}^{\rm LHC}/d\eta)/(dN_{\rm ch}^{\rm RHIC}/d\eta)$.

6.15.2. Quarkonium suppression In lattice QCD, the temperature dependent potential between a heavy quark and anti-quark has been calculated as a function of their separation L. At finite temperature, this potential is screened above a length $L_s \sim 0.5/T$ (see references in [264]). These studies indicate that the J/Ψ dissociates at a temperature between $1.5\,T_c$ and $2.5\,T_c$. For $N = 4$ SYM theory, one finds $L_s \sim 0.277/T$. In contrast to QCD, the calculation in theories with gravity dual can be done also for heavy quark-antiquark pairs which are moving with a velocity v through the heat bath. One finds that the screening length decreases with increasing $\gamma = \sqrt{1/(1-v^2)}$ [264]:

$$L_s(v,T) \simeq L_s(0,T)/\sqrt{\gamma} \longrightarrow T_{\rm diss}(v) \simeq T_{\rm diss}(0)/\sqrt{\gamma}\,. \tag{54}$$

So, bound states with a dissociation temperature $T_{\rm diss}(v)$ will survive if at rest in a medium at temperature T if $T_{\rm diss}(0) > T$. Yet, they will dissociate if they move sufficiently fast through the medium, such that $T_{\rm diss}(v) < T$. LHC data may test this prediction, depending on the quarkonium formation mechanism. Let us consider three possibilities for the latter: i) A parent quark (c or b) propagates through the medium but the quarkonium forms later, outside the medium. ii) As in (i) but with a parent gluon. iii) A quarkonium bound state forms (from either a parent quark or gluon) and propagates through the medium. These three scenarios can be discriminated as follows: i) The nuclear modification factor of quarkonium is the same as that of open charm or beauty, which are known to be dominated by quark parents. It is the same for all quarkonium bound states. ii) The nuclear modification factor of quarkonium is the same as that of light hadrons, which at the LHC are dominated by gluon parents. Again, all bound states are equally suppressed. iii) The nuclear modification factor will differ for different bound states, since they will dissociate for different values of the transverse momentum p_T. The hierarchy in the p_T-dependence of the quarkonium suppression pattern would test (54). For example, Υ (or J/Ψ) suppression could set in only above some p_T while Υ' (or Ψ') are

suppressed even at low p_T. Details of the formation mechanism cancel in ratios like Υ/Υ', making the p_T-dependent pattern predicted by (54) visible as long as the quarkonia form in the medium.

6.16. High-p_T observables in PYQUEN model

I. P. Lokhtin, A. M. Snigirev and C. Yu. Teplov

Predictions of PYQUEN energy loss model for high-p_T observables at the LHC are discussed. Nuclear modification factors and elliptic flow for hard jets and high-p_T hadrons, medium-modified jet fragmentation function, p_T-imbalance for dimuon tagged jets, high-mass dimuon and secondary J/ψ spectra are calculated for PbPb collisions.

In this paper, the various high-p$_T$ observables in PbPb collisions at $\sqrt{s_{\rm NN}} = 5.5A$ TeV are analyzed in the frame of PYQUEN partonic energy loss model [265]. The pseudorapidity cuts for jets $|\eta^{\rm jet}| < 3$, charged hadrons $|\eta^{\rm h^{\pm}}| < 2.5$ and muons $|\eta^{\mu}| < 2.5$ were applied. The jet energy was determined here as the total transverse energy of the final particles around the direction of a leading particle inside a cone $R = \sqrt{\Delta\eta^2 + \Delta\varphi^2} = 0.5$ (φ is the azimuthal angle).

6.16.1. Nuclear modification factors for jet and high-p_T hadrons The nuclear modification factor is defined as a ratio of particle yields in AA and pp collisions normalized on the number of binary nucleon-nucleon collisions. Figures 91 and 92 show p_T-dependences of nuclear modification factors for inclusive charged hadrons (in central PbPb events triggered on jets with $E_T^{\rm jet} > 100$ GeV) and for jets respectively. The number of entries and the statistical errors correspond to the estimated event rate for one month of LHC run and a nominal integrated luminosity of 0.5 nb^{-1} [266]. The predicted hadron suppression factor slightly increases with p_T(> 20 GeV), from ~ 0.25 at $p_T \sim 20$ GeV to ~ 0.4 at $p_T \sim 200$ GeV. This behaviour manifests the specific implementation of partonic energy loss in the model, rather weak energy dependence of loss and the shape of initial parton spectra. Without event triggering on high-E_T jet(s), the suppression factor is stronger (~ 0.15 at 20 GeV and slightly increasing with p_T up to ~ 0.3 at 200 GeV). The predicted jet suppression factor (due to partial gluon bremsstrahlung out of jet cone and collisional loss) is about 2 and almost independent on jet energy. It is clear that the measured jet nuclear modification factor will be very sensitive to the fraction of partonic energy loss carried out of the jet cone.

6.16.2. Medium-modified jet fragmentation function The "jet fragmentation function" (JFF), $D(z)$, is defined as the probability for a given product of the jet fragmentation to carry a fraction z of the jet transverse energy. Figure 93 shows JFF's in central PbPb collisions with and without partonic energy loss. The number of entries and the statistical errors correspond again to the estimated event rate for one month of LHC run. Significant softening of the JFF (by a factor of ~ 4 and slightly increasing with z) is predicted.

The medium-modified JFF is sensitive to a fraction ε of partonic energy loss carried out of the jet cone. Figure 94 shows the ε-dependences of jet nuclear modification factor $R_{\rm AA}^{\rm jet}$ and

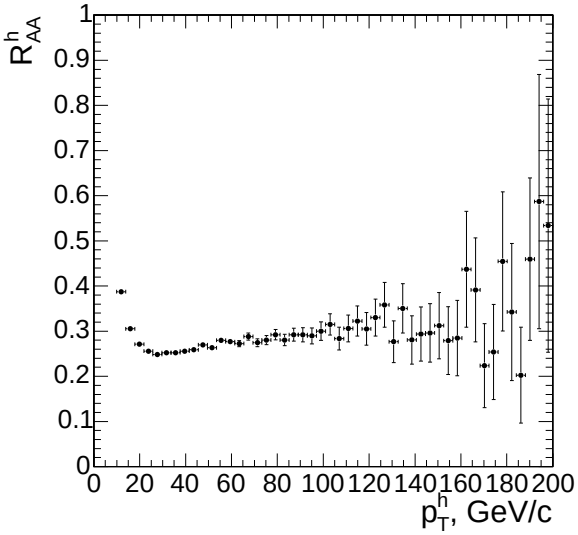

Figure 91: The nuclear modification factor for charged hadrons in central PbPb collisions triggered on jets with $E_T^{\rm jet} > 100$ GeV.

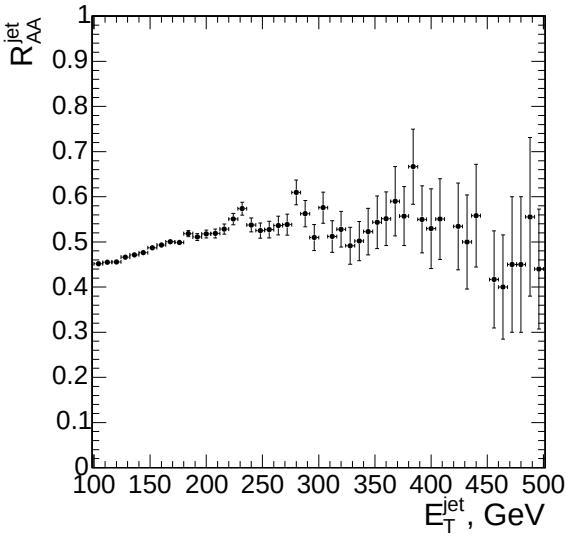

Figure 92: The nuclear modification factor for jets in central PbPb collisions.

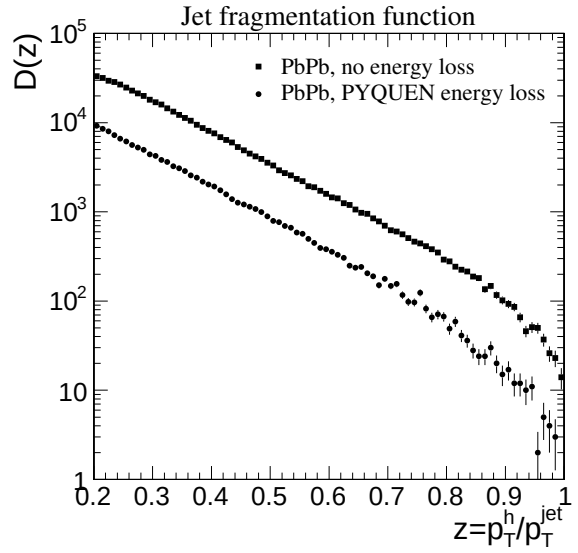

Figure 93: Jet fragmentation function for leading hadrons in central PbPb collisions triggered on jets with $E_T^{\rm jet} > 100$ GeV without (squares) and with (circles) partonic energy loss.

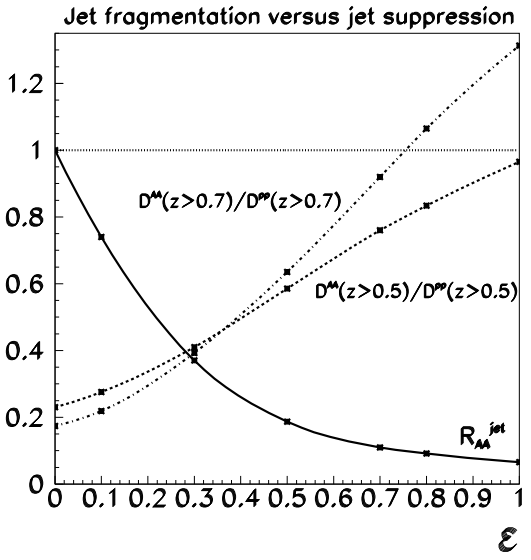

Figure 94: Jet nuclear modification factor (solid curve) and ratio of JFF with loss to JFF without loss (dashed, dash-dotted curves) as a function of ε (see text).

ratio of JFF with energy loss to JFF without loss, $D^{\rm AA}(z > z_0)/D^{\rm pp}(z > z_0)$, for $z_0 = 0.5$ and 0.7. If ε close to 0, then $R^{\rm jet}_{\rm AA} \sim 1$ (there is no jet rate suppression), and JFF softening is maximal. Increasing ε results in stronger jet rate suppression, but effect on JFF softening becomes smaller. Indeed, final jet transverse momentum (which is the denominator in definition of z) decreases in this case without an influence on the numerator of z and, as a consequence, the effect on JFF softening reduces, while the integral jet suppression factor becomes larger. Thus a novel study of the softening of the JFF and suppression of the absolute jet rates can be carried out in order to differentiate between various energy loss mechanisms ("small-angular" radiative loss versus "wide angular" and collisional loss) [267].

Other correlation measurements which also can be useful extracting information about medium-modified jets are jet shape broadening and jet quenching versus rapidity [268] and monojet-to-dijet ratio versus dijet acoplanarity [269].

6.16.3. Azimuthal anisotropy of jet quenching The azimuthal anisotropy of particle spectrum is characterized by the second coefficient of the Fourier expansion of particle azimuthal distribution, elliptic flow coefficient, v_2. The non-uniform dependence of medium-induced partonic energy loss in non-central heavy ion collisions on the parton azimuthal angle φ (with respect to the reaction plane) is mapped onto the final hadron spectra [270, 271]. Figure 95 shows the calculated impact parameter dependence of v_2 coefficient for jets with $E^{\rm jet}_T > 100$ GeV and for inclusive charged hadrons with $p_T > 20$ GeV/c in PbPb events triggered on jets. The absolute values of v_2 for high-p_T hadrons is larger that one's for jets by a factor of $\sim 2-3$. However, the shape of b-dependence of $v^{\rm h}_2$ and $v^{\rm jet}_2$ is similar: it increases almost linearly with the growth of b and becomes a maximum at $b \sim 1.6R_A$ (where R_A is the nucleus radius). After that, the v_2 coefficients drop rapidly with increasing b.

6.16.4. P_T-imbalance in dimuon tagged jet events An important probe of medium-induced partonic energy loss in ultrarelativistic heavy ion collisions is production of a single jet opposite to a gauge boson such as $\gamma^\star/Z^0$ decaying into dileptons. The advantage of such processes is that the mean initial transverse momentum of the hard jet equal to the mean initial/final transverse momentum of boson, and the energy lost by the parton can be estimated from the observed p_T-imbalance between the leading particle in a jet and the lepton pair. Figure 96 shows the difference between the transverse momentum of a $\mu^+\mu^-$ pair from $\gamma^\star/Z^0$ decay, $p_{\rm T}^{\mu^+\mu^-}$, and five times the transverse energy of the leading particle in a jet (since the average fraction of the parent parton energy carried by a leading hadron at these energies is $z \approx 0.2$) for minimum bias PbPb collisions [272]. The cuts, $p_{\rm T}^{\mu^+\mu^-}, E^{\rm jet}_{\rm T} > 50$ GeV/c were applied. Despite the fact that the initial distribution is smeared and asymmetric due to initial-state gluon radiation, hadronization effects, etc., one can clearly see the additional smearing and the displaced mean and maximum values of the $p_{\rm T}$-imbalance due to partonic energy loss. The $p_{\rm T}$-imbalance between the $\mu^+\mu^-$ pair and a leading particle in a jet is directly related to the absolute value of partonic energy loss, and almost insensitive to the form of the angular spectrum of the emitted gluons and to the experimental jet energy resolution [272].

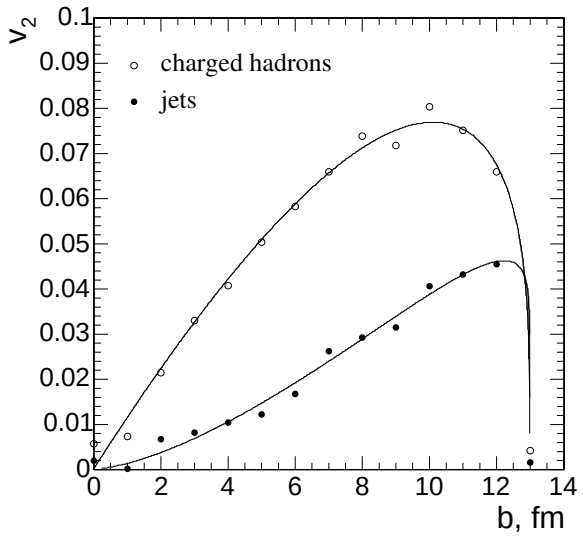

Figure 95: The impact parameter dependence of elliptic flow coefficients $v_2^{\rm jet}$ for jets with $E_T^{\rm jet} > 100$ GeV (black circles) and $v_2^{\rm h}$ for inclusive charged hadrons with $p_T > 20$ GeV/c (open circles) in PbPb events triggered on jets.

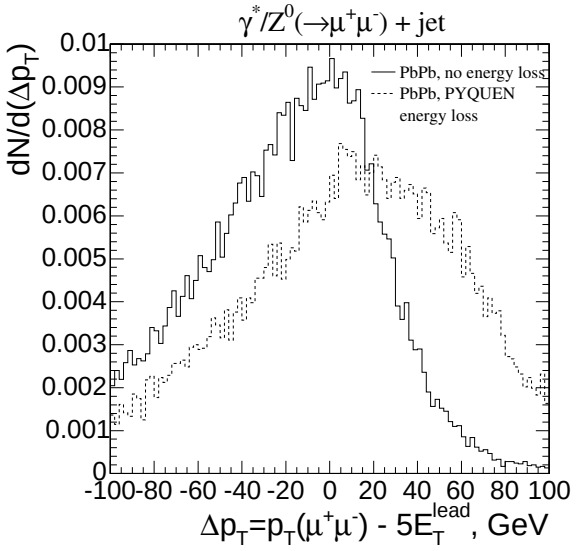

Figure 96: The distribution of the difference between the transverse momentum of a $\mu^+\mu^-$ pair and five times the transverse energy of the leading particle in a jet in PbPb collisions with (dashed histogram) and without (solid histogram) energy loss.

6.16.5. High-mass dimuon and secondary J/ψ spectra While the study of inclusive high-$p_{\rm T}$ jet production in heavy ion collisions provides information on the response of created medium to gluons and light quarks, the study of open heavy flavour production gives corresponding information on massive colour charges. The open charm and bottom semileptonic decays are the main sources of muon pairs in the resonance-free high invariant mass region, $10 < M_{\mu^+\mu^-} < 70$ GeV/c^2 [266]. Other processes which also carry information about medium-induced bottom rescattering are secondary J/ψ production from the B meson decay [273, 274] and muon tagged b-jets [275]. Figures 97 and 98 show the spectra of high-mass $\mu^+\mu^-$ pairs and the $p_{\rm T}$-distributions of the secondary J/ψ's respectively, for minimum bias PbPb collisions with and without energy loss of bottom quarks ($p_{\rm T}^{\mu} > 5$ GeV/c). A factor of around 2.5 suppression for $b\bar{b} \to \mu^+\mu^-$ and 2 for secondary J/ψ would be clearly observed over the initial state nuclear shadowing expected in this kinematic region [273, 274].

6.17. Predictions for LHC heavy ion program within finite sQGP formation time

V. S. Pantuev

Predictions for some experimental physical observables in nucleus-nucleus collisions at LHC energies are presented. I extend the previous suggestion that the retarded jet absorption, at RHIC by time about 2.3 fm/c, in opaque core is a natural explanation of many experimental data. At LHC this time should be inversely proportional to the square root of parton hard scattering density, thus about 2 times shorter than at RHIC, or 1.2 fm/c. Predictions were done for hadrons, including charm

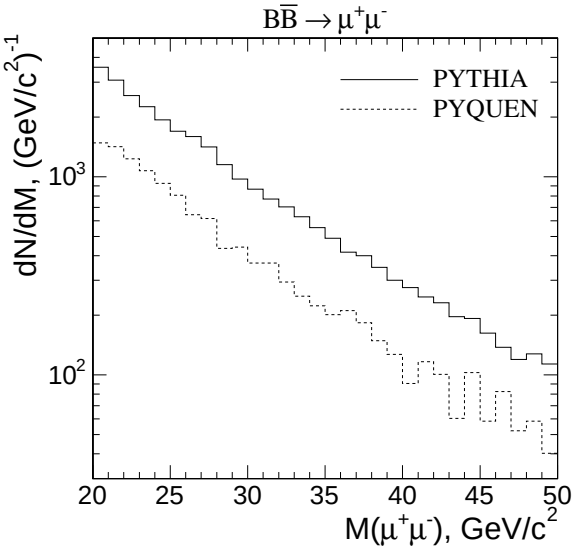

Figure 97: Invariant mass distribution of $\mu^+\mu^-$ pairs from $b\bar{b}$ decays in minimum bias PbPb collisions, with (dashed histogram) and without (solid histogram) bottom quark energy loss.

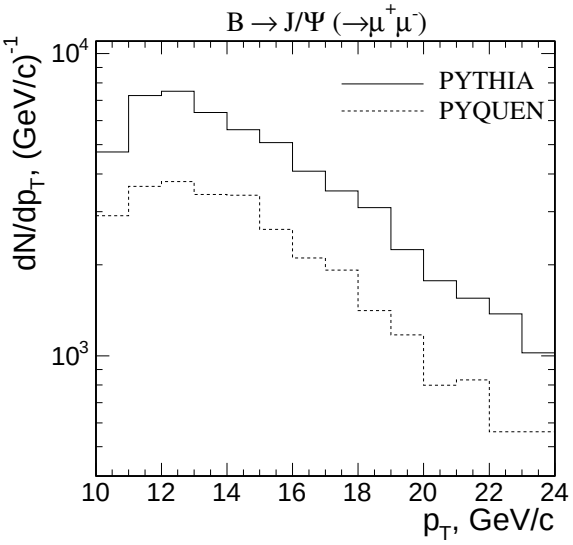

Figure 98: Transverse momentum spectrum of secondary J/ψ in minimum bias PbPb collisions, with (dashed histogram) and without (solid histogram) bottom quark energy loss.

hadrons, with transverse momentum above 5 GeV/c. I calculate nuclear modification factor $R_{\rm AA}$, azimuthal anisotropy parameter v_2, jet suppression $I_{\rm AA}$ for the away side jet and its dependence versus the reaction plane orientation. The system under consideration is Au+Au at central rapidities.

In previous paper [276] I propose a simple model, driven by experimental data, to explain the angular dependence of the nuclear modification factor $R_{\rm AA}$ at high transverse momentum in and out the reaction plane. I introduce one free parameter $L \simeq 2.3$ fm to describe the the thickness of the corona area with no absorption wich was adjusted to fit the experimental data of Au-Au collisions at centrality 50-60%. The model uses realistic Woods-Saxon nuclear density distribution and nicely describes the $R_{\rm AA}$ dependence for all centrality classes. I extract the second Fourier component amplitude, v_2, for high p_T particle azimuthal distribution and found v_2 should be at the level of 11-12% purely from the geometry of the collision with particle absorption in the core. At that time I made a prediction for $R_{\rm AA}$ in Cu+Cu collisions at 200 GeV which, as later was found, is in very good agreement with experimental data. Physical interpretation of the parameter L could be that it is actually retarded jet absorption caused by **the plasma formation time** $T = L/c \simeq 2.3$ fm/c at RHIC, or at least non-trivial response of strongly interacting plasma to fast moving color charge.

From experimental data at 62 GeV center-of-mass beam energy I found that this time should be about 3.5 fm/c. This follows the expectation on the significance of mean distance between the centers with mini jet production (hard scatterings) at particular beam energy. At LHC energy of about 5 TeV we expect $\simeq 1.2$ fm/c formation time [277].

In figure 99 I show predictions for $R_{\rm AA}$ and $I_{\rm AA}$ at central rapidities. As usual, nuclear

modification factor $R_{\rm AA}$ is defined as:

$$R_{\rm AA}(p_T) = \frac{(1/N_{\rm evt})\, {\rm d}^2N^{\rm AA}/{\rm d}p_T{\rm d}\eta}{(\langle N_{\rm binary}\rangle/\sigma^{NN}_{\rm inel})\, {\rm d}^2\sigma^{NN}/{\rm d}p_T{\rm d}\eta},$$

where $\langle N_{\rm binary}\rangle$ is a number of binary nucleon-nucleon collisions at particular centrality class.

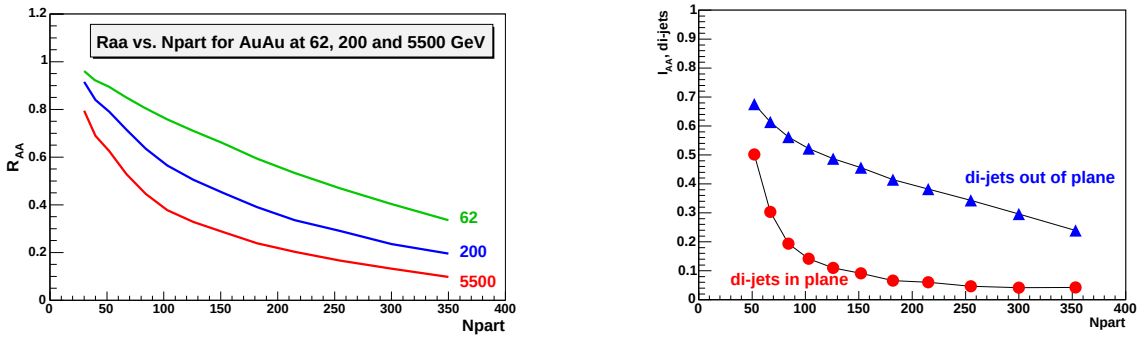

Figure 99: $R_{\rm AA}$, nuclear modification factor, (left) and $I_{\rm AA}$, suppression of away-side jet compared to pp data versus number of participants, right. Hadrons are at transverse momentum 5 to 20 GeV/c. Width of the away side jet was assumed to be $\sigma = 0.22$ radians.

In all cases I consider hadrons (mesons and baryons, including charm) at p_T above 4-5 GeV/c. $R_{\rm AA}(p_T)$ at a such momentum should be independent on p_T, flat distribution at least to 20 GeV/c.

$I_{\rm AA}$ is defined as a ratio of away-side yield per trigger high p_T particle to the similar value from pp collisions. The major feature of this model is the dominant tangential back to back di-jet production from the surface region. Because of that we may expect **significantly larger di-jet production out of the reaction plane**, figure 99, in contrast to punch through jet scenario. Predictions for azimuthal asymmetry parameter v_2 are shown in figure 100.

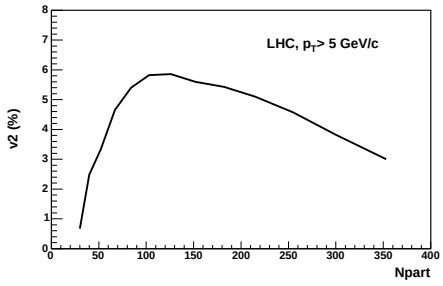

Figure 100: Azimuthal assimetry parameter v_2 for mesons and baryons at transverse momentum between 5 to 20 GeV/c.

6.18. Hadrochemistry of jet quenching at the LHC

S. Sapeta and U. A. Wiedemann

We point out that jet quenching can leave signatures not only in the longitudinal and transverse multiplicity distributions, but also in the hadrochemical composition of the jet fragments. As a theoretical framework, we use the MLLA+LPHD formalism, supplemented by medium-modified splitting functions.

In heavy ion collisions at the LHC, the higher energies of produced jets will facilitate their separation from the soft background. The interactions of jets with the matter produced in these collisions is expected to modify both the longitudinal and transverse jet distributions. In addition, we expect that these interactions affect also the hadrochemical composition of jets.

Within current models of jet quenching, this may be expected, since color is transfered between the projectile and the medium - and a changed color flow in the parton shower can be expected to change the hadronization. More generally, one may imagine that partonic fragments of the jet participate in hadronization mechanisms not available in the vacuum (such as a recombination mechanism, which depends on the density of recombination partners), or that recoil effects kick components of the medium into the jet cone. Also, any exchange of quantum numbers between medium and jet (e.g. baryon number or strangeness) may be reflected in the hadrochemical composition. In the following, we consider a model which does not implement such mechanisms, but considers solely the enhanced parton splitting due to medium effects [278].

To calculate multiplicities of the identified hadrons we use the framework of Modified Leading Logarithmic Approximation (MLLA) [279]. This perturbative approach supplemented by the hypothesis of Local Parton-Hadron Duality (LPHD) was shown to reproduce correctly the single inclusive hadron spectra in jets both in e^+e^- and $pp/p\bar{p}$ collisions. It provides good description not only for the distributions of all charged particles but also for the spectra of identified hadrons such as pions, kaons and protons [280, 281]. Moreover, the dependence on jet opening angle can be implemented. The general form of the multiplicity of hadrons of mass M_h in the jet of energy $E_{\rm jet}$ and opening angle θ_c is given by

$$\frac{dN^h}{d\xi} = K_{\rm LPHD}\, D(\xi, E_{\rm jet}, \theta_c, M_h, \Lambda)\,, \tag{55}$$

where $\xi = \ln 1/x$ and $x = p/E_{\rm jet}$ is the fraction of the jet energy carried by the hadron h. The regularization scale Λ is a parameter of the model.

The medium-modification of jets is formulated within the MLLA formalism [282] by enhancing the singular parts of the LO splitting functions by a factor $1 + f_{\rm med}$. This accounts for the nuclear modification factor at RHIC when $f_{\rm med}$ is of the order of 1, and it provides a model for the distribution of subleading jet fragments.

One result of our studies is shown in Figure 101. We observe a significant difference of the $K^\pm/\pi^\pm$ and $p^\pm/\pi^\pm$ ratios of medium-modified (with $f_{\rm med} = 1$) and 'standard' vacuum fragmenting jets. We have also shown, that Figure 101 remains largely unchanged if the soft

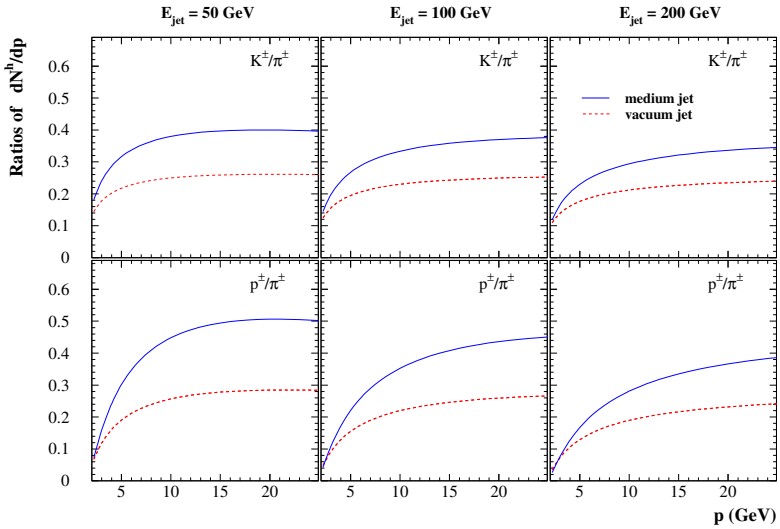

Figure 101: Ratios of kaons and protons to pions in the jets with or without medium modification for jet opening angle $\theta_c = 0.28$ rad. The θ_c-dependence is weak. The kaon multiplicity was in adjusted by a strangeness suppression factor 0.73 as in [281].

background is included in forming the ratio [278].

The precise numerical change of the hadrochemical composition, shown in Figure 101, is model-depement of course. We emphasize, however, that in our model, medium effects are implemented on the partonic level only, and the hadronization mechanism remains unchanged. Nevertheless, the observed change is significant. Thus, our model provides a first example for our expectation, that the hadrochemical composition of jets may be very fragile to medium effects, and provides additional information about the microscopic mechanism underlying jet quenching.

6.19. GLV predictions for light hadron production and suppression at the LHC

I. Vitev

Simulations of neutral pion quenching in Pb+Pb reactions at $s^{1/2} = 5.5$ A.TeV at the LHC are presented to high transverse momentum p_T. At low and moderate p_T, we study the contribution of medium-induced gluon bremsstrahlung to single inclusive hadron production. At the LHC, the redistribution of the lost energy is shown to play a critical role in yielding nuclear suppression that does not violate the participant scaling limit. Energy loss in cold nuclear matter prior to the formation of the QGP is also investigated and shown to have effect on particle suppression as large as doubling the parton rapidity density.

Pb+Pb collisions at the LHC represent the future energy frontier of QGP studies in heavy ion reactions. Energy loss of jets in the final state is calculated in the GLV formalism [184]. Numerical simulations follow the technique outlined in [283] and incorporate the Cronin effect [284]. We have explored the sensitivity of $R_{AA}(p_T)$ to the parton rapidity density in

central nuclear reactions with $dN^g/dy \simeq 2000, 3000$ and 4000. In this work we adhere to a more modest two- to four-fold increase of the soft hadron rapidity density and emphasize that future measurements of jet quenching must be correlated to $dN^g/dy \approx (3/2)dN^{ch}/dy$ [283, 284] to verify the consistency of the phenomenological results. See left panel of Fig. 102. The contribution of the bremsstrahlung gluons to low- and moderate-p_T inclusive particle production at the LHC is shown to be significant. See right panel of Fig. 102.

Energy loss of jets in cold nuclear matter has not been considered before. Recent calculations in the GLV approach show that, in contract to final-state energy loss, the cancellation of the bremsstrahlung in the initial-state is finite [285]. With $\Delta E/E$ ~few %, the observable effect of the bremsstrahlung associated with the multiple soft scattering in nuclei is non-negligible even for very energetic partons in the nuclear rest frame. See left panel of Fig. 103. At the LHC, in central Pb+Pb collisions, the effect of cold nuclear matter energy loss can be as large as doubling the parton rapidity density dN^g/dy mainly due to reduced sensitivity in the final state. See right panel of Fig. 103.

6.20. NLO Predictions for Single and Dihadron Suppression in Heavy-ion Collisions at LHC

E. Wang, X.-N. Wang and H. Zhang

Suppresions of high transverse momentum single and dihadron spectra at LHC are calculated within a next-to-leading order perturbative QCD model with energy parton energy loss.

The predictions presented here are calculated within a NLO pQCD Monte Carlo based program [286]. For the study of large p_T single and dihadron production in $A+A$ collisions,

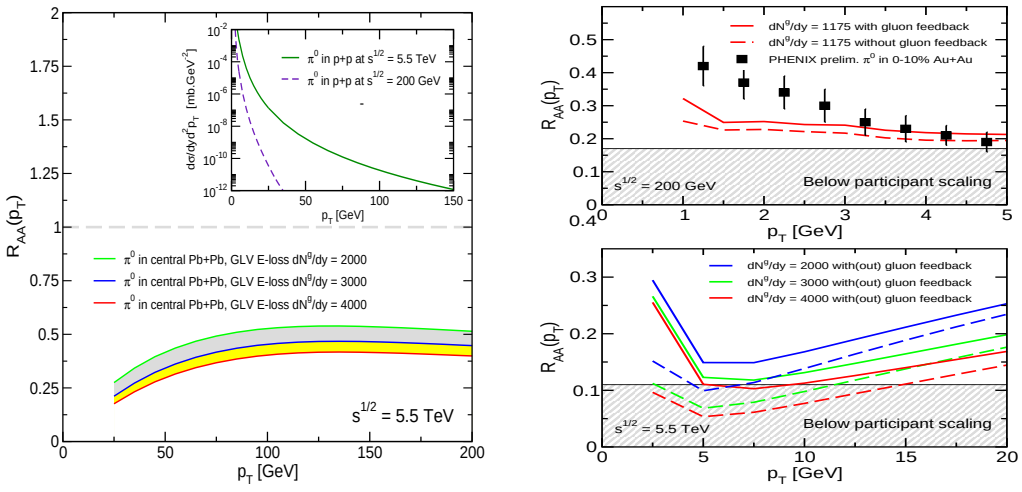

Figure 102: Left panel: Suppression of π^0 production in central Pb+Pb collisions at the LHC as a function of the parton rapidity density. Insert shows the baseline p+p π^0 cross section at $\sqrt{s} = 200$ GeV and $\sqrt{s} = 5.5$ TeV [283, 284]. Right panel: nuclear modification factor R_{AA} in central Au+Au collisions at moderate p_T with (solid line) and without (dashed line) gluon feedback, $dN^g/dy = 1175$. Central Pb+Pb collisions with (solid line) and without (dashed line) gluon feedback are shown, $dN^g/dy \simeq 2000, 3000, 4000$ [284].

we assume that the initial hard scattering cross sections are factorized as in $p+p$ collisions. We further assume that the effect of final-state interaction between produced parton and the bulk medium can be described by the effective medium-modified FF's. The total parton energy loss in a finite and expanding medium is approximated as a path integral,

$$\Delta E \approx \langle \frac{dE}{dL} \rangle_{1d} \int_{\tau_0}^{\infty} d\tau \frac{\tau - \tau_0}{\tau_0 \rho_0} \rho_g(\tau, \mathbf{b}, \mathbf{r} + \mathbf{n}\tau), \tag{56}$$

for a parton produced at a transverse position $\mathbf{r}$ and traveling along the direction $\mathbf{n}$. $\langle dE/dL \rangle_{1d}$ is the average parton energy loss per unit length in a 1-d expanding medium with an initial uniform gluon density ρ_0 at a formation time τ_0 for the medium gluons. The energy dependence of the energy loss is parameterized as

$$\langle \frac{dE}{dL} \rangle_{1d} = \epsilon_0 (E/\mu_0 - 1.6)^{1.2} / (7.5 + E/\mu_0), \tag{57}$$

from the numerical results in Ref. [287, 288]. The parameter ϵ_0 should be proportional to the initial gluon density ρ_0. The gluon density distribution in a 1-d expanding medium in $A+A$ collisions at impact-parameter $\mathbf{b}$ is assumed to be proportional to the transverse profile of participant nucleons ,

$$\rho_g(\tau, \mathbf{b}, \mathbf{r}) = \frac{\tau_0 \rho_0}{\tau} \frac{\pi R_A^2}{2A} [t_A(\mathbf{r}) + t_A(|\mathbf{b} - \mathbf{r}|)]. \tag{58}$$

In fitting the RHIC data [289] we have chosen the parameters as $\mu_0 = 1.5$ GeV, $\tau_0 = 0.2$ fm/c and $\epsilon_0 = 1.68$ GeV/fm. We assume ϵ_0 is proportional to the final multiplicity density and $\epsilon_0 = 5.6$ GeV/fm in the central $Pb+Pb$ collisions $\sqrt{s} = 5.5$ TeV.

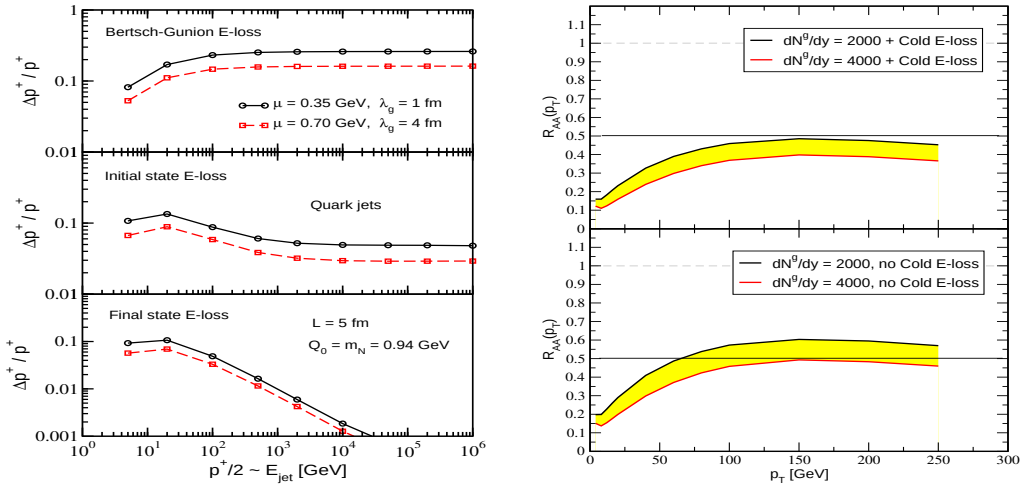

Figure 103: Left panel: Comparison of Bertsch-Gunion, initial-state and final-state quark energy loss in a large nucleus, such as Au or Pb. The cancellation of initial-state energy loss is finite and cannot be neglected even at high parton energies [285]. Right panel: Effects of could nuclear matter energy loss on suppressed π^0 production in central Pb+Pb collisions at the LHC. Two parton rapidity densities $dN^g/dy \simeq 2000, 4000.$ are shown; cold nuclear matter energy loss effects can be as large as the effect of doubling the parton rapidity density [284, 285].

We use the factorization scale $\mu = 1.2p_T$ in both $p+p$ and $A+A$ collisions in our calculation. Shown in Fig. 104(a) are the single π^0 spectra in both $p+p$ and $Pb+Pb$ collisions at $\sqrt{s} = 5.5$ TeV and the corresponding nuclear modification factor, $R_{AA} = d\sigma_{AA}/dp_T^2 dy[\int d^2bT_{AA}(\mathbf{b})d\sigma_{NN}/dp_T^2 dy]^{-1}$.

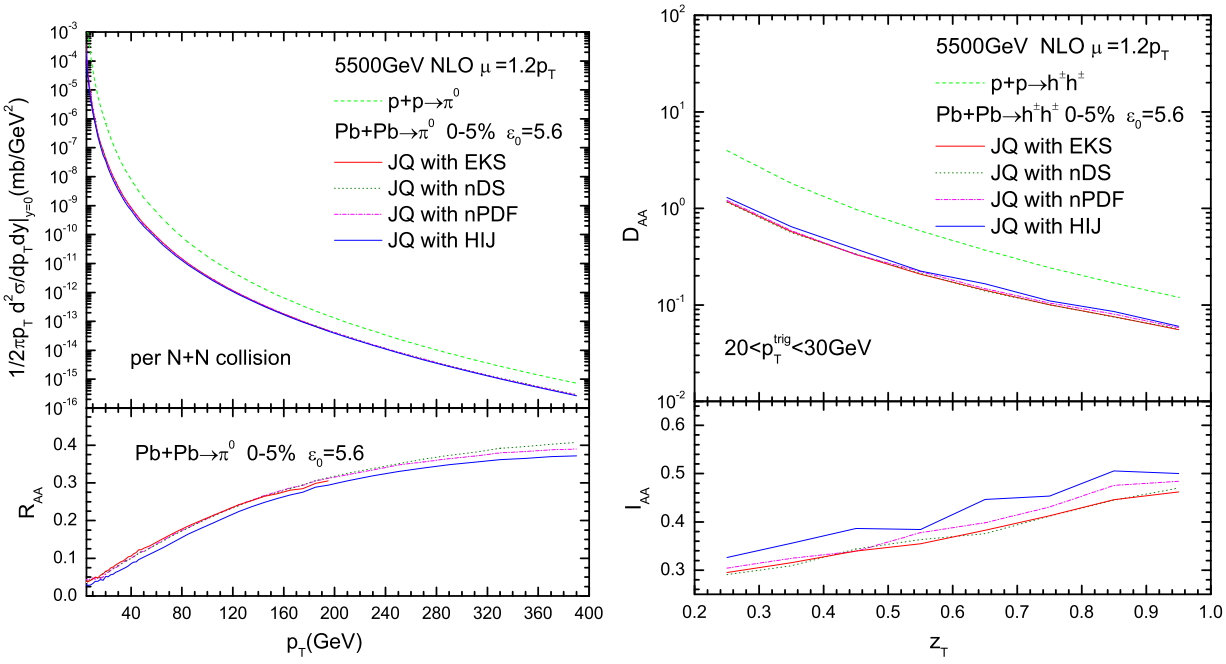

Figure 104: (a) π^0 spectra and suppression factor in $Pb+Pb(0-5\%)$ collisions at $\sqrt{s} = 5.5$ TeV. (b)Hadron-triggered fragmentation functions $D_{AA}(z_T)$ and the medium modification factors $I_{AA}(z_T)$ in NLO pQCD in central $Pb+Pb$ collisions at $\sqrt{s} = 5.5$ TeV.

The hadron-triggered fragmentation function, $D_{AA}(z_T, p_T^{\rm trig}) \equiv p_T^{\rm trig} d\sigma_{AA}^{h_1h_2}/dy^{\rm trig}dp_T^{\rm trig}dy^{\rm asso}dp_T^{\rm asso}[d\sigma_{AA}^{h_1}/dy^{\rm trig}dp_T^{\rm trig}]^{-1}$ as a function of $z_T = p_T^{\rm asso}/p_T^{\rm trig}$ is essentially the away-side hadron spectrum associated with a triggered hadron within $|y^{\rm trig,asso}| < 0.5$ and the azimuthal angle relative to the triggered hadron is integrated over $|\Delta\phi| > 2.5$.

The factorization scale in the NLO calculation of dihadron spectra is chosen to be $\mu = 1.2M$, where M is the invariant mass of the dihadron $M^2 = (p_1+p_2)^2$. The associated hadron spectra $D_{pp}(z_T, p_T^{\rm trig})$ in $p+p$ and central $Pb+Pb$ collisions at $\sqrt{s} = 5.5$ TeV and the suppression factor $I_{AA} = D_{AA}(z_T, p_T^{\rm trig})[D_{pp}(z_T, p_T^{\rm trig})]^{-1}$ for central $Pb+Pb$ collision at LHC are shown in Fig. 104(b).

7. Heavy quarks and quarkonium

7.1. Statistical hadronization model predictions for charmed hadrons

A. Andronic, P. Braun-Munzinger, K. Redlich and J. Stachel

We present predictions of the statistical hadronization model for charmed hadrons production in Pb+Pb collisions at LHC.

The results presented below are discussed in detail in our recent publication [290]. We summarize here the values of the model parameters: i) characteristics at chemical freeze-out: temperature, T=161±4 MeV; baryochemical potential, μ_b=$0.8^{+1.2}_{-0.6}$ MeV; volume corresponding to one unit of rapidity V=6200 fm^3; ii) charm production cross section: $\underline{\sigma^{pp}_{c\bar{c}}}/\underline{y} = 0.64^{+0.64}_{-0.32}$ mb.

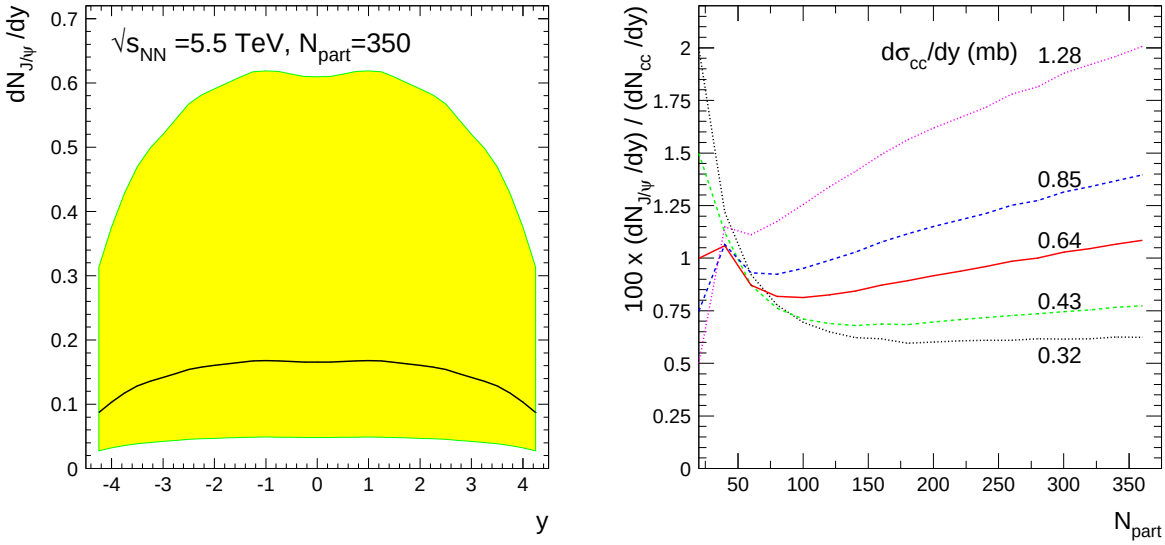

Figure 105: Predictions for J/ψ yield: rapidity distribution for central collisions (left panel) and centrality dependence of the yield relative to the charm production yield for different values of the charm cross section indicated on the curves (right panel).

In Fig. 105 we present predictions for the yield of J/ψ. The left panel shows the rapidity distribution with the band reflecting the uncertainty in the charm production cross section. The right panel shows the centrality dependence of the yield relative to the charm production yield for five values of the input charm cross section.

The statistical hadronization model predictions for charmed hadron yield ratios in central Pb+Pb collisions at LHC are shown in Table 5. We expect that these ratios are independent of centrality down to values of $N_{part} \simeq$100.

Following from our model assumption of charm quark thermalization and assuming decoupling of charm at hadronization, the transverse momentum spectra of charmed hadrons can be calculated [290]. As seen in Fig. 106, a precision measurement of the spectrum of J/ψ meson will allow the determination of the expansion velocity in QGP.

7.2. Nuclear suppression for heavy flavors in PbPb collisions at the LHC

N. Armesto, M. Cacciari, A. Dainese, C. A. Salgado and U. A. Wiedemann

We predict the nuclear suppression factors for D and B mesons, and for electrons from their semi-leptonic decays, in PbPb collisions at the LHC. The results are obtained supplementing a perturbative next-to-leading order + next-to-leading log (FONLL) calculation with appropriate non-perturbative fragmentation functions and radiative energy loss.

Table 5: Predictions of the statistical hadronization model for charmed hadron ratios for Pb+Pb collisions at LHC. The numbers in parantheses represent the error in the last digit(s) due to the uncertainty of T.

D^-/D^+	$\bar{D}_0/D_0$	D^{*-}/D^{*+}	D_s^-/D_s^+	$\bar{\Lambda}_c/\Lambda_c$	D^+/D_0	D^{*+}/D_0
1.00(0)	1.01(0)	1.01(0)	1.00(1)	1.00(1)	0.425(18)	0.387(15)

D_s^+/D_0	Λ_c/D_0	ψ'/ψ	η_c/ψ	χ_{c1}/ψ	χ_{c2}/ψ
0.349(14)	0.163(16)	0.031(3)	0.617(14)	0.086(5)	0.110(8)

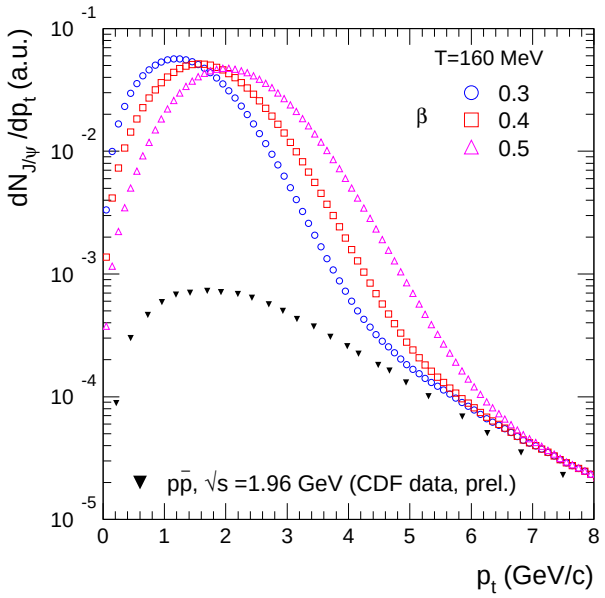

Figure 106: Predictions for momentum spectrum of J/ψ meson for different values of the average expansion velocity, β, for central Pb+Pb collisions (N_{part}=350). Also included is the measured spectrum in p$\bar{p}$ collisions at Tevatron [291], which is used to calculate the contribution from the corona (see ref. [290]).

Medium-induced gluon radiation is usually identified as the dominant source of energy loss of high-p_T particles traversing a hot medium. Different models which use different approximations to this physical mechanism of energy loss, provide a successful phenomenological description of available experimental data for light hadron suppression. Most of these calculations assume independent multiple gluon emission to model the exclusive distributions essential to compute the suppression which convolutes the fragmentation functions with a steeply falling perturbative spectrum. This convolution biases the observed particle yields to small in-medium energy losses and surface emission which, on the other hand, leads to a lack of precision in the determination of the medium parameters [80, 231]. The value of the transport coefficient obtained in these approaches, by using the

multiple soft scattering approximation is [80, 231]

$$\hat{q} = 5 \div 15\,\mathrm{GeV}^2/\mathrm{fm}. \tag{59}$$

One proposal to increase the sensitivity to the value of the transport coefficient is to measure the corresponding effects on heavy mesons as the formalism predicts a calculable hierarchy of energy losses $\Delta E^g > \Delta E^q_{\mathrm{m_q}=0} > \Delta E^Q_{\mathrm{m_Q}\neq 0}$, due color factors for the first and mass terms for the second inequality [292]. The implementation of mass effects does not add any new parameter to the calculation once the transport coefficient $\hat{q}$ is fixed by e.g. light hadrons (59). The description of non-photonic electrons data from RHIC given by this formalism is reasonable [293] although the uncertainties in the benchmark relative contribution from beauty and charm quarks are still large.

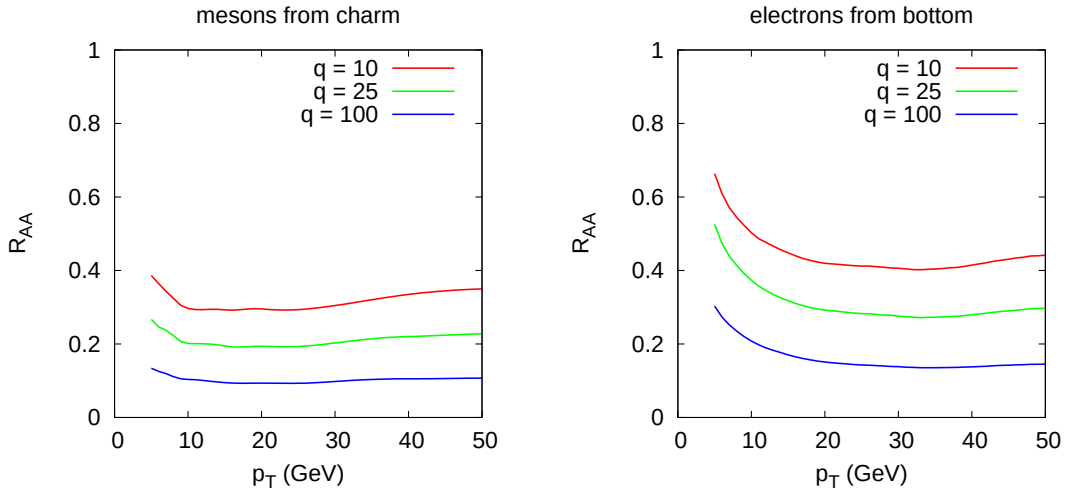

Figure 107: R_{AA} for D's (left) and for electrons coming from bottom decays (right) at $y = 0$ for 10% PbPb collisions at $\sqrt{s} = 5.5$ TeV/A, for different $\hat{q}$ (in GeV^2/fm).

At the LHC, where charm and beauty suppression will be measured separately, the situation will be improved and a definite check on the influence of mass terms in the medium-induced gluon radiation and the corresponding energy loss will be done. We here present predictions based on the formalism developed in references [80, 231, 292–294], for $0-10\%$ and $30-60\%$ PbPb collisions at LHC energy. This also updates the calculations in [294] by taking into account the FONLL baseline for the perturbative calculation (see [293] and references therein).

In Figs. 107 and 108 we present our predictions for R_{AA}, double ratios and v_2, for mesons and/or decay electrons at $y = 0$. While the mass effects in charm are very modest, they are clearly visible for bottom quarks at $p_T \lesssim 20$ GeV. At larger p_T they tend to disappear and the typical suppression is that of massless particles [80, 231]. We have used several values of $\hat{q}$ ranging from 10 GeV^2/fm, which is the lowest one still compatible with RHIC non-photonic electrons data, to 100 GeV^2/fm, which is our estimated upper limit, from the most extreme extrapolation of the multiplicities at the LHC.

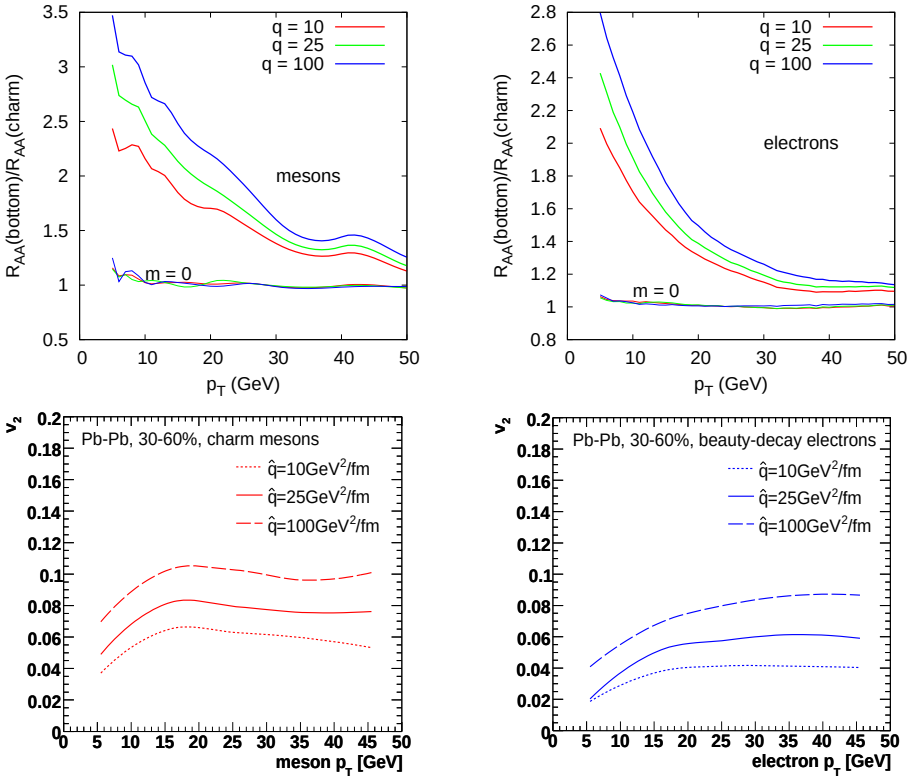

Figure 108: Upper plots: double ratio for mesons (left) and decay electrons (right) for 10% PbPb collisions at $\sqrt{s} = 5.5$ TeV/A for $y = 0$, for different $\hat{q}$ (in GeV^2/fm). Lower plots: v_2 for D's (left) and from electrons coming from bottom decays (right) at $y = 0$ for $30-60\%$ PbPb collisions at $\sqrt{s} = 5.5$ TeV/A, for different $\hat{q}$.

7.3. Heavy-quark production from Glauber-Gribov theory at LHC

I. C. Arsene, L. Bravina, A. B. Kaidalov, K. Tywoniuk and E. Zabrodin

We present predictions for heavy-quark production for proton-lead collisions at LHC energy 5.5 TeV from Glauber-Gribov theory of nuclear shadowing. We have also made predictions for baseline cold-matter (in other words inital-state) nuclear effects in lead-lead collisions at the same energy that has to be taken into account to understand properly final-state effects.

7.3.1. Introduction In the Glauber-Gribov theory [21] nuclear shadowing at low-x is related to diffractive structure functions of the nucleon, which are studied experimentally at HERA. The space-time picture of the interaction for production of a heavy-quark state on nuclei changes from longitudinally ordered rescatterings at energies below the critical energy, corresponding to x_2 of an active parton from a nucleus becoming smaller than $1/m_N R_A$, to the coherent interaction of constituents of the projectile with a target nucleus at energies higher thant the critical one [295]. For production of J/ψ and Υ in the central rapidity region the transition happens at RHIC energies. In this kinematical region the contribution of Glauber-type diagrams is small and it is necessary to calculate diagrams with interactions between pomerons, which, in our approach, are accomodated in the gluon shadowing. A similar model

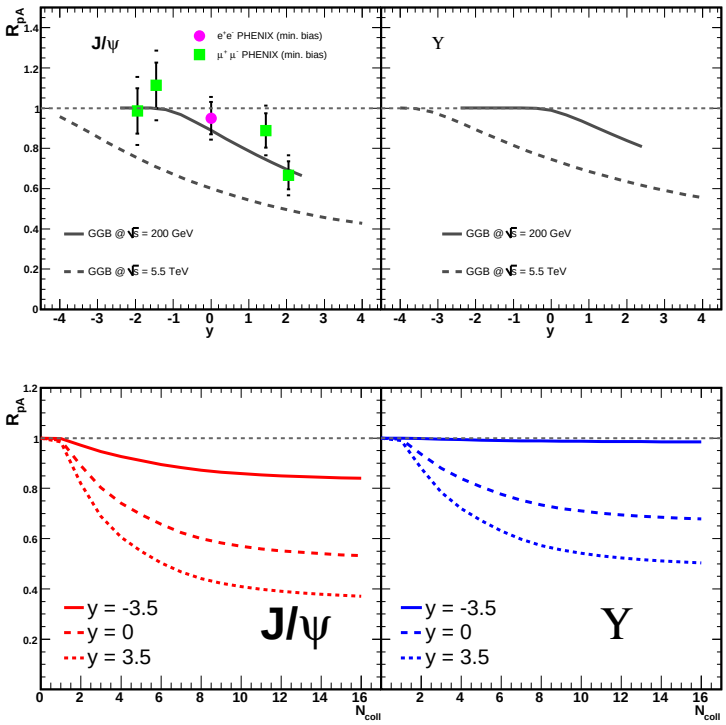

Figure 109: Rapidity (top) and centrality (bottom) dependence of the nuclear modification factor for J/ψ (left) and Υ (right) production in p+Pb (d+Au) collisions at $\sqrt{s}$ = 5500 (200) GeV. Experimental data are from [296].

for J/ψ-suppression in d+Au collisions at RHIC has been considered in Ref. [51].

Calculation of gluon shadowing was performed in our recent paper [22], where Gribov approach for the calculation of nuclear structure functions was used. The gluon diffractive distributions were taken from the most recent experimental parameterizations of HERA data [23]. The Schwimmer model was used to account for higher-order rescatterings.

7.3.2. Heavy-quark production at the LHC We present predictions for the rapidity and centrality dependence of the nuclear modification factor in proton-lead (p+Pb) collisions for both J/ψ and Υ in Fig. 109 (the data on J/ψ suppression at $\sqrt{s}$ = 200 GeV is taken from [296], where also a definition of the nuclear modification factor can be found). We predict a similar suppression for open charm, $c\bar{c}$, and bottom, $b\bar{b}$, as for the hidden-flavour particles. The observed x_F scaling at low energies of the parameter α (from $\sigma_{pA} = \sigma_{pp}A^{\alpha}$) for J/ψ production, which is broken already at RHIC, will go to a scaling in x_2 at higher energies. This will also be the case for Υ and open charm and bottom.

In Fig. 110 we present predictions for cold-nuclear matter effects due to gluon shadowing in lead-lead (Pb+Pb) collisions at LHC energy $\sqrt{s}$ = 5.5 TeV for the production of J/ψ and Υ. The suppression is given as a function of rapidity and centrality. .

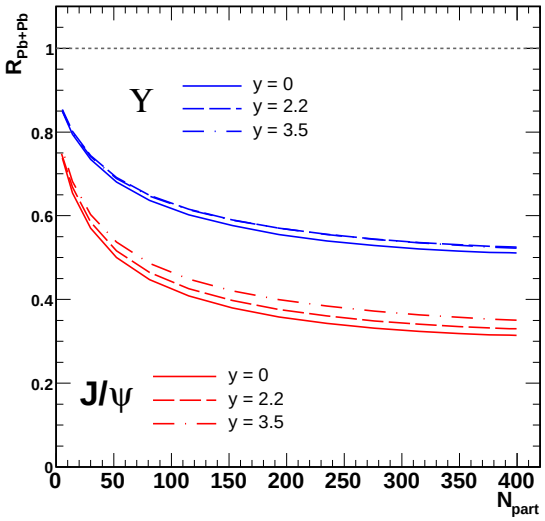

Figure 110: Baseline cold-nuclear matter effects in Pb+Pb collisions at 5.5 TeV for J/ψ and Υ production.

7.4. $R_{\rm AA}(p_{\rm t})$ and $R_{\rm CP}(p_{\rm t})$ of single muons from heavy quark and vector boson decays at the LHC

Z. Conesa Del Valle, A. Dainese, H.-T. Ding, G. Martínez and D. Zhou

We study the effect of heavy-quark energy loss on the nuclear modification factors $R_{\rm AA}$ and $R_{\rm CP}$ of the high-$p_{\rm t}$ distribution of single muons in Pb–Pb collisions at $\sqrt{s_{\rm NN}}$=5.5 TeV. The energy loss of heavy quarks is calculated using the mass-dependent BDMPS quenching weights and taking into account the decrease of medium density at large rapidity. Muons from W and Z decays, that dominate the yield at high $p_{\rm t}$, can be used as a medium-blind reference that scales with the number of binary collisions.

The PHENIX and STAR experiments at RHIC have measured a suppression, in central Au–Au relative to pp collisions, of the high-$p_{\rm t}$ yield of non-photonic electrons, which are assumed to come from semi-electronic decays of charm and beauty particles. This suppression is interpreted as an indication of a strong energy loss of c and b quarks in the medium formed in Au–Au collisions. At the LHC, the nuclear modification factors $R_{\rm AA}$ and $R_{\rm CP}$ of the single-muon inclusive $p_{\rm t}$ distribution will be among the first measurements sensitive to heavy-quark energy loss. Moreover, the very high $p_{\rm t}$ domain ($p_{\rm t} > 30$ GeV/c) of the muon spectrum will be dominated by muonic decays of electroweak boson W (mainly) and Z, that should be medium-insensitive and follow binary scaling, thus making of the nuclear modification factor a self-normalized observable.

We obtain the charm and beauty contributions to the muon spectrum from the NLO pQCD calculation (MNR [297]) supplemented with the mass-dependent BDMPS quenching weights for radiative energy loss [294], quark fragmentation à la Peterson and semi-muonic

decay with the spectator model. We account for the medium density decrease at large rapidity by assuming the transport coefficient to scale as $\hat{q}(\eta) \propto dN_{ch}/d\eta$. We use PYTHIA to calculate the W and Z decay contribution [298]. More details can be found in Ref. [299].

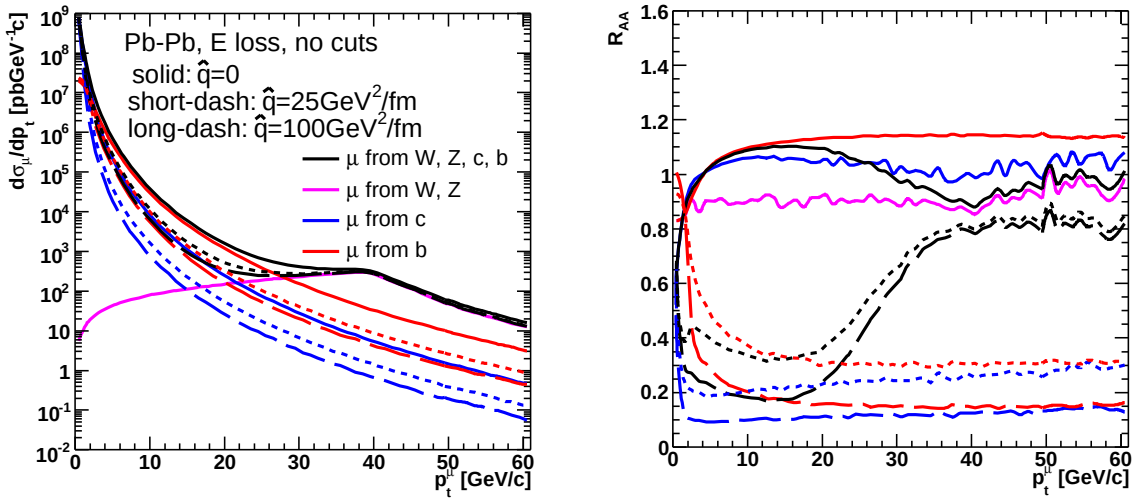

Figure 111: $p_{\rm t}$ distribution (left) and $R_{\rm AA}$ (right) of single muons in central (0–10%) Pb–Pb collisions at $\sqrt{s_{\rm NN}} = 5.5$ TeV.

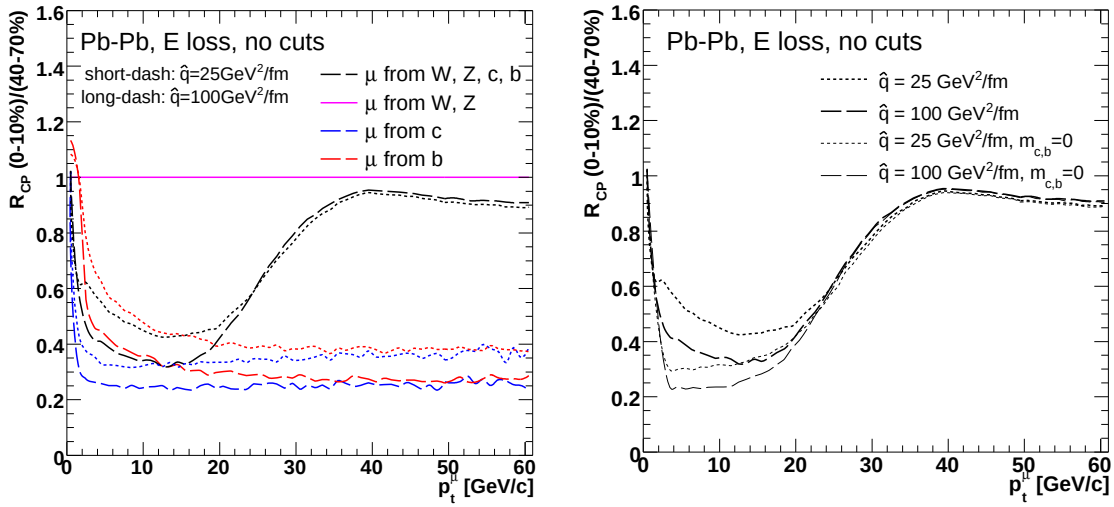

Figure 112: $R_{\rm CP}$ (0–10%)/(40–70%) of single muons in Pb–Pb collisions at $\sqrt{s_{\rm NN}} = 5.5$ TeV.

Fig. 111 shows the $p_{\rm t}$ spectrum and $R_{\rm AA}(p_{\rm t})$ of the single muons from heavy quark and W/Z bosons in the central Pb–Pb collisions at $\sqrt{s_{\rm NN}} = 5.5$ TeV, with the transport coefficient values $\hat{q} = 0, 25, 100$ GeV^2/fm. The crossing point of b and W decay muons shifts down by 5–7 GeV/c. $R_{\rm AA}$ rapidly increases from 0.3 to 0.8 between 20 (b-dominated) and 40 GeV/c (W-dominated), as does $R_{\rm CP}$ (0–10%)/(40–70%), shown in Fig. 112. The effect of the heavy-quark mass on the medium-induced suppression of $R_{\rm CP}$ is shown in the left-hand panel of

Fig. 112.

7.5. Quarkonium production in coherent pp/AA collisions and small-x physics

V. P. Gonçalves and M. V. T. Machado

We study the photoproduction of quarkonium in coherent proton-proton and nucleus-nucleus interactions at the LHC. The integrated cross sections and rapidity distributions are estimated using the Color Glass Condensate (CGC) formalism, which takes into account the parton saturation effects at high energies. Nuclear shadowing effects are also taken into account.

In this contribution we study the photoproduction of vector mesons in the coherent pp/AA interactions at the LHC energies. The main advantage of using colliding hadrons and nuclear beams for studying photon induced interactions is the high equivalent photon energies and luminosities that can be achieved at existing and future accelerators (for a review see reference [300]). Consequently, studies of γp interactions at LHC could provide valuable information on the QCD dynamics at high energies. The basic idea in coherent hadron collisions is that the total cross section for a given process can be factorized in terms of the equivalent flux of photons of the hadron projectile and the photon-photon or photon-target production cross section. In exclusive processes, a certain particle is produced while the target remains in the ground state (or is only internally excited). The typical examples of these processes are the exclusive vector meson production, described by the process $\gamma h \to Vh$ ($V = \rho, J/\Psi, \Upsilon$). In the last years we have discussed this process in detail considering pp [301], pA [302] and AA [301] collisions as an alternative to investigate the QCD dynamics at high energies. Here, we revised these results and present for the first time our predictions for the Υ production.

The cross section for the photoproduction of a vector meson X in an ultra-peripheral hadron-hadron collision is given by

$$\sigma(h_1 h_2 \to h_1 h_2 X) = \int_{\omega_{min}}^{\infty} \mathrm{d}\omega \frac{\mathrm{d}N_\gamma(\omega)}{\mathrm{d}\omega} \sigma_{\gamma h \to X h}(W^2_{\gamma h}),$$

where ω is the photon energy and $\mathrm{d}N_\gamma(\omega)/\mathrm{d}\omega$ is the equivalent flux of photons from a charged hadron. The total cross section for vector meson photoproduction is calculated considering the color dipole approach, which is directly related with the dipole-target forward amplitude $\mathcal{N}$. In the Color Glass Condensate (CGC) formalism (see e.g. [303]), $\mathcal{N}$ encodes all the information about the hadronic scattering, and thus about the non-linear and quantum effects in the hadron wave function. In our analyzes we have used the phenomenological saturation model proposed in references [33, 304]. Nuclear effects are also properly taken into account.

Our predictions for the rapidity distributions are presented in figure 113 and for the total cross section in table 6. The main uncertainties are the photon flux, the quark mass and the size of nuclear effects for the photonuclear case. In addition, specific predictions for ρ and J/Ψ phoproduction in pA collisions can be found in reference [302]. The rates are very high, mostly for light mesons. Although the rates are lower than hadroproduction, the coherent

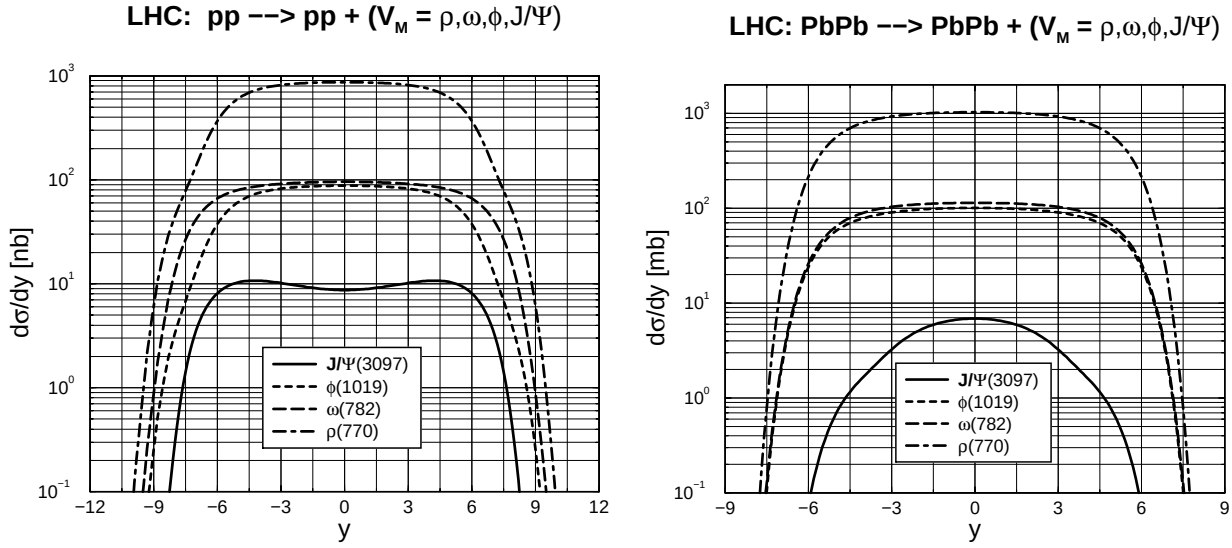

Figure 113: *The rapidity distribution for nuclear vector meson photoproduction on coherent pp (left panel) and* AA *(right panel) reactions at the LHC.*

Table 6: *The integrated cross section for nuclear vector mesons photoproduction in coherent pp and* AA *collisions at the LHC.*

	$\Upsilon(9460)$	$J/\Psi(3097)$	$\phi(1019)$	$\omega(782)$	$\rho(770)$
pp	0.8 nb	132 nb	980 nb	1.24 μb	9.75 μb
Ca-Ca	9.7 μb	436 μb	12 mb	14 mb	128 mb
Pb-Pb	96 μb	41.5 mb	998 mb	1131 mb	10069 mb

photoproduction signal would be clearly separated by applying a transverse momentum cut $p_T < 1$ GeV and two rapidity gaps in the final state.

7.6. Heavy-Quark Kinetics in the QGP at LHC

H. van Hees, V. Greco and R. Rapp

We present predictions for the nuclear modification factor and elliptic flow of D and B mesons, as well as of their decay electrons, in semicentral Pb-Pb collisions at the LHC. Heavy quarks are propagated in a Quark-Gluon Plasma using a relativistic Langevin simulation with drag and diffusion coefficients from elastic interactions with light anti-/quarks and gluons, including non-perturbative resonance scattering. Hadronization at T_c is performed within a combined coalescence-fragmentation scheme.

In Au-Au collisions at the Relativistic Heavy Ion Collider (RHIC) a surprisingly large suppression and elliptic flow of "non-photonic" single electrons ($e^{\pm}$, originating from semileptonic decays of D and B mesons) has been found, indicating a strong coupling of charm (c) and bottom (b) quarks in the Quark-Gluon Plasma (QGP).

We employ a Fokker-Planck approach to evaluate drag and diffusion coefficients for c and b quarks in the QGP based on elastic scattering with light quarks and antiquarks via D- and B-meson resonances (supplemented by perturbative interactions in color non-singlet channels) [305]. This picture is motivated by lattice QCD computations which suggest a survival of mesonic states above the critical temperature, T_c. Heavy-quark (HQ) kinetics in the QGP is simulated with a relativistic Langevin process [306]. Since the initial temperatures at the LHC are expected to exceed the resonance dissociation temperatures, we implement a "melting" of D- and B-mesons above $T_{\rm diss}$=$2T_c$=360 MeV by a factor $(1+\exp[(T-T_{\rm diss})/\Delta])^{-1}$ (Δ=50 MeV) in the transport coefficients.

The medium in a heavy-ion reaction is modeled by a spatially homogeneous elliptic thermal fireball which expands isentropically. The temperature is inferred from an ideal gas QGP equation of state with N_f=2.5 massless quark flavors, with the total entropy fixed by the number of charged hadrons which we extrapolate to $\mathrm{d}N_{\rm ch}/\mathrm{d}y\simeq$1400 for central $\sqrt{s_{NN}}$=5.5 TeV Pb-Pb collisions. The expansion parameters are adjusted to hydrodynamic simulations, resulting in a total lifetime of $\tau_{\rm fb}\simeq$6 fm/c at the end of a hadron-gas QGP mixed phase and an inclusive light-quark elliptic flow of $\langle v_2\rangle$=7.5%. The QGP formation time, τ_0, is estimated using $\tau_0 T_0$=const (T_0: initial temperature), which for semicentral collisions (impact parameter $b\simeq$7 fm) yields $T_0\simeq$520 MeV.

Initial HQ p_T spectra are computed using PYTHIA with parameters as used by the ALICE Collaboration. c and b quarks are hadronized into D and B mesons at T_c by coalescence with light quarks [62]; "left over" heavy quarks are hadronized with δ-function fragmentation. For semileptonic electron decays we assume 3-body kinematics [306].

Fig. 114 summarizes our results for HQ diffusion in a QGP in terms of $R_{AA}(p_T)$ and $v_2(p_T)$ at the quark, meson and $e^{\pm}$ level for b=7 fm Pb-Pb collisions at the LHC (approximately representing minimum-bias conditions). Our most important findings are: (a) resonance interactions substantially increase (decrease) v_2 (R_{AA}) compared to perturbative interactions; (b) b quarks are much less affected than c quarks, reducing the effects in the $e^{\pm}$ spectra; (c) there is a strong correlation between a large v_2 and a small R_{AA} at the quark level, which, however, is partially reversed by coalescence contributions which increase *both* v_2 and R_{AA} at the meson (and $e^{\pm}$) level. This feature turned out to be important in the prediction of $e^{\pm}$ spectra at RHIC; (d) the predictions for LHC are quantitatively rather similar to our RHIC results [306, 307], due to a combination of harder initial HQ-p_T spectra with a moderate increase in interaction strength in the early phases where non-perturbative resonance scattering is inoperative.

7.7. Ratio of charm to bottom R_{AA} as a test of pQCD vs. AdS/CFT energy loss

W. A. Horowitz

The theoretical framework of a weakly-coupled QGP used in pQCD models that quantitatively describe the high-p_T π^0, η suppression at RHIC is challenged by several experimental observables, not limited to high-p_T only, suggesting the possibility that a

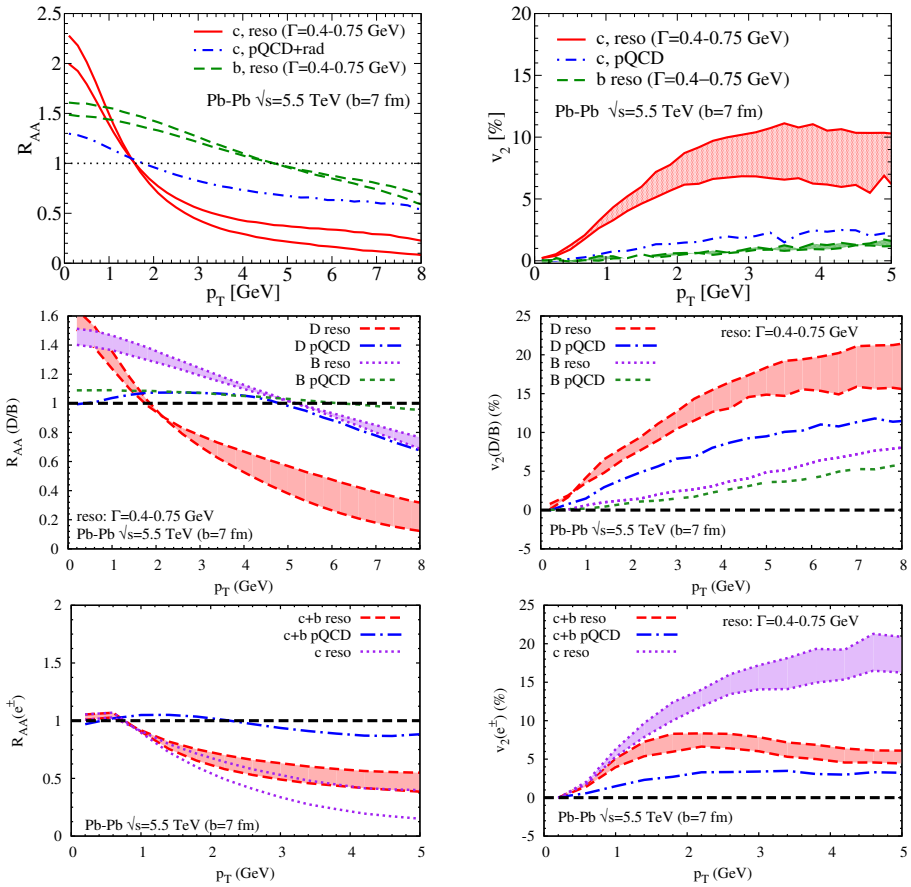

Figure 114: (Color online) Predictions of relativistic Langevin simulations for heavy quarks in a sQGP for b=7 fm $\sqrt{s_{NN}}$=5.5 TeV Pb-Pb collisions: R_{AA} (left column) and v_2 (right column) for heavy quarks (1$^{\rm st}$ row), D and B mesons (2$^{\rm nd}$ row) and decay-$e^{\pm}$ (3$^{\rm rd}$ row).

strongly-coupled picture might be more accurate. One seeks a measurement that may clearly falsify one or both approaches; heavy quark jet suppression is one possibility. Strongly-coupled calculations, utilizing the AdS/CFT correspondence, have been applied to high-p_T jets in three ways [263, 308, 309]. We will focus on predictions from the AdS/CFT heavy quark drag model and compare them to pQCD predictions from the full radiative and elastic loss WHDG model and radiative alone WHDG model [244]. Comparisons between AdS/CFT models and data are difficult. First, one must accept the double conjecture of QCD↔SYM↔AdS/CFT. Second, to make contact with experiment, one must make further assumptions to map quantities such as the coupling and temperature in QCD into the SUGRA calculation. For example, the AdS/CFT prediction for the heavy quark diffusion coefficient is $D = 4/\sqrt{\lambda}(/2\pi T)$ [308], where $\lambda = g^2_{SYM}N_c$ is the 't Hooft coupling. The "obvious" first such mapping [310] simply equates constant couplings, $g_s = g_{SYM}$, and temperatures, $T_{SYM} = T_{QCD}$. Using this prescription with the canonical $N_c = 3$ and $\alpha_s = .3$ yields $D \approx 1.2(/2\pi T)$. It was claimed in [308] that $D = 3(/2\pi T)$ agrees better with data; this requires $\alpha_s \approx .05$. An "alternative" mapping [310] equates the quark-antiquark force found on the lattice to that computed using AdS/CFT, giving $\lambda \approx 5.5$, and the QCD and SYM energy densities, yielding

$T_{SYM} = T_{QCD}/3^{1/4}$.The medium density to be created at LHC is unknown; we will take the PHOBOS extrapolation of $dN_g/dy = 1750$ and the KLN model of the CGC, $dN_g/dy = 2900$, as two sample values.We will search for general trends associated with AdS/CFT drag (denoted hereafter simply as AdS/CFT) or pQCD as these uncertainties mean little constrains the possible normalizations of AdS/CFT R^Q_{AA} predictions for LHC.

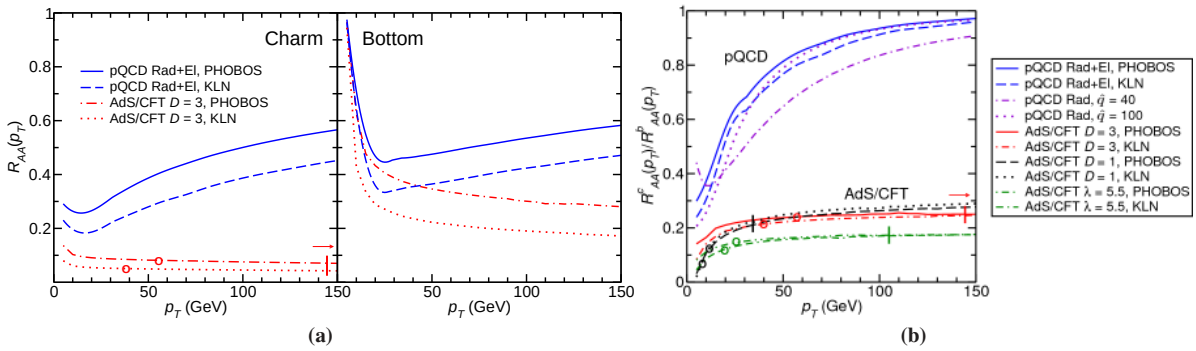

Figure 115: (a) Charm and bottom $R_{AA}(p_T)$ predictions with representative input parameters for LHC. The generic trend of pQCD curves increasing with p_T while AdS/CFT curves decrease is seen for representative input parameters; similar trends occurred for the other input possibilities considered. (b) Ratio of charm to bottom $R_{AA}(p_T)$ bunches the two models for a wide range of input parameters; the LHC should easily distinguish between the two trends.

AdS/CFT calculations of the drag on a heavy quark yield $dp_T/dt = -\mu_Q p_T = -(\pi\sqrt{\lambda}T^2_{SYM}/2m_Q)p_T$ [309], giving an average fractional energy loss of $\bar{\epsilon} = 1 - \exp(-\int dt\mu_Q)$. Asymptotic pQCD energy loss for heavy quarks in a static medium goes as $\bar{\epsilon} \approx \kappa L^2\hat{q}\log(p_T/m_Q)/p_T$, where κ is a proportionality constant and L is the pathlength traversed by the heavy quark. Note that AdS/CFT fractional momentum loss is independent of momentum while pQCD loss decreases with jet energy. The heavy quark production spectrum may be approximated by a slowly varying power law of index $n_Q(p_T) + 1$, then $R^Q_{AA} \approx (1-\bar{\epsilon})^{n_Q(p_T)}$. Since $n_Q(p_T)$ is a slowly increasing function of momentum, we expect $R^Q_{AA,SYM}(p_T)$ to decrease while $R^Q_{AA,pQCD}(p_T)$ to increase as momentum increases. This behavior is reflected in the full numerical calculations shown in Fig. 115 (a); details of the model can be found in [311].

For high suppression pQCD predicts nearly flat R^Q_{AA}, masking the difference between AdS/CFT and pQCD. One can see in Fig. 115 (b) that the separation of AdS/CFT and pQCD predictions is enhanced when the double ratio of charm to bottom nuclear modification, $R^{cb}(p_T) = R^c_{AA}(p_T)/R^b_{AA}(p_T)$, is considered. Asymptotic pQCD energy loss goes as $\log(m_Q/p_T)/p_T$, becoming insensitive to quark mass for $p_T \gg m_Q$; hence $R^{cb}_{pQCD} \to 1$. Expanding the R_{AA} formula for small ϵ yields $R^{cb}_{pQCD}(p_T) \approx 1 - p_{cb}/p_T$, where $p_{cb} = \kappa n(p_T)L^2\log(m_b/m_c)\hat{q}$ and $n_c \approx n_b = n$. Therefore the ratio approaches unity more slowly for larger suppression. This behavior is reflected in the full numerical results for the moderately quenched pQCD curves, but is violated by the highly oversuppressed $\hat{q} = 100$ curve. The AdS/CFT drag, however, is independent of p_T. A back of the envelope approximation gives

$R_{AA}^{Q} \approx \int_0^L d\ell \exp(-n_Q \mu_q \ell) \approx 1/n_Q \mu_q$ which yields $R^{cb}(p_T) \approx n_b(p_T) m_c / n_c(p_T) m_b \approx m_c/m_b \approx .27$. This behavior is also reflected in the full numerical results shown in Fig. 115 (b), and so, remarkably, the pQCD and AdS/CFT curves fall into easily distinguishable bunches, robust to changes in input parameters. An estimate for the momentum after which corrections to the above AdS/CFT drag formula are needed, $\gamma > \gamma_c$, found in the static string geometry is $\gamma_c = 1/1 + (2m_Q/T\sqrt{\lambda})$ [312]. Since temperature is not constant we show the smallest speed limit, using $T(\tau_0, \vec{x} = \vec{0})$, and largest, from T_c, represented by "O" and "|," respectively. A deviation of R^{cb} away from unity at LHC in year 1 would pose a serious challenge to the usual pQCD paradigm. An observation of a significant increase in R^{cb} with jet momenta would imply that the current AdS/CFT picture is only applicable at low momenta, if at all. For a definitive statement to be made a $p + Pb$ control run will be crucial.

7.8. Thermal charm production at LHC

B.-W. Zhang, C. M. Ko and W. Liu

Charm production from an equilibrated quark-gluon plasma (QGP) produced in heavy ion collisions at LHC is studied to the next-to-leading order in perturbative QCD [313]. Specifically, we consider the process $q(g) + \bar{q}(g) \to c + \bar{c}$ and its virtual correction as well as the processes $q(g) + \bar{q}(g) \to c + \bar{c} + g$, and $g + q(\bar{q}) \to c + \bar{c} + q(\bar{q})$. The amplitudes for these processes are taken from Refs. [314–317] using massless quarks and gluons, the QCD coupling constant $\alpha_s(m_c) \approx 0.37$, and a charm quark mass $m_c = 1.3$ GeV. The charm quark production rate in the QGP is then evaluated by integrating over the thermal quark and gluon distributions in the QGP. Both thermal quarks and gluons are taken to have thermal masses given by $m_q = m_g = gT/\sqrt{6}$, where T is the temperature of the QGP and g is related to the thermal QCD coupling constant $\alpha_s(2\pi T) = g^2/4\pi$, which has values ranging from ~ 0.23 for $T = 700$ MeV to ~ 0.42 for $T = 170$ MeV.

For the dynamics of formed QGP in central Pb+Pb collisions at $\sqrt{s_{NN}} = 5.5$ TeV at LHC, we assume that it evolves boost invariantly in the longitudinal direction but with an accelerated transverse expansion. Specifically, its volume expands in the proper time τ according to $V(\tau) = \pi R^2(\tau)\tau c$, where $R(\tau) = R_0 + a(\tau - \tau_0)^2/2$ is the transverse radius with an initial value $R_0 = 7$ fm, the QGP formation time τ_0=0.2 fm/c, and the transverse acceleration $a = 0.1\ c^2$/fm. Starting with an initial temperature $T_0 = 700$ MeV, which gives an initial energy density of about 50% higher than that predicted by the AMPT model [52] or the Color Glass Condensate [179], the time dependence of the temperature is obtained from entropy conservation, leading to the critical temperature $T_C = 170$ MeV at proper time $\tau_C = 6.4$ fm/c. The initial number of charm pairs is taken to be $dN_{c\bar{c}}/dy = 20$ at midrapidity, which is of similar magnitude as that estimated from initial hard nucleon-nucleon collisions based on the next-to-leading order pQCD calculations.

In the left window of Fig. 116, we show the temperature dependence of the charm quark pair production rates from the leading order (dashed line) and the next-to-leading order (solid line) with their ratio shown in the inset. The contributions from the leading order and next-

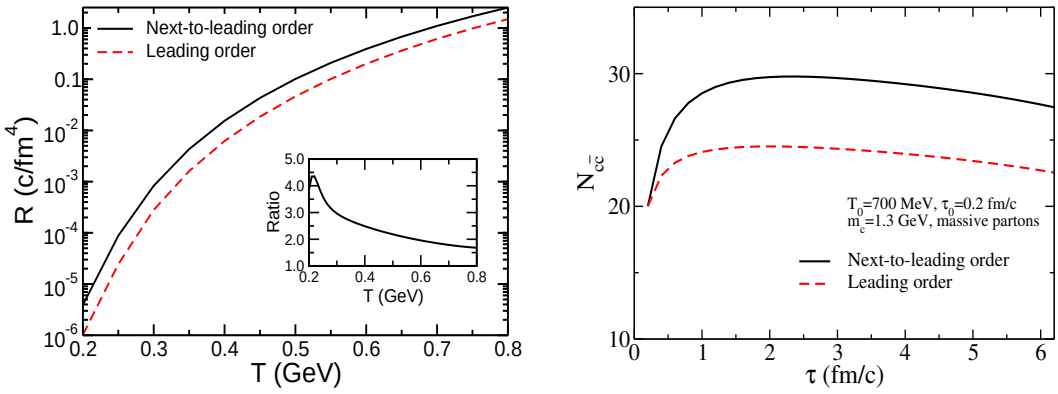

Figure 116: Time evolution of charm pair production rate (left window) and number (right window) in central Pb+Pb collisions at $\sqrt{s_{NN}}$ = 5.5 TeV for an initial QGP temperature of 700 MeV. Dashed and solid lines are results from the leading order and next-to-leading order calculations, respectively. The inset in left window gives the ratio of charm production rate in the next-to-leading order to that in the leading order.

leading order are of similar magnitude and both are appreciable at high temperatures. The total number of charm pairs as a function of the proper time τ in an expanding QGP produced at LHC is shown in the right window of Fig. 116. As shown by the dashed line, including only the leading-order contribution from two-body processes increases the number of charm pairs by about 10% during the evolution of the QGP. Adding the next-leading-order contribution through virtual corrections to two-body precesses as well as the $2 \to 3$ processes further increases the charm quark pair number by about 25% as shown by the solid line. The charm quark pair number reaches its peak value at $\tau \sim 2$ fm/c and then deceases with the proper time as a result of larger charm annihilation than creation rates when the temperature of the QGP drops. At the end of the QGP phase, it remains greater than both its initial value and the chemically equilibrium value of about 5 at T_C = 170 MeV. The number of charm quark pairs produced from the QGP would be reduced by a factor of about 3 if a larger charm quark mass of 1.5 GeV or a lower initial temperature of T_0 = 630 MeV is used. It is, however, not much affected by using massless gluons due to increase in the gluon density. On the other hand, increasing the initial temperature to 750 MeV would enhance the thermally produced charm quark pairs by about a factor of 2.

7.9. Charm production in nuclear collisions

B. Z. Kopeliovich and I. Schmidt

Nuclear suppression of heavy flavor inclusive production in hard partonic collisions has a leading twist component related to gluon shadowing, as well as a higher twist contribution related to the nonzero separation of the produced $\bar{Q}Q$ pair. Both terms are evaluated and suppression for charm production in heavy ion collisions at LHC is predicted.

7.9.1. Higher twist shadowing Heavy flavors are produced via gluon fusion, therefore they serve as a good probe for the gluon distribution function in nuclei. The light-cone dipole approach is an effective tool for the calculation of nuclear effects in these processes, since the phenomenological dipole cross section includes by default all higher order and higher twist terms.

The production of heavy flavors can be treated as freeing of a $\bar{Q}Q$ fluctuation in the incoming hadron, in which the interaction with such a small dipole (actually, with a three-body $\bar{Q}Qg$ dipole) results in nuclear shadowing, which is a higher twist, $1/m_Q^2$, effect. Although very small, it steeply rises with energy and reaches sizable magnitude at the energy of LHC. The effect of this higher twist shadowing on charm production in minimal bias and central collisions of heavy ions at the energies of RHIC and LHC is shown in figure 117 as the difference between solid and dashed curves.

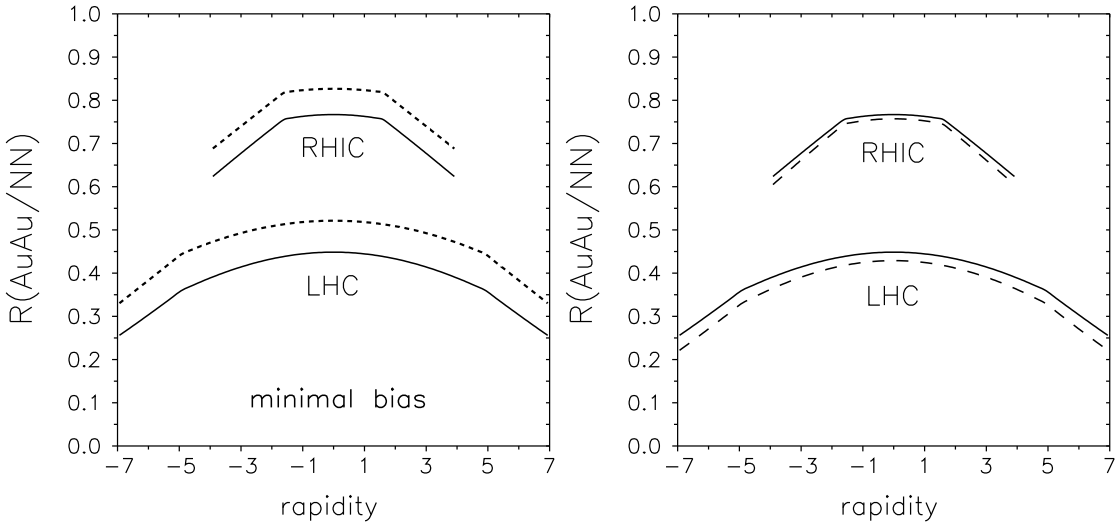

Figure 117: Results for $R_{\mathrm{AA}/NN}$ as function of rapidity for minimal bias (plot on the left) and central (plot on the right) collisions, for RHIC (upper curves) and LHC (lower curves) energies. The difference between solid and dashed or dotted lines shows the effect of higher twist shadowing, see the text.

7.9.2. Process dependent leading twist gluon shadowing The projectile fluctuations containing, besides the $\bar{Q}Q$, also gluons, are responsible for gluon shadowing, which is a leading twist effect. Indeed, the aligned jet configurations, i.e. the fluctuation in which the $\bar{Q}Q$ pair carries the main fraction of the momentum, have a large and scale independent, transverse size. Gluon shadowing is expected to be a rather weak effect [318] due to the localization of the glue inside small spots in the proton [96]. This is confirmed by the latest NLO analysis [15] of data on DIS on nuclei.

Unlike for the DIS case, where the produced $\bar{q}q$ is predominantly in a color octet state, in the case of hadroproduction the $\bar{Q}Q$ may be either colorless or a color octet. Moreover, in the latter case it may have different symmetries [319, 320]. Nonperturbative effects, which

cause a contraction of the gluon cloud, may be absent for a colorless $\bar{Q}Q$, leading to a much stronger shadowing compared to DIS. This possibility was taken into account predicting the rather strong nuclear effects depicted in figure 117. This part of the prediction should be taken with precaution, since it has never been tested by data.

Figure 117 shows our results for $R_{\mathrm{AA}/NN}$ as function of rapidity for minimal bias and central collisions. These calculations do not include the suppression caused by energy conservation at the ends of the rapidity interval [321].

The rather strong suppression of charm production that we found should be taken into account as part of the strong suppression of high p_T charm production observed in central nuclear collisions at RHIC. At high p_T this effect should fade away because of the rise of x_2, although at the LHC this may be a considerable correction.

7.10. Charm and Beauty Hadrons from Strangeness-rich QGP at LHC

I. Kuznetsova and J. Rafelski

The yields of heavy flavored hadrons emitted by strangeness rich QGP are evaluated within chemical non-equilibrium statistical hadronization model, conserving strangeness, heavy flavor, and entropy yields at hadronization.

A relatively large number of hadrons containing charm ($dN_c/dy \simeq 10$) and bottom ($dN_b/dy \simeq 1$) quarks are expected to be produced at central rapidity in heavy ion (Pb–Pb) collisions at the Large Hadrons Collider (LHC). This report summarized results of our more extensive recent report [322], and amplifies its findings with reference to the 'first day' LHC-ion results. Differing from other recent studies which assume that the hadron yields after hadronization are in chemical equilibrium [323], we form the charm hadron yields in the statistical hadronization approach based on an abundance of u, d, s quark pairs fixed by the bulk properties of a practically chemically equilibrated QGP phase.

In proceeding in this fashion we are respecting the constraints of the recombinant dynamic model [324]. The absolute yields (absolute chemical equilibrium) depend in addition to recombination on absolute heavy quark yield $dN_{b,c}/dy$. We are fully implementing the relative chemical equilibrium, that is the formation of heavy (charmed) hadrons according the the relative phase space, thus ratios of yields presented here are a complete and reliable prediction characterized by QGP entropy and strangeness content.

It is energetically more effective for strange quarks to emerge bound to heavy quarks. Said differently, the reaction $\mathrm{K} + D \to \pi + D_s$ is strongly exothermic, with $\Delta Q \simeq 240\,\mathrm{MeV}$, and similarly for the bottom quark. Considering that the phase space for hadronization is characterized by a domain temperature $T = 160 \pm 20$ MeV, in presence of strangeness the yield tilts in favor D_s over D, and B_s over B.The variability in the light and strange quark content at given hadronization temperature T is accomplished introducing the phase space occupancy $\gamma_s^{\mathrm{H}} > 1$, $\gamma_q^{\mathrm{H}} > 1$ of strange, and, respectively, light constituent quarks in the hadron phase. In chemical equilibrium $\gamma_s^{\mathrm{H}} = \gamma_q^{\mathrm{H}} = 1$.

A phase space evaluation of the relative yields leads to the results presented in figure 118,

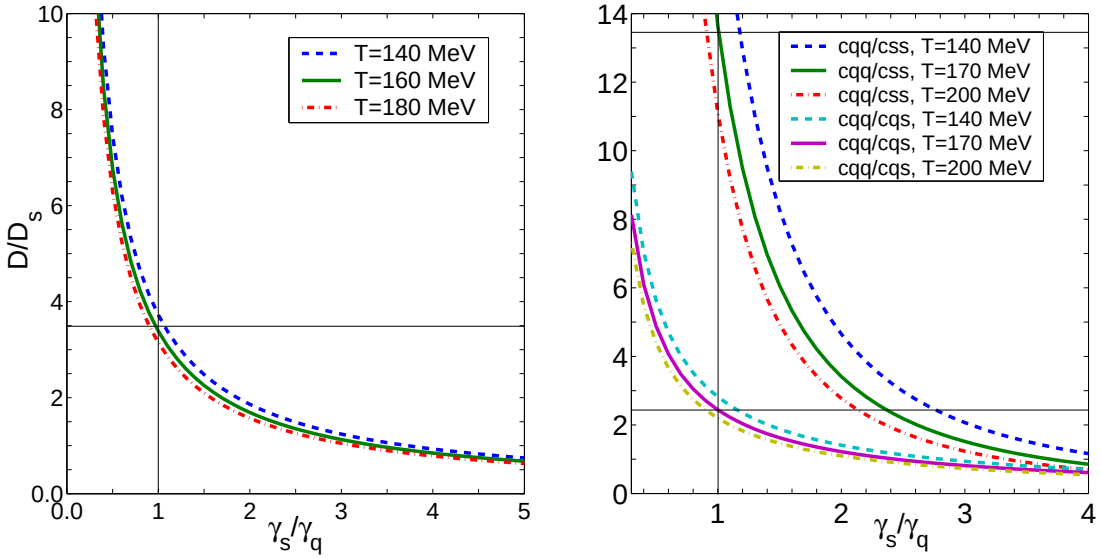

Figure 118: As a function of $\gamma_s^{\rm H}/\gamma_q^{\rm H}$ on left: D/D_s ratio and on right: $cqq/css = (\Lambda_c + \Sigma_c)/\Omega_c$ (upper lines) and $cqq/cqs = (\Lambda_c + \Sigma_c)/\Xi_c$ (lower lines) ratios.

where we show ratio of open charm strange meson and baryons with the corresponding 'less' strange open charmed (strange) meson and baryons, as a function of $\gamma_s^{\rm H}/\gamma_q^{\rm H}$, which is the controlling variable for three values $T = 200$ MeV, $T = 180$–160 MeV and $T = 140$ MeV. The corresponding chemical reference results are indicated by the crossing vertical and horizontal lines. For B, B_s mesons the results are the same as for D, D_s mesons, see [322] for details.

The challenge is to understand what values of $\gamma_s^{\rm H}/\gamma_q^{\rm H}$ a fast hadronizing QGP implies. We obtain these by requiring that the hadronization of QGP proceeds conserving the entropy dS/dy and strangeness $ds/dy = d\bar{s}/dy$ content of QGP. For LHC the expected ratio $s/S = 0.038$ [169] at $T = 140$–180 MeV which implies in the hadron phase $\gamma_s/\gamma_q = 1.8$–2 [168]. This entails a considerable shift of open charm hadrons away from hadron chemical equilibrium yield towards states containing strangeness in all cases considered in figure 118 (and similarly for the bottom flavor). The hadronization process, as expected, favors formation of strange charmed meson and baryons, once the actual QGP strangeness yield near/above-chemical equilibrium is allowed for.

7.11. Charmonium Suppression in Strangeness-rich QGP

I. Kuznetsova and J. Rafelski

The yields of $c\bar{c}$ mesons formed in presence of entropy and strangeness rich QGP are evaluated within chemical non-equilibrium statistical hadronization model, conserving strangeness and entropy yields at hadronization. We find that for a given dN_c/dy charm yield, the abundant presence of light an strange quarks favors formation of D, D_s mesons and to suppression of charmonium.

There is considerable energetic advantage for a charm quark to bind with a strange quark – most, if not all, charmonium–strange meson/baryon reactions of the type $c\bar{c} + sX \to cX + \bar{c}s$,

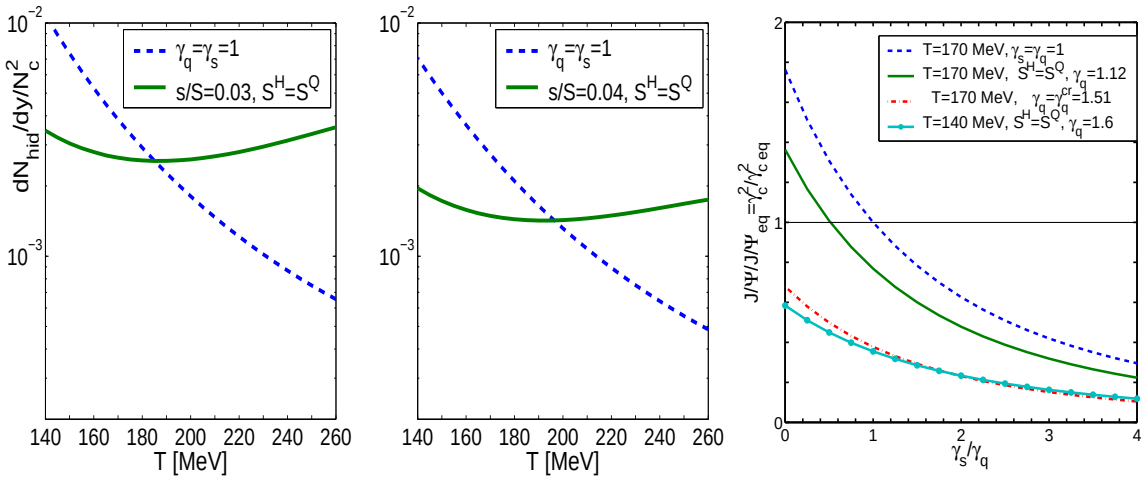

Figure 119: Left two panels: $c\bar{c}/N_c^2$ relative yields as a function of hadronization temperature T, right panel ratio $J/\Psi/J/\Psi_{eq}$ as a function of $\gamma_s^{\rm H}/\gamma_q^{\rm H}$, see tex.

where $X \equiv \bar{q} = \bar{u}, \bar{d}$ or $X \equiv qq, qs, ss$ are strongly exothermic. In statistical hadronization this phase space effect favors formation of D_s over $c\bar{c}$. Seen from the kinetic model perspective [324], this observation shows a strong channel of charmonium destruction. Thus presence of strangeness facilitates a novel charmonium suppression mechanism [322, 325]. To implement this effect hadronization of QGP must conserve strangeness and entropy and thus cannot be ad-hoc associated with chemical equilibrium.

In the non-equilibrium statistical hadronization model we balance total yield of charmed particles within a given volume dV/dy to the level available in the QGP phase $dN_c/dy \propto dV/dy(\gamma_c^{\rm H}\gamma_i^H + \ldots)$, where a few percent of the yield is in multi-charm baryons and charmonium involving higher powers of $\gamma_c^{\rm H}$. This constraint determines a value of γ_c^H, which for the case of LHC can be considerably above unity. Therefore, the hadronization yields we compute for hidden charm mesons: $dN_{c\bar{c}}/dy \propto dV/dy\gamma_c^{H\,2} \propto (dN_c/dy)^2/(\gamma_i^{H\,2}dV/dy)$. depends on the inverse of the model dependent reaction volume, and scales with the square of the total charm yields [324]. We also show above that for the case that $\gamma_i^H > 1$ a hereto unexpected suppression of 'onium yield is expected.

In figure 119 the yield of all hidden charm $c\bar{c}$ (sum over all $c\bar{c}$ mesons) is shown, normalized by the square of $dN_c/dy = 10$ (middle panel for LHC environment) and $dN_c/dy = 3$ (left panel, RHIC environment), as a function of hadronization temperature T. We show result for $s/S = 0.03$ with $dV/dy = 600\,\mathrm{fm}^3$, $T = 200$ MeV (solid line, left panel) and for $s/S = 0.04$ with $dV/dy = 800\,\mathrm{fm}^3$, $T = 200$ MeV (solid line, middle panel). Results shown for chemical equilibrium case (dashed lines) are for the values $\gamma_s = \gamma_q = 1$. For the chemical non-equilibrium hadronization (solid lines $\gamma_i^H > 1, i = q, s$), the QGP and hadron phase space is evaluated conserving entropy $S^Q = S^H$ and strangeness $s^Q = s^H$ between phases.

We see, comparing the left and middle panel that the yield of $c\bar{c}$ mesons decreases with

increasing specific strangeness content (note logarithmic scale). The chemical suppression effect is further quantified in third, right panel in figure 119, where we show the ratio $J/\Psi/J/\Psi_{eq} = \gamma_c^2/\gamma_{ceq}^2$ as a function of $\gamma_s^{\rm H}/\gamma_q^{\rm H}$ at fixed value of $\gamma_q^{\rm H}$ and, as required, entropy conservation for $T = 140, 170$ MeV. For $T = 140$ MeV we show result with $\gamma_q = 1.6$ (solid dotted line) which corresponds entropy conservation between QGP and hadronic phase for this hadronization temperature. For $T = 170$ MeV we show results with $\gamma_q \approx \gamma_q^{cr} = 1.51 \equiv e^{m_\pi/2T}$ (dash-dot line), $\gamma_q = 1.12$ (solid line) and $\gamma_q = 1$ (dashed line). For $\gamma_q = 1.12$ entropy is conserved in hadronization at $T = 170$ MeV .

The formation of the $B_c(\bar{b}c)$ proposed as another QGP signature [326] has not been evaluated in the present work, since this particle yield suffers from additional (canonical) suppression. Kinetic formation models suggest significant enhancement of this double exotic meson, as compared to a cascade of NN reactions.

7.12. J/ψ p_T spectra from in-medium recombination

R. L. Thews and M. L. Mangano

We consider production of J/ψ by recombination of c, $\bar{c}$ quarks produced in separate N-N interactions during Pb-Pb collisions. Inputs for the calculation include the NLO pQCD spectra of charm quarks, plus a range of nuclear parameters taken from extrapolation of results at RHIC energy.

The possibility that J/ψ could be formed in AA collisions by recombination in a region of color deconfinement was first developed in Ref. [324]. It was motivated by the realization that the total formation probability would be proportional to the square of the total number of $c\bar{c}$ pairs, which at RHIC and especially LHC provide a large enhancement factor. One can calculate the p_T and y spectra of J/ψ formed either through recombination or direct initial production, using the corresponding quark spectra from a pQCD NLO calculation [297] in individual nucleon-nucleon interactions. The method involves generating a sample of these initially-produced $c\bar{c}$ pairs, smearing the transverse momentum with a gaussian distribution of width $\langle {k_T}^2 \rangle$ to simulate nuclear broadening and confinement effects, and weighting each pair with a formation cross section. This procedure naturally divides the total pair sample into two categories: the so-called “diagonal" sample, which pairs the c and $\bar{c}$ from the same nucleon-nucleon interaction and the “off-diagonal" sample, where c and $\bar{c}$ come from different nucleon-nucleon interactions. The spectra of the resulting J/ψ will retain some memory of the charm quark spectra and provide signatures of the two different origins. For example, one expects the p_T spectrum of non-diagonal pairs to be softer, since it is less likely for high-p_T c and $\bar{c}$ quarks from independent scatterings to be close enough in phase-space to coalesce into a J/ψ. Results for RHIC were presented in Ref. [327], where the primary signal was found to be a narrowing of the non-diagonal y and p_T spectra, relative to the diagonal ones. We show in Fig. 120 the calculated J/ψ width $\langle {p_T}^2 \rangle$ as a function of $\langle {k_T}^2 \rangle$, for central and forward production in ALICE. $\langle {p_T}^2 \rangle$ grows with $\langle {k_T}^2 \rangle$ for both the direct initial production and the in-medium formation, but the latter widths are always smaller than the former. Widths at small y are also greater than at large y, reflecting the underlying pQCD distributions. To fix

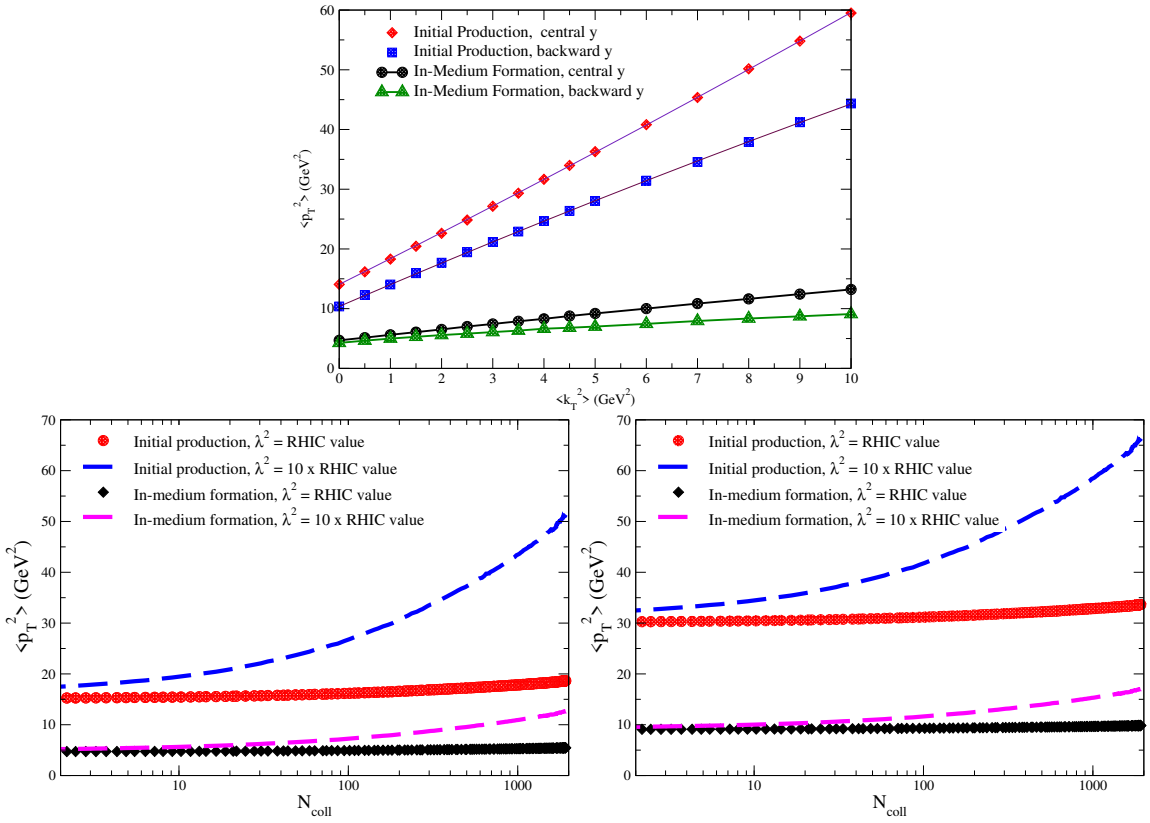

Figure 120: Upper: Variation of J/ψ $\langle {p_T}^2 \rangle$ with the nuclear smearing parameter. Lower: dependence on the intrinsic $\langle {k_T}^2 \rangle_{pp}$, with $\langle {k_T}^2 \rangle_{pp}$ = 0.0 (left) and 5.0 (right).

the nuclear smearing parameter values, we use a relation between measurable $\langle {p_T}^2 \rangle$ in pp and pA interactions,

$$\langle {p_T}^2 \rangle_{pA} - \langle {p_T}^2 \rangle_{pp} = \lambda^2 \, [\bar{n}_A - 1], \tag{60}$$

where $\bar{n}_A$ is the impact-averaged number of inelastic interactions of the proton projectile in nucleus A, and λ^2 is proportional to the square of the transverse momentum transfer per initial state collision. We use a Glauber model to calculate the centrality dependence of the $\bar{n}_A$, and parameterize the centrality by the total number of collisions, N_{coll}. Thus with measurements of $\langle {p_T}^2 \rangle_{pp}$ and $\langle {p_T}^2 \rangle_{pA}$ one can extract λ^2 and calculate the corresponding nuclear broadening for AA interactions. The lower plots of Fig. 120 show the results for Pb-Pb at 5.5 TeV, with $\langle {k_T}^2 \rangle_{pp}$=0 and 5 GeV^2. For both cases the J/ψ widths will provide a clear discrimination between direct initial production and in-medium formation. In general, one would expect some combination of initial production and in-medium formation, so the prediction is bounded from above and below. There is almost no change in the $p_T(c)$ spectra between 5.5 and 14 TeV. Thus we can use the 14 TeV pp data to determine $\langle {k_T}^2 \rangle_{pp}$ at 5.5 TeV. One can then expect that the absence of energy dependence will also hold for p-Pb results, allowing us to also determine λ^2 at 5.5 TeV from a measurement at any LHC energy, thus fixing the prediction for curves such as those in Fig. 120.

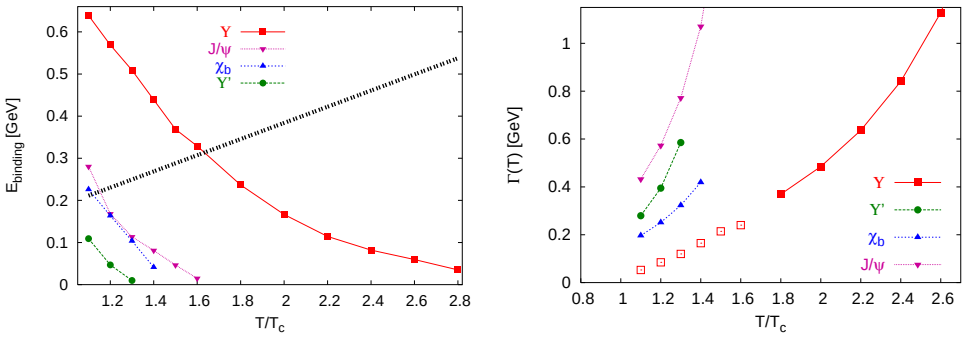

Figure 121: Upper limit of the binding energy (left) and the width (right) of quarkonium states. For better visibility, in the limit of small binding, the open squares show the width of the 1S bottomonium state multiplied by six.

7.13. Predictions for quarkonia dissociation

Á. Mócsy and P. Petreczky

We predict the upper bound on the dissociation temperatures of different quarkonium states.

In a recent paper [328] we analyzed in detail the quarkonium spectral functions. This analysis has shown that spectral functions calculated using potential model for the non-relativistic Green's function combined with perturbative QCD can describe the available lattice data on quarkonium correlators both at zero and finite temperature in QCD with no light quarks [328]. Charmonia, however, were found to be dissolved at temperatures significantly lower than quoted in lattice QCD studies, and in contradiction with other claims made in recent years from different potential model studies. In [329] we extended the analysis to real QCD with one strange quark and two light quarks using new lattice QCD data on quark anti-quark free energy obtained with small quark masses [330].

Here we briefly outline the main results of the analysis of [329], in particular the estimate for the upper limit on the dissociation temperatures. There is an uncertainty in choosing the quark-antiquark potential at finite temperature. In [329] we considered two choices of the potential, both consistent with the lattice data [330]. The more extreme choice, still compatible with lattice data, leads to the largest possible binding energy. In this most binding potential some of the quarkonium states survive above deconfinement, but their strongly temperature-dependent binding energy is significantly reduced. This is shown in figure 121. Due to the reduced binding energy thermal activation can lead to the dissociation of quarkonia, even when the corresponding peak is present in the spectral function. Knowing the binding energy we estimate the thermal width using the analysis of [331]. The expression of the rate of thermal excitation has particularly simple form in the two limiting cases:

$$\Gamma(T) = \frac{(LT)^2}{3\pi} M \mathrm{e}^{-E_{\rm bin}/T}\,,\ E_{\rm bin} \gg T \qquad \Gamma(T) = \frac{4}{L}\sqrt{\frac{T}{2\pi M}}\,,\ E_{\rm bin} \ll T\,.$$

Here M is the quarkonium mass, L is the size of the spatial region of the potential, given by the distance from the average quarkonium radius to the top of the potential, i.e. $L = r_{\rm med} - \langle r^2\rangle^{1/2}$,

$r_{\rm med}$ being the effective range of the potential [329]. Using the above formulas we estimate the thermal width of charmonium and bottomonium states. Since in the deconfined phase $E_{\rm bin} < T$ the $1S$ charmonium and $2S$ and $1P$ bottomonium states are in the regime of weak binding, and their width is large, as shown in figure 121. The $1S$ bottomonium is strongly bound for $T < 1.6T_c$ and its thermal width is smaller than 40 MeV. For $T > 1.6T_c$, however, even the 1S bottomonium states is in the weak binding regime resulting in the large increase of the width, see figure 121. When the thermal width is significantly larger than the binding energy no peak structure will be present in the spectral functions, even though the simple potential model calculation predicts a peak. Therefore, we define a conservative dissociation temperature by the condition $\Gamma > 2E_{\rm bin}$. The obtained dissociation temperatures are summarized in table 7.13.

Table 7: Upper bound on quarkonium dissociation temperatures.

state	χ_c	ψ'	J/ψ	Υ'	χ_b	Υ
$T_{\rm dis}$	$\leq T_c$	$\leq T_c$	$1.2T_c$	$1.2T_c$	$1.3T_c$	$2T_c$

From the table it is clear that all quarkonium states, except the $1S$ bottomonium, will melt at temperatures considerably smaller than previous estimates, and will for certain be dissolved in the matter produced in heavy ion collision at LHC. Furthermore, it is likely that at energy densities reached at the LHC a large fraction of the $1S$ bottomonium states will also dissolve. It has to be seen to what extent these findings will result in large R_{AA} suppression at LHC. For this more information about initial state effects is needed. Moreover, the spectral functions are strongly enhanced over the free case even when quarkonium states are dissolved [328, 329] indicating significant correlations between the heavy quark and antiquark. Therefore, one should take into account also the possibility of quarkonium regeneration from correlated initial quark-antiquark pairs.

7.14. Heavy flavor production and suppression at the LHC

I. Vitev

Predictions for the baseline D- and B-mesons production cross sections at $s^{1/2} = 5.5$ TeV at the LHC in p+p collisions are given for $p_T > M_{c,b}$, respectively. New measurements that allow to identify the underlying hard partonic processes in heavy flavor production are discussed. Based on the short D- and B-mesons formation times, medium-induced dissociation is proposed as a mechanism of heavy flavor suppression in the QGP at intermediate p_T. In contrast to previous results on heavy quark modification, this approach predicts suppression of B-mesons comparable to that of D-mesons at transverse momenta as low as $p_T \sim 10$ GeV. Suppression of non-photonic electrons form the primary semi-leptonic decays of charm and beauty hadrons is calculated in the p_T region where collisional dissociation is expected to be relevant.

Predictions for the baseline $D^0, D+, B^0, B+$ cross sections in p+p collisions at the LHC at $s^{1/2} = 5.5$ TeV are given in the left panel of Fig. 122 [332]. At lowest order we also include

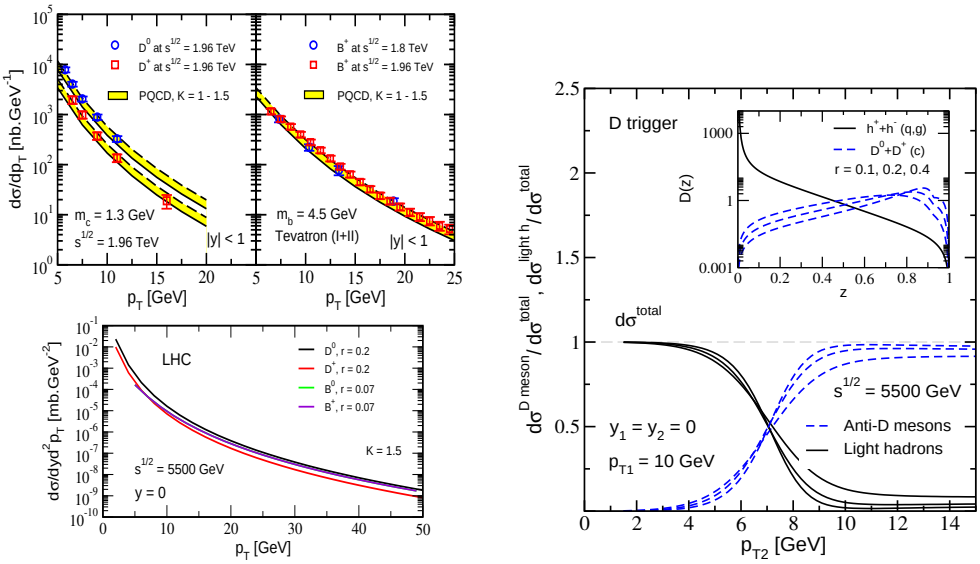

Figure 122: Left panel: D- and B-meson production cross sections st $s^{1/2} = 5.5$ TeV [332]. Comparison to available data at Tevatron is also shown. Away-side hadron composition of $p_T = 10$ GeV D-meson triggered jet [332]. Right panel: Hadron composition of the away-side D-meson triggered jet at LHC energies as a function of the hardness of the heavy quark fragmentation function.

$Q + g \to Q + g$, $Q + q(\bar{q}) \to Q + q(\bar{q})$ and processes that give a dominant contribution to the single inclusive D- and B-mesons [332]. The right panel of Fig. 122 illustrates a method to determine the underlying heavy flavor production mechanism through the away-side hadron composition of $D-$ and $B-$meson triggered jets [332].

The GLV approach is to multiple parton scattering [333] can be easily generalized to various compelling high energy nuclear physics problems, such as meson dissociation in dense nuclear matter [334]. $R_{AA}(p_T)$ results for charm and beauty from this novel suppression mechanism at RHIC and LHC are shown in the left panel of Fig. 123. Attenuation rate similar to the light hadron quenching from radiative energy loss [333] is achieved. The right panel of Fig. 123 shows the suppression of the single non-photonic $0.5(e^+ + e^-)$ in central Au+Au and Pb+Pb collisions at RHIC and LHC respectively [334]. The separate measurement of intermediate p_T $D-$ and $B-$meson quenching will allow to experimentally determine the correct physics mechanism of heavy flavor suppression [335].

7.15. Quarkonium shadowing in pPb and Pb+Pb collisions

R. Vogt

The d+Au data from RHIC, including the pA results from the fixed-target CERN SPS pA data, suggest increased importance of initial-state shadowing and decreasing nuclear absorption with increasing energy [336]. This is not surprising since smaller x is probed

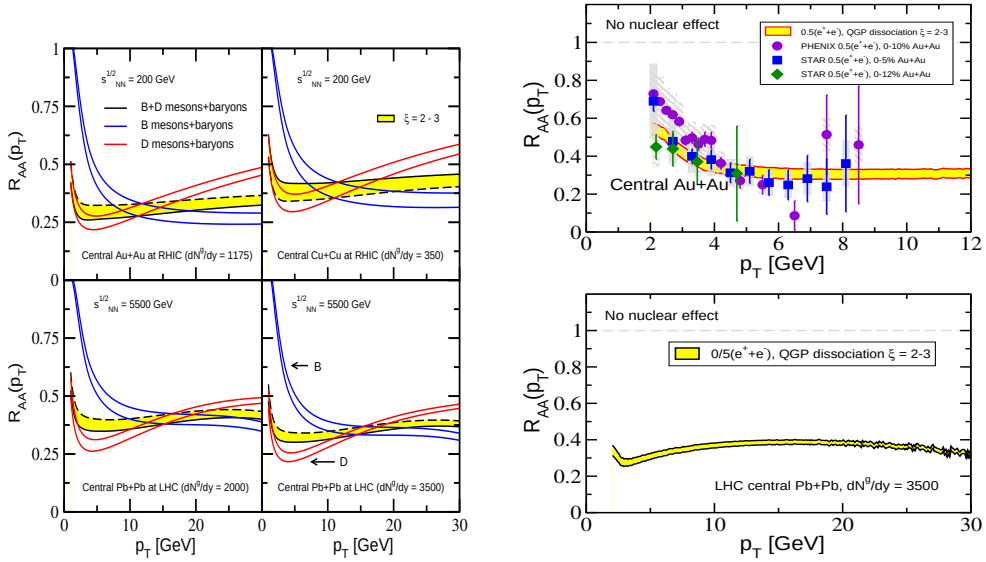

Figure 123: Left panel: Suppression of D- and B-meson production via collisional dissociation in the QGP. Results on $R_{AA}(p_T)$ in central Pb+Pb collisions at the LHC are compared to central Au+Au and Cu+Cu collisions at RHIC [334, 335]. Right panel: Suppression of inclusive non-photonic electrons from D- and B-meson spectra softened by collisional dissociation in central Au+Au collisions at RHIC compared to data and Pb+Pb collisions at the LHC.

at higher energy while absorption due to multiple scattering is predicted to decrease with energy [337]. The CERN SPS data suggest a J/ψ absorption cross section of about 4 mb without shadowing, and a larger absorption cross section if it is included since the SPS x range is in the antishadowing region. The d+Au RHIC data support smaller absorption, $\sigma^{J/\psi}_{\rm abs} \sim 0-2$ mb. Thus our predictions for J/ψ and Υ production in pPb and Pb+Pb interactions at the LHC are shown for initial-state shadowing alone with no absorption or dense matter effects. We note that including absorption would only move the calculated ratios down in proportion to the absorption survival probability since, at LHC energies, any rapidity dependence of absorption is at very large $|y|$ [338], outside the detector acceptance.

We present $R_{p\rm Pb}(y) = p{\rm Pb}/pp$ and $R_{\rm PbPb}(y) = {\rm PbPb}/pp$ for J/ψ and Υ. Since the pp, pPb and Pb+Pb data are likely to be taken at different energies (14 TeV, 8.8 TeV and 5.5 TeV respectively), to make the calculations as realistic as possible we show several different scenarios for $R_{p\rm Pb}(y)$ and $R_{\rm PbPb}(y)$. The lead nucleus is assumed to come from the right in pPb. All the pA calculations employ the EKS98 shadowing parameterization [339, 340]. The difference in the J/ψ and Υ results is primarily due to the larger Υ mass which increases the x values by about a factor of three. In addition, the higher Q^2 reduces the overall shadowing effect.

The top of Fig. 124 shows $R_{p\rm Pb}(y)$ for pPb/pp with both systems at $\sqrt{S_{NN}} = 8.8$ and 5.5 TeV (dashed and dot-dashed curves respectively), ignoring the $\Delta y = 0.46$ rapidity shift at 8.8 TeV. For the J/ψ, these ratios are relatively flat at forward rapidity where the x in the lead

is small. The larger x and greater Q^2 for the Υ brings the onset of antishadowing closer to midrapidity, within the range of the ALICE dimuon spectrometer. At far backward rapidity, a rise due to the antishadowing region is seen. The lower energy moves the antishadowing peak to the right for both quarkonia states. We show $R_{p\mathrm{Pb}}(y)$ with pPb at 8.8 TeV and pp at 14 TeV with $\Delta y = 0$ in the dotted curves. The effect on the J/ψ is an apparent lowering of the dashed curve. Since the Υ rapidity distribution is narrower at 8.8 TeV than at 14 TeV in the rapidity range shown here, the Υ curve turns over at large $|y|$. (This effect occurs at $|y| > 6$ for the J/ψ.) The solid curves show $R_{p\mathrm{Pb}}(y)$ for 8.8 TeV pPb and 14 TeV pp with the rapidity shift. Both the J/ψ and Υ ratios are essentially constant for $y > -2.5$. Thus relying on ratios of pA to pp collisions at different energies to study shadowing (or other small x effects) may be difficult because the shadowing function is hard to unfold when accounting for the pA Δy as well as the difference in x. If d+Pb collisions were used, Δy would be significantly reduced [341].

The lower part of Fig. 124 shows $R_{\mathrm{PbPb}}(y)$ for the J/ψ and Υ at 5.5 TeV for both systems. No additional dense matter effects such as $Q\overline{Q}$ coalescence or plasma screening are included. The EKS98 (dashed) and nDSg [15] (dot-dashed) shadowing parameterizations are compared. The results are very similar over the entire rapidity range. (Other shadowing parameterizations,which do not agree with the RHIC d+Au data, give different $R_{\mathrm{PbPb}}(y)$.) There are antishadowing peaks at far forward and backward rapidity. As at RHIC, including shadowing on both nuclei lowers the overall ratio relative to $R_{p\mathrm{Pb}}(y)$ as well as making $R_{\mathrm{PbPb}}(y > 2)$ similar to or larger than $R_{\mathrm{PbPb}}(y = 0)$ because, without any other effects, $R_{\mathrm{PbPb}}(y) \sim R_{p\mathrm{Pb}}(y)R_{p\mathrm{Pb}}(-y)$ when all systems are compared at the same $\sqrt{S_{NN}}$. The solid curves show the ratios for Pb+Pb at 5.5 TeV relative to pp at 14 TeV with the EKS98 parameterization. The trends are similar but the magnitude is lower.

Since these calculations reflect what should be seen if nothing else occurs, $R_{\mathrm{PbPb}}(y)$ is expected to differ significantly due to dense matter effects. If the initial J/ψ production is strongly suppressed by plasma screening, then the only observed J/ψ's would be from $c\overline{c}$ coalesence [327] or B meson decays. It should be possible to experimentally distinguish secondary production from the primordial distributions by displaced vertex cuts. Secondary J/ψ production should have a narrower rapidity distribution and a lower average p_T. Both are indicated in central Au+Au collisions at $\sqrt{S_{NN}} = 200$ GeV at RHIC [342]. If J/ψ production in central collisions is dominated by secondary J/ψ's, peripheral collisions should still reflect initial-state effects. Predictions of the centrality dependence of shadowing on J/ψ production at RHIC agree with the most peripheral Au+Au data.

Finally, the J/ψ and Υ rapidity distributions are likely to be inclusive, including feed down from higher quarkonium states. Initial-state effects should be the same for all members of a quarkonium family so that these ratios would be the same for direct and inclusive production.

7.16. Quarkonium suppression as a function of p_T

R. Vogt

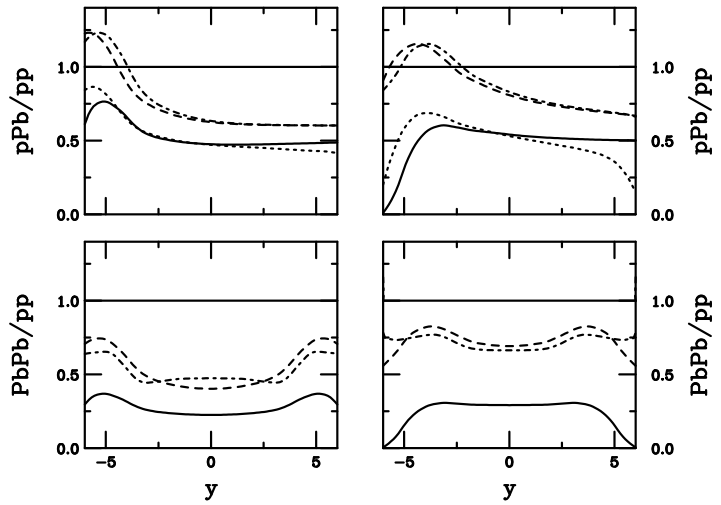

Figure 124: The J/ψ (left) and Υ (right) pPb/pp (top) and PbPb/pp (bottom) ratios as a function of rapidity. The pPb/pp ratios are given for 8.8 (dashed) and 5.5 (dot-dashed) TeV collisions in both cases and 8.8 TeV pPb to 14 TeV pp without (dotted) and with (solid) the beam rapidity shift taken into account. The Pb beam comes from the right. The PbPb/pp ratios are shown for 5.5 TeV in both cases with EKS98 (dashed) and nDSg (dot-dashed) shadowing and also for 5.5 TeV Pb+Pb and 14 TeV pp (solid).

We present a revised look at the predictions of Ref. [343], taking into account newer calculations of the screening mass with temperature and the quarkonia dissociation temperature based on both potential models and calculations of quarkonium spectral functions. The estimates of Digal *et al.* [344] predict lower quarkonium dissociation temperatures, $1.1T_c$ for the J/ψ and $2.3T_c$ for the Υ, with $\mu = 1.15T$. A later review by Satz [345], predicts higher values, more in line with the recent calculations of quarkonium spectral functions, $2.1T_c$ for the J/ψ and $4.1T_c$ for the Υ, as well as $\mu \sim 1.45T$ for $T > 1.1T_c$. We assume $700 < T_0 < 850$ MeV and $\tau_0 = 0.2$ fm [346]. The p_T dependence of the screening is calculated as first discussed in Ref. [347]. Since it may be unlikely for feed down contributions to be separated from the inclusive ψ and Υ yields in AA collisions, we present the indirect ψ'/ψ and Υ'/Υ ratios, with feed down included, in Fig. 125. While the individual suppression factors are smooth as a function of p_T, as shown in Fig. 126 for all four sets of initial conditions and dissociation temperatures, due to their different predicted dissociation temperatures and formation times, they contribute differently to the ratios in Fig. 125.

We have assumed that the ψ'/ψ and Υ'/Υ ratios are independent of p_T, as predicted in the color evaporation model [348]. However, if this is not the case, any slope of the p_T ratios in pp collisions can be calculated and/or evalulated experimentally and deconvoluted from the data. Quarkonium regeneration by coalescence [327] has not been included here. While it is unknown how coalescence production populates the quarkonium levels, since the p_T of quarkonium states produced by coalescence is lower than those produced in the initial NN collisions, higher p_T quarkonia should have a smaller coalescence contribution. The lower

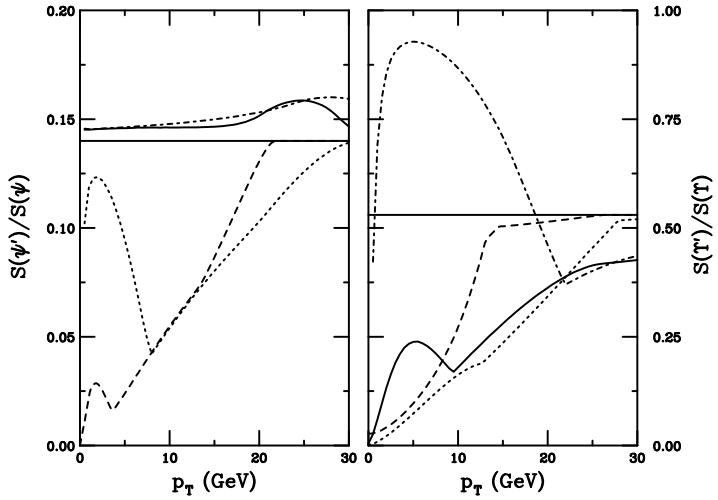

Figure 125: The indirect ψ'/ψ (left) and Υ'/Υ (right) ratios as a function of p_T in Pb+Pb collisions at 5.5 TeV for $T_0 = 700$ MeV (solid and dashed) and 850 MeV (dot-dashed and dotted). The ψ (Υ) results are shown for assumed dissociation temperatures of $1.1T_c$ ($2.3T_c$) (solid and dot-dashed) and $2.1T_c$ ($4.1T_c$) (dashed and dotted) respectively.

$B\overline{B}$ rates should reduce the coalescence probability of Υ production. By taking the ψ'/ψ and Υ'/Υ ratios, we reduce systematics and initial-state effects.

In the case where $T_D = 1.1T_c$ for the J/ψ, its shorter formation time leads to suppression over a larger p_T range than that for the χ_c and ψ', leading to a larger ψ'/ψ ratio than the pp value over all p_T. On the other hand, for the higher dissociation temperature, the p_T range of J/ψ suppression is shorter than for the other charmonium states, giving a smaller ratio than in pp. The low p_T behavior of the dashed and dotted curves in the left-hand side of Fig. 125 is due to the disappearance of χ_c suppression since the χ_c is suppressed over a shorter p_T range than the ψ'.

Since there are more states below the $B\overline{B}$ threshold for the Υ family, the suppression is more complicated, in part because there are also feed down contributions to the Υ', leading to more structure in the Υ'/Υ ratios on the right-hand side of Fig. 125. For $\mu = 1.15T$, the Υ itself is suppressed, albeit over a short p_T range. The dips in the solid and dashed curves occur at the p_T where direct Υ suppression ceases. In the case where $T_D = 4.1T_c$ for the Υ, the initial temperature is not large enough to suppress direct Υ production so that $\Upsilon'/\Upsilon < 1$ for all p_T. The χ_b contributions are responsible for the slopes of the ratios at $p_T > 12$ GeV.

8. Leptonic probes and photons

8.1. Thermal photons to dileptons ratio at LHC

J. K. Nayak, J. Alam, S. Sarkar and B. Sinha

Photons and dileptons are considered to be efficient probes of quark gluon plasma

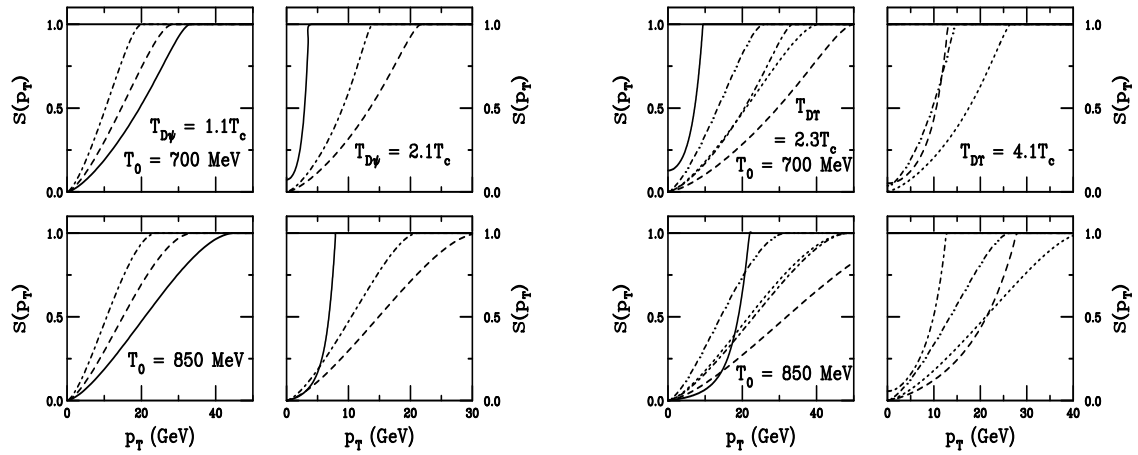

Figure 126: The survival probabilities as a function of p_T for the charmonium (left-hand side) and bottomonium (right-hand side) states for initial conditions at the LHC. The charmonium survival probabilities are J/ψ (solid), χ_c (dot-dashed) and ψ' (dashed) respectively. The bottomonium survival probabilities are given for Υ (solid), χ_{1b} (dot-dashed), Υ' (dashed), χ_{2b} (dot-dot-dash-dashed) and Υ'' (dotted) respectively. The top plots are for $T_0 = 700$ MeV while the bottom are for $T_0 = 850$ MeV. The left-hand sides of the plots for each state are for the lower dissociation temperatures, $1.1T_c$ for the J/ψ and $2.3T_c$ for the Υ while the right-hand sides show the results for the higher dissociation temperatures, $2.1T_c$ for the J/ψ and $4.1T_c$ for the Υ.

(QGP) expected to be created in heavy ion collisions at ultra-relativistic energies. However, the theoretical calculations of the transverse momentum (p_T) spectra of photons ($d^2N_\gamma/d^2p_Tdy_{y=0}$) and dileptons ($d^2N_{\gamma^*}/d^2p_Tdy_{y=0}$) depend on several parameters which are model dependent (see [349, 350] and references therein). In the present work it is shown that the model dependences involved in individual photon and dilepton spectra are canceled out in the ratio, R_{em} defined as: $R_{em} = (d^2N_\gamma/d^2p_Tdy)_{y=0}/(d^2N_{\gamma^*}/d^2p_Tdy)_{y=0}$.

The invariant yield of thermal photons can be written as $d^2N_\gamma/d^2p_Tdy = \sum_{i=Q,M,H}\int_i\left(d^2R_\gamma/d^2p_Tdy\right)_i d^4x$, where Q, M and H represent QGP, mixed (coexisting phase of QGP and hadrons) and hadronic phases respectively. $(d^2R/d^2p_Tdy)_i$ is the static rate of photon production from the phase i, which is convoluted over the expansion dynamics through the integration over d^4x. The thermal photon rate from QGP up to $O(\alpha\alpha_s)$ have been considered. For photons from hadronic matter an exhaustive set of reactions (including those involving strange mesons) and radiative decays of higher resonance states have been considered in which form factor effects have been included.

Similar to photons, the p_T distribution of thermal dileptons is given by, $d^2N_{\gamma^*}/d^2p_Tdy = \sum_{i=Q,M,H}\int_i\left(d^2R_{\gamma^*}/d^2p_Tdydm^2\right)_i dM^2d^4x$. The limits for the integration over M are fixed from experimental measurements. Here we consider $2m_\pi < M < 1.05$ GeV. Thermal dilepton rate from QGP up to $O(\alpha^2\alpha_s)$ has been considered. For the hadronic phase we include the

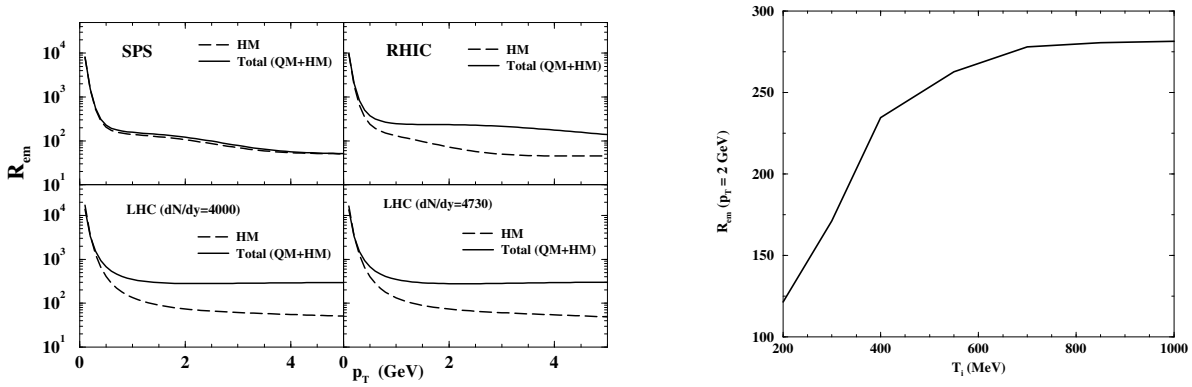

Figure 127: Left panel: Variation of R_{em} with p_T, right panel: variation of $R_{em}(p_T = 2\text{GeV})$ with T_i.

Table 8: The values of various parameters - thermalization time (τ_i), initial temperature (T_i), freeze-out temperature (T_f) and hadronic multiplicity dN/dy - used in the present calculations.

Accelerator	$\frac{dN}{dy}$	$\tau_i(fm)$	$T_i(GeV)$	$T_f(MeV)$
SPS	700	1	0.2	120
RHIC	1100	0.2	0.4	120
LHC	4000	0.08	0.85	120
LHC	4730	0.08	0.905	120

dileptons from the decays of light vector mesons [349]. The space time evolution of the system has been studied using (2+1) dimensional relativistic hydrodynamics with longitudinal boost invariance and cylindrical symmetry. The calculations have been performed for the initial conditions mentioned in table 8 (see also [349]). The values of parameters shown in table 8 reproduce the various experimental data from SPS and RHIC. For LHC we have chosen two values of T_i corresponding to two values of dN/dy. We use the Bag model EOS for the QGP phase. For EOS of the hadronic matter all resonances with mass ≤ 2.5 GeV have been considered

The variation of R_{em} with p_T for different initial conditions are depicted in Fig. 127 (left panel). At SPS, the contributions from hadronic matter (HM) coincides with the total and hence it becomes difficult to make any conclusion about the formation of QGP. However, for RHIC and LHC the contributions from HM are less than the total indicating large contributions from quark matter. The quantity, R_{em}, reaches a plateau beyond $p_T = 1$ GeV for all the three cases *i.e.* for SPS, RHIC and LHC. However, it is very important to note that the values of R_{em} at the plateau region are different, *e.g.* $R_{em}^{LHC} > R_{em}^{RHIC} > R_{em}^{SPS}$. Now for all the three cases, SPS, RHIC and LHC, except T_i all other quantities *e.g.* T_c, v_0, T_f and EOS are same, indicating that the difference in the value of R_{em} in the plateau region originates only due to different values of T_i for the three cases (Fig. 127, right panel). This, hence can be used as a measure of T_i.

We have observed that although the individual p_T distribution of photons and lepton pairs are sensitive to different EOS (lattice QCD, for example) the ratio R_{em} is not. It is also noticed that R_{em} in the plateau region is not sensitive to the medium effects on hadrons, radial flow, T_c, T_f and other parameters.

It is interesting to note that the nature of variation of the quantity, R_{em}^{pQCD}, which is the corresponding ratio of photons and lepton pairs from hard processes only is quite different from $R_{em}^{thermal}$ for p_T up to ~ 3 GeV indicating that the observed saturation is a thermal effect.

8.2. Prompt photon in heavy ion collisions at the LHC: A "multi-purpose" observable

F. Arleo

I emphasize in this contribution how prompt photons can be used to probe nuclear parton densities as well as medium-modified fragmentation functions in heavy ion collisions. Various predictions in p–A and A–A collisions at LHC energies are given.

Prompt photon production in hadronic collisions has been extensively studied, both experimentally and theoretically, over the past 25 years (see [351] and references therein). As indicated in Ref. [351], it is remarkable that almost all existing data from fixed-target to collider energies can be very well understood within perturbative QCD at NLO. In these proceedings, I briefly discuss how prompt photons in nuclear collisions (p–A and A–A) may allow for a better understanding of interesting aspects discussed in heavy-ion collisions, namely the physics of nuclear parton distribution functions and medium-modified fragmentation functions. Parton distribution functions in nuclei are so far poorly constrained, especially in contrast with the high degree of accuracy currently reached in the proton channel, over a wide x and Q^2 domain. In particular, only high-x ($x \gtrsim 10^{-2}$) and low Q^2 ($Q^2 \lesssim 100$ GeV^2) have been probed in fixed-target experiments. In order to predict hard processes in nuclear collisions at the LHC, a more accurate knowledge on a wider kinematic range is necessary. As stressed in [352], the nuclear production ratio of isolated photons in p-A collisions,

$$R_{p\mathrm{A}}(x_T, y) = \frac{1}{A} \; \frac{\mathrm{d}^3\sigma}{\mathrm{d}y\, \mathrm{d}^2 p_\perp}(p + \mathrm{A} \to \gamma + \mathrm{X}) \Big/ \frac{\mathrm{d}^3\sigma}{\mathrm{d}y\, \mathrm{d}^2 p_\perp}(p + p \to \gamma + \mathrm{X})$$

can be related to a good accuracy (say, less than 5%) to the parton density ratios

$$R^{\mathrm{approx}}(x_T, y = 0) \simeq 0.5\, R^{\mathrm{A}}_{F_2}(x_T) + 0.5\, R^{\mathrm{A}}_{G}(x_T)\; ;\; R^{\mathrm{approx}}(x_T, y = 3) \simeq R^{\mathrm{A}}_{G}(x_T e^{-y}),$$

with $x_T = 2p_\perp/\sqrt{s_{\mathrm{NN}}}$. To illustrate this, the ratio $R_{p\mathrm{A}}$ is computed for isolated photons produced at mid-rapidity in p–Pb collisions at $\sqrt{s_{\mathrm{NN}}} = 8.8$ TeV in Fig. 128 (solid line), assuming the de Florian and Sassot (nDSg) nuclear parton distributions [15]. The above analytic approximation $R^{\mathrm{approx}}_{y=0}$ (dotted line) demonstrates how well this observable is connected to the nuclear modifications of the gluon density and structure function; see also the agreement $(R_{p\mathrm{A}} - R^{\mathrm{approx}}_{y=0})/R_{p\mathrm{A}}$ as a dash-dotted line in Fig. 128. In nucleus-nucleus scattering, the energy loss of hard quarks and gluons in the dense medium presumably produced at LHC may lead to the suppression of prompt photons coming from the collinear fragmentation

process. In Fig. 129, the expected photon quenching in Pb–Pb collisions at $\sqrt{s_{\rm NN}}$ = 5.5 TeV is plotted. A significant suppression due to energy loss (taking ω_c = 50 GeV, see [16] for details) is observed, unlike what is expected when only nuclear effects in the parton densities are assumed in the calculation (dash-dotted line).

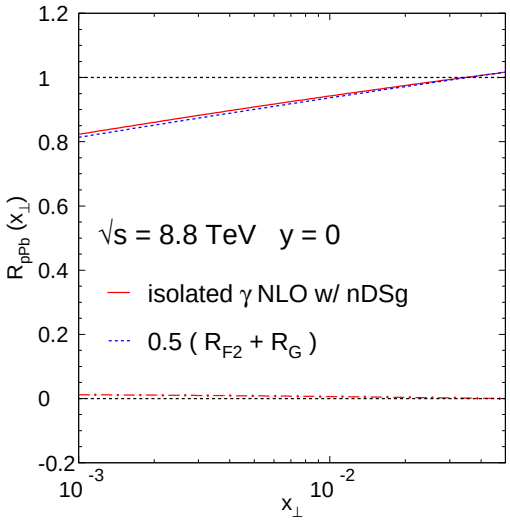

Figure 128: $R_{p\rm Pb}$ of $y = 0$ isolated photons in p–Pb collisions at $\sqrt{s_{\rm NN}}$ = 8.8 TeV.

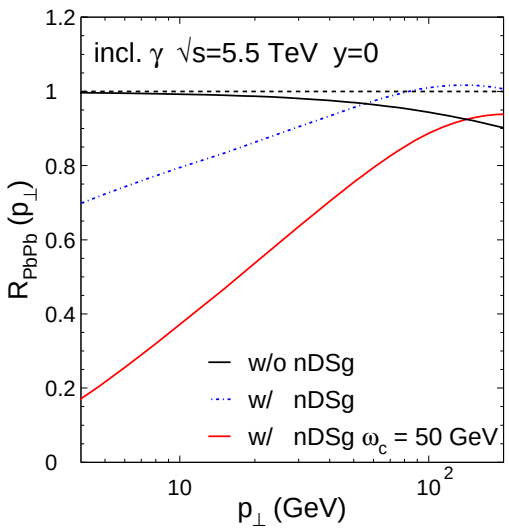

Figure 129: $R_{\rm PbPb}$ of $y = 0$ inclusive photons in Pb–Pb collisions at $\sqrt{s_{\rm NN}}$ = 5.5 TeV.

Finally performing momentum correlations between a prompt photon and a leading hadron in p–p and A–A collisions, yet experimentally challenging, appears to be an interesting probe of vacuum and medium-modified fragmentation function, as discussed in detail in Refs. [353, 354]. We refer in particular the interested reader to Fig. 10 of [353] for the predictions of γ–π^0 momentum-imbalance distributions at the LHC.

8.3. Direct photon spectra in Pb-Pb at $\sqrt{s_{\rm NN}}$ = 5.5 TeV: hydrodynamics+pQCD predictions

F. Arleo, D. d'Enterria and D. Peressounko

The p_T-differential spectra for direct photons produced in Pb-Pb collisions at the LHC, including thermal (hydrodynamics) and prompt (pQCD) emissions are presented.

We present predictions for the transverse momentum distributions of direct-γ (i.e. photons not coming from hadron decays) produced at mid-rapidity in Pb-Pb collisions at $\sqrt{s_{\rm NN}}$ = 5.5 TeV based on a combined hydrodynamics+pQCD approach. Thermal photon emission in Pb-Pb at the LHC is computed with a hydrodynamical model successfully used in nucleus-nucleus collisions at RHIC energies [10]. The initial entropy density of the produced system at LHC is obtained by extrapolating empirically the hadron multiplicities measured at RHIC [355]. Above $p_T \approx 3$ GeV/c, additional prompt-γ production from parton-parton scatterings is computed perturbatively at next-to-leading-order (NLO) accuracy [356]. We use recent parton distribution functions (PDF) [13] and parton-to-photon fragmentation functions

(FF) [357], modified resp. to account for initial-state shadowing+isospin effects [15] and final-state parton energy loss [358].

We follow the evolution of the hot and dense system produced in central Pb-Pb at LHC by solving the equations of (ideal) relativistic 2D+1 hydrodynamics [10, 355] starting at a time $\tau_0 = 1/Q_s \approx 0.1$ fm/c. The system is assumed to have an initial entropy density of $s_0 = 1120$ fm^{-3}, which corresponds to a maximum temperature at the center of $T_0 \approx 650$ MeV ($\langle T_0 \rangle \approx 470$ MeV). We use a quark gluon plasma (QGP) and hadron resonance gas (HRG) equation of state above and below $T_{\rm crit} \approx 170$ MeV resp., connected by a standard Maxwell construction assuming a first-order phase transition at $T_{\rm crit}$. Thermal photon emission is computed using the most recent parametrizations of the QGP and HRG γ rates. For the QGP phase we use the AMY complete leading-log emission rates including LPM suppression [240]. For the HRG phase, we employ the improved parametrization from Turbide *et al.* [359].

Our NLO pQCD predictions are obtained with the code of ref. [356] with all scales set to $\mu = p_T$. Pb-Pb yields are obtained scaling the NLO cross-sections by the number of incoherent nucleon-nucleon collisions: $N_{\rm coll} = 1670$, 12.9 for 0-10% central ($\langle b \rangle = 3.2$ fm) and 60-90% peripheral ($\langle b \rangle = 13$ fm). Nuclear (isospin and shadowing) corrections of the CTEQ6.5M PDFs [13] are introduced using the NLO nDSg parametrization [15]. At relatively low p_T, prompt photon yields have a large contribution from jet fragmentation processes. As a result, final-state parton energy loss in central Pb-Pb affects also the expected prompt γ yields. We account for medium-effects on the γ-fragmentation component by modifying the BFG parton-to-photon FFs [357] with BDMPS quenching weights. The effects of the energy loss are encoded in a single parameter, $\omega_c = \langle \hat{q} \rangle L^2 \approx 50$ GeV, extrapolated from RHIC. The combination of initial-state (shadowing) and final-state (energy loss) effects results in a quenching factor for prompt photons of $R_{PbPb} \approx 0.2$ (0.8) at $p_T = 10$ (100) GeV/c [358].

Our predictions for the direct photon spectra at y=0 in Pb-Pb at 5.5 TeV are shown in Fig. 130. The thermal contribution dominates over the (quenched) pQCD one up to $p_T \approx 4$ (1.5) GeV/c in central (peripheral) Pb-Pb. Two differences are worth noting compared to RHIC results [10]: (i) the thermal-prompt crossing point moves up from $p_T \approx 2.5$ GeV/c to $p_T \approx 4.5$ GeV/c, and (ii) most of the thermal production in this transition region comes solely from the QGP phase. Both characteristics make of semi-hard direct photons at LHC, a valuable probe of the thermodynamical properties of the system.

8.4. Elliptic flow of thermal photons from RHIC to LHC

R. Chatterjee, E. Frodermann, U. Heinz and D. K. Srivastava

We use the longitudinally boost-invariant relativistic ideal hydrodynamic code AZHYDRO [130] to predict the evolution from RHIC to LHC of the transverse momentum spectra and elliptic flow of thermal photons and dileptons at mid-rapidity in ($A\approx200$)+($A\approx200$) collisions. Here we discuss only photons for Au+Au collisions at $b = 7$ fm; for other results and more details see Refs. [360].

The hydrodynamic initial conditions for RHIC collisions are described in [360]. For the

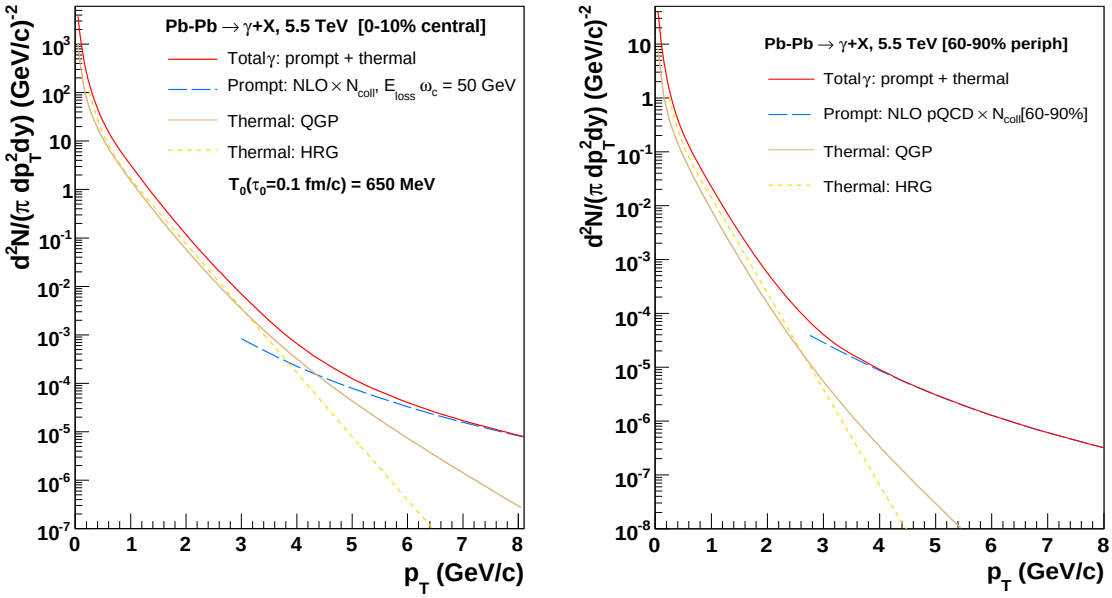

Figure 130: Direct-γ spectra in 0-10% central (left) and 60-90% peripheral (right) Pb-Pb at $\sqrt{s_{\rm NN}}$ = 5.5 TeV, with the thermal (QGP and HRG) and prompt (pQCD) contributions differentiated.

LHC simulations shown in comparison we assume a final charged hadron multiplicity near the upper end of the predicted range: $\frac{dN_{\rm ch}}{dy}(b{=}y{=}0) = 2350$ (680 at RHIC). Correspondingly we increase the initial peak entropy density in central Au+Au collisions from $s_0 = 351\,{\rm fm}^{-3}$ at $\tau_0 = 0.2\,{\rm fm}/c$ for RHIC to $s_0 = 2438\,{\rm fm}^{-3}$ at $\tau_0 = 0.1\,{\rm fm}/c$ for LHC.

1. Thermal photon spectra: Figure 131 shows the thermal photon p_T-spectra (angle-integrated) for RHIC and LHC. At both collision energies the total spectrum is dominated by quark matter once p_T exceeds a few hundred MeV. Its inverse slope ("effective temperature") in the range $1.5 < p_T < 3\,{\rm GeV}/c$ increases by almost 50%, from 303 MeV at RHIC to 442 MeV at LHC, reflecting the higher initial temperature and significantly increased radial flow (visible in the HM contribution) at LHC.

2. Thermal photon elliptic flow: Figure 132 shows the differential elliptic flow of thermal photons at RHIC and LHC, with quark matter (QM) and hadronic matter (HM) radiation shown separately for comparison. The decrease at high p_T of the QM and total photon v_2 reflects the dominance of QM radiation at high p_T (emission from the early, hot stage when radial and elliptic flow are still small). At fixed p_T, the photon elliptic flow from QM radiation is larger at LHC than at RHIC since the LHC fireballs start hotter and fluid cells with a given temperature thus flow more rapidly. At low p_T, hadronic radiation dominates, and since it flows more rapidly at LHC than at RHIC the corresponding photon elliptic is significantly larger at LHC than RHIC. This is different from hadrons whose elliptic flow at low p_T *decreases* from RHIC to LHC, reflecting a redistribution of the momentum anisotropy to higher p_T by increased radial flow [361]. For photons, the elliptic flow is not yet saturated at RHIC, and at low p_T it keeps increasing towards LHC at a rate that overwhelms the loss of momentum anisotropy to the high-p_T domain via radial flow. Contrary to pion v_2 [361], the

p_T-integrated photon elliptic flow roughly doubles (!) from RHIC to LHC.

8.5. Asymmetrical in-medium mesons

I. M. Dremin

Cherenkov gluons may be in charge of mass asymmetry of in-medium mesons which reveals itself in the asymmetry of dilepton spectra.

The hypothesis about the nuclear analogue of the well known Cherenkov effect [194–198] is widely discussed now. The necessary condition for Cherenkov effect in usual or hadronic media is the excess of the corresponding refractive index n over 1. There exists the general linear relation between this excess $\Delta n = n - 1$ and the real part of the forward scattering amplitude $F(E, 0^o)$. In electrodynamics, it is the dipole excitation of atoms in the medium by light which results in the Breit-Wigner shape of the photon amplitude. In a nuclear medium, this should be the amplitude of gluon scattering on some internal modes of the medium. In absence of the theory of such media I prefer to rely on our knowledge of hadronic reactions. From experiments at comparatively low energies we learn that the resonances are abundantly produced. They are described by the Breit-Wigner amplitudes which have a common feature

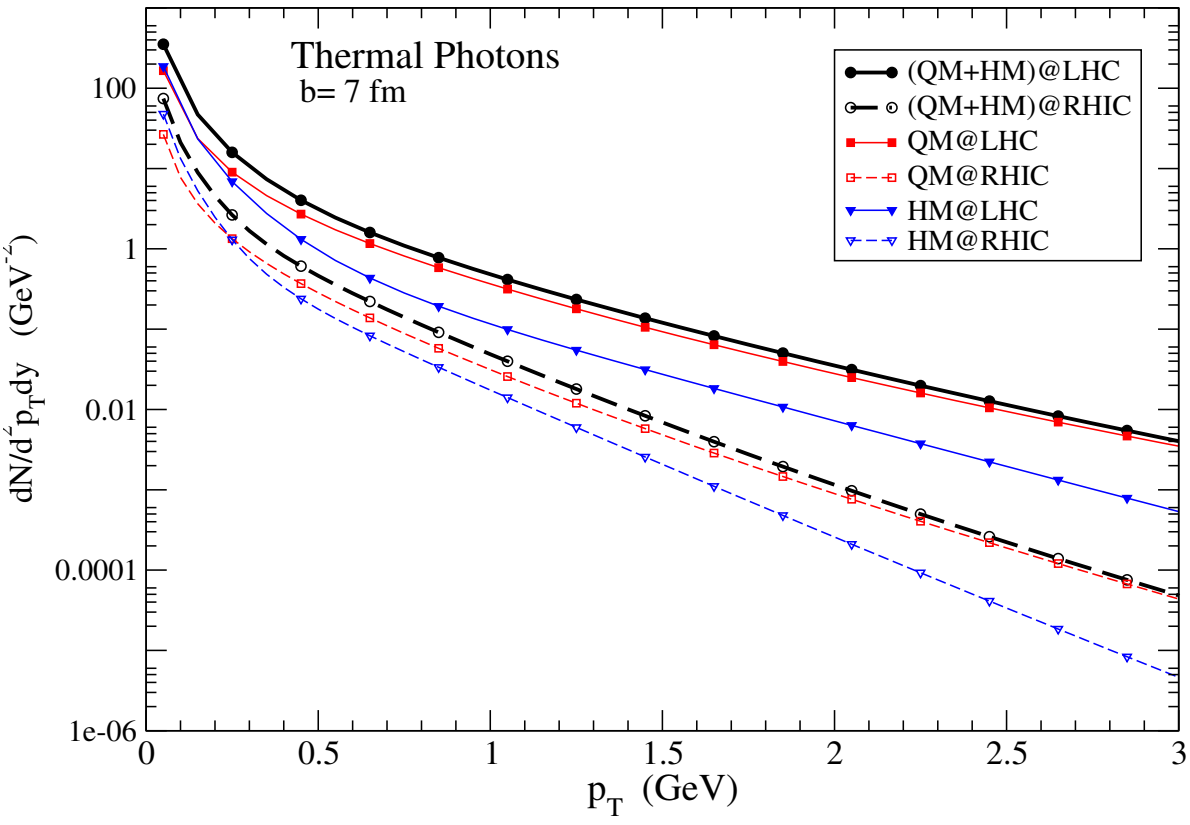

Figure 131: (Color online) Thermal photon spectra Au+Au collisions at RHIC and Pb+Pb collisions at LHC, both at $b = 7$ fm.

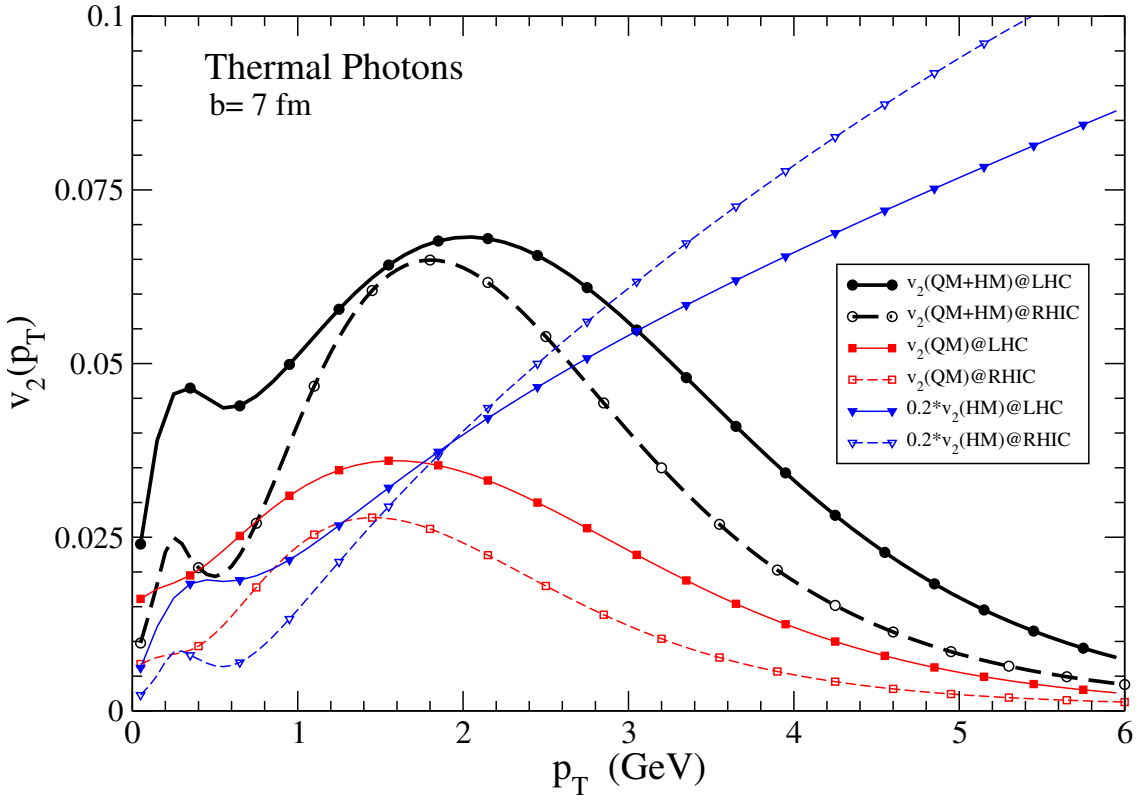

Figure 132: (Color online) Thermal photon elliptic flow for Au+Au collisions at RHIC (dashed) and Pb+Pb at LHC (solid lines), both at $b = 7$ fm.

of the positive real part in the low-mass wing (for the electrodynamic analogy see, e.g., Feynman lectures). Therefore the hadronic refractive index exceeds 1 in these energy regions.
Prediction Masses of Cherenkov states are less than in-vacuum meson masses. This leads to the asymmetry of decay spectra of resonances with increased role of low masses.
Proposal Plot the mass distribution of $\pi^+\pi^-$, $\mu^+\mu^-$, e^+e^--pairs near resonance peaks. Thus, apart from the ordinary Breit-Wigner shape of the cross section for resonance production, the dilepton mass spectrum would acquire the additional term proportional to Δn (that is typical for Cherenkov effects) at masses below the resonance peak [362]. Therefore its excess (e.g., near the ρ-meson) can be described by the following formula♯

$$\frac{dN_{ll}}{dM} = \frac{A}{(m_\rho^2 - M^2)^2 + M^2\Gamma^2}\left(1 + w\frac{m_\rho^2 - M^2}{M^2}\theta(m_\rho - M)\right) \tag{61}$$

Here M is the total c.m.s. energy of two colliding objects (the dilepton mass), $m_\rho = 775$ MeV is the in-vacuum ρ-meson mass. The first term corresponds to the Breit-Wigner cross section. According to the optical theorem it is proportional to the imaginary part of the forward scattering amplitude. The second term is proportional to Δn where the well known ratio of real to imaginary parts of Breit-Wigner amplitudes has been used. It vanishes for $M > m_\rho$ because

♯ We consider only ρ-mesons here because the most precise experimental data are available for them. To include other mesons, one should evaluate the corresponding sum of similar expressions.

only positive Δn lead to the Cherenkov effect. Namely it describes the distribution of masses of Cherenkov states. In Eq.(61) one should take into account the in-medium modification of the height of the peak and its width. We just fit the parameters A and Γ by describing the shape of the mass spectrum at $0.75 < M < 0.9$ GeV measured in [363–365]. Let us note that w is not used in this procedure. The values $A = 104\,\mathrm{GeV}^3$ and $\Gamma = 0.354$ GeV were obtained. The width of the in-medium peak is larger than the in-vacuum ρ-meson width equal to 150 MeV.

Thus the low mass spectrum at $M < m_\rho$ depends only on a single parameter w which is determined by the relative role of Cherenkov effects and ordinary mechanism of resonance production. It is clearly seen from Eq.(61) that the role of the second term in the brackets increases for smaller masses M. The excess spectrum [363–365]. in the mass region from 0.4 GeV to 0.75 GeV has been fitted by $w = 0.19$. The slight downward shift about 40 MeV of the peak of the distribution compared with m_ρ may be estimated from Eq.(61) at these values of the parameters.

Whether the in-medium Cherenkov gluonic effect is strong can be verified by measuring the angular distribution of the lepton pairs with different masses. The trigger-jet experiments similar to that at RHIC are necessary to check this prediction. One should measure the angles between the companion jet axis and the total momentum of the lepton pair. The Cherenkov pairs with masses between 0.4 GeV and 0.7 GeV should tend to fill in the rings around the jet axis. The angular radius θ of the ring is determined by the usual condition

$$\cos\theta = \frac{1}{n} \tag{62}$$

Another way to demonstrate it is to measure the average mass of lepton pairs as a function of their polar emission angle (pseudorapidity) with the companion jet direction chosen as z-axis. Some excess of low-mass pairs may be observed at the angle (62).

The prediction of asymmetric in-medium widening of any resonance at its low-mass side due to Cherenkov gluons is universal. This universality is definitely supported by experiment. Very clear signals of the excess on the low-mass sides of ρ, ω and ϕ mesons have been seen in KEK. This effect for ω-meson is also studied by CBELSA/TAPScollaboration. There are some indications at RHIC on this effect for J/ψ-meson.

To conclude, the universal asymmetry of in-medium mesons with an excess over the usual Breit-Wigner form at low masses is predicted as a signature of Cherenkov gluons produced with energies which fit the left wings of resonances where n exceeds 1.

8.6. Photons and Dileptons at LHC

R. J. Fries, S. Turbide, C. Gale and D. K. Srivastava

We discuss real and virtual photon sources in heavy ion collisions and present results for dilepton yields in Pb+Pb collisions at the LHC at intermediate and large transverse momentum p_T.

Electromagnetic radiation provides a valuable tool to understand the dynamics of heavy ion collisions. Due to their long mean free path real and virtual photons carry information

from very early times and from deep inside the fireball. We discuss the sources of photons which will be important for the upcoming heavy ion experiments at LHC. We focus on intermediate and large transverse momenta p_T and masses M. We also present our numerical results for dilepton yields.

At asymptotically large p_T the most important source of real and virtual photons is the direct hard production in primary parton-parton collisions between the nuclei, via Compton scattering, annihilation, and the Drell-Yan processes. These photons do not carry any signature of the fireball. They are augmented by photons fragmenting from hard jets also created in primary parton-parton collisions. The emission of this vacuum bremsstrahlung is described by real and virtual photon fragmentation functions. Vacuum fragmentation is assumed to happen outside the fireball, so the jets are subject to the full energy loss in the medium. This contribution to the photon and dilepton yield is therefore depleted in heavy ion collisions analogous to the high-p_T hadron yield.

At intermediate scales jet-induced photons from the medium become important. It has been shown that high-p_T jets interacting with the medium can produce real and virtual photons by one of two processes: (i) by Compton scattering or annihilation with a thermal parton, leading to an effective conversion of the jet into a photon [366]; (ii) by medium induced Bremsstrahlung [367]. Jet-medium photons have a steeper spectrum than primary photons and carry information about the temperature of the medium. They are also sensitive to the partial energy loss that a jet suffers from its creation to the point of emission of the photon. At even lower p_T and M thermal radiation from the quark gluon plasma (and also the hadronic phase not considered here) has to be taken into account.

Figure 133 shows numerical evaluations of the different contributions discussed above to the e^+e^- transverse momentum and mass spectrum for central Pb+Pb collisions at LHC. We use next-to-leading order pQCD calculations for Drell Yan and a leading order calculation for jet production. Energy loss of jets is computed with the AMY formalism [368]. Jet-medium emission and thermal emission have been evaluated in the Hard Thermal Loop (HTL) resummation scheme. For the mass spectrum we also show the expected background from correlated heavy quark decays. The full calculation for dileptons with a more extended discussion is presented in [369]. Predictions for direct photon yields including jet-medium photons can be found in [368].

Dileptons from jet-medium interactions will be more important at LHC than at previous lower energy experiments. They will be as important or even exceeding the Drell-Yan yields at intermediate masses up to about 8 GeV. They offer a new way to access information about the temperature and the partonic nature of the fireball.

8.7. Direct photons at LHC

A. H. Rezaeian, B. Z. Kopeliovich, H. J. Pirner and I. Schmidt

The DGLAP improved color dipole approach provides a good description of data for inclusive direct photon spectra at the energies of RHIC and Tevatron. Within the same framework we predict the transverse momentum distribution of direct photons at the CERN LHC energies.

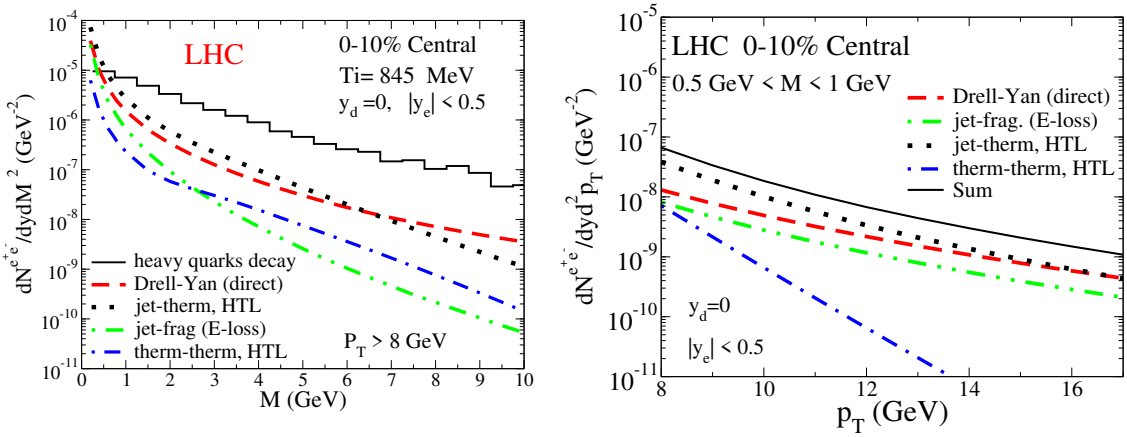

Figure 133: The yield of e^+e^- pairs in central Pb+Pb collisions at $\sqrt{s_{\rm NN}} = 5.5$ TeV. *Left*: Mass spectrum $dN/(dy_d dM^2)$ integrated over the transverse momentum p_T of the pair for $p_T > 8$ GeV/c. *Right*: Transverse momentum spectrum $dN/(dy_d d^2p_T)$ integrated over a mass range 0.5 GeV $< M <$ 1 GeV. Both panels show the case $y_d = 0$ for the pair rapidity y_d and a cut $|y_e| < 0.5$ for the single electron rapidity.

8.7.1. Introduction Direct photons, i.e. photons not from hadronic decay, provide a powerful probe for the initial state of matter created in heavy ion collisions, since they interact with the medium only electromagnetically and therefore provide a baseline for the interpretation of jet-quenching models. The primary motivation for studying the direct photons has been to extract information about the gluon density inside proton in conjunction with DIS data. However, this task has yet to be fulfilled due to difference between the measurement and perturbative QCD calculation which is difficult to explain by altering the gluon density function (see Ref. [370] and references therein). We have recently shown that the color dipole formalism coupled to DGLAP evolution is an viable alternative to the parton model and provided a good description of inclusive photon and dilepton pair production in hadron-hadron collisions [370]. Here we predict the transverse momentum spectra of direct photons at the LHC energies $\sqrt{s} = 5.5$ TeV and 14 TeV within the same framework.

8.7.2. Color dipole approach and predictions for LHC Although in the process of electromagnetic bremsstrahlung by a quark no dipole participates, the cross section can be expressed via the more elementary cross section $\sigma_{q\bar{q}}$ of interaction of a $\bar{q}q$ dipole. For the dipole cross section, we employ the saturation model of Golec-Biernat and Wüsthoff coupled to DGLAP evolution (GBW-DGLAP) [371] which is better suited at large transverse momenta. Without inclusion of DGLAP evolution, the direct photon cross section is overestimated [370]. In Fig. 134, we show the GBW-DGLAP dipole model predictions for inclusive direct photon production at midrapidities for RHIC, CDF and LHC energies. We stress that the theoretical curves in Fig. 134, are the results of a parameter free calculation. Notice also that in contrast to the parton model, neither K-factor (NLO corrections), nor higher twist corrections are to be added. No quark-to-photon fragmentation function is needed either.

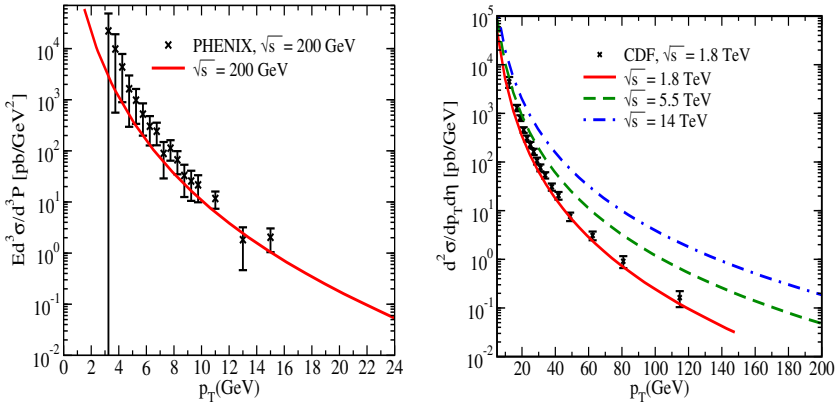

Figure 134: Direct photon spectra obtained from GBW-DGLAP dipole model at midrapidity for RHIC, CDF and LHC energies. Experimental data (right) are for inclusive isolated photon from CDF experiment for $|\eta| < 0.9$ at $\sqrt{s} = 1.8$ TeV [372] and (left) for direct photon at $\eta = 0$ for RHIC energy $\sqrt{s} = 200$ GeV [373]. The error bars are the linear sum of the statistical and systematic uncertainties.

Indeed, the phenomenological dipole cross section is fitted to DIS data and incorporates all perturbative and non-perturbative radiation contributions. For the same reason, in contrast to the parton model, in the dipole approach there is no ambiguity in defining the primordial transverse momentum of partons. Such a small purely non-perturbative primordial momentum does not play a significant role for direct photon production at the given range of p_T in Fig. 134. Notice that the color dipole picture accounts only for Pomeron exchange from the target, while ignoring its valence content. Therefore, Reggeons are not taken into account, and as a consequence, the dipole is well suited mainly for high-energy processes. As our result for RHIC and CDF energies indicate, we expect that dipole prescription to be at work for the LHC energies. At the Tevatron, in order to reject the overwhelming background of secondary photons isolation cuts are imposed [372]. Isolation conditions are not imposed in our calculation. However, the cross section does not vary by more than 10% under CDF isolation conditions [370]. One should also notice that the parametrizations of the dipole cross section and proton structure function employed in our computation have been fitted to data at considerably lower p_T values [370].

8.8. Thermal Dileptons at LHC

H. van Hees and R. Rapp

We predict dilepton invariant-mass spectra for central 5.5 ATeV Pb-Pb collisions at LHC. Hadronic emission in the low-mass region is calculated using in-medium spectral functions of light vector mesons within hadronic many-body theory. In the intermediate-mass region thermal radiation from the Quark-Gluon Plasma, evaluated perturbatively with hard-thermal loop corrections, takes over. An important source over the entire mass range are decays of correlated open-charm hadrons, rendering the nuclear modification of charm and bottom spectra a critical ingredient.

Due to their penetrating nature, electromagnetic probes (dileptons and photons) are an invaluable tool to investigate direct radiation from the hot/dense matter created in heavy-ion collisions. At low invariant mass, $M \leq 1$ GeV, the main source of dileptons is the decay of the light vector mesons, ρ, ω and ϕ, giving unique access to their in-medium spectral properties, most prominently for the short-lived ρ meson. If the chiral properties of the ρ-meson can be understood theoretically, dilepton spectra can serve as a signal for the restoration of chiral symmetry at high temperatures and densities.

We employ medium-modified vector-meson spectral functions in hot/dense matter following from hadronic many-body theory, phenomenologically constrained by vacuum $\pi\pi$ scattering, decay branching ratios for baryonic and mesonic resonances, photo-absorption cross sections on nucleons and nuclei, etc. [374]. The resulting spectral functions, especially for the ρ meson, exhibit large broadening with little mass shift, with baryonic interactions as the prevalent agent, especially in the mass region below the resonance peaks. Note that CP invariance of strong interactions implies equal interactions with baryons and antibaryons. Thus, even in a net-baryon free environment, the ρ resonance essentially "melts" around the expected phase transition temperature, $T_c \simeq 180$ MeV. Other sources of thermal dileptons taken into account are (i) four-pion type annihilation in the hadronic phase (augmented by chiral vector-axialvector mixing) [375], which takes over the resonance contributions at intermediate mass, and (ii) radiation from the Quark-Gluon Plasma (QGP), computed within hard-thermal loop improved perturbation theory for in-medium q-$\bar{q}$ annihilation.

Thermal dilepton spectra are computed by evolving pertinent emission rates over the time evolution of the medium in central 5.5 ATeV Pb-Pb collisions. To this end, we employ a cylindrical homogeneous thermal fireball with isentropic expansion and a total entropy fixed by the number of charged particles, which we estimate from a phenomenological extrapolation to be $\mathrm{d}N_{\mathrm{ch}}/\mathrm{d}y \simeq 1400$. We use an ideal-gas equation of state (EoS) with massless gluons and $N_f = 2.5$ quark flavors for the QGP, and a resonance gas for the hadronic EoS with chemical freezeout at $(\mu_B^c, T_c) = (2, 180)$ MeV (finite meson and anti-/baryon chemical potentials are implemented to conserve the particle ratios until thermal freezeout at $T_{\mathrm{fo}} \simeq 100$ MeV, with a mass-action law for short-lived resonances). We start the evolution in the QGP phase at initial time $\tau_0 = 0.17$ fm/c, translating into $T_0 \simeq 560$ MeV. The volume expansion parameters are taken to resemble hydrodynamic simulations. A standard mixed-phase construction connects QGP and hadronic phase at T_c, and the total fireball lifetime is $\tau_{\mathrm{fb}} \simeq 18$ fm/c.

As for non-thermal sources, we include primordial Drell-Yan annihilation and decays of correlated charm pairs. The latter are estimated by scaling the spectrum at RHIC with a charm-cross section anticipated at LHC, which implies somewhat softer charm spectra than expected for primordial N-N collisions (and thus softer invariant-mass spectra). We neglect contributions from jet-plasma interactions.

Our predictions are summarized in Fig. 135. At low mass thermal dileptons are dominated by hadronic radiation, with large modifications due to in-medium vector-meson spectral functions. The QGP contribution takes over at around $M \gtrsim 1.1$ GeV. The yield from correlated open-charm decays is comparable to hadronic emission already at low mass, and dominant at intermediate mass. However, this result will have to be scrutinized by

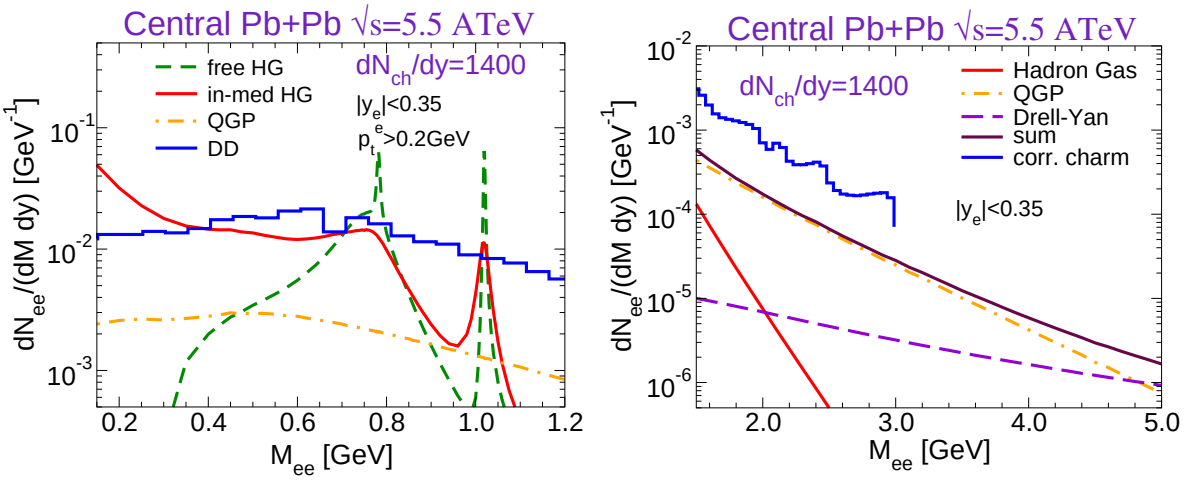

Figure 135: (Color online) Predictions for dilepton spectra in central 5.5 ATeV Pb-Pb collisions at LHC in the low- (left panel) and intermediate-mass region (right panel).

including the nuclear modification of heavy-quark spectra in the QGP (as well as analogous contributions from correlated bottom decays). Also, larger values of $\mathrm{d}N_{\mathrm{ch}}/\mathrm{d}y$ would help to outshine correlated open-charm decays, at least at low mass.

8.9. Direct γ production and modification at the LHC

I. Vitev

Baseline direct photon production cross sections are studied in $\sqrt{s} = 5.5$ TeV p+p collisions at the LHC. The fraction of fragmentation photons, which suffer QGP effects, is shown to be non-negligible even at very high $p_T \sim 200$ GeV. We first examine important cold nuclear matter effects for direct photon production, related to dynamical shadowing, isospin and initial state energy loss, in comparison to neutral pion production at $\sqrt{s} = 200$ GeV. Simulations of direct γ suppression in Pb+Pb reactions at $s^{1/2} = 5.5$ A.TeV at the LHC are also presented to high transverse momentum. Results are given in for central nuclear collisions and energy loss in the QGP calculated in the GLV approach. Direct photon quenching is shown to strongly depend on the ratio $\gamma_{\mathrm{prompt}}/\gamma_{\mathrm{fragmentation}}$ At high $p_T > 100$ GeV cold nuclear matter attenuation can be as large as the QGP effects for the net suppression of direct photons.

It has been argued that direct photon production and direct photon tagged jets provide error-free gauge for the quenching of quarks and gluons and for fixing their initial energy. We show that quantitatively large nuclear corrections must be taken into account for direct γ to become precision probes of the QGP. The left panel of Fig. 136 shows the direct photon production cross section in p+p collisions at $\sqrt{s} = 5.5$ TeV the LHC compared to the corresponding cross section at RHIC $\sqrt{s} = 200$ GeV to LO in perturbative QCD [376]. Insert shows the fraction of fragmentation to prompt photons versus p_T. The right panel of Fig. 136 shows cold nuclear effects, the Cronin [283], dynamical shadowing [377] and cold nuclear matter energy loss [285], in d+A reactions at LHC energies. Comparison to data in 0-20% central d+Au collisions at RHIC is also presented.

The left panel of Fig. 137 shows the QGP effect (final-state interactions) in central Pb+Pb collisions at $\sqrt{s} = 5.5$ TeV. Parton rapidity densities $dN^g/dy \sim 2000 - 4000$ [283], as for π^0 quenching and heavy meson dissociation, are used. Direct photon quenching closely follows the ratio $\gamma_{\rm prompt}/\gamma_{\rm fragmentation}$ [376]. At low p_T attenuation is QGP-dominated with significant and measurable suppression $R_{AA}(p_T) \sim 0.5$. Nevertheless, such quenching is smaller than the one for π^0's and reflects the C_F/C_A average squared color charge difference for quark and gluon jets. The right panel of Fig. 137 includes the effect of initial-state cold nuclear matter energy loss. At high p_T these can be comparable to the final-state quenching in the QGP [285, 376, 377].

9. Others

9.1. The effects of angular momentum conservation in relativistic heavy ion collisions at the LHC

F. Becattini and F. Piccinini

We argue that in peripheral heavy ion collisions at the LHC there might be the formation of a spinning plasma with large intrinsic angular momentum. If the angular momentum is sufficiently large, there could be striking observable effects: a decrease of chemical freeze-out temperature and an increase of transverse momentum spectra broadening (enhanced radial flow) as a function of centrality;

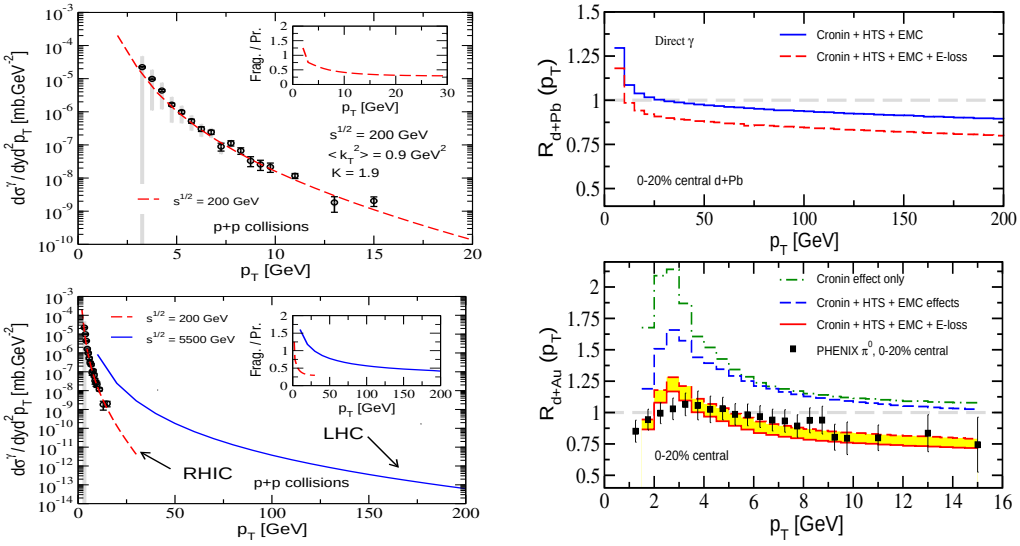

Figure 136: Left panel: Direct photon production cross section in p+p collisions at the LHC $\sqrt{s} = 5.5$ TeV. Comparison to the same cross section calculation at RHIC at $\sqrt{s} = 200$ GeV and to current high p_T data is also shown. Insert illustrates the ratio of fragmentation to prompt photons vs p_T at LO. Right panel: Nuclear modification factor R_{dA} in central d+Au collisions at RHIC and central d+Pb at the LHC, 0-20%. The high p_T behavior indicates the isospin (charge) effect and initial-state energy loss in cold nuclear matter. Comparison to similar effects on neutral pion production in d+Au collisions at RHIC, indicative for the first time for cold nuclear matter $-\Delta E_{\rm rad}$ effects at high p_T is also shown.

a large enhancement of elliptic flow; a polarization of emitted particles along the direction of angular momentum. The latter would be the cleanest signature of such effect.

In peripheral relativistic heavy ion collisions colliding ions have a large relative orbital angular momentum. While the fragments keep flying away from the interaction region essentially unaffected, a fraction of the initial angular momentum is transferred to the interaction region. Much of it is probably spent into relative orbital angular momentum of the newly formed fireballs at large rapidity, but it may happen that another significant fraction is given to the midrapidity region giving rise to a spinning plasma with an intrinsic angular momentum J. If J is sufficiently large, one has remarkable observable effects. It has been suggested that such a phenomenon can produce an azimuthal anisotropy in the transverse plane very similar to the well known elliptic flow [150]. Also, a large J may result in a polarization of emitted particles [378]. We make a quantitative determination of observable effects by assuming that the spinning system is at statistical equilibrium, taking advantage of a recent calculation of the microcanonical partition function of a relativistic quantum gas with fixed angular momentum [379, 380] which allowed us to provide the expression of particle spin density matrix and polarization in a rotating thermodynamical system. Here, a possible scenario for the LHC energy is just sketched; a more detailed paper will appear [380].

Under reasonable assumptions, the main observables which signal the presence of an equilibrated spinning system are (see figure 138): a decrease of chemical freeze-out temperature and an increase of transverse momentum spectra broadening (enhanced radial flow) as a function of centrality; a large enhancement of elliptic flow and a polarization of emitted particles along the direction of angular momentum. The latter is the cleanest signature of a spinning system. These observables scale with the parameter $J/T_c^4R^4$, T_c being the critical temperature and R the maximal transverse radius of the system. They are shown in figures below, as a function of the impact parameter or transverse momentum, for the upper bound

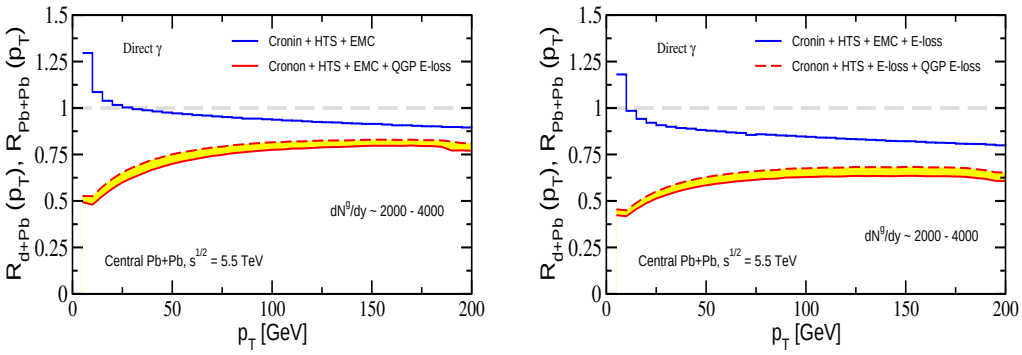

Figure 137: Left panel: Comparison of cold nuclear matter effects to QGP effects on direct photon production at the LHC. Central d+Pb and central Pb+Pb at $\sqrt{s} = 5.5$ TeV are shown. Calculations do not include initial-state energy loss. QGP suppression trend with $dN^g/dy \sim 2000 - 4000$ follows the fragmentation/prompt ratio for direct γ. Right panel: Similar calculations including initial-state cold nuclear matter energy loss effects. Note that these can yield 50% larger suppression at high p_T.

of this parameter set by the RHIC Λ polarization measurement (=0.2, blue line) and at LHC (=1.0, black line) under the assumption of a scaling of $J/T_c^4R^4$ by $\sqrt{s}/\ln\sqrt{s}^{5/3}$.
Caveat: the calculations shown in the plots concern only primary hadrons emitted from an equilibrated source. Dilution effects such as resonance decays, perturbative production at large p_T and partial equilibration are not taken into account.

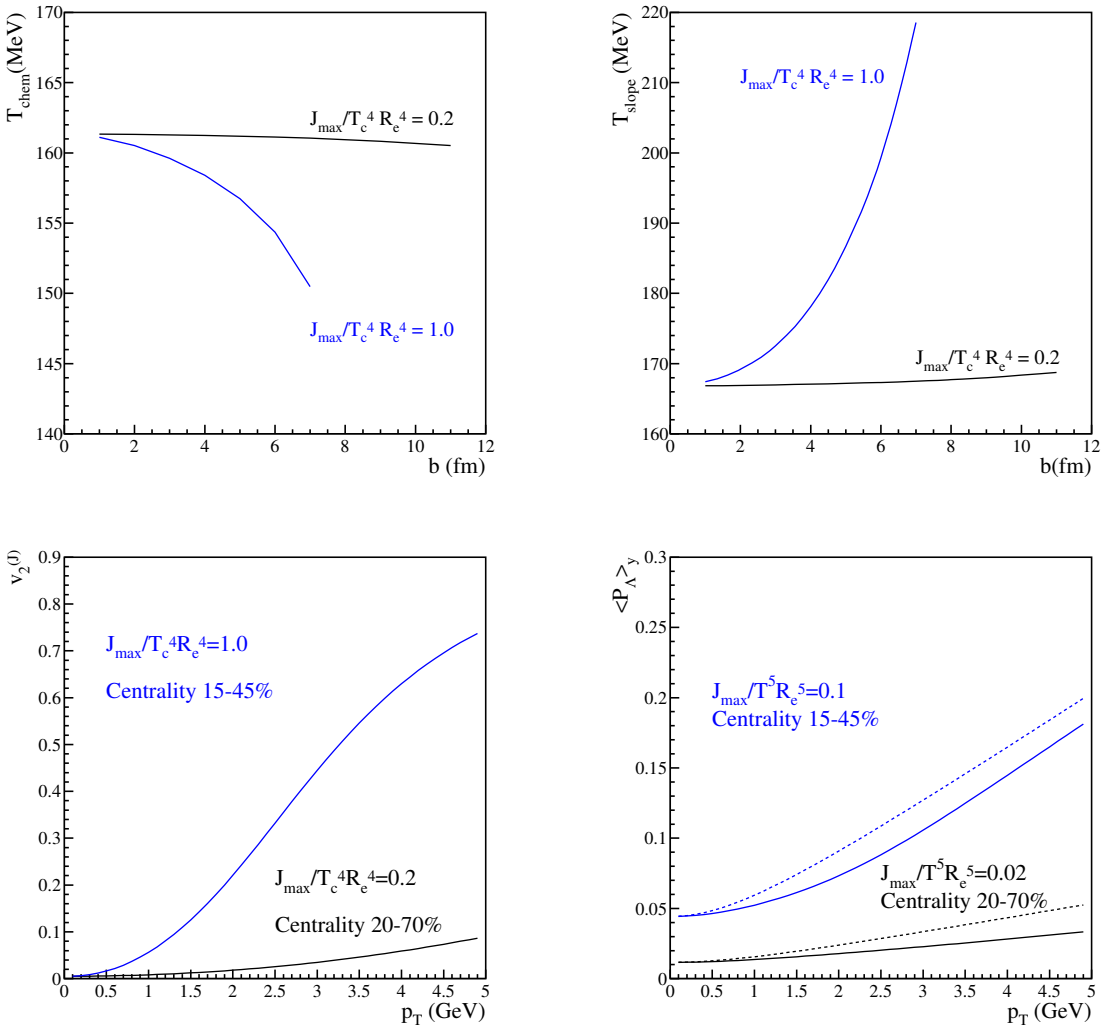

Figure 138:

9.2. Black hole predictions for LHC

H. Stöcker and B. Koch

The speculative prediction of the production of microscopical black holes, which would be possible at the large hadron collider due to large extra dimensions, is discussed. We review observables for such black holes and for the their possibly stable final state.

9.2.1. From the hierarchy-problem to black holes in large extra dimensions One of the problems in the search for a unified description of gravity and the forces of the standard model (SM), is the fact that the Planck-scale $m_{Pl} \sim 10^{19}$ GeV (derived from Newtons constant G_N) is much bigger than the energy scales like the Z-mass $m_Z \sim 90$ GeV. This huge difference is the so-called hierarchy problem. Several theories can explain this hierarchy by the assumption of extra spatial dimensions [381–383]. These theories assume a true fundamental scale M_f which is of the order of just a few TeV and they interpret the Planck scale m_{Pl} as an effective magnitude which comes into the game due to unobservable and compactified extra spatial dimensions. In the model suggested by Arkani-Hamed, Dimopoulos and Dvali [381, 382] the d extra space-like dimensions are compactified on tori with radii R. In this model the SM particles are confined to our 3+1-dimensional sub-manifold (brane) and the gravitons are allowed to propagate freely in the (3+d)+1-dimensional bulk. Planck mass m_{Pl} and the fundamental mass M_f are related by

$$m_{Pl}^2 = M_f^{d+2} R^d \quad . \tag{63}$$

One exciting consequence of such models is that up to 10^9 black holes (BH) might be produced at the Large Hadron Collider (LHC) [384]. The intuitive approximation of the cross section for such events can be made by using the Hoop conjecture and taking the classical area of the (to be produced) BH with radius R_H

$$\sigma(M) \approx \pi R_H^2 \quad , \tag{64}$$

where M is the BH mass. The Scharzschild radius is given at distances smaller than the size of the extra dimensions by

$$R_H^{d+1} = \frac{2}{d+1} \left(\frac{1}{M_f} \right)^{d+1} \frac{M}{M_f} \quad . \tag{65}$$

This radius is much larger than the Schwarzschild radius corresponding to the same BH mass in 3+1 dimensions, which translates directly into a much larger cross section (64). This estimate seems to keep its validity also in more elaborated picture .

9.2.2. From black hole evaporation to LHC observables Once a BH is produced it is assumed to undergo a rapid evaporation process. This happens first in the so called bolding phase where angular momentum and internal degrees of freedom are assumed to be radiated off. For a BH mass much bigger than the fundamental mass scale ($M \gg M_f$) the following phase is the Hawking phase, where particles are thermally radiated off according to the Hawking temperature †† [385] $T_H \approx M_f (M_f/M)^{1/(d+1)}$. As soon as the BH mass becomes comparable to the fundamental mass scale, the underlying physics of the BH is not understood and exact predictions are hardly possible at the current state of knowledge. Discussed scenarios reach from a sudden final explosion over a slowed down evaporation to the formation of stable black hole remnant (BHR) As most BHs would be produced close to

††The process of Hawking radiation would in principle allow to transform the BH mass into thermal energy and was therefore subject to further speculations

the production threshold the experimental outcome will be influenced strongly by this final phase of BH evolution.

We analyzed the predictions for different scenarios. It turned out that the, suppression of hard (TeV) di-jets above the BH formation threshold would be the most scenario independent observable for the LHC. Other observables such as event multiplicities or p_T distributions should be definitely studied although they are more model dependent. Speculations about the formation of BHRs can be tested experimentally at the LHC: Charged stable BHRs would leave single stiff tracks in the LHC detectors. Uncharged BHRs with their very small reaction cross sections could be observed by searching for events with $\sim$ 1 TeV missing energy and quenching of the high p_T hadron spectra. For further references on BHs, BHRs and their observables please see [386].

We conclude that BHs at the LHC could provide a unique experimental window to the understanding of quantum gravity. As many principles of BH production and decay are not fully understood, a large variability of experimental observables is absolutely essential to pin down the underlying physics.

9.3. Charmed exotics from heavy ion collision

S. H. Lee, S. Yasui, W. Liu and C. M. Ko

We discuss why charmed multiquark hadrons are likely to exist and explore the possibility of observing such states in heavy ion reactions at the LHC.

Multiquark hadronic states are usually unstable as their quark configurations are energetically above those of combined meson and/or baryon states. However, constituent quark model calculations suggest that multiquark states might become stable when some of the light quarks are replaced by heavy quarks. Two possible states that could be realistically observed in heavy ion collisions at LHC are the tetraquark $T_{cc}(ud\bar{c}\bar{c})$ [387] and the pentaquark $\Theta_{cs}(uds\bar{c})$ [388]. The driving mechanism for the stability of these states can be traced to the quark color-spin interaction, which can be effectively parameterized as $C_H \sum_{i>j} \vec{s_i} \cdot \vec{s_j} \frac{1}{m_i m_j}$. Baryon mass splittings between states sensitive to the color-spin interaction are well explained with a single constant coefficient $\frac{C_B}{m_u^2} = 193$ MeV [389]. Similarly, corresponding meson mass splittings are well reproduced with $\frac{C_M}{m_u^2} = 635$ MeV [389]. Hence, the correlation energy in a quark-antiquark pair is about a factor 3 larger than that in a quark-quark pair that is in the color antitriplet channel. For heavy quarks, the size of the relative wave function decreases substantially, and the parameter C_H extracted from the mass difference between J/ψ and η_c is $\frac{C_{c\bar{c}}}{m_c^2} = 117$ MeV. As in the case of light quarks, we choose $\frac{C_{cc}}{m_c^2} = \frac{1}{3}\frac{C_{c\bar{c}}}{m_c^2} = 39$ MeV. These numbers suggest that two quarks and two antiquarks would rather become two mesons than form a single tetraquark state. However, when one or both of the antiquarks become heavy, the attractions to form mesons are relatively suppressed compared to the strong diquark correlation among light quarks, making multiquark states possibly stable. Using the constants C_H discussed above, we find that the mass of T_{cc} (Θ_{cs}) is -79 MeV below (8 MeV above) its hadronic decay threshold. These results are well reproduced by full constituent quark model

calculations. Although the binding becomes larger when the c quark is replaced by a b quark, the expected number of b quarks produced in a heavy ion collision at the LHC is small for a realistic observation of such states. Therefore, we only give predictions for the multiquark states containing c quarks.

Employing the coalescence model [390], we have studied T_{cc} and Θ_{cs} production in central Au+Au collisions at RHIC and Pb+Pb collisions at LHC. Using the u (or d) quark numbers 245 and 662, the anti-strange quark numbers 150 and 405, and the charm quark numbers 3 and 20 based on initial hard collisions at RHIC and LHC, respectively all in one unit of midrapidity, we find that the numbers of T_{cc} produced at RHIC and LHC are about 5.4×10^{-6} and 8.9×10^{-5}, respectively, while those of Θ_{cs} are about 1.2×10^{-4} and 8.3×10^{-4}, respectively. Since these numbers are significantly smaller than 7.5×10^{-4} and 8.6×10^{-3} for T_{cc}, and 4.5×10^{-3} and 2.7×10^{-2} for Θ_{cs} from the statistical hadronization model for RHIC and LHC, respectively, we expect additional production of these exotic charmed hadrons from the hadronic stage of the collisions. We note that these charmed hadrons would be more abundantly produced, particularly the T_{cc}, if charm quarks are produced from the QGP formed in these collisions.

Table 9: Possible decay modes of T_{cc}. Additional $(\pi^+\pi^-)$'s are possible in the bracket.

threshold	decay mode	life time
$M_{T_{cc}} > M_{D^*} + M_D$	$D^{*-}\bar{D}^0$	hadronic decay
$2M_D + M_\pi < M_{T_{cc}} < M_{D^*} + M_D$	$\bar{D}^0\bar{D}^0\pi^-$	hadronic decay
$M_{T_{cc}} < 2M_D + M_\pi$	$D^{*-}(K^+\pi^-)$	0.41×10^{-12} s
	$\bar{D}^0(\pi^-K^+\pi^-)$	weak decay

Table 10: Possible decay modes of Θ_{cs}.

threshold	decay mode	life time
$M_{\Theta_{cs}} > M_N + M_{D_s}$	pD_s^-	hadronic decay
$M_\Lambda + M_D < M_{\Theta_{cs}} < M_N + M_{D_s}$	$\Lambda\bar{D}^0$	hadronic decay
	ΛD^-	hadronic decay
$M_{\Theta_{cs}} < M_\Lambda + M_D$	$\Lambda K^+\pi^-$, $\Lambda K^+\pi^+\pi^-\pi^-$	0.41×10^{-12} s
	$\Lambda K^+\pi^-\pi^-$	1.05×10^{-12} s

To observe T_{cc} and Θ_{cs} in experiments, we need to know their decay modes. While our analysis suggests that T_{cc} is bound and Θ_{cs} is slightly unbound with respect to their hadronic decays, we give predictions in tables 9 and 10 for all possible T_{cc} and Θ_{cs} masses. These exotic hadrons can then be observed through reconstructed final states if they decay hadronically or reconstructed final-state vertices if they decay weakly.

9.4. Alignment as a result from QCD jet production or new still unknown physics at the LHC?

I. P. Lokhtin, A. M. Managadze, L. I. Sarycheva and A. M. Snigirev

We would like to draw attention of the high-energy physics community to very important experimental results indicating our lack of understanding of features of hadron interactions at super-high energies and the necessity of improving recent theories.

The intriguing phenomenon of the strong collinearity of cores in emulsion experiments, closely related to coplanar scattering of secondary particles in the interaction, has been observed a long time ago. So far there is no simple satisfactory explanation of these cosmic ray observations in spite of numerous attempts to find it (see, for instance, [391, 392] and references therein). Among them, the jet-like mechanism [393] looks very attractive and gives a natural explanation of alignment of three spots along a straight line which results from momentum conservation in a simple parton picture of scattering.

In the Pamir experiment [391] the families with the total energy of the γ-quanta larger than a certain threshold and at least one hadron present were selected and analyzed. The alignment becomes apparent considerably at $\sum E_\gamma > 0.5$ PeV (that corresponds to interaction energies $\sqrt{s} \geq 4$ TeV). The families are produced, mostly, by a proton with energy $\geq 10^4$ TeV interacting at a height h of several hundred meters to several kilometers in the atmosphere above the chamber [391]. The collision products are observed within a radial distance $r_{\max}$ up to several centimeters in the emulsion where the spot separation $r_{\min}$ is of the order of 1 mm.

Our analysis [394, 395] shows that the jet-like mechanism can, in principle, attempt to explain the results of emulsion experiments. For such an explanation it is necessary that particles from both hard jets (with rapidities close to zero in the center-of-mass system) hit the observation region due to the large Lorentz factor under the transformation from the center-of-mass system to the laboratory one. This is possible when the combination of h, $\sqrt{s}$ and $r_{\max}$ meets the following condition:

$$2hm_p/\sqrt{s} \leq kr_{\max}, \tag{66}$$

where m_p is the proton mass. $k \sim 1/2$ is needed in order to have particles with adjoint positive and negative rapidities in the center-of-mass system that hit the detection region. At the height $h = 1000$ m (mostly used in emulsion experiment estimations) and $r_{\max} = 15$ mm the condition (66) is fulfilled at the energy $\sqrt{s} \geq 270$ TeV that is much higher than the LHC energies $\sqrt{s} \simeq 5.5 \div 14$ TeV and the threshold efficient interaction energies $\sqrt{s_{\text{eff}}} \simeq 4$ TeV [391, 392], corresponding to the alignment phenomenon. Eq. (66) can be fulfilled and at the LHC energy (14 TeV) also, but at the considerably lesser height $h \leq 50$ m which is in some contradiction with emulsion experiment vague estimations.

On the other hand if particles from the central rapidity region and the jet-like mechanism are insufficient to describe the observed alignment, and there is another *still unknown* mechanism of its appearance at the energy $\sqrt{s} \sim 5.5 \div 14$ TeV and the accepted height $h \sim 1000$ m, then in any case some sort of alignment should arise at the LHC too in the

mid-forward rapidity region (following from the laboratory acceptance criterion for, e.g., pp collisions) [394, 395]:

$$r_{\min} < r_i \Longrightarrow \eta_i < \eta_{\max} = \ln(r_0/r_{\min}) \simeq 4.95, \tag{67}$$

$$r_i < r_{\max} \Longrightarrow \eta_i > \eta_{\min} = \ln(r_0/r_{\max}) \simeq 2.25, \tag{68}$$

where $r_0 = 2h/e^{\eta_o}$, $\eta_0 = 9.55$ is the rapidity of center-of-mass system in the laboratory reference frame, η_i is the particle rapidity in the center-of-mass system, r_i is the radial particle spacing in the x-ray film. Namely, at the LHC the *strong azimuthal anisotropy of energy flux (almost all main energy deposition along a radial direction) will be observed* for all events with the total energy deposition in the rapidity interval (67, 68) larger than some threshold ~ 1 TeV. Stress once more that at present there are no models or theories giving such azimuthal anisotropy following from the experimentally observed alignment phenomenon at $\sqrt{s} \geq \sqrt{s_{\text{eff}}} \simeq 4$TeV and $h \sim 1000$ m [391, 392].

This mid-forward rapidity region must be investigated more carefully on the purpose to study the azimuthal anisotropy of energy flux in accordance with the procedure applied in the emulsion and other experiments, i.e. one should analyze the energy deposition in the cells of $\eta \times \phi$-space in the rapidity interval (67, 68). Note that the absolute rapidity interval can be shifted in correspondence with the variation of the height: it is necessary only that the difference $(\eta_{\max} - \eta_{\min})$ is equal to $\simeq 2.7$ in accordance with the variation of radial distance by a factor of ~ 15 ($r_{\max}/r_{\min} = 15$ independently of $r_0(h)$) due to the relationship $r_i \simeq r_0/e^{\eta_i}$.

Such an investigation both in pp and in heavy ion collisions (to differentiate between hadronic and nuclear interaction effects) at the LHC can clarify the origin of the alignment phenomenon, give the new restrictions on the values of height and energy, and possibly discover new still unknown physics.

Acknowledgements

The research of J. L. Albacete is sponsored in part by the U.S. Department of Energy under Grant No. DE-FG02-05ER41377.

The work of D. Antonov has been supported by the Marie-Curie fellowship through the contract MEIF-CT-2005-024196.

Part of the work of F. Arleo has been done in collaboration with T. Gousset [352] and P. Aurenche, Z. Belghobsi, and J.-P. Guillet [353].

N. Armesto acknowledges financial support by MEC of Spain under a contract Ramón y Cajal. J. G. Milhano acknowledges the financial support of the Fundação para a Ciência e a Tecnologia of Portugal (contract SFRH/BPD/12112/2003). C. A. Salgado is supported by the 6th Framework Programme of the European Community under the Marie Curie contract MEIF-CT-2005-024624. They and L. Cunqueiro, J. Dias de Deus, E. G. Ferreiro and C. Pajares acknowledge financial support by MEC under grant FPA2005-01963, and by Xunta de Galicia (Consellería de Educación).

The work of G. G. Barnaföldi, P. Levai, B. A. Cole, G. Fai and G. Papp was supported in part by Hungarian OTKA T047050, NK62044 and IN71374, by the U.S. Department of

Energy under grant U.S. DE-FG02-86ER40251, and jointly by the U.S. and Hungary under MTA-NSF-OTKA OISE-0435701. Special thanks to Prof. John J. Portman for computer time at Kent State University.

The work of V. Topor Pop, J. Barrette, C. Gale and S. Jeon was partly supported by the Natural Sciences and Engineering Research Council of Canada and by the U. S. DOE under Contract No. DE-AC03-76SF00098 and DE-FG02-93ER-40764. M. Guylassy gratefully acknowledges partial support also from FIAS and GSI, Germany.

D. Boer, A. Utermann and E. Wessels thank Adrian Dumitru and Jamal Jalilian-Marian for helpful discussions.

W. Busza wishes to acknowledge Alex Mott, Yen-Jie Lee and Andre Yoon for help with many of the plots, and Yetkin Yilmaz for N_{part} calculations.

The work of C. M. Ko was supported by the US National Science Foundation under Grant PHY-0457265 and the Welch Foundation under Grant No. A-1358, that of B. Zhang by NSF under Grant PHY-0554930, that of B.-A. Li by NSF under Grant PHY-0652548 and the Research Corporation, that of B.-W. Zhang by the NNSF of China under Grant No. 10405011 and MOE of China under project IRT0624, that of L.-W. Chen by the SRF for ROCS, SEM of China, and their joint work by the NNSF of China under Grants Nos. 10575071 and 10675082, MOE of China under project NCET-05-0392 and Shanghai Rising-Star Program under Grant No. 06QA14024.

H.-T. Ding and D. C. Zhou acknowledge respectively support from the NSFC (grants No. 10575044 and 10635020), and the Key Project of the Chinese Ministry of Education (grants No. 306022 and IRT0624).

The work of G. Kestin and U. Heinz was supported by NSF grant PHY-0354916, and theirs and the one of M. Djordjevic by U.S. DOE grant DE-FG02-01ER41190. The work of E. Frodermann was supported by an Ohio State University Presidential Fellowship.

D. d'Enterria and D. Peressounko acknowledge respectively support from 6th EU FP contract MEIF-CT-2005-025073 and MPN Russian Federation grant NS-1885.2003.2.

K. J. Eskola, H. Niemi, P. V. Ruuskanen and S. S. Räsänen thank the Academy of Finland, Projects 206024, 115262, and GRASPANP for financial support.

The work of R. Fries, S. Turbide, C. Gale and D. K. Srivastava was supported in parts by DOE grants DE-FG02-87ER40328, DE-AC02-98CH10886, RIKEN/BNL, the Texas A&M College of Science, and the Natural Sciences and Engineering Research Council of Canada.

G. Y. Qin, J. Ruppert, S. Turbide, C. Gale and S. Jeon thank the authors of [31] for providing their hydrodynamical evolution calculation at RHIC and LHC energies, T. Renk for discussions, and the Natural Sciences and Engineering Research Council of Canada for support.

The work of H. van Hees and R. Rapp is supported by a U.S. NSF CAREER Award, grant no. PHY-0449489.

The work of Z.-B. Kang and J.-W. Qiu is supported in part by the US Department of Energy under Grant No. DE-FG02-87ER40371 and contract number DE-AC02-98CH10886.

The work of D. Kharzeev was supported by the U.S. Department of Energy under Contract No. DE-AC02-98CH10886. The work of E. Levin was supported in part by the

grant of Israeli Science Foundation founded by Israeli Academy of Science and Humanity.

The work of H. Stöcker and B. Koch was supported by GSI and BMBF.

The work of A. H. Rezaeian, B. Z. Kopeliovich, H. J. Pirner, I. K. Potashnikova and I. Schmidt was supported in part by Fondecyt (Chile) grants 1070517and 1050519, and by DFG (Germany) grant PI182/3-1.

The work of I. Kuznetsova, J. Letessier and J. Rafelski has been supported by a grant from the U.S. Department of Energy DE-FG02-04ER4131. LPTHE, Univ. Paris 6 et 7 is: Unité mixte de Recherche du CNRS, UMR7589.

The work of M. Mannarelli and C. Manuel has been supported by the Ministerio de Educación y Ciencia (MEC) under grant AYA 2005-08013-C03-02.

D. Molnár thanks RIKEN, Brookhaven National Laboratory and the US Department of Energy [DE-AC02-98CH10886] for providing facilities essential for the completion of his work.

G. Torrieri thanks the Alexander Von Humboldt foundation, the Frankfurt Institute for Theoretical Physics and FIAS for continued support, and CERN theory division for providing local support necessary for attending the workshop where this work is presented. He would also like to thank Sangyong Jeon, Marek Gazdzicki, Mike Hauer, Johann Rafelski and Mark Gorenstein for useful and productive discussions.

K. Tuchin is grateful to Javier Albacete for showing me the results of his calculations of open heavy quark production; his results are in a qualitative agreement with Fig. 43 and Fig. 44. He would like to thank RIKEN, BNL and the U.S. Department of Energy (Contract No. DE-AC02-98CH10886) for providing the facilities essential for the completion of this work.

The work of R. Vogt was performed under the auspices of the U.S. Department of Energy by University of California, Lawrence Livermore National Laboratory under Contract W-7405-Eng-48 and supported in part by the National Science Foundation Grant NSF PHY-0555660.

The work of E. Wang, X. N. Wang and H. Zhang was supported by DOE under contracts No. DE-AC02-05CH11231, by NSFC under Project No. 10440420018, No. 10475031 and No. 10635020, and by MOE of China under projects No. NCET-04-0744, No. SRFDP-20040511005 and No. IRT0624.

References

[1] Bass S A *et al.* 1999 *Nucl. Phys.* A **661** 205
[2] Dias de Deus J and Milhano J G 2007 *Nucl. Phys.* A **795** 98
[3] Brogueira P, Dias de Deus J and Pajares C 2007 *Phys. Rev.* C **75** 054908
[4] Back B B *et al.* [PHOBOS Collaboration] 2005 *Nucl. Phys.* A **757** 28
[5] Kharzeev D, Levin E and Nardi M 2005 *Nucl. Phys.* A **747** 609
[6] Albacete J L 2007 *Preprint* arXiv:0707.2545 [hep-ph]
[7] Kharzeev D and Levin E 2001 *Phys. Lett.* B **523** 79
[8] Albacete J L and Kovchegov Y V 2007 *Phys. Rev.* D **75** 125021
[9] McLerran L D and Venugopalan R 1994 *Phys. Rev.* D **49** 2233
[10] d'Enterria D and Peressounko D 2006 *Eur. Phys. J.* C **46** 451, and references therein

[11] Adler S S *et al.* [PHENIX Collaboration] 2005 *Phys. Rev.* C **71** 034908 [Erratum-ibid. 049901]
[12] Aurenche P *et al* 2000 *Eur. Phys. J.* C **13** 347
[13] Pumplin J *et al.* 2002 *JHEP* **0207** 012
[14] Albino S, Kniehl B A and Kramer G 2005 *Nucl. Phys.* B **725** 181; 2006 *ibid.* B **734** 50
[15] de Florian D and Sassot R 2004 *Phys. Rev.* D **69** 074028
[16] Arleo F 2007 *JHEP* **0707** 032
[17] Stasto A M, Golec-Biernat K J and Kwiecinski J 2001 *Phys. Rev. Lett.* **86** 596
[18] Armesto N, Salgado C A and Wiedemann U A 2005 *Phys. Rev. Lett.* **94** 022002
[19] Albacete J L *et al.* 2005 *Eur. Phys. J.* C **43** 353
[20] Back B B *et al.* [PHOBOS Collaboration] 2006 *Phys. Rev.* C **74** 021901
[21] Gribov V N 1969 *Sov. Phys. JETP* **29** 483
[22] Tywoniuk K *et al.* 2007 *Preprint* arXiv:0705.1596 [hep-ph]
[23] Aktas A *et al.* [H1 Collaboration] 2006 *Eur. Phys. J.* C **48** 715; *ibid.* **48** 749
[24] Topor Pop V *et al.* 2005 *Phys. Rev.* C **72** 054901
[25] Kharzeev D 1996 *Phys. Lett.* B **378** 238
[26] Vance S E, Gyulassy M and Wang X N 1998 *Phys. Lett.* B **443** 45
[27] Topor Pop V, Barrette J, Gale C, Jeon S and Gyulassy M, these proceedings
[28] Armesto N and Pajares C 2000 *Int. J. Mod. Phys.* A **15** 2019
[29] Wiedemann U A 2007 *J. Phys. G: Nucl. Part. Phys.* **34** S503
[30] Videbaek F 2006 *J. Phys. Conf. Ser.* **50** 134
[31] Eskola K J *et al.* 2005 *Phys. Rev.* C **72** 044904
[32] Bearden I G *et al.* [BRAHMS Collaboration] 2004 *Phys. Rev. Lett.* **93** 102301
[33] Golec-Biernat K and Wusthoff M 1999 *Phys. Rev.* D **59** 014017
[34] Dumitru A, Hayashigaki A and Jalilian-Marian J 2006 *Nucl. Phys.* A **770** 57
[35] Boer D, Dumitru A and Hayashigaki A 2006 *Phys. Rev.* D **74** 074018
[36] Boer D, Utermann A and Wessels E 2007 *Phys. Rev.* D **75** 094022
[37] Boer D and Dumitru A 2003 *Phys. Lett.* B **556** 33
[38] Engel R 1995 *Z. Phys.* C **66** 203
[39] Engel R and Ranft J 1996 *Phys. Rev.* D **54** 4244
[40] Roesler S, Engel R and Ranft J 2001 *Advanced Monte Carlo 2000* (Springer) p. 1033
[41] Roesler S, Engel R and Ranft J 2003 *Nucl. Phys.* B (Proc. Suppl.) **122** 392
[42] Benecke J, Chou T T, Yang C N and Yen E 1969 *Phys. Rev.* **188** 2159
[43] Earlier discussions of the trends seen and references can be found in Busza W *et al.* [E178 Collaboration] 1975 *Phys. Rev. Lett.* **34** 836; Elias J *et al.* [E178 Collaboration] 1980 *Phys. Rev.* D **22** 13; Barton D *et al.* [E451 Collaboration] 1983 *Phys. Rev.* D **27** 2580; Busza W 1977 *Acta. Phys. Pol.* B **8** 333
[44] Busza W 2004 Acta Phys. Polon. B **35** 2873
[45] Roland G [PHOBOS Collaboration], talk at QM2005; Nouicer R [PHOBOS Collaboration], talk at PANIC 2005
[46] Otterlund I *et al.* 1978 *Nucl. Phys.* B **142** 445; Abduzhamilov A 1987 *Phys. Rev.* D **35** 3536
[47] Back B B *et al.* [PHOBOS Collaboration] 2005 *Phys. Rev. Lett.* **94** 122302; Roland G, talk at PANIC 2005
[48] Alt C *et al.* 2003 *Phys. Rev.* C **68** (2003) 034903
[49] Capella A and Ferreiro E G 2005 *Eur. Phys. J.* C **42** 419
[50] Capella A, Ferreiro E G and Kaidalov A B 2000 *Phys. Rev. Lett.* **85** 2080
[51] Capella A and Ferreiro E G 2006 *Preprint* arXiv:hep-ph/0610313
[52] Lin Z W *et al.* 2005 *Phys. Rev.* C **72** 064901
[53] Wang X N and Gyulassy M 1991 *Phys. Rev.* D **44** 3501
[54] Zhang B 1998 *Comput. Phys. Commun.* **109** 193
[55] Li B A and Ko C M 1995 *Phys. Rev.* C **52** 2037
[56] Zhang B, Ko C M, Li B A and Lin Z W 2000 *Phys. Rev.* C **61** 067901
[57] Lin Z W and Ko C M 2002 *Phys. Rev.* C **65** 034904

[58] Ko C M, Chen L W and Zhang B W 2007 *Braz. J. Phys.* **37** 969
[59] Lin Z W *et al. Phys. Rev.* C **64** 011902
[60] Zhang B, Chen L W and Ko C M 2005 *Phys. Rev.* C **72** 024906
[61] Lin Z W and Molnár D 2003 *Phys. Rev.* C **68** 044901
[62] Greco V, Ko C M and Rapp R 2004 *Phys. Lett.* B **595** 202
[63] Pratt S *et al.* 1994 *Nucl. Phys.* A **566** 103c
[64] Lin Z-W, Ko C M and Pal S 2002 *Phys. Rev. Lett.* **89** 152301
[65] Armesto N, Braun M A, Ferreiro E G and Pajares C 1996 *Phys. Rev. Lett.* **77** 3736
[66] Dias de Deus J and Ugoccioni R 2000 *Phys. Lett.* B **494** 53
[67] Pajares C 2005 *Eur. Phys. J.* C **43** 9
[68] van Eijndhoven N *et al.* 1995 *Preprint* ALICE/GEN 95-32
[69] Xu Z and Greiner C 2005 *Phys. Rev.* C **71** 064901
[70] Xu Z and Greiner C 2007 *Preprint* arXiv:hep-ph/0703233
[71] Xu Z and Greiner C 2006 *Nucl. Phys.* A **774** 787
[72] Xu Z and Greiner C, work in progress
[73] El A, Greiner C and Xu Z 2007 *Nucl. Phys.* A **785** 132; manuscript in preparation
[74] Eskola K J, Kajantie K, Ruuskanen P V and Tuominen K 2000 *Nucl. Phys.* B **570** 379
[75] Eskola K J, Ruuskanen P V, Räsänen S S and Tuominen K 2001 *Nucl. Phys.* A **696** 715
[76] Eskola K J, Niemi H, Ruuskanen P V and Räsänen S S 2003 *Phys. Lett.* B **566** 187
[77] Eskola K J, Kajantie K and Lindfors J 1989 *Nucl. Phys.* B **323** 37
[78] Gribov L V, Levin L M and Ryskin M G 1983 Phys. Rept. **100** 1
[79] Eskola K J and Honkanen H 2003 *Nucl. Phys.* A **713** 167
[80] Eskola K J, Honkanen H, Salgado C A and Wiedemann U A 2005 *Nucl. Phys.* A **747** 511
[81] Gelis F and Venugopalan R 2006 *Acta Phys. Polon.* B **37** 3253
[82] Gelis F, Stasto A M and Venugopalan R 2006 *Eur. Phys. J.* C **48** 489
[83] Gelis F and Venugopalan R 2006 *Nucl. Phys.* A **779** 177
[84] Fujii H, Gelis F and Venugopalan R 2005 *Phys. Rev. Lett.* **95** 162002
[85] Iancu E, Itakura K and Triantafyllopoulos D N 2004 *Nucl. Phys.* A **742** 182
[86] Mueller A H and Triantafyllopoulos D N 2002 *Nucl. Phys.* B **640** 331
[87] Mueller A H 2003 *Nucl. Phys.* A **724** 223
[88] Iancu E, Itakura K and McLerran L 2002 *Nucl. Phys.* A **708** 327
[89] Dumitru A *et al.* 2007 *Preprint* arXiv:0706.2540
[90] Back B B *et al.* [PHOBOS Collaboration] 2003 *Phys. Rev. Lett.* **91** 052303
[91] Jeon S, Topor Pop V and Bleicher M 2004 *Phys. Rev.* C **69** 044904
[92] Kharzeev D and Nardi M 2001 *Phys. Lett.* B **507** 121
[93] Kharzeev D, Levin E and Nardi M 2005 *Phys. Rev.* C **71** 054903
[94] Kharzeev D, Levin E and Nardi M 2004 *Nucl. Phys.* A **730** 448
[95] Kharzeev D and Levin E, *to appear*
[96] Kopeliovich B Z, Povh B and Schmidt I 2007 *Nucl. Phys.* A **782** 24
[97] Kopeliovich B Z and Povh B 2004 *J. Phys. G: Nucl. Part. Phys.* **30** S999
[98] Kopeliovich B Z, Nemchik J, Schäfer A and Tarasov A V 2002 *Phys. Rev. Lett.* **88** 232303
[99] Wang X N 2000 *Phys. Rev.* C **61** 064910
[100] Kharzeev D, Levin E and McLerran L 2003 *Phys. Lett.* B **561** 93
[101] Kopeliovich B Z, Raufeisen J and Tarasov A V 2000 *Phys. Rev.* C **62** 035204
[102] Kozlov M, Shoshi A I and Xiao B W 2007 *Nucl. Phys.* A **792** 170
[103] Iancu E, Mueller A H and Munier S 2005 *Phys. Lett.* B **606** 342
[104] Mueller A H and Shoshi A I 2004 *Nucl. Phys.* B **692** 175
[105] Drescher H J *et al.* 2001 *Phys. Rept.* **350** 93
[106] Werner K, Liu F M and Pierog T 2006 *Phys. Rev.* C **74** 044902
[107] Werner K 2007 *Phys. Rev. Lett.* **98** 152301
[108] Kharzeev D, Kovchegov Y V and Tuchin K 2003 *Phys. Rev.* D **68** 094013

[109] Kharzeev D, Kovchegov Y V and Tuchin K 2004 *Phys. Lett.* B **599** 23
[110] Kharzeev D and Tuchin K 2004 *Nucl. Phys.* A **735** 248
[111] Tuchin K 2004 *Phys. Lett.* B **593** 66
[112] Wolschin G 2007 *Nucl. Phys.* A **787** 68
[113] Kuiper R and Wolschin G 2007 *Annalen Phys.* **16** 67
[114] Peshier A *et al.* 1994 *Phys. Lett.* B **337** 235
[115] Peshier A *et al.* 1996 *Phys. Rev.* D **54** 2399
[116] Peshier A *et al.* 2000 *Phys. Rev.* C **61** 045203
[117] Peshier A *et al.* 2002 *Phys. Rev.* D **66** 094003
[118] Bluhm M *et al.* 2007 *Eur. J. Phys.* C **49** 205
[119] Karsch F *et al.* 2003 *Eur. J. Phys.* C **29** 549
[120] Karsch F *et al.* 2003 *Phys. Lett.* B **571** 67
[121] Bluhm M *et al.* 2007 *Phys. Rev.* C **76** 034901
[122] Kolb P F *et al.* 1999 *Phys. Lett.* B **459** 667
[123] Kolb P F *et al.* 2000 *Phys. Rev.* C **62** 054909
[124] Drescher H J, Dumitru A, Gombeaud C and Ollitrault J-Y 2007 *Phys. Rev.* C **76** 024905
[125] Drescher H J and Nara Y 2007 *Phys. Rev.* C **75** 034905
[126] Back B B *et al.* [PHOBOS Collaboration] 2005 *Phys. Rev.* C **72** 051901
[127] Kolb P F *et al.* 2001 *Nucl. Phys.* A **696** 197
[128] Adams J *et al.* [STAR Collaboration] 2005 *Phys. Rev.* C **72** 014904
[129] Adler S S *et al.* [PHENIX Collaboration] 2003 *Phys. Rev. Lett.* **91** 182301
[130] http://nt3.phys.columbia.edu/people/molnard/OSCAR/ and references listed there
[131] Kestin G and Heinz U 2007, *to be published*
[132] Hirano T *et al.* 2006 *Phys. Lett.* B **636** 299
[133] Hirano T *et al.* 2007 *J. Phys. G: Nucl. Part. Phys.* **34** S879
[134] Kolb P F and Heinz U 2003 *Preprint* arXiv:nucl-th/0305084
[135] Meyer H B 2007 *Preprint* arXiv:0704.1801 [hep-lat], and *to be published*
[136] Gyulassy M and Danielewicz P 1985 *Phys. Rev.* D **31** 53
[137] Kovtun P, Son D T and Starinets A O 2005 *Phys. Rev. Lett.* **94** 111601
[138] Israel W and Stuart J M 1979 *Ann. Phys.* **118** 349
[139] Molnar D and Gyulassy M 2002 *Nucl. Phys.* **A697** 495
[140] de Groot S R, van Leeuwen W A and van Weert Ch G 1980 *Relativistic Kinetic Theory* (North Holland)
[141] Molnár D and Huovinen P 2005 *Phys. Rev. Lett.* **94** 012302
[142] Zhang B, Gyulassy M and Ko C M 1999 *Phys. Lett.* B **455** 45
[143] Adil A, Gyulassy M and Hirano T 2006 *Phys. Rev.* D **73** 074006
[144] Andronic A, Braun-Munzinger P and Stachel J 2006 *Nucl. Phys.* A **772** 167
[145] Adams J *et al.* [STAR Collaboration] 2006 *Phys. Rev. Lett.* **97** 132301
[146] Topor Pop V *et al.* 2007 *Phys. Rev.* C **75** 014904
[147] Fries R J, Muller B, Nonaka C and Bass S A 2003 *Phys. Rev.* C **68** 044902
[148] Rafelski J and Muller B 1982 *Phys. Rev. Lett.* **48** 1066 [Erratum-ibid. 1986 **56** 2334]
[149] Soff S *et al.* 2004 *J. Phys. G: Nucl. Part. Phys.* **30** L35
[150] Castorina P, Kharzeev D and Satz S 2007 *Eur. Phys. J.* C **52**, 187
[151] Muller B 2007 *Nucl. Phys.* A **783** 403
[152] Acosta D *et al.* [CDF Collaboration] 2005 *Phys. Rev.* D **72** 052001
[153] Ma Y G 2006 *J. Phys.* G **32** S373
[154] Veneziano G 1976 *Nucl. Phys.* B **117** 519; Rossi G C and Veneziano G 1977 *Nucl. Phys.* B **123** 507; 1980 *Phys. Rept.* **63** 153
[155] Bartels J, Lipatov L N and Vacca G P 2000 *Phys. Lett.* **B477** 178
[156] Bopp F and Shabelski Y M 2006 *Eur. Phys. J.* A **28** 237
[157] Roesler S, Engel R and Ranft J 2000 *Preprint* hep-ph/0012252, Proc. of Monte Carlo 2000, Lisboa, October 2000, Springer, p.1033

[158] Bopp F W, Ranft J, Engel R and Roesler S 2005 *Preprint* arXiv:hep-ph/0505035v2
[159] Cleymans J, Oeschler H, Redlich K and Wheaton S 2006 *Phys. Rev.* C **73** 034905
[160] Cleymans J *et al.* 2006 *Phys. Rev.* C **74** 034903
[161] Kraus I *et al.* 2006 *J. Phys. G: Nucl. Part. Phys.* **32** S495
[162] Kraus I, Oeschler H and Redlich K 2005 *PoS* (HEP2005) 140
[163] Kraus I *et al.* 2007 *Preprint* arXiv:0707.3879 [hep-ph]
[164] Braun M A and Pajares C 2000 *Phys. Rev. Lett.* **85** 4864
[165] Dias de Deus J, Ferreiro E G, Pajares C and Ugoccioni R 2005 *Eur. Phys. J.* C **40** 229
[166] Ferreiro E G, del Moral F and Pajares C 2004 *Phys. Rev.* C **69** 034901
[167] Cunqueiro L, Ferreiro E G, del Moral F and Pajares C 2005 *Phys. Rev.* C **72** 024907
[168] Rafelski J and Letessier J 2006 *Eur. Phys. J.* C **45** 61
[169] Letessier J and Rafelski J 2007 *Phys. Rev.* C **75** 014905
[170] Torrieri G, Jeon S, Letessier J and Rafelski J 2006 *Comput. Phys. Commun.* **175** 635
[171] Torrieri G *et al.* 2005 *Comput. Phys. Commun.* **167** 229
[172] Rafelski J and Letessier J 2000 *Phys. Rev. Lett.* **85** 4695
[173] Sinyukov Yu M, Akkelin S V and Hama Y 2002 *Phys. Rev. Lett.* **89** 052301
[174] Akkelin S V, Hama Y, Karpenko Iu A and Sinyukov Yu M, in preparation
[175] Hirano T 2002 *Phys. Rev.* C **65** 011901
[176] Hirano T and Tsuda K 2002 *Phys. Rev.* C **66** 054905
[177] Hirano T, private communication
[178] Laine M and Schroder Y 2006 *Phys. Rev.* D **73** 085009
[179] Lappi T 2006 *Phys. Lett.* B **643** 11
[180] Ulery J G [STAR Collaboration] 2007 *Preprint* arXiv:0704.0224 [nucl-ex]
[181] Satarov L M, Stoecker H and Mishustin I N 2005 *Phys. Lett.* B **627** 64
[182] Baeuchle B, Csernai L P and Stoecker H 2007 *Preprint* arXiv:0710.1476 [nucl-th]
[183] Clare R B and Strottman D 1986 *Phys. Rept.* **141** 177
[184] Gyulassy M, Levai P and Vitev I 2001 *Nucl. Phys.* B **594** 371
[185] Stöcker H 2005 *Nucl. Phys.* A **750** 121; Antinori F and Shuryak E V 2005 *J. Phys.* G **31** L19; Adams J *et al.* [STAR Collaboration] 2003 *Phys. Rev. Lett.* **91** 072304
[186] Adler S S *et al.* [PHENIX Collaboration] 2006 *Phys. Rev.* C **73** 054903; Grau N [PHENIX Collaboration] 2006 *Preprint* arXiv:nucl-ex/0612019; Ajitanand N N [PHENIX Collaboration] 2007 *Nucl. Phys.* A **783** 519
[187] Adams J *et al.* [STAR Collaboration] 2005 *Phys. Rev. Lett.* **95** 152301
[188] Rischke D H *et al.* 1995 *Heavy Ion Phys.* **1** 309
[189] Dias de Deus J, Pajares C and Salgado C A 1997 *Phys. Lett.* B **407** 335
[190] Braun M A, Pajares C and Vechernin V V 2000 *Phys. Lett.* B **493** 54
[191] Brogueira P and Dias de Deus J 2007 *Phys. Lett.* B **653** 202
[192] Brogueira P, Dias de Deus J and Milhano J G 2007 *Preprint* arXiv:0709.3913 [hep-ph]
[193] Armesto N, Braun M A and Pajares C 2007 *Phys. Rev.* C **75** 054902
[194] Dremin I M 1979 *JETP Lett.* **30** 140
[195] Dremin I M 1981 *Sov. J. Nucl. Phys.* **33** 726
[196] Dremin I M 2006 *Nucl. Phys.* **A 767** 233
[197] Dremin I M 2007 *Nucl. Phys.* **A 785** 365
[198] Koch V, Majumder A and Wang X N 2006 *Phys. Rev. Lett.* **96** 172302
[199] Apanasenko A V, Dobrotin N A, Dremin I M and Kotelnikov K A 1979 *JETP Lett.* **30** 145
[200] Lisa M A, Pratt S, Soltz R and Wiedemann U 2005 *Ann. Rev. Nucl. Part. Sci.* **55** 357
[201] Frodermann E, Chatterjee R and Heinz U 2007 *J. Phys. G: Nucl. Part. Phys.* **34** 2249
[202] Frodermann E, Heinz U and Lisa M A 2006 *Phys. Rev.* C **73** 044908
[203] Retiere F and Lisa M A 2004 *Phys. Rev.* C **70** 044907
[204] Amelin N S *et al.* 2006 *Phys. Rev. C* **74** 064901
[205] Adams J *et al.* [STAR Collaboration] 2005 *Phys. Rev. C* **71** 044906

[206] Casalderrey-Solana J, Shuryak E V and Teaney D 2005 *J. Phys. Conf. Ser.* **27** 22
[207] Casalderrey-Solana J, Shuryak E V and Teaney D 2006 *Preprint* hep-ph/0602183
[208] Adler S S *et al.* (PHENIX Collaboration) 2006 *Phys. Rev. Lett.* **97** 052301
[209] Mannarelli M and Manuel C 2007 *Preprint* arXiv:0705.1047 [hep-ph]
[210] Pavlenko O P 1992 *Sov. J. Nucl. Phys.* **55** 1243
[211] Manuel C and Mrowczynski S 2006 *Phys. Rev.* D **74** 105003
[212] Torrieri G, Jeon S and Rafelski J 2006 *Phys. Rev.* C **74** 024901
[213] Jeon S and Koch V1999 *Phys. Rev. Lett.* **83** 5435
[214] Pruneau C, Gavin S and Voloshin S 2002 *Phys. Rev.* C **66** 044904
[215] Begun V V, Gazdzicki M, Gorenstein M I and Zozulya O S 2004 *Phys. Rev.* C **70** 034901
[216] Liu H, Rajagopal K and Wiedemann U A 2007 *JHEP* **0703** 066
[217] For a review see: Di Giacomo A *et al.* 2002 *Phys. Rept.* **372** 319
[218] Baier R *et al.* 1997 *Nucl. Phys.* B **483** 291
[219] Agasian N O 2003 *Phys. Lett.* B **562** 257
[220] Shoshi A I *et al.* 2003 *Phys. Rev.* D **68** 074004
[221] Barnaföldi G G *et al.* 2007 *Preprint* arXiv:hep-ph/0703059
[222] STAR preliminary data, presented by Ming Y at SQM'07 conference
[223] Abelev B I *et al.* [STAR Collaboration] 2006 *Phys. Rev. Lett.* **97** 152301
[224] Lévai P, Papp G, Fai G and Gyulassy M 2006 *Acta. Phys. Hung.* A **27** 459
[225] Capella A, Ferreiro E G, Kaidalov A B and Sousa D 2005 *Eur. Phys. J.* C **40** 129
[226] Capella A and Ferreiro E G 2007 *Preprint* arXiv:0706.1880 [hep-ph]
[227] Capella A and Ferreiro E G 2007 *Phys. Rev.* C **75** 024905
[228] Baier R *et al.* 1997 *Nucl. Phys.* B **484** 265
[229] Gribov L V, Levin E M and Ryskin M G 1981 *Nucl. Phys.* B **188** 555
[230] Casalderrey-Solana J and Wang X N 2007 *Preprint* arXiv:0705.1352 [hep-ph]
[231] Dainese A, Loizides C and Paić G 2005 *Eur. Phys. J.* C **38** 461
[232] Salgado C A and Wiedemann U A 2003 *Phys. Rev.* D **68** 014008
[233] Adler S S *et al.* [PHENIX Collaboration] 2007 *Phys. Rev.* C **76** 034904
[234] Brambilla N *et al.* 2004 *Preprint* hep-ph/0412158.
[235] Guylassy M, Vitev I, Wang X N and Zhang B W, in *Quark Gluon Plasma 3*, edited by R. C. Hwa and X. N. Wang, p. 123 (World Scientific, Singapore, 2003)
[236] Djordjevic M 2006 *Phys. Rev.* C **74** 064907
[237] Djordjevic M and Heinz U 2007 *Preprint* arXiv:0705.3439 [nucl-th]
[238] Renk R and Eskola K J 2007 *Phys. Rev.* C **75** 054910
[239] Arnold P, Moore G D and Yaffe L G 2001 *JHEP* **0111** 057
[240] Arnold P, Moore G D and Yaffe L G 2001 *JHEP* **0112** 009
[241] Arnold P, Moore G D and Yaffe L G 2001 *JHEP* **0206** 030
[242] Qin G Y *et al.* 2007 *Preprint* arXiv:0705.2575 [hep-ph]
[243] Mustafa M G 2005 *Phys. Rev.* C **72** 014905
[244] Wicks S, Horowitz W, Djordjevic M and Gyulassy M 2007 *Nucl. Phys.* A **784** 426
[245] Bassetto A, Ciafaloni M and Marchesini G 1980 *Nucl. Phys.* B **163** 477
[246] Braun J and Pirner H J 2007 *Phys. Rev.* D **75** 054031
[247] Ellis R K, Stirling W J and Webber B R 1996 *QCD and Collider Physics* (Cambridge University Press)
[248] Borghini N and Wiedemann U A 2006 *Nucl. Phys.* A **774** 549
[249] Jeon S, Jalilian-Marian J and Sarcevic I 2003 *Nucl. Phys.* A **715** 795c
[250] Jeon S, Jalilian-Marian J and Sarcevic I 2003 *Phys. Lett.* B **562** 45
[251] Jeon S, Jalilian-Marian J and Sarcevic I 2003 *Nucl. Phys.* A **723** 467
[252] Wang X N, Huang Z and Sarcevic I 1996 *Phys. Rev. Lett.* **77** 231
[253] Frantz J 2007 *J. Phys. G: Nucl. Part. Phys.* **34** S389
[254] Luo M, Qiu J-W and Sterman G 1994 *Phys. Rev.* D **49** 4493; D **50** 1951
[255] X F Guo 1998 *Phys. Rev.* D **58** 114033

[256] Kang Z B and Qiu J-W, *in preparation*
[257] Peng J C 1999 *AIP Conf. Proc.* **494** 503
[258] Liu W, Ko C M and Zhang B W 2007 *Phys. Rev.* C **75** 051901
[259] Kaczmarek O, Karsch F, Zantow F and Petreczky P 2004 *Phys. Rev.* D **70** 074505 [Erratum-ibid 2005 D **72** 059903]
[260] Kopeliovich B Z *et al.* 2004 *Nucl. Phys.* A**740** 211
[261] Berger E L 1979 *Phys. Lett.* **B 89** 241
[262] Kopeliovich B Z *et al.* 2007 *Preprint arXiv:0706.3059*
[263] Liu H, Rajagopal K and Wiedemann U A 2006 *Phys. Rev. Lett.* **97** 182301
[264] Liu H, Rajagopal K and Wiedemann U A 2007 *Phys. Rev. Lett.* **98** 182301
[265] Lokhtin I P and Snigirev A M 2006 *Eur. Phys. J.* **C 45** 211
[266] d'Enterria D *et al.* 2007 *J. Phys. G: Nucl. Part. Phys.* **34** 2307
[267] Lokhtin I P and Snigirev A M 2003 *Phys. Lett.* **B 567** 39
[268] Lokhtin I P, Petrushanko S V, Sarycheva L I and Snigirev A M 2006 *Phys. Rev.* **C 73** 064905
[269] Lokhtin I P, Sarycheva L I and Snigirev A M 1999 *Phys. Atom. Nucl.* **62** 1258
[270] Lokhtin I P, Petrushanko S V, Sarycheva L I and Snigirev A M 2003 *Pramana* **60** 1045
[271] Lokhtin I P, Petrushanko S V, Sarycheva L I and Snigirev A M 2002 *Phys. At. Nucl.* **65** 943
[272] Lokhtin I P, Sherstnev A V and Snigirev A M 2004 *Phys. Lett.* **B 599** 260
[273] Lokhtin I P and Snigirev A M 2001 *J. Phys. G: Nucl. Part. Phys.* **27** 2365
[274] Lokhtin I P and Snigirev A M 2002 *Nucl. Phys.* **A 702** 346
[275] Lokhtin I P, Sarycheva L I, Snigirev A M and Teplov K Yu 2004 *Eur. Phys. J.* **C 37** 465
[276] Pantuev V S 2007 *JETP Lett.* **85** 104
[277] Pantuev V S 2006 *Preprint* hep-ph/0604268
[278] Sapeta S and Wiedemann U A 2007 *Preprint* arXiv:0707.3494 [hep-ph]
[279] Dokshitzer Y L , Khoze V A and Troian S I 1988 *Adv. Ser. Direct. High Energy Phys.* **5** 241
[280] Azimov Y I, Dokshitzer Y L, Khoze V A and Troian S I 1985 *Z. Phys.* C **27** 65
[281] Azimov Y I, Dokshitzer Y L, Khoze V A and Troian S I 1986 *Z. Phys.* C **31** 213
[282] Borghini N and Wiedemann U A 2005 *Preprint* arXiv:hep-ph/0506218
[283] Vitev I and Gyulassy M 2002 *Phys. Rev. Lett.* **89** 252301
[284] Vitev I 2003 *Phys. Lett.* B **562** 36
[285] Vitev I 2007 *Phys. Rev.* C **75** 064906
[286] Owens J F 2002 *Phys. Rev.* D **65** 034011
[287] Wang E and Wang X N 2001 *Phys. Rev. Lett.* **87** 142301
[288] Wang E and Wang X N 2002 *Phys. Rev. Lett.* **89** 162301
[289] Zhang H, Owens J F, Wang E and Wang X N 2007 *Phys. Rev. Lett.* **98** 212301
[290] Andronic A, Braun-Munzinger P, Redlich K and Stachel J 2007 *Nucl. Phys.* A **789** 334
[291] Pauletta G [CDF and D0 Collaborations] 2005 *J. Phys. G: Nucl. Part. Phys.* **31** S817
[292] Armesto N, Salgado C A and Wiedemann U A 2004 *Phys. Rev.* D **69** 114003
[293] Armesto N *et al.* 2006 *Phys. Lett.* B **637** 362
[294] Armesto N, Dainese A, Salgado C A and Wiedemann U A 2005 *Phys. Rev.* D **71** 054027
[295] Boreskov K, Capella A, Kaidalov A and Tran Thanh Van J 1993 *Phys. Rev.* D **47** 919
[296] Adler S S *et al.* [PHENIX Collaboration] 2003 *Phys. Rev. Lett.* **96** 012304
[297] Mangano M, Nason P and Ridolfi G 1992 *Nucl. Phys.* B **373** 295
[298] Conesa del Valle Z, Martínez G, Aphecetche L and Finck C 2006 *Preprint* ALICE-INT-2006-021
[299] Ding H-T *et al.* 2007 *Preprint* hep-ph/0702118
[300] Gonçalves V P and Machado M V T 2006 *J. Phys. G: Nucl. Part. Phys.* **32** 295
[301] Gonçalves V P and Machado M V T 2005 *Eur. Phys. J.* C **40** 519
[302] Gonçalves V P and Machado M V T 2006 *Phys. Rev.* C **73** 044902
[303] Jalilian-Marian J and Kovchegov Yu V 2006 *Prog. Part. Nucl. Phys.* **56** 104
[304] Iancu E, Itakura K and Munier S 2004 *Phys. Lett.* B **590** 199
[305] van Hees H and Rapp R 2005 *Phys. Rev.* C **71** 034907

[306] van Hees H, Greco V and Rapp R 2006 *Phys. Rev.* C **73** 034913
[307] van Hees H and Rapp R 2006 *J. Phys. G: Nucl. Part. Phys.* G **32** S351
[308] Casalderrey-Solana J and Teaney D 2006 *Phys. Rev.* D **74** 085012
[309] Herzog C P *et al.* 2006 *JHEP* **0607** 013; Gubser S S 2006 *Phys. Rev.* D **74** 126005
[310] Gubser S S 2006 *Preprint* arXiv:hep-th/0611272
[311] Horowitz W A and Gyulassy M 2007 *Preprint* arXiv:0706.2336 [nucl-th]
[312] Gubser S S 2006 *Preprint* arXiv:hep-th/0612143
[313] Zhang B W, Ko C M and Liu W 2007 *Preprint* arXiv:0709.1684 [nucl-th]
[314] Beenakker W, Kuijf H, van Neerven W L and Smith J 1989 *Phys. Rev.* D **40** 54
[315] Beenakker W *et al.* 1991 *Nucl. Phys.* B **351** 507
[316] Nason P, Dawson S and Ellis R K 1988 *Nucl. Phys.* B **303** 607
[317] Nason P, Dawson S and Ellis R K 1989 *Nucl. Phys.* B **327** 49
[318] Kopeliovich B Z, Schäfer A and Tarasov A V 2000 *Phys. Rev.* D **62** 054022
[319] Kopeliovich B Z and Tarasov A V 2002 *Nucl. Phys.* A **710** 180
[320] Kopeliovich B Z, Tarasov A V and Hüfner J 2001 *Nucl. Phys.* A **696** 669
[321] Kopeliovich B Z *et al.* 2005 *Phys. Rev.* C**72** 054606
[322] Kuznetsova I and Rafelski J 2007 *Eur. Phys. J.* C **51** 113
[323] Becattini F 2005 *Phys. Rev. Lett.* **95** 022301
[324] Thews R L, Schroedter M and Rafelski J 2001 *Phys. Rev.* C **63** 054905
[325] Kuznetsova I and Rafelski J 2006 *J. Phys. G: Nucl. Part. Phys.* **32** S499
[326] Schroedter M, Thews R L and Rafelski J 2000 *Phys. Rev.* C **62** 024905
[327] Thews R L andMangano M L 2006 *Phys. Rev.* C **73** 014904
[328] Mócsy Á and P. Petreczky 2007 *Preprint* arXiv:0705.2559 [hep-ph]
[329] Mócsy Á and P. Petreczky 2007 *Preprint* arXiv:0706.2183 [hep-ph]
[330] Petrov K [RBC-Bielefeld Collaboration] 2006 *Preprint* hep-lat/0610041
[331] Kharzeev D, McLerran L D and Satz H 1995 *Phys. Lett.* B **356** 349
[332] Vitev I, Goldman J T, Johnson M B and Qiu J W 2006 *Phys. Rev.* D **74** 054010
[333] Gyulassy M, Levai P and Vitev I 2002 *Phys. Rev.* D **66** 014005
[334] Adil A and Vitev I 2007 *Phys. Lett.* B **649** 139
[335] Vitev I, Adil A and van Hees H 2007 *J. Phys. G: Nucl. Part. Phys.* **34** S769
[336] Leitch M, Lourenco C and Vogt R, presented at Quark Matter'06, Shanghai, China
[337] Braun M A *et al.* 1998 *Nucl. Phys.* B **509** 357
[338] Vogt R 2005 *Phys. Rev.* C **71** 054902
[339] Eskola K J, Kolhinen V J and Ruuskanen P V 1998 *Nucl. Phys.* B **535** 351
[340] Eskola K J, Kolhinen V J and Salgado C A 1999 *Eur. Phys. J.* C **9** 61
[341] Klein S R and Vogt R 2003 *Phys. Rev. Lett.* **91** 142301
[342] Adare A *et al.* [PHENIX Collaboration] 2007 *Phys. Rev. Lett.* **98** 232301
[343] Gunion J F and Vogt R 1997 *Nucl. Phys.* B **492** 301
[344] Digal S, Petreczky P and Satz H 2001 *Phys. Rev.* D **64** 094015
[345] Satz H 2006 *J. Phys. G: Nucl. Part. Phys.* **32** R25
[346] Vitev I 2004 *J. Phys. G: Nucl. Part. Phys.* **30** S791
[347] Karsch F and Petronzio R 1988 *Z. Phys.* C **37** 627
[348] Gavai R *et al.* 1995 *Int. J. Mod. Phys.* A **10** 3043
[349] Nayak J K, Alam J, Sarkar S and Sinha B 2007 *Preprint* arXiv:0705.1591 [nucl-th]
[350] Alam J e *et al.* 2007 *J. Phys. G: Nucl. Part. Phys.* **34** 871
[351] Aurenche P *et al.* 2006 *Phys. Rev.* D **73** 094007
[352] Arleo F and Gousset T, work in preparation
[353] Arleo F, Aurenche P, Belghobsi Z and Guillet J-P 2004 *JHEP* **0411** 009
[354] Arleo F 2006 *JHEP* **0609** 015
[355] Arleo F, d'Enterria D and Peressounko D 2007 *Preprint* arXiv:0707.2356 [nucl-th]
[356] Aurenche P *et al.* 1999 *Eur. Phys. J.* C **9** 107

[357] Bourhis L, Fontannaz M, Guillet J P and Werlen M 2001 *Eur. Phys. J* C **19** 89
[358] Arleo F 2007 *Preprint* arXiv:0707.2320 [hep-ph]
[359] Turbide S, Rapp R and Gale C 2004 *Phys. Rev.* C **69** 014903
[360] Chatterjee R, Frodermann E, Heinz U and Srivastava D K 2006 *Phys. Rev. Lett.* **96** 202302; Chatterjee R, Srivastava D K, Heinz U and Gale C 2007 *Phys. Rev.* C **75** 054909; Chatterjee R, Frodermann E, Heinz U, and Srivastava D K 2007, *to be published*
[361] Kestin G and Heinz U, *these proceedings, Sec. 2.4*
[362] Dremin I M and Nechitailo V A 2007 *Preprint* arXiv:0704.1081 [hep-ph].
[363] Arnaldi R *et al.* [NA60 Collaboration] 2006 *Phys. Rev. Lett.* **96** 162302
[364] Damjanovic S 2007 *Eur. Phys. J.* **C 49** 235
[365] Damjanovic S *et al.* [NA60 Collaboration] 2007 *Nucl. Phys.* **A 783** 327
[366] Fries R J, Müller B and Srivastava D K 2003 *Phys. Rev. Lett.* **90** 132301
[367] Zakharov B G 2004 JETP Lett. **80** 1
[368] Turbide S, Gale C, Jeon S and Moore G D 2005 *Phys. Rev.* C **72** 014906
[369] Turbide S, Gale C, Srivastava D K and Fries R J 2006 *Phys. Rev.* C **74** 014903
[370] Kopeliovich B Z, Rezaeian A H, Pirner H J and Schmidt I 2007 *Phys. Lett.* B **653** 210
[371] Bartels J, Golec-Biernat K J and Kowalski H 2002 *Phys. Rev.* D **66** 014001
[372] F. Abe *et al.* [CDF Collaboration] 1994 *Phys. Rev. Lett.* **73** 2662 [Erratum 1995 *Phys. Rev. Lett.* **74** 1891]
[373] Adler S S *et al.* [PHENIX Collaboration] 2007 *Phys. Rev. Lett.* **98** 012002
[374] Rapp R and Wambach J 1999 *Eur. Phys. J.* A **6** 415
[375] van Hees H and Rapp R 2006 *Phys. Rev. Lett.* **97** 102301
[376] Vitev I, in preparation
[377] Qiu J w and Vitev I 2006 *Phys. Lett.* B **632** 507; 2004 *Phys. Rev. Lett.* **93** 262301
[378] Liang Z T and Wang X N 2005 *Phys. Rev. Lett.* **94** 102301
[379] Becattini F and Ferroni L 2007 *Preprint* arXiv:0707.0793.
[380] Becattini F and Piccinini F, in preparation
[381] Arkani-Hamed N, Dimopoulos S and Dvali G R 1998 *Phys. Lett.* B **429** 263
[382] Antoniadis I, Arkani-Hamed N, Dimopoulos S and Dvali G R 1998 *Phys. Lett.* B **436** 25 (1998)
[383] Randall L and Sundrum R 1999 *Phys. Rev. Lett.* **83** 4690
[384] Banks T and Fischler W 1999 *Preprint* arXiv:hep-th/9906038
[385] Stoecker H 2006 *J. Phys. G: Nucl. Part. Phys.* **32** S429
[386] Koch B, Bleicher M and Stoecker H 2007 *J. Phys. G: Nucl. Part. Phys.* **34** S535
[387] Navarra F S, Nielsen M and Lee S H 2007 *Phys. Lett.* B **649** 166
[388] Sarac Y, Kim H and Lee S H 2006 *Phys. Rev.* D **73** 014009
[389] Lee S H, Yasui S, Liu W and Ko C M 2007 *Preprint* arXiv:0707.1747 [hep-ph]
[390] Chen L W, Ko C M, Liu W and Nielsen M 2007 *Phys. Rev.* C **76** 014906
[391] Kopenkin V V, Managadze A K, Rakobolskaya I V and Roganova T M 1995 *Phys. Rev.* **D 52** 2766
[392] Mukhamedshin R A 2005 *JHEP* **0505** 049
[393] Halzen F and Morris D A 1990 *Phys. Rev.* **D 42** 1435
[394] Lokhtin I P, Managadze A K, Sarycheva L I and Snigirev A M 2005 *Eur. Phys. J* **C 44** 51
[395] Lokhtin I P, Managadze A K, Sarycheva L I and Snigirev A M 2006 *Phys. Atom. Nucl.* **69** 113